Mathematical Models of Pro-remodelling Growth Factor Activation in Asthmatic Airways

Hannah J Pybus

Thesis submitted to The University of Nottingham
for the degree of Doctor of Philosophy

December 2019

Dedicated to
Steven J Pybus

Abstract

Asthma is a highly prevalent chronic disease of the lungs, characterised by inflammation, airway hyperresponsiveness and remodelling. Activation of the latent regulatory cytokine transforming growth factor β (TGF-β), during bronchoconstriction, triggers a cascade of inflammatory injury repair responses that may initiate airway remodelling, leading to asthma exacerbations and impaired lung function. The underlying mechanisms linking the characteristics of asthma and the mechanical activation of TGF-β, however, are not yet clear.

In this thesis we first develop a model comprising a system of coupled ODEs to investigate the change in density of the key airway wall constituents in response to TGF-β-induced subcellular signalling. We demonstrate that external stimuli, mimicking an asthmatic exacerbation, perturb the healthy homeostatic state to a diseased state and show that the properties of the time-dependent stimuli are critical determinants of long-term airway remodelling.

Thereafter, we develop a biomechanical model informed by precision-cut lung-slice (PCLS) experiments. PCLS, in which viable airways embedded within lung parenchyma are stretched or induced to contract, are a widely used *ex vivo* assay to investigate bronchoconstriction and, more recently, mechanical activation of TGF-β in asthmatic airways. In this thesis we develop a nonlinear fibre-reinforced biomechanical model of TGF-β activation accounting for airway smooth muscle (ASM) contraction and extracellular matrix (ECM) strain-stiffening. Through numerical simulation, we predict the stresses and deformation of an axisymmetric airway within a PCLS of finite thickness, exposing the importance of PCLS geometry, imposed stretch and ASM contractility. Motivated by the typically thin geometry of the PCLS, we then consider two simplifying limits of the model, a one-dimensional membrane representa-

tion and an asymptotic reduction in the thin-PCLS-limit, that permit analytical progress. Comparison against numerical solution of the full problem shows that the asymptotic reduction successfully captures the key elements of the full model behaviour that the membrane model does not.

Finally, we couple subcellular mechanotransductive signalling pathways to the nonlinear biomechanical models and simulate TGF-β mediated contraction and the subsequent change in effective mechanical properties as TGF-β activation continues. Crucially, the computational tractability of the asymptotically reduced biomechanical model permits efficient parameter sweeps and increases coupling feasibility. In agreement with experimental observations, we find that ASM contraction and ECM strain-stiffening increases TGF-β activation as the PCLS deforms with prescribed axisymmetric cyclic stretch. Our findings highlight, and potentially elucidate, the underlying mechanotransductive feedback mechanisms linking airway mechanics and TGF-β activation in asthma.

Acknowledgements

Firstly, I would like to thank my supervisors, Bindi Brook and Reuben O'Dea, who have provided continuous help, reassurance and insightful guidance. Their positivity and unparalleled patience has been invaluable throughout this PhD and I am very fortunate to have worked alongside them. An extra thank you to Bindi, for all of the thoughtful encouragement and support ever since my undergraduate years. I extend my appreciation to Amanda Tatler, for providing essential data, and to Lowell Edgar, for contributing expertise in FEBio, both of whom have also shown tremendous kindness during this PhD.

I am incredibly thankful to my best friends and brilliant family, near and far, for their endless encouragement, uplifting laughter and infinite amounts of love; notably to Phoebe, and all of the Pybus pets, who have kept me smiling on the rainiest of days; and especially to my awesome sister Zoe, brother George, boyfriend Tom, Mum and Dad, who have always believed in me and held my hand every step of the way, in body and in spirit.

To my Dad, who will forever be my hero, for fuelling the determination in all that I pursue; and to Tom, who I would be lost without, for making it possible to complete all that we started, thank you for everything.

Contents

CHAPTER 1

Introduction

Understanding asthma is of vital importance. Around 334 million individuals suffer from asthma and it is estimated that over 250,000 of these people die prematurely each year as a result (Forum of International Respiratory Societies 2017). Asthma is the most prominent chronic disease amongst youths, affecting over 14% of children globally (Pearce et al. 2007), yet despite its rising prevalence, the cause and onset of asthma remains unknown.

Asthma is characterised by inflammation, airway hyperresponsiveness and remodelling (Brightling et al. 2012; Berair et al. 2013). Airway hyperresponsiveness refers to excessive bronchoconstriction (narrowing of the airway) due to rapid contraction of airway smooth muscle (ASM) in response to a relatively low dose of contractile agonist (King et al. 1999; West et al. 2013). Chronic inflammation causes swelling of the airway tissue, narrowing the airway (León 2017), and resulting in overall restricted pulmonary function. The persistent structural changes due to inflammatory injury repair, airway thickening and scarring constitute airway remodelling (Bossé et al. 2008; Al Alawi et al. 2014). Until recently, airway remodelling has been predominantly attributed to chronic inflammation (Saglani and Lloyd 2015). Current experimental evidence, however, suggests that bronchoconstriction induced airway narrowing may play a key role in promoting remodelling (Grainge et al. 2011). Bronchoconstriction activates the regulatory cytokine, transforming growth factor β (TGF-β) (Buscemi et al. 2011; Tatler et al. 2011; Wipff et al. 2007), which may further stimulate ASM contraction (Ojiaku et al. 2018), ASM proliferation (Chen and Khalil 2006), and deposition of extracellular matrix (ECM) (Pohlers et al. 2009),

altering the airway mechanics (Makinde et al. 2007; Burgess et al. 2016). In the healthy airway, regulatory mechanisms terminate this process (Hinz 2015), thereby maintaining homeostasis. We hypothesise that in asthma this homeostatic state is lost, resulting in accumulation of ECM and contraction of ASM, further up-regulating TGF-β production through a positive mechanotransductive feedback loop. However, the mechanisms underlying cell-mediated TGF-β activation, during an asthmatic exacerbation, are not clear.

In this introductory chapter we review the relevant biological background (glossary of the introduced biological acronyms provided in Appendix A.1) required to explain our mathematical model development. We describe the composition of the airway with focus on the key airway wall components, ASM and ECM, and the cytokine TGF-β. Thereafter, we detail the hallmarks of asthma that affect the normal function of the airway and how structural alterations of ASM and ECM (potentially TGF-β induced) may contribute to these factors. We then describe some of the existing experimental models and, importantly, outline the protocol of the precision-cut lung-slice (PCLS) stretching experiments, performed by our collaborator Tatler (2016), that we base our biomechanical model development upon. We review relevant mathematical models and approaches that inform the development of our biomechanical PCLS description and finally, provide an overview of the structure of this thesis.

1.1 Respiratory system

The following descriptions of the respiratory system and airway wall anatomy are well-established observations from the extensive literature and covered in detail in the text books West (2008) and West (2011).

1.1.1 Airway wall anatomy

The airway wall is composed of a variety of cells, fibres and structures (illustrated in Figure 1.1). The strong and flexible basement membrane, made up of collagenous fibres, separates subsets of the different cell types into two distinct layers, namely the mucosa and submucosa layers. Epithelial and goblet

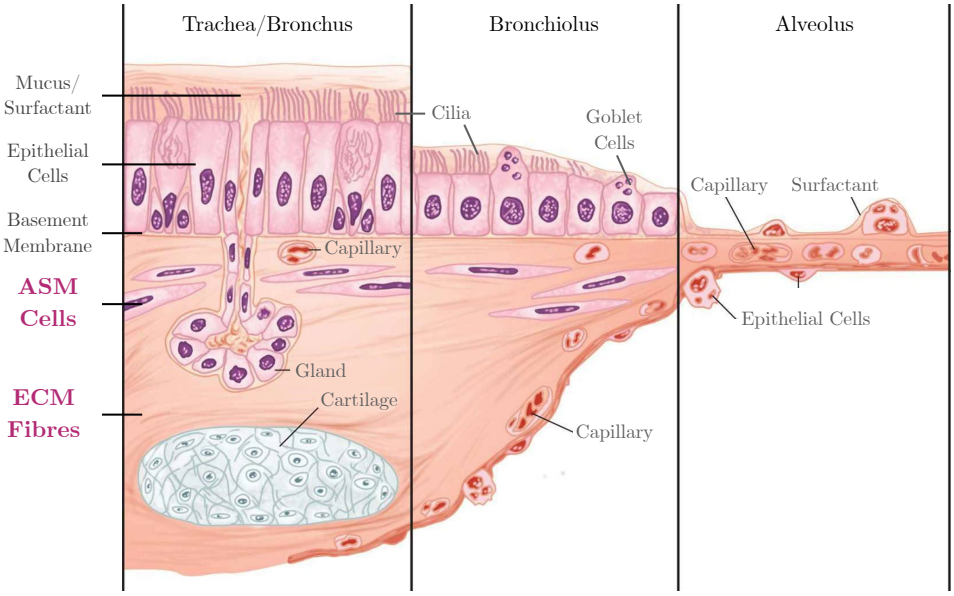

Figure 1.1: Airway wall structure, above the basement membrane is the mucosa cell layer, below is the submucosa cell layer. Image adapted from Barrett et al. (2009).

cells are found within the mucosa layer that is above the basement membrane. Epithelial cells line the lumen and have a protruding hair-like cilia on the surface. Goblet cells, responsible for mucus secretion, are interspaced between the epithelial cells. In order to cleanse inhaled air within the lungs, particles are trapped by the mucus and then transported up the airway by the cilia. The submucosal layer is beneath the basement membrane and comprises blood vessels, submucosal glands, fibroblast cells, mast cells and ASM cells embedded within a delicate mesh of ECM. Like the goblet cells, the submucosal glands secrete mucus. Fibroblast cells secrete proteins (alongside having other roles), that form ECM. Mast cells are a type of white blood cell responsible for secreting cytokines and other mediators in the presence of inflammation. The surrounding blood vessels transport oxygenated blood to the cells within this area. Cartilage is found in strong and flexible rings in the upper airways and offers support to the trachea during breathing motions.

Model development in the subsequent chapters of this thesis is applicable to airway generations 1–10 (see bronchiolus Figure 1.1) and in particular, the interactions between the ASM cells and ECM.

1.1.2 Airway smooth muscle

The spindle-shaped ASM cells (Kuo et al. 2003) form bundles that surround the lumen of the bronchi, the orientation of which depends on the location within the bronchial tree (Ijpma et al. 2017). In the larger bronchi, the bundles are mainly circumferential (Amrani and Panettieri 2003), whereas within the smaller bronchi and bronchioles the ASM bundles tend to arrange themselves in a more helical structure. It is thought that the helical formation of ASM bundles in the smaller bronchi enhances the muscle's ability to contract the airway (referred to as bronchoconstriction) (Amrani and Panettieri 2003). Myosin and actin filaments are contractile proteins in the ASM cell. Binding and unbinding of myosin cross-bridges to actin binding sites (referred to as cross-bridge cycling) causes the filaments to slide over each other and causes contraction of the ASM cell (Lavoie et al. 2009).

Contraction, proliferation, cytokine production and ECM secretion are the primary roles of the ASM. It is suggested that ASM cells express fewer contractile proteins whilst proliferating and therefore generate less contractile force than non-proliferating ASM cells (Bentley and Hershenson 2008). Hence, the roles of the proliferating and contractile ASM phenotype differ, whereby the contractile phenotype initiates contraction and the proliferative increases ASM mass. Both ASM contraction and growth generates tissue stresses, deforming neighbouring cells, and connective tissues, which can in turn affect the growth and mechanical properties of those airway constituents (Stolarska et al. 2009). ASM cell shortening stretches surrounding connective tissue, which in part provides a recoil force to open the airway once the ASM relaxes (Khan 2016). Relaxation of the ASM is associated with decreased airway wall stiffness (Ito et al. 2006), whilst contraction of the ASM is associated with increased airway wall stiffness (An et al. 2002). Contraction may exaggerate the thickness of the ASM cell layer (Bentley and Hershenson 2008) and the thickness of the ASM layer has been signified as a determinant for airway wall compliance in the presence of muscle tone but not following relaxation (Tiddens et al. 1999), suggesting that the contractile properties of the ASM are more influential than the passive components determining airway wall stiffness (Noble et al. 2014).

Connective tissues and cells, including ECM and ASM cells, interact and trans-

mit mechanical strain between one another via focal adhesions comprising transmembrane receptors known as integrins (Kanchanawong et al. 2010; Irons et al. 2018). Mechanotransduction is the cellular response to transmitted strain (Noble et al. 2014) and regulates many of the ASM properties including phenotype, stiffness, contractility, proliferation and cytokine production (Amrani and Panettieri 2003; Khan 2016; Januskevicius et al. 2016). Mechanotransductive feedback occurs as the ASM secretes components forming ECM and in turn becomes functionally responsive to the composition of the ECM (Chan et al. 2006; Johnson et al. 2004). Importantly, airway wall stiffness, due to stiffened ECM, impacts the ASM cells contractile response and as a result, the extent to which the airway narrows during bronchoconstriction (Khan 2016).

1.1.3 Extracellular matrix

The ECM is a delicate mesh of deposited connective tissue and fibrous proteins (Cheng et al. 2016), surrounding ASM cell bundles, that provides physical support and stability to the lung (Burgess et al. 2016; Khan 2016). Freyer et al. (2001) report that the ECM constituents fibronectin, laminin and collagen appear to aid the survival of the embedded ASM, which in turn secrete compounds to replenish the ECM to form a positive feedback loop. However, the overall accumulation of ECM does not significantly change over time within the normal healthy airway as the ECM appears to exhibit a balance between its deposition and degradation (Makinde et al. 2007).

Relatively stiff collagen fibres, the main component of ECM, group together to form wavy bands and protect the airways and the lung from over expansion (Kadler et al. 1996) by straightening (Mercer and Crapo 1990) thereby stiffening the airway when they are stretched. Similarly, the relatively more compliant elastin fibres within the ECM form concentric bands and are responsible for recoil within the lungs (Shifren and Mecham 2006; Starcher 1986). These ECM proteins display linear elastic behaviour when subject to small deformations yet strain-stiffen at greater length changes (Wells 2013). Alteration to the stiffness and structure of the ECM, during deformation, transmits mechanical signals from the ECM to intracellular domains via integrins (Tatler and Jenkins 2015) and stimulate mechanotransductive pathways that determine the resultant cel-

lular response to the subjected strain (Noble et al. 2014).

1.1.4 Transforming growth factor β

Initially identified in human platelets as a protein associated with signalling in wound healing (Assoian et al. 1983), the pro-inflammatory cytokine TGF-β plays a vital role in regulating the immune system (Letterio and Roberts 1998). The vast majority of structural and immune cells, including ASM, epithelial and fibroblast cells secrete TGF-β (Xu et al. 2003; Leivonen et al. 2005; Al Alawi et al. 2014), of which there are five known isoforms, three identified in mammals (Munger et al. 1998; Memon et al. 2008), each with a specific role in regulation of inflammation, cell growth and differentiation (Li et al. 2007; Al Alawi et al. 2014). The studies of Tatler et al. (2011); Tatler and Jenkins (2012); Al Alawi et al. (2014); Aschner and Downey (2016) suggest that the concentration of first isoform, TGF-β1, within the airway is paramount, since TGF-β2 and 3 expression is postponed in the absence of TGF-β1, consequently delaying wound healing processes (Crowe et al. 2000).

TGF-β is secreted as part of the large latent complex (LLC) that resides in the ECM (Tatler et al. 2011) and which comprises the latency associated protein (LAP), latent TGF-β binding protein (LTBP) and latent TGF-β (Annes et al. 2004; Koli et al. 2005; Wipff et al. 2007; Vehviläinen et al. 2009) (illustrated in Figure 1.2). The LTBP-1 provides anchorage for the LLC to proteins within the ECM (Hinz 2015) which acts as a reservoir of latent TGF-β (Shi et al. 2011). Forces are generated during a cell contraction in response to applied stretch, cytoskeletal reorganisation or reaction to chemical trigger. The contractile force generated within the ASM cell is transmitted via the integrins attaching the LAP and the LLC to the cell surface (Wipff et al. 2007; Tatler and Jenkins 2012; 2015; Tatler et al. 2016). For a compliant ECM, the LLC is dragged in an intact form towards the contracting cell (Buscemi et al. 2011). Due to the lack of mechanical resistance, there is little to no conformational change and the TGF-β remains latent. When the LLC is anchored in a comparably stiff ECM, cell-mediated stress induces conformational changes in the LTBP, allowing the LAP to unfold, leading to the liberation of TGF-β from the LAP and therefore the activation of TGF-β (Keski-Oja et al. 2004; Wipff et al. 2007). We use the term 'TGF-β activation' to

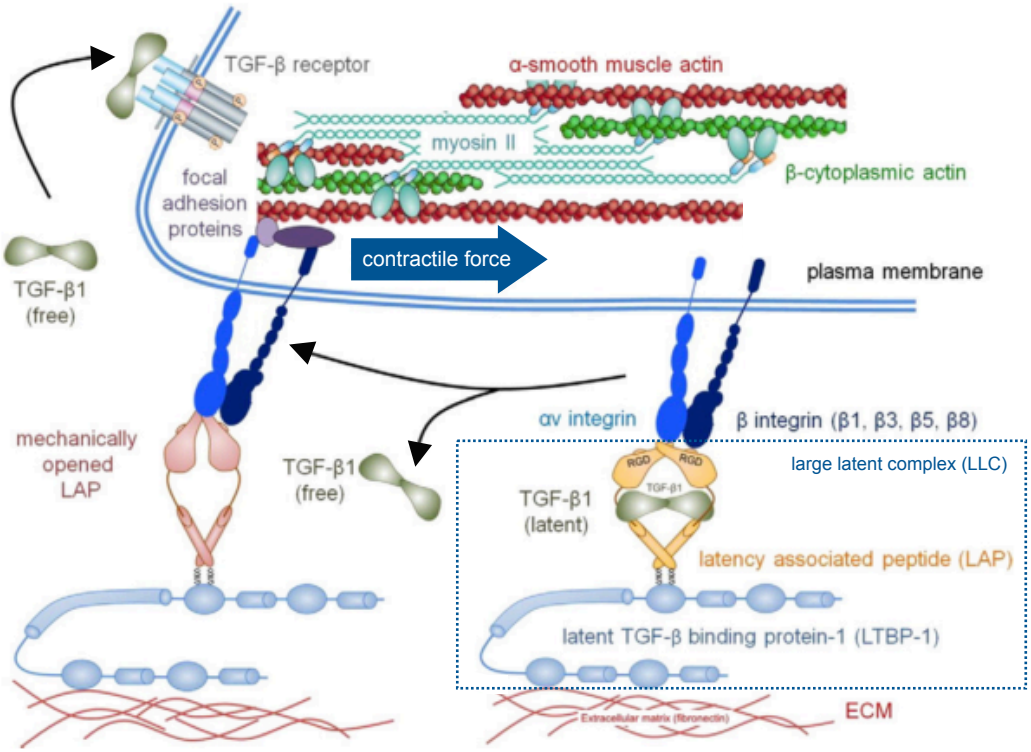

Figure 1.2: Mechanical activation of latent TGF-β. Active TGF-β is liberated from the LLC (indicated by the dotted inset) following LAP conformational changes, induced by actin and myosin mediated cell contraction and transmitted via integrins. Image adapted from (Hinz 2015).

denote the separation of TGF-β from the LLC (Annes et al. 2003) and 'latent' indicates its inactive storage (Gleizes et al. 1997). Both the contractile ASM and the ECM are required for the mechanical activation of TGF-β (Tatler and Jenkins 2012; 2015; Tatler et al. 2016); however, the process does not reduce their densities.

Latent TGF-β requires activation for functionality (Keski-Oja et al. 2004; Tatler et al. 2011). Hence, the circulation of active TGF-β to target destinations within the tissue, and the concentration of active TGF-β within these regions, is regulated by the rate-limiting activation of the latent form (Gleizes et al. 1997; Jolly et al. 2014; Tatler and Jenkins 2015). Significant quantities of latent TGF-β are contained within tissues, yet activation of only a small fraction of the latent form generates a maximal cellular response (Annes et al. 2003). Once activated, TGF-β binds to cell surface receptors (Derynck and Zhang 2003; Shi et al. 2011; Aschner and Downey 2016) to stimulate complex molecular signal trans-

mission, which initiates multiple cellular responses including cell contraction, apoptosis, differentiation, migration, proliferation, survival and ECM secretion (Khalil et al. 2005; Perng et al. 2006; Berair et al. 2013; Ojiaku et al. 2018). For example, TGF-β contributes to the regulation of ECM formation in lung tissue during lung development (Kaartinen et al. 1995; Al Alawi et al. 2014) by directing fibroblast and ASM cells to secrete proteins which influence the composition of the ECM. Importantly, relevant to our hypothesis, TGF-β stimulates ASM contraction (Ojiaku et al. 2018) which may further up-regulate TGF-β production.

Active TGF-β binds to cell surface receptors to stimulate complex molecular signal transmission via intracellular intermediates known as Smads (Derynck and Zhang 2003; Aschner and Downey 2016) . Once activated, TGF-β receptors regulate the Smad proteins that are used to convert proteins in gene expression (Itoh et al. 2003). Smad independent pathways are likewise activated by TGF-β (Yu et al. 2002).

1.2 Asthmatic airways

Asthmatics suffer intense repeated episodes of serious coughing, wheezing, breathlessness and experience tightness in the chest (Brightling et al. 2012). Severe asthmatics develop irreversible airway obstruction (Brown et al. 1984). For the most part symptoms are induced following exposure to an irritant (King et al. 1999). Commonly, the trigger is an allergen such as pollens, mould and animal fur (Bossé et al. 2008). Others may include tobacco smoke, exercise, aspirin, insulin and respiratory infections (Wenzel 2006; Schaafsma et al. 2007; Kim et al. 2011). The characteristics of asthma that are illustrated in Figure 1.3 are explained in the following sections.

TGF-β expression is increased within the asthmatic airway (Ojiaku et al. 2018) and correlates with asthma severity (Chen and Khalil 2006; Al Alawi et al. 2014). Continual exposure to an allergen causes TGF-β to stimulate a dysregulated repair process of inflammation-induced injury to the epithelial cell surface by promoting ECM deposition which consequently thickens the subepithelial basement membrane (Al Alawi et al. 2014). Furthermore, increased ASM mass

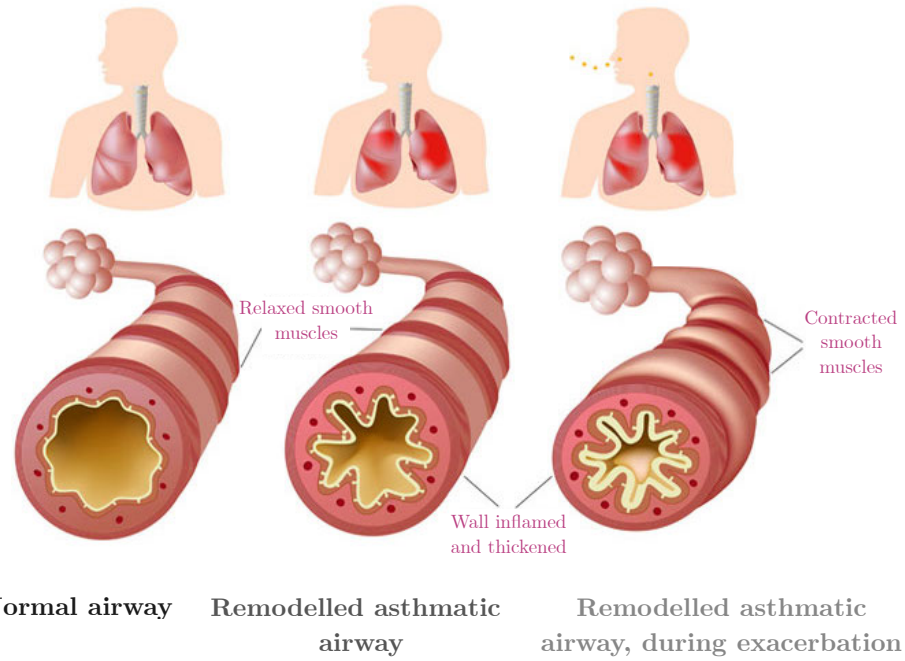

Figure 1.3: Image illustrating the characteristics and physical differences of a normal healthy airway (left), asthmatic airway (centre) and asthmatic airway during an asthma attack (right). Image adapted from DoveMed (2018).

throughout the lungs is identified in severe asthma (Tatler et al. 2011; Al Alawi et al. 2014). ASM contraction is chronically elevated in the asthmatic airway (Noble et al. 2014), which may up-regulate contraction-induced activation of TGF-β. Supporting evidence (Tatler et al. 2011; Tatler and Jenkins 2012) demonstrates that ASM cells, in both asthmatic and non-asthmatic airways, are capable of mechanically activating TGF-β via integrins in response to a trigger. Furthermore, inhibition or deficiencies of integrins *in vivo* lead to a reduction in ASM layer remodelling (Tatler et al. 2011; Tatler and Jenkins 2012). In light of such findings, it is thought that uncontrolled bronchoconstriction in asthma stimulates TGF-β activation and hence promotes airway remodelling in asthma (Noble et al. 2014; Ojiaku et al. 2018).

1.2.1 Inflammation

Sustained inflammation, caused by inhaled irritants, injures the airways (Jeffery 2001) and triggers a repair response (Jeffery 2001; Xia et al. 2013) (see Figure

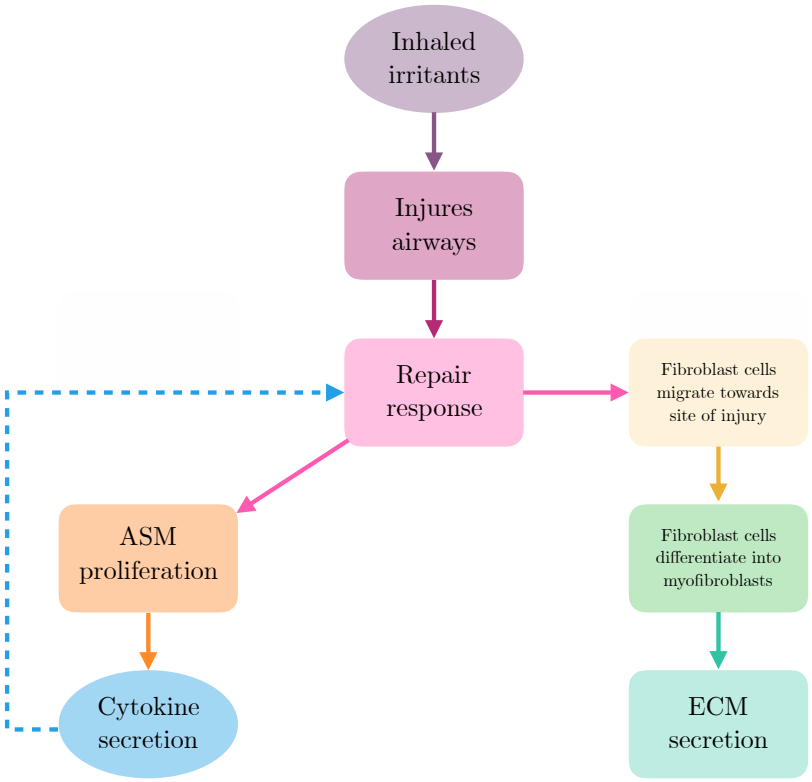

Figure 1.4: Flowchart diagram illustrating the processes of airway inflammation.

1.4). Initially, this response promotes ASM cell proliferation and fibroblast cell migration towards the site of injury. The recruited fibroblasts differentiate into myofibroblasts, which specialise in ECM production (Parker et al. 2014) and the increase of ASM mass, due to enhanced ASM proliferation, increases cytokine secretion (Amrani and Panettieri 2003). Further injury repair responses are therefore initiated by the presence of cytokines, including active TGF-β, which in turn lead to an increase in connective tissue deposition (Chen and Khalil 2006). Physiological tissue repair restores the mechano-protective properties of the ECM and in the normal airway is terminated via regulatory mechanisms once homeostasis is re-established (Hinz 2015). Failure of this mechanism is thought to maintain continual activation of repair responses and leads to an excessive accumulation of altered ECM (Hinz 2015). The imbalanced ECM constituent profile (Johnson et al. 2004; Bergeron et al. 2009; Cheng et al. 2016; Januskevicius et al. 2016) subsequently impacts the stiffness of the ECM (Booth et al. 2012) and correlates with the severity of asthma and airway hyperresponsiveness (Bergeron et al. 2009).

1.2.2 Airway hyperresponsiveness

Mucus is continually produced to protect the airways by trapping harmful inhaled particles. Mucus hypersecretion, apparent in asthmatic airways, is the excessive production of mucus leading to possible blockages in the airway (Rogers 2004) (Figure 1.3). Despite the protective properties of mucus, some inhaled allergens may still interfere with the sensitive epithelial cell layer and cause an allergic response (Jeffery 2001). Exposure to an allergen thereby activates a vast range of mediators, including TGF-β, following a cascade of complex intracellular signalling processes (Holgate and Polosa 2008), which result in mucus secretion, fibroblast transition (Reeves et al. 2015), ASM cell contraction and increased vascular permeability that allows immune system cells to leave the blood stream (Pundir et al. 2013). Excessive cellular reactions subsequently hinder the lungs function by restricting airflow (Aschner and Downey 2016). Airway hyperresponsiveness is defined as rapid contraction of ASM, during bronchoconstriction, in response to a relatively lose dose of contractile agonist (Postma and Kerstjens 1998). Airway hyperresponsiveness and mucus hypersecretion cause significant airway narrowing (Pelaia et al. 2008) (Figure 1.3).

Continual contractile activation of ASM cells causes the ASM to experience sustained periods at a shortened length (Bossé et al. 2009; Ojiaku et al. 2018). ASM may adapt to length changes by remodelling intracellular actin and myosin filaments to shift the peak of the active force-length curve towards the new length, and are therefore capable of generating maximum force over a wide range of lengths (Bossé et al. 2009; Stålhand and Holzapfel 2016). Length adaption of the ASM is much faster in the presence of contractile activation (Wang et al. 2001). Consequently, the ASM may have an increased shortening capacity and progressively narrow the airway (Bullimore et al. 2011). Airway narrowing, further augmented by increased ASM mass, may exaggerate the degree of bronchochonstriction, contributing to airway hyperresponsiveness (Naghshin et al. 2003; Noble et al. 2014). Structural changes of the airway wall may likewise induce airway hyperresponsiveness (Amrani and Panettieri 2003) by altering the forces imposed on the ASM and the contractility of those ASM cells.

1.2.3 Airway remodelling

Airway remodelling is the alteration to the structural components and composition of the airway wall and is caused by progressive changes to the organisation of cellular and molecular constituents within (Panettieri 1998; Jeffery 2001; Bossé et al. 2008). The long term effects of disrupted inflammatory injury repair processes, airway thickening, narrowing and scarring constitute airway remodelling (Bossé et al. 2008; Al Alawi et al. 2014), subsequently leading to overall restricted pulmonary function (Bousquet et al. 2000) (Figure 1.3). Some modifications may be reversible (Alrifai et al. 2014; Brook et al. 2019); however, others are partially irreversible and predominantly associated with severe asthma (Tatler et al. 2011; Al Alawi et al. 2014).

Fibrosis development and stiffening of the ECM during remodelling affects cell adhesion and thereby encourages cells to migrate towards a stiffer ECM (Plotnikov and Waterman 2013). This generates anisotropy within the airway wall as the elastic modulus of the ECM will be higher in the vicinity of contracting cells than in cell-free regions (Hinz 2015). An abnormal increase in tissue volume due to the formation and growth of new cells is defined as hyperplasia (Berair et al. 2013), whereas an abnormal increase in tissue volume derived entirely by the enlargement of the existing constituent cells is defined as hypertrophy (Benayoun et al. 2003). A combination of both ASM hyperplasia and hypertrophy may be the cause of an increase in ASM mass which thickens the airway. Furthermore, it is suggested that the increase in ASM mass correlates with asthma severity rather than duration (Ebina et al. 1990; Bai et al. 2000; Woodruff et al. 2004; Kaur et al. 2010; Girodet et al. 2011; Cheng et al. 2016). Although hypertrophy is observed (Benayoun et al. 2003), hyperplasia is generally believed to be key in ASM mass accumulation (Girodet et al. 2011) and various authors suggest that this may be due to elevated ASM proliferation and survival rates (Johnson et al. 2001; Trian et al. 2007; Pelaia et al. 2008; Januskevicius et al. 2016). However, the findings of Kaur et al. (2010) and Ward et al. (2008) indicate that *in vitro* ASM proliferation and survival rates are not significantly different between asthmatic and non-asthmatic cells, suggesting that there may be underlying mechanisms, other than increased proliferation, responsible for ASM accumulation in asthma. Note, however, that cultured

cell populations contain higher numbers of proliferative rather than contractile phenotype (which is likely not the case *in vivo*) (Tatler 2016).

Continual exposure to a contractile agonist is thought to increase TGF-β expression in the asthmatic airway (Abe et al. 2001; Chen and Khalil 2006; Makinde et al. 2007; Bossé et al. 2008), which generates further TGF-β mediated ECM deposition and ASM contraction (Tatler et al. 2011; Al Alawi et al. 2014; Cheng et al. 2016; Januskevicius et al. 2016; Ojiaku et al. 2018), essentially leading to airway remodelling. Chen and Khalil (2006) observe increased ASM proliferation and survival induced by TGF-β signalling. Furthermore, Goldsmith et al. (2006) find changes in ASM hypertrophy, contractile protein expression and synthesis following treatment with TGF-β. As a result, the thickness of the ASM layer and ECM correlates with the higher concentration of TGF-β and hence the severity of the asthma (Chen and Khalil 2006; Al Alawi et al. 2014).

It is known that the secretion of inflammatory mediators induces bronchoconstriction in the short term, over minutes to hours whereas, repeated episodes of intense inflammation cause remodelling in the long term, over days to months (Kariyawasam et al. 2007; Mauad et al. 2007). Thus Grainge et al. (2011) suggest that bronchoconstriction and airway remodelling may be sequential as opposed to parallel events. However, the main criticism of these studies is that the short time-scale of contraction-linked mechanical experiments are incapable of replicating longer time periods associated with chronic disease.

1.2.4 Diagnosis and treatment

Current treatments of asthma are ineffective at addressing specific reversal of airway remodelling (Al Alawi et al. 2014). Nevertheless, corticosteroids are showing promising inhibitory effects, reducing excessive TGF-β expression, subsequently stalling irreversible airway remodelling (Al Alawi et al. 2014).

The studies Tatler et al. (2011) and Al Alawi et al. (2014) identify a positive correlation in an elevated concentration of active TGF-β and the severity of asthma. Thus, in attempt to combat asthmatic symptoms, it appears necessary to investigate therapies targeting excessive activation of TGF-β (Aschner and Downey 2016).

Blocking the activity of TGF-β has been shown to inhibit mucus hypersecretion, ASM cell hypertrophy and hyperplasia (Laping et al. 2002; Yano et al. 2006). However, due to uncontrolable side effects, clinical tests that completely block activated TGF-β ahev been unsuccessful (Buscemi et al. 2011). A large enough force is required to unfold the LAP in the LLC (Figure 1.2), thus it is reasonable to infer that mechanical activation of latent TGF-β is restricted to stronger integrins, sufficiently stiff ECM and cells that allow for a large enough force transmission to the LAP (Buscemi et al. 2011). Hence, therapeutic strategies that aim to suppress excessive TGF-β activity may begin with effective alterations in the mechanical activation of TGF-β (Buscemi et al. 2011).

1.3 Review of experimental models

Ovalbumin (OVA)-induced experimental asthma is a widely studied animal model of allergic asthma that recapitulates many of the hallmarks of allergic asthma in humans. OVA challenges cause inflammation of the airways, mucus hypersecretion, goblet cell hyperplasia, epithelial hypertrophy and elevates the concentrations of active cytokines in the airways (corresponding to the characteristics of asthma outlined in Section 1.2). For example, it has been shown that after the allergic inflammation and airway hyperresponsiveness resolves, ASM proliferation persists in OVA-challenged mice (McMillan and Lloyd 2004). Other animal models examining features of airway remodelling in humans include the guinea pig (Kistemaker et al. 2016), rat (Li and Shang 2014; Lilburn et al. 2016), dog (Royer et al. 2013), primate (Plopper and Hyde 2008) and horse (Leclere et al. 2012). As a cost saving technique in such studies, short and intense challenge to allergen protocols are used to induce remodelling rapidly; however, this does not replicate the slow developing nature observed in humans due to persistent, intermittent exacerbations (Prakash et al. 2017).

Cell cultures are an *in vitro* assay used to examine the physiology and biochemistry of cells in control conditions. Cultured ASM cells proliferate in response to multiple stimuli (Bentley and Hershenson 2008) and the study of Chen and Khalil (2006) shows that incubation of bovine ASM cells with TGF-β induces a concentration-dependent increase in ASM cell proliferation; however, very

high doses of TGF-β inhibit proliferation. Treatment of ASM cells with TGF-β for 48 hours increases ASM cell proliferation more than treatment for 24 hours, suggesting that the duration of TGF-β treatment also affects the increase in ASM cell proliferation (Chen and Khalil 2006).

Precision-cut lung-slice (PCLS), in which viable airways embedded within lung parenchyma are stretched or induced to contract, are a widely used *ex vivo* assay (Sanderson 2011) to investigate bronchoconstriction (Tan and Sanderson 2014), and more recently, mechanical activation of TGF-β in asthmatic airways (Tatler 2016). In order to examine the effects of bronchoconstriction in asthma, methacholine (MCh) doses may be administered to cause significant narrowing of the airways via sustained contraction of the ASM (Tan and Sanderson 2014). Studies that induce contraction of the ASM via MCh challenge demonstrate that bronchoconstriction promotes TGF-β activation (Oenema et al. 2013; Tatler 2016) and suggest that bronchoconstriction-induced remodelling may depend on increased activation of TGF-β (Noble et al. 2014). The study of Polio et al. (2019) suggests that remodelling of the ECM leads to an increase in the number of ASM-ECM connections and a significant increase in the contractile force generated by the ASM. Other studies investigate the effect of imposed stretch, for example, Froese et al. (2016) demonstrate that fibrotic tissue in rat PCLS activates more TGF-β1 in response to mechanical stretch than normal lung tissue. Similarly, Morioka et al. (2011) find that cyclic stretches of the PCLS promote cell alignment perpendicular to the stretch axis and enhances the feedback on mechanotransductive pathways.

1.3.1 Cyclically stretched lung-slices

In this section we describe the PCLS stretching experiment, performed by our collaborators in the Division of Respiratory Medicine, that motivates our biomechanical model development. The experimental data, obtained and provided by Tatler (2016), is illustrated in Chapter 6 where we compare our model results to those obtained experimentally.

The airways within PCLS are still functional in their native tissue and are obtained by inflating lung tissue with liquid agarose, allowing to set and solidify before finely slicing (method in Appendix A.2 provided by Tatler (2016)). The

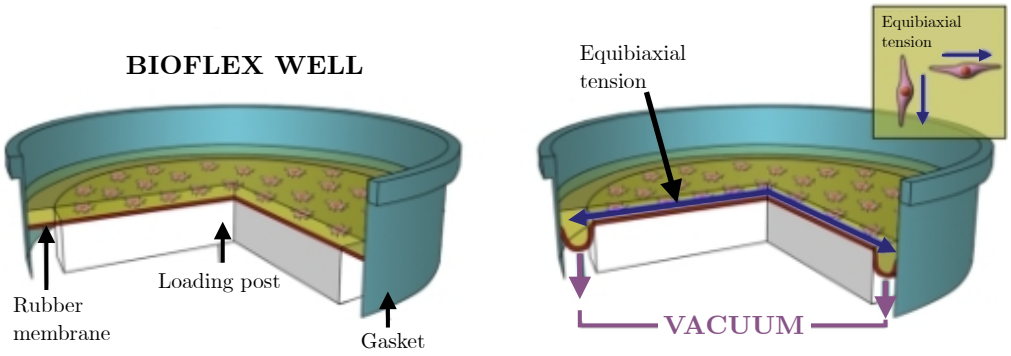

Figure 1.5: Axisymmetric cyclic stretching of PCLS via the BioFlex method (Tatler 2016). The PCLS are adhered to a circular deformable rubber membrane and then an axisymmetric cyclic stretch is applied to the membrane (via a vacuum) in order to stretch the attached PCLS.

PCLS are stretched using the Bioflex method (Figure 1.5). The PCLS are adhered to a circular deformable membrane and then an axisymmetric cyclic stretch is applied to the membrane (via a vacuum) in order to stretch the attached PCLS.

Although quantification of TGF-β concentration is not possible in stretched cells or PCLS (Tatler 2016), a surrogate biomarker of TGF-β signalling, phosphorylated Smad 2 (PSmad2), is measured instead using a Phospho-SMAD2 (S245/250/255) ELISA Kit. The degree of change in PSmad2 activity accurately correlates with the change in TGF-β activity (Tatler 2016) and the results indicate that TGF-β activation is increased in the cyclically stretched case compared to the unstretched case (Tatler 2016).

1.3.2 Chronic ovalbumin-challenged mouse model

In this section we describe the study of Brook et al. (2019) that provides a detailed quantitative analysis of airway remodelling and resolution speed across a large number of airways in a well-characterised mouse model of chronic OVA-induced asthma. The mathematical model of Hill et al. (2018) suggests that inflammation resolution speed is a critical determinant of long-term airway remodelling and hence, directs the investigation. Previous studies have not given such factors the in-depth attention required and only examine a small number of airways of limited sizes.

In the study of Brook et al. (2019), mice underwent OVA sensitisation and multiple challenges over 34 days, which generates airway remodelling. The mice were sacrificed at days 35, 37, 39 and 41. Software (developed by Brook et al. (2019)) was used to quantify the airway size and the amount of ASM and collagen airway fractions for prepared and stained mouse PCLS. The results of Brook et al. (2019) show that the amount of ASM and collagen is elevated in the day 34 OVA case compared to saline controls. The greatest increase of which is observed in the larger airways (1000 – 1500μm) followed by a lesser increase in the medium airways (500 – 1000μm) and finally the small airways (<500μm). Post challenge, Brook et al. (2019) observe that the amount of ASM fell daily and by day 41 had reduced close to baseline, whereas the increase in collagen persisted in the large and medium airways. Brook et al. (2019) observe a heterogeneity in the remodelling and the resolution across the airway size that has not previously been identified. Moreover, Brook et al. (2019) suggest that the persistence of collagen, despite the resolution of inflammatory cells, may indicate a possible mechanism that is responsible for maintained hypercontractility of ASM.

In this study, Tatler (2019) performs additional experiments to asses the effect of increased ASM and ECM mass, ASM contraction, and cyclic stretch on the activity of TGF-β in remodelled mouse PCLS. To do so, Tatler (2019) quantifies PS-mad2 activity in the cyclically stretched PCLS from OVA- and MCh-challenged cases compared to the saline (and OVA) controls, respectively. The experimental data, provided by Tatler (2019), is described in further detail in Chapter 6 where we compare our model results to those obtained experimentally.

1.4 Review of mathematical models

Experiments *in vitro* are typically reductionist in nature. To understand interactions of complex biochemical and mechanical processes requires integrative, predictive mathematical models. In this section we discuss some of the existing mathematical models and approaches that are applicable to the asthmatic airways.

1.4.1 Mathematical models of the airways

There are various mathematical models that account for cell signalling events based upon experimental data (*e.g.* Haberichter et al. (2002); Brumen et al. (2005); Croisier et al. (2013)), the majority of which employ the Law of Mass Action to obtain ordinary differential equations (ODEs) that describe the rates of change in constituent density. Chernyavsky et al. (2014) present an ODE model representing ASM phenotype switching between a proliferative and contractile state. In the proliferative state, ASM is assumed to grow logistically which implicitly incorporates spatial constraints. With a large number of simulations, Chernyavsky et al. (2014) consider the occurrence of both periodic and irregular exacerbations, following a random Poisson process, in order to investigate the range of possible outcomes an individual may experience, given average airway characteristics. They found that the likelihood of developing moderately to severely remodelled airways is crtically dependent on the inflammatory resolution rate and that the individual's history of induced remodelling events and accumulation of successive triggers have a long term impact on the degree of ASM hyperplasia (Chernyavsky et al. 2014).

Similarly, the morphoelastic model of Hill et al. (2018) explores airway remodelling in response to transient inflammatory or contractile agonist challenges. Consistent with the findings of Chernyavsky et al. (2014), Hill et al. (2018) find that when the inflammation resolution is slow, a small number of exacerbation events may lead to significant and persistent airway remodelling. The results of Hill et al. (2018) suggest that the sustained contractility of the ASM observed in asthmatics may be due to either a mechanotransductive feedback loop, insufficient clearance of contractile agonists, or a combination of the two.

Multiple mechanical models predict the local stress environment at both the cellular-level (*e.g.* Brook and Jensen (2014); Brook (2014)) and the tissue-level, (*e.g.* Bates et al. (2009); Khan et al. (2010); Hiorns et al. (2014)). Those developed to study ASM contraction typically employ cross-bridge cycling and a classical Huxley-Hai-Murphy (HHM) model developed by Mijailovich et al. (2000). Based on experimental data, Wang et al. (2008) present a modified Hai-Murphy cross-bridge model of ASM contraction that accounts for the regulation of calcium. The linear elastic model of Wang et al. (2008) assumes that a ring of

ASM is embedded in a linearly elastic isotropic, homogeneous sheet and exerts a circumferential contractile force. Contraction of the airway is radially symmetric and driven by the cross-bridge kinetics. Wang et al. (2008) find that fast activation of calcium initiates (and slow activation inhibits) contraction of the ASM and the airway. Furthermore, the presence of contractile agonist inhibits calcium sensitivity of the ASM. However, Böl et al. (2012) and Liu (2014) suggest that the Hai-Murphy model neglects the strain rate effect on the kinetics of cross-bridge interactions with actin filaments in the isotonic (force with length change) contractions.

Many early tissue-level models (*e.g.* Latourelle et al. (2002); Affonce and Lutchen (2006); Ma and Lutchen (2006)) of the intact airway, that account for tension generated by the smooth muscle contraction and mechanical properties of the airway wall, build upon the fundamental, but empirical, stress-strain relationships for the whole airway (Lambert et al. 1982; 1993; 1994; Lambert and Wilson 2005) and the Laplace thin-airway wall approximation (Anafi and Wilson 2001). With these models, it is not possible to determine tissue stresses within the airway wall nor separate ASM and ECM contributions to the mechanics. Similarly, Bates and Lauzon (2005; 2007) assume the thin-wall Laplace approximation to develop a two-dimensional computational model of a dynamically contracting airway comprising a circular ring of activated ASM embedded in homogeneously elastic lung parenchyma. The activated ASM dynamics within the model of Bates and Lauzon (2005; 2007) is governed by the Hill force-velocity relationship (an empirical relationship between the shortening velocity of muscle and the load on the muscle which lacks precision in predicting velocities at high and low loads (Seow 2013)) to determine the rate of airway lumen narrowing. Khan et al. (2010) compare their experimental results to the simulated results of Bates and Lauzon (2005; 2007) and predict that pathological remodelling changes in the elastic properties of the airway wall and parenchymal attachments are significant modulators of airway responsiveness. Breathing motions cyclically stretch ASM and the tissue-level model of Bates et al. (2009) replicates, to some extent, the oscillatory force-length behaviour; however, the model is unable to predict decreases in isometric force (force without length change) for large stretches. They suggest that this may be due to reversal of bronchoconstriction *in vivo* during deep inhalation or a simplistically modelled

Hill force-velocity relationship. Brook et al. (2010) extended these early models to account for multiple airway constituents assuming a finite airway wall thickness for both the intact airway and PCLS models under a plane strain and plane stress approximation, respectively. While these allowed for tissue stresses to be determined within the airway wall, the linear elastic framework used meant that predictions were only qualitatively useful. Breen et al. (2012) considered a finite element finite-elasticity model of the PCLS but neglected airway wall thickness and focused on stresses in the lung parenchyma.

The detailed review of Donovan (2011) highlights the potential importance of spatial multi-scale interactions and the limitations of reduced models whereby dynamics observed at one isolated sub-scale may not extend to the lower. Addressing such issues, Politi et al. (2010) focus on airway hyperresponsiveness and consider connections between models at four different spatial scales: at the molecular scale, MCh stimulates intracellular calcium dynamics in the ASM generating force at the cell scale. At the tissue scale, contractile force generated at the cell scale together with parenchymal tethering influences airway wall mechanics. Finally, at the organ scale, breathing and gravity affects the resultant mechanical deformation of the lung. Importantly, the multi-scale model of Politi et al. (2010) accounts for spatial distribution while including a complex cross-bridge model of ASM dynamics and a physiologically realistic model at the organ level. Similarly, Anafi and Wilson (2001) show that small differences on the largest scale are exaggerated by alterations on the smallest scale. Likewise, Wall et al. (2010) divide the lung into two major subsystems, the conducting airways and the lung parenchyma, and develop detailed individual models for parts of the separated subscales that are then connected at each level (*i.e.* the output at the subscale informs the above scale).

To investigate the effects of airway constriction induced by aerosol challenges, Amin et al. (2010) introduce a dynamic multi-scale model to account for the kinetics of agonist molecules binding to ASM cell receptors and emergent multi-scale interactions. Ultimately, Amin et al. (2010) create a protective feedback mechanism where a two-state model couples to Lambert et al. (1982) airway wall mechanics determining the airway radii. The model of Amin et al. (2010) replicates intrabreath dynamics whilst simulating a time series of hundreds of breaths and the results identify a link between pressure fluctuations within a

single breath to the entire duration of an inhalation challenge.

Brook and Jensen (2014) combine intracellular events to investigate whole cell behaviour by modelling contractile units in parallel and series tethered to a nonlinear elastic cytoskeleton. Brook and Jensen (2014) simulate a classic experiment which consists of a period of isometric force generation in the presence of contractile agonist followed by ASM oscillatory length fluctuations, and demonstrate that a number of important interactions may be of significance in molecular-level force generation mechanisms. Similarly, the model of Brook (2014) includes dynamic reorganisation of subcellular machinery as the cell lengthens and shortens. Results show that sustained disconnectivity of contractile filaments within the ASM cell could explain the banana-shaped force-length loops and strain-stiffening observed experimentally during applied length fluctuations. Furthermore, the results of Brook (2014) suggest that dynamic rearrangement of subcellular contractile machinery controls many mechanisms involved with tidal breathing.

1.4.2 Other relevant mathematical models

Eskandari and Kuhl (2015) review the numerous mechanisms that are responsible for cell proliferation, hypertrophgy and migration, including excessive or insufficient hormone signalling, the imbalance of homeostasis and the response to irritants, many of which are applicable in asthma. Buckling of the airways is also an important feature, as observed in Figures 1.3; however, this is generally in the epithelial layers of the airway and beyond the scope of this thesis. Examples of models that account for mucosal growth, buckling and folding are: Wiggs et al. (1997); Moulton and Goriely (2011); Li et al. (2011); Eskandari et al. (2015). More generally, the mechanics of growth in thin biological membranes is described by Kroon and Holzapfel (2008) and Rausch and Kuhl (2014).

Based upon experimental data, Baker et al. (2017) study cell signalling events, cytokine regulation and feedback mechanisms which may be altered to observe mono-stable and bi-stable behaviour. Although the application of the model proposed by Baker et al. (2017) is not specifically within asthma, the assembly, development and methods of analysis used aid our model development in Chapter 2. In subsequent chapters our attention turns to soft tissue mechan-

ics; in-depth descriptions of nonlinear hyperelastic heterogeneous anisotropic materials are provided by Bowen (1976); Truesdell and Toupin (1960); Truesdell and Noll (1992) and the formulation for obtaining the constitutive mechanical relation for this type of material is given in detail by Humphrey and Rajagopal (2002); Ateshian (2007); Ateshian and Ricken (2010). Furthermore, there is a substantial amount of literature covering arterial and cardiovascular mechanics that is relevant and applicable when modelling the airways (*e.g.* Holzapfel and Ogden (2010); Gasser et al. (2006); Hill et al. (2012)). Some later cardiovascular developments consider multiple scales that accounts for the contractile dynamics and and fibrous network of the arterial wall (*e.g.* Coccarelli et al. (2018); Rocha et al. (2018)).

A biomechanical description of the intact airway that accounts for both dynamic force generation by ASM cells and strain-stiffening within collagen fibres of the ECM is presented by Hiorns et al. (2014). The airway is modelled as an axisymmetric thick-walled cylinder under the assumption of plane-strain with no axial displacement. The cylinder contains two layers representing the airway wall and parenchyma. The airway wall is modelled as an incompressible nonlinear elastic material, whilst the parenchyma is modelled as a compressible linear elastic material. Helical fibres are embedded within the airway wall and represent the passive ECM component and active ASM component. Active force generation is the result of cross-bridge interactions between myosin and actin filament contractile units in a HHM model.

In subsequent chapters, we develop a biomechanical model of a fibre-reinforced airway similar to that of Hiorns et al. (2014); however, instead of an intact airway under plane strain, we develop a description of an airway within a PCLS, assuming a single layered airway slice of finite thickness with traction-free upper, lower, and inner surface boundary conditions, and prescribe a displacement at the outer boundary. Furthermore, for simplicity we do not employ the HHM model to determine the active force generation, and instead incorporate ASM contraction more phenomenologically and driven by active TGF-β dynamics.

More generally, approximate solutions for axisymmetric stretching of thin elastic membranes with traction-free surfaces have previously been determined for

isotropic materials (Wong and Shield 1969; Yang 1967) but do not account for anisotropy or active contraction. Others consider finite deformations of incompressible rubber membranes with a central solid inclusion and under uniform pressure (Jianbing et al. 2015).

1.5 Review of mathematical techniques

In this section we present some of the theory underlying soft tissue mechanics required to develop our biomechanical model of TGF-β activation in the stretched PCLS tissue. Here, we introduce nonlinear elasticity, the formulation of strain-energy functions and the inclusion of active force in the direction of embedded fibres. We then define stress and mechanical equilibrium before we briefly discuss constrained mixtures. Amongst the extensive literature, the following is covered in great detail by: Bowen (1976); Truesdell and Toupin (1960); Truesdell and Noll (1992); Ogden (1997); Holzapfel (2000); Ateshian (2017), and is particularly well-established in the cardiovascular literature (*e.g.* Holzapfel et al. (2000); Humphrey (2002); Ogden (2003); Gasser et al. (2006)).

1.5.1 Nonlinear elasticity

The deformation gradient tensor, $\mathbf{F}$, maps the deformation of a tissue (and each constituent constrained within the tissue) from the reference configuration to the deformed configuration and is defined by

$$\mathbf{F} = \boldsymbol{\nabla}\mathbf{x}, \qquad F_{ij} = \frac{\partial x_i}{\partial X_j}, \tag{1.5.1}$$

where, $\mathbf{X}$ denotes the position vector of a point in the reference configuration and $\mathbf{x}$ denotes the position vector of a point in the deformed configuration. The components of $\mathbf{F}$ in Lagrangian cylindrical co-ordinates are (Humphrey and

Rajagopal 2002)

$$\mathbf{F} = \begin{pmatrix} \frac{\partial r^*}{\partial R^*} & \frac{1}{R^*}\frac{\partial r^*}{\partial \Theta} & \frac{\partial r^*}{\partial Z^*} \\ r^*\frac{\partial \theta}{\partial R^*} & \frac{r^*}{R^*}\frac{\partial \theta}{\partial \Theta} & r^*\frac{\partial \theta}{\partial Z^*} \\ \frac{\partial z^*}{\partial R^*} & \frac{1}{R^*}\frac{\partial z^*}{\partial \Theta} & \frac{\partial z^*}{\partial Z^*} \end{pmatrix}, \tag{1.5.2}$$

where (R^*, Θ, Z^*) denotes the reference configuration and (r^*, θ, z^*) denotes the deformed configuration. The deformation gradient tensor, $\mathbf{F}$, can be split into an orthogonal rotation tensor, $\mathbf{R}$, and either the left or right symmetric stretch tensors, $\mathbf{U}$ and $\mathbf{V}$ respectively (Ogden 2003), such that

$$\mathbf{F} = \mathbf{VR}, \qquad \mathbf{F} = \mathbf{RU}. \tag{1.5.3}$$

Correspondingly, the left and right Cauchy Green deformation tensors, $\mathbf{B}$ and $\mathbf{C}$, respectively, are related to the square of the stretch and are given by

$$\mathbf{B} = \mathbf{F}\mathbf{F}^T \equiv \mathbf{V}^2, \qquad \mathbf{C} = \mathbf{F}^T\mathbf{F} \equiv \mathbf{U}^2. \tag{1.5.4}$$

The left and right Cauchy Green deformation tensors, $\mathbf{B}$ and $\mathbf{C}$, depend on the co-ordinate system used, whereas the stress invariants do not. The principal isotropic invariants of $\mathbf{B}$, and equivalently for $\mathbf{C}$, are defined by

$$I_1 = \mathrm{tr}[\mathbf{B}] = \lambda_1^2 + \lambda_2^2 + \lambda_3^2, \tag{1.5.5}$$

$$I_2 = \frac{1}{2}\left((\mathrm{tr}[\mathbf{B}])^2 - \mathrm{tr}[\mathbf{B}^2]\right) = \lambda_1^2\lambda_2^2 + \lambda_2^2\lambda_3^2 + \lambda_3^2\lambda_1^2, \tag{1.5.6}$$

$$I_3 = \det[\mathbf{B}] = J^2 = \lambda_1^2\lambda_2^2\lambda_3^2, \tag{1.5.7}$$

where λ_k for $k \in \{1, 2, 3\}$ are the principal stretches of the the deformation gradient tensor, $\mathbf{F}$ and $J = \det[\mathbf{F}]$. For incompressible materials $J = 1$ (compressible materials are not considered in this thesis) and thus, the third invariant, I_3, is constant through deformation.

Tissues comprising ASM and ECM are embedded with extensible fibres, such as collagen, and have anisotropic material properties. When there are two families of fibres, with orientations denoted $\mathbf{G}_1$ and $\mathbf{G}_2$ in the reference configuration, respectively, there are the following additional anisotropic invariants Ogden

(2003):

$$I_4 = \mathbf{G}_1 \cdot (\mathbf{C}\mathbf{G}_1)\,, \qquad I_5 = \mathbf{G}_1 \cdot (\mathbf{C}^2\mathbf{G}_1), \qquad I_6 = \mathbf{G}_2 \cdot (\mathbf{C}\mathbf{G}_2),$$
$$I_7 = \mathbf{G}_2 \cdot (\mathbf{C}^2\mathbf{G}_2), \qquad I_8 = \mathbf{G}_1 \cdot (\mathbf{C}\mathbf{G}_2), \qquad I_9 = (\mathbf{G}_1 \cdot \mathbf{G}_2)^2. \tag{1.5.8}$$

The fourth and sixth invariants, I_4 and I_6, have a clear physical interpretation and represents the square of the stretch in the direction of the fibres (Holzapfel et al. 2000); however, the other invariants have no simple interpretation (Hiorns 2014). It should be noted that the ninth invariant, I_9, is constant through deformation as it does not depend upon the deformation. In the deformed configuration, the fibres $\mathbf{G}_1$ and $\mathbf{G}_2$ have the orientations

$$\mathbf{g}_1 = \mathbf{F}\mathbf{G}_1, \qquad \mathbf{g}_2 = \mathbf{F}\mathbf{G}_2, \tag{1.5.9}$$

respectively.

1.5.2 Strain-energy functions

Hyperelastic material properties are characterised in terms of a strain-energy function that is defined on the space of deformation gradients, $W^* = W^*(\mathbf{F})$ (Ogden 2003). Strain-energy functions (typically phenomenological descriptions) relate the energy put into the material with the resulting strain and depends on the invariants in (1.5.5) and (1.5.8) to ensure that they are independent of the co-ordinate system used. The choice of function is free; however, it is required that

$$\left(\frac{\partial W^*}{\partial I_1} + 2\frac{\partial W^*}{\partial I_2} + \frac{\partial W^*}{\partial I_3}\right)\Bigg|_{I_1=I_2=3, I_3=1} = 0, \tag{1.5.10}$$

to ensure that the reference configuration is unstressed.

Some of the widely used strain-energy functions describing isotropic incompressible materials include, Neo-Hookean, Mooney-Rivlin, Ogden and Fung. The incompressible Neo-Hookean formulation is given by

$$W^* = \frac{\mu_1^*}{2}(I_1 - 3)\,, \tag{1.5.11}$$

where, μ_1^* is a material constant that describes the shear modulus and I_1 is the

first invariant, as defined in (1.5.5) (Rivlin 1948). The incompressibe Mooney-Rivlin formulation is given by

$$W^* = \frac{\mu_1^*}{2}(I_1 - 3) + \frac{\mu_2^*}{2}(I_2 - 3), \tag{1.5.12}$$

and again, μ_1^* and μ_2^* are material constants (Mooney 1940). Note that the Neo-Hookean material in (1.5.11) is a special case of the Mooney-Rivlin material in (1.5.12) for $\mu_2^* = 0$. Stretched Neo-Hookean and Mooney-Rivlin materials require a smaller increase in force to stretch the material further. Conversely, Ogden materials strain-stiffen when stretched meaning that they require a larger increase in force to stretch the material further. The Ogden stain-energy function depends on the prinicpal stretches, λ_k for $k \in \{1, 2, 3\}$, of the deformation gradient tensor, $\mathbf{F}$, (instead of the strain invariants) and is given by

$$W^* = 2\gamma^* \frac{\lambda_1^\nu + \lambda_2^\nu + \lambda_3^\nu}{\nu}, \tag{1.5.13}$$

where, γ^* and ν are positive material constants (Ogden 1972).

Fung-elastic material is also described in terms of the principal stretches, λ_k for $k \in \{1, 2, 3\}$, and is given by

$$\begin{aligned} W^* = \frac{1}{2}\Big(&\gamma_1^*(\lambda_1^2 + \lambda_2^2 + \lambda_3^2 - 3) \\ &+ \gamma_2^*\left(\exp\left(\xi(\lambda_1^2 + \lambda_2^2 + \lambda_3^2 - 3)\right) - 1\right)\Big), \end{aligned} \tag{1.5.14}$$

where γ_1^*, γ_2^* and ξ are material constants (Fung 1993). The exponential term in (1.5.14) is negligible for small strains; however, it dominates the linear term in (1.5.14) for larger strains (Fung 1993).

Strain-energy functions may be constructed by summing isotropic, W_{iso}^*, and anisotropic, W_{ani}^*, components with material properties that depend upon the strain invariants in (1.5.5) and (1.5.8) such that

$$W^*(I_1, \ldots, I_9) = W_{\text{iso}}^*(I_1, I_2, I_3) + W_{\text{ani}}^*(I_1, \ldots, I_9). \tag{1.5.15}$$

Holzapfel et al. (2000) model an incompressible material representing the arterial wall and for simplicity (to minimise the number of material parameters),

reduce the form of (1.5.15) to

$$W^*\left(I_1, I_4, I_6\right) = W^*_{\text{iso}}\left(I_1\right) + W^*_{\text{ani}}\left(I_4, I_6\right). \tag{1.5.16}$$

The isotropic component of (1.5.16) is Neo-Hookean, as given in (1.5.11), and the anisotropic component is given by

$$W^*_{\text{ani}}(I_4, I_6) = \frac{\omega^*}{2\zeta} \sum_{j=4,6} \left(\exp\left(\zeta(I_j - 1)^2\right) - 1\right). \tag{1.5.17}$$

The constant ω^* has measures of stress, whereas ζ is dimensionless and describes the amount of strain-stiffening. For small stretches there is little resistance to stretch in the fibres; however, for larger stretches, the resistance to stretch in the fibres increases exponentially (Holzapfel et al. 2000).

The derivatives of the strain-energy function, W^*, with respect to the invariants, I_j, denoted W^*_j, are given by

$$W^*_j = \frac{\partial W^*}{\partial I_j}, \qquad\qquad j \in \{1, \ldots, 8\}. \tag{1.5.18}$$

Recall that the ninth invariant, I_9, is constant through deformation (see (1.5.8)) and hence $j \in \{1, \ldots, 8\}$ in (1.5.18).

As outlined by Ambrosi and Pezzuto (2012), active force generation is usually represented in terms of an active stress component, $\boldsymbol{\sigma}^*_{\text{act}}$, that is added to the passive stress, $\boldsymbol{\sigma}^*_{\text{pas}}$ such that

$$\boldsymbol{\sigma}^* = \boldsymbol{\sigma}^*_{\text{act}} + \boldsymbol{\sigma}^*_{\text{pas}}, \tag{1.5.19}$$

where, $\boldsymbol{\sigma}^*$ denotes the Cauchy stress (defined in the subsequent section) of the tissue. The general form for the active component is

$$\boldsymbol{\sigma}^*_{\text{act}} = \frac{f(I_4)^*}{J}(\mathbf{g}_1 \otimes \mathbf{g}_1 + \mathbf{g}_2 \otimes \mathbf{g}_2), \tag{1.5.20}$$

where, $\mathbf{g}_1$ and $\mathbf{g}_2$ are the orientations of the deformed fibres defined in (1.5.9), and $f(I_4)^*$ is a function that accounts for the activation of the fibres. Similarly, active force generation may be described via an active component of the strain-energy function, W^*_{act}, and added to the passive components of the strain-

energy function in (1.5.16). Alternately, another approach is to introduce a multiplicative decomposition of the deformation gradient tensor, $\mathbf{F}$, into active, $\mathbf{F}_{\text{act}}$, and passive components, $\mathbf{F}_{\text{pas}}$, (which include isotropic and anisotropic properties) such that

$$\mathbf{F} = \mathbf{F}_{\text{act}}\mathbf{F}_{\text{pas}}. \tag{1.5.21}$$

1.5.3 Stress and mechanical equilibrium

The Cauchy stress tensor for an incompressible material is defined by (Holzapfel 2000)

$$\boldsymbol{\sigma}^* = \mathbf{F}\frac{\partial W^*}{\partial \mathbf{F}} - \mathscr{P}^*\mathbf{I}, \tag{1.5.22}$$

where the pressure, $\mathscr{P}^*$, is included to enforce incompressibility. When there are two families of fibres, (1.5.22) is equivalent to (Ogden 2003)

$$\begin{aligned}\boldsymbol{\sigma}^* = &-\mathscr{P}^*\mathbf{I} + 2W_1^*\mathbf{B} + 2W_2^*(I_1\mathbf{B} - \mathbf{B}^2) + 2W_4^*\mathbf{g}_1 \otimes \mathbf{g}_1 \\ &+ 2W_5^*(\mathbf{g}_1 \otimes \mathbf{B}\mathbf{g}_1 + \mathbf{B}\mathbf{g}_1 \otimes \mathbf{g}_1) + 2W_6^*\mathbf{g}_2 \otimes \mathbf{g}_2 \\ &+ 2W_7^*(\mathbf{g}_2 \otimes \mathbf{B}\mathbf{g}_2 + \mathbf{B}\mathbf{g}_2 \otimes \mathbf{g}_2) + 2W_8^*(\mathbf{g}_1 \otimes \mathbf{g}_2 + \mathbf{g}_2 \otimes \mathbf{g}_1),\end{aligned} \tag{1.5.23}$$

where, W_j^* for $j \in \{1,\ldots,8\}$, denotes the derivatives for the strain-energy function, W^*, with respect to the invariants, I_j for $j \in \{1,\ldots,8\}$ as in (1.5.18), $\mathbf{g}_1$ and $\mathbf{g}_2$ denote the deformed fibres as in (1.5.9), and $\mathbf{B}$ denotes the left Cauchy Green stress tensors as defined in (1.5.4). The components of the Cauchy stress tensor, (1.5.22), in the deformed cylindrical polar co-ordinates system (r^*, θ^*, z^*), is

$$\boldsymbol{\sigma}^* = \begin{pmatrix} \sigma_{rr}^* & \sigma_{r\theta}^* & \sigma_{rz}^* \\ \sigma_{\theta r}^* & \sigma_{\theta\theta}^* & \sigma_{\theta z}^* \\ \sigma_{zr}^* & \sigma_{z\theta}^* & \sigma_{zz}^* \end{pmatrix}. \tag{1.5.24}$$

The diagonal components of (1.5.24) represent the radial stress, σ_{rr}^*, the circumferential stress, $\sigma_{\theta\theta}^*$, and the axial stress, σ_{zz}^*, respectively. The off-diagonal components of (1.5.24) represent the shear stresses, σ_{rz}^* and σ_{zr}^*, and the torsional stresses, $\sigma_{r\theta}^*$, $\sigma_{\theta r}^*$, $\sigma_{z\theta}^*$ and $\sigma_{\theta z}^*$. von Mises stress, σ_{VM}^*, is a scalar quantity that encompasses all of the Cauchy stress components and (corresponding to that

in (1.5.24)) is given by

$$\sigma^*_{\mathrm{VM}} = \frac{1}{\sqrt{2}}\Big((\sigma^*_{rr}-\sigma^*_{\theta\theta})^2+(\sigma^*_{\theta\theta}-\sigma^*_{zz})^2 + (\sigma^*_{zz}-\sigma^*_{rr})^2+6\left({\sigma^*_{r\theta}}^2+{\sigma^*_{\theta z}}^2+{\sigma^*_{zr}}^2\right)\Big)^{\frac{1}{2}}. \tag{1.5.25}$$

The von Mises stress is commonly uses in solid mechanics to determine if a given material will yield or fracture and is often used to describe fibre dispersion in soft tissues (*e.g.* Wang et al. (2012)).

In mechanical equilibrium, and assuming that there are no body forces on the tissue, the balance of linear momentum requires

$$\nabla\cdot\boldsymbol{\sigma}^* = \mathbf{0}. \tag{1.5.26}$$

In cylindrical co-ordinates, (1.5.26) corresponds to three equations in the deformed configuration,

$$\frac{\partial\sigma^*_{rr}}{\partial r^*}+\frac{1}{r^*}\frac{\partial\sigma^*_{\theta r}}{\partial\theta}+\frac{\partial\sigma^*_{zr}}{\partial z^*}+\frac{1}{r^*}(\sigma^*_{rr}-\sigma^*_{\theta\theta})=0, \tag{1.5.27a}$$

$$\frac{\partial\sigma^*_{r\theta}}{\partial r^*}+\frac{1}{r^*}\frac{\partial\sigma^*_{\theta\theta}}{\partial\theta}+\frac{\partial\sigma^*_{z\theta}}{\partial z^*}+\frac{1}{r^*}(\sigma^*_{r\theta}+\sigma^*_{\theta r})=0, \tag{1.5.27b}$$

$$\frac{\partial\sigma^*_{rz}}{\partial r^*}+\frac{1}{r^*}\frac{\partial\sigma^*_{\theta z}}{\partial\theta}+\frac{\partial\sigma^*_{zz}}{\partial z^*}+\frac{1}{r^*}\sigma^*_{rz}=0. \tag{1.5.27c}$$

1.5.4 Constrained mixture theory

An in-depth explanation of constrained mixture theory is provided by Ateshian (2007); here, we briefly summarise the components that are required in our model development.

A constrained mixture may consist of solid and liquid constituents and it is assumed that there is no relative motion among the solid constituents, *i.e.* the velocities of the individual solid constituents are equal at all times. For a constrained solid mixture comprising i constituents denoted ρ^*_i, in order to conserve mass, the volume fractions of the constituents, Φ_i, are given by

$$\Phi_i = \frac{{\rho^*_i}^{\mathrm{A}}}{{\rho^*_i}^{\mathrm{T}}}, \tag{1.5.28}$$

where $\rho_i^{*\mathrm{A}}$ represents the apparent density and $\rho_i^{*\mathrm{T}}$ represents the true density of the constituent ρ_i^*, respectively. True density refers to the mass of constituent per volume of that constituent, whereas volume fraction of constituent refers to the volume of constituent per mixture volume (Ateshian 2017). Assuming that there are no voids, saturation of the tissue demands

$$\sum_i \Phi_i = 1. \tag{1.5.29}$$

The strain-energy function for the entire tissue, comprising the constituents ρ_i^*, is given by the addition of the weighted contributions from each constituent such that

$$W^*\left(I_1, \ldots, I_9\right) = \sum_i \Phi_i W_i^*\left(I_1, \ldots, I_9\right), \tag{1.5.30}$$

where, the strain-energy function for each constituent is given by

$$\begin{aligned} W_i^*\left(I_1, \ldots, I_9\right) = W_{i\ \mathrm{iso}}^*\left(I_1, I_2, I_3\right) \\ + W_{i\ \mathrm{ani}}^*\left(I_4, \ldots, I_9\right) + W_{i\ \mathrm{act}}^*\left(I_4, \ldots, I_9\right). \end{aligned} \tag{1.5.31}$$

Correspondingly, the overall Cauchy stress tensor, $\boldsymbol{\sigma}^*$, is given by

$$\boldsymbol{\sigma}^* = \sum_i \Phi_i \boldsymbol{\sigma}_i^*, \tag{1.5.32}$$

where, the Cauchy stress for each constituent, $\boldsymbol{\sigma}_i^*$, is given by (1.5.22). As an example, the differing material properties and fibre orientations of elastin and collagen are modelled by Rachev and Shazly (2019) following (1.5.30).

1.6 Thesis structure

In Chapter 2 we develop dynamical models to describe the change in number density of the airway wall constituents and account for subcellular signalling pathways that lead to TGF-β activation. We present two ordinary differential equation (ODE) models that demonstrate a bi-stability with biologically relevant steady states which represent a healthy and diseased (asthmatic) state. We show that external stimuli (mimicking an asthmatic exacerbation) may alter the

steady state and therefore initiate disease progression.

In Chapters 3 and 4, our focus turns to soft tissue mechanics and we develop a biomechanical model of the PCLS stretching experiments, outlined in Section 1.3.1, to quantify mechanical stress experienced by the airway wall constituents in response to cyclic stretching that consequently activates TGF-β. In particular, we carefully assess the applicability of various simplifying assumptions of the PCLS geometry to determine the most appropriate representation for use in future modelling efforts. Specifically, we demonstrate that asymptotic expansions may be used to sufficiently approximate a full numerical simulation (obtained using the finite element software FEBio (Maas et al. 2012)).

Thereafter, in Chapter 5, we couple subcellular mechanotransductive signalling pathways (explored in Chapter 2) to nonlinear hyperelastic models of airway mechanics (developed in Chapters 3 and 4) to predict the levels of TGF-β activation in different conditions. We account for TGF-β mediated contraction of the ASM and the subsequent change in effective mechanical properties of the PCLS as TGF-β activation progresses. In Chapter 6, we compare our model results to those obtained experimentally (Tatler 2016; 2019) and demonstrate that they are in agreement.

Finally, in Chapter 7, we discuss areas of further investigation, future developments and propose new experiments that provide potential for model validation and calibration.

CHAPTER 2

Dynamical Models of TGF-β Activation

In this Chapter we develop two ordinary differential equation (ODE) models that describe the change in number density of the key airway wall constituents, ASM and ECM, and that account for sub-cellular signalling pathways that lead to the activation of TGF-β. We identify bi-stable parameter regimes where there are two positive steady states; one with a low concentration of active TGF-β and the other with a high concentration of active TGF-β (and as a result, increased ASM and ECM density). We associate the former with a healthy homeostatic state and the latter with a diseased (asthmatic) state. We demonstrate that external stimuli (mimicking an asthmatic exacerbation), that induce TGF-β activation via ASM contraction, perturb the system from a healthy state to a diseased state. We show that the properties of the stimuli, such as the frequency, strength and the clearance of surplus activate TGF-β, are important in determining the long-term dynamics and the development of disease.

2.1 Cell-level dynamics

As outlined in Section 1.1.4, active TGF-β binds to receptors expressed by proliferating ASM, contractile ASM and other surrounding cells which initiates multiple cellular responses (Al Alawi et al. 2014; Aschner and Downey 2016; Derynck and Zhang 2003). These responses include the triggering of ASM proliferation and stimulation of ASM contraction. We investigate the activation of

latent TGF-β (as described in Section 1.1.4) and the downstream effects of TGF-β binding at the cell-level by considering two ODE models and compare their behaviour.

Following discussions with our collaborators in the Division of Respiratory Medicine (Tatler 2016), and suitable literature, we have developed the schematic diagram in Figure 2.1 to illustrate the interactions between the key airway wall components, ASM and ECM, and the effects of TGF-β activation. First, we develop a general model (Section 2.1.1) in which we account for TGF-β activation, cell signalling pathways and the subsequent up-regulation of cellular responses. In this general case, we neglect TGF-β-receptor binding events and simply consider the cellular response to the presence of active TGF-β. We then present a refined model (Section 2.1.2) that incorporates density-dependent removal of active TGF-β due to TGF-β-receptor binding events. In this refined model we account for TGF-β-receptor binding by adjusting the interaction rates (developed in Section 2.1.1) to also depend upon the density of the specific air-

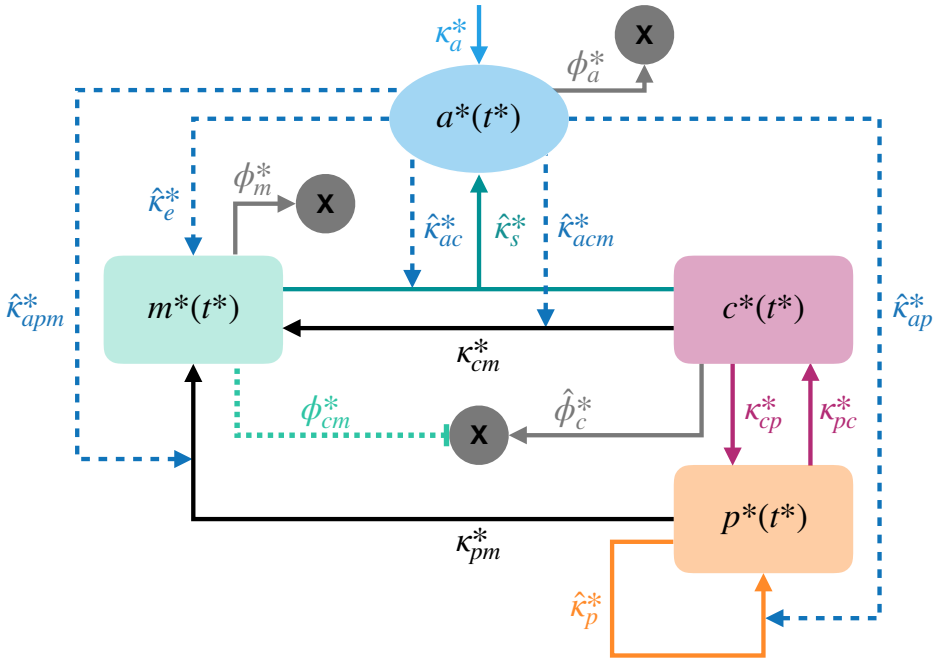

Figure 2.1: Schematic diagram detailing the interactions between the key components, proliferating ASM, $p^*(t^*)$, contractile ASM, $c^*(t^*)$, ECM, $m^*(t^*)$ and active TGF-β, $a^*(t^*)$, at rates κ and ϕ as listed, explained and non-dimensionalised in Table C.1 in Appendix C.1. Dashed blue lines represent TGF-β signalling pathways and the grey circles, labelled X, represent degradation of each of the respective components.

way wall components that express the associated receptors and thereby account for the availability and type of receptor required to initiate the distinct pathway.

2.1.1 Model development

With reference to the schematic in Figure 2.1, we describe the rate of change in number density of the ASM, ECM and concentration of active TGF-β with a system of four ODEs such that

$$\frac{\mathrm{d}p^*}{\mathrm{d}t^*} = \hat{\kappa}_p^*(p^*)p^*\left(1+\hat{\kappa}_{ap}^*(a^*)\right) + \kappa_{cp}^* c^* - \kappa_{pc}^* p^*, \tag{2.1.1a}$$

$$\frac{\mathrm{d}c^*}{\mathrm{d}t^*} = \kappa_{pc}^* p^* - \kappa_{cp}^* c^* - \hat{\phi}_c^*(m^*)c^*, \tag{2.1.1b}$$

$$\frac{\mathrm{d}a^*}{\mathrm{d}t^*} = \kappa_a^* + \left(\hat{\kappa}_s^*(t^*) + \hat{\kappa}_{ac}^*(a^*)\right)c^* m^* - \phi_a^* a^*, \tag{2.1.1c}$$

$$\frac{\mathrm{d}m^*}{\mathrm{d}t^*} = \left(\kappa_{cm}^* + \hat{\kappa}_{acm}^*(a^*)\right)c^* + \left(\kappa_{pm}^* + \hat{\kappa}_{apm}^*(a^*)\right)p^* + \hat{\kappa}_e^*(a^*) - \phi_m^* m^*, \tag{2.1.1d}$$

where, following Chernyavsky et al. (2014), we assume that the ASM may be divided into two separate sub-populations namely, the proliferative phenotype, $p^*(t^*)$, and contractile phenotype, $c^*(t^*)$. Furthermore, we assume that phenotype switching may occur between these two ASM sub-populations. The rate constant κ_{pc}^* represents phenotype switching from the proliferative to contractile state and the rate constant κ_{cp}^* represents phenotype switching from the contractile to proliferative state. It is thought that ASM cells express fewer contractile proteins whilst proliferating and therefore generate less contractile force than non-proliferating ASM cells (Bentley and Hershenson 2008). Hence, the roles of the proliferating ASM and contractile ASM differ (Chernyavsky et al. 2014), and the contractile ASM phenotype is exclusively responsible for contraction, whereas the proliferative phenotype is exclusively responsible for ASM growth. The proliferation rate, $\hat{\kappa}_p^*(p^*)$, is assumed to be logistic such that

$$\hat{\kappa}_p^*(p^*) = \kappa_p^*\left(1 - \frac{p^*}{p_{max}^*}\right). \tag{2.1.2}$$

This implicitly accounts for a spatial constraint, p_{max}^*, defining the carrying capacity of the proliferating ASM cell density. ASM proliferation is thought to increase with asthma severity (Johnson et al. 2001; Trian et al. 2007; Pelaia et al.

2008; Januskevicius et al. 2016) and thus, the rate constant κ_p^*, defining the rate of ASM proliferation, may be altered to reflect the severity of asthma.

The rate function $\hat{\kappa}_{ap}^*(a^*)$ represents active TGF-β-induced proliferation (Chen and Khalil 2006; Makinde et al. 2007; Bentley and Hershenson 2008) and acts in addition to baseline proliferation $\hat{\kappa}_p^*$. Following the methods of Baker et al. (2017), we assume that rates that depend on the concentration of active TGF-β are biologically limited and take the form of saturating Hill functions,

$$\hat{\kappa}_i^*(a^*) = \frac{\kappa_i^* a^*}{\eta_i^* + a^*}, \qquad i \in \{ap, ac, acm, apm, e\}. \tag{2.1.3}$$

The rate function $\hat{\kappa}_{ac}^*(a^*)$ in (2.1.3) represents activation of further TGF-β as a result of active TGF-β-induced contraction of the ASM. The rate functions $\hat{\kappa}_{acm}^*(a^*)$, $\hat{\kappa}_{apm}^*(a^*)$ and $\hat{\kappa}_e^*(a^*)$ represent the rate of secretion of ECM from the contractile ASM, proliferating ASM and other surrounding cells, respectively, that is induced by active TGF-β signalling pathways (Chen and Khalil 2006; Makinde et al. 2007; Al Alawi et al. 2014; Jolly et al. 2014; Cheng et al. 2016). In addition, baseline secretion of ECM (independent of active TGF-β concentration) occurs at rates κ_{cm}^* and κ_{pm}^* from the contractile and proliferative ASM cells, respectively. Furthermore, it is assumed that the density of proliferating and contractile ASM is not changed as a result of secretion of ECM.

ECM presence has been shown to aid the survival of contractile ASM (Freyer et al. 2001). We therefore assume that the apoptosis rate of contractile ASM depends on the ECM density such that

$$\hat{\phi}_c^*(m^*) = \phi_c^* - \frac{\phi_{cm}^* m^*}{\eta_{cm}^* + m^*}, \tag{2.1.4}$$

where, in the absence of ECM aided survival, apoptosis of contractile ASM occurs at a maximum rate ϕ_c^*. In order to ensure that the presence of ECM does not directly increase the density of ASM, yet reduces the ASM apoptosis rate towards a minimum as the further addition of ECM no longer significantly aids ASM survival, we enforce $\phi_c^* > \phi_{cm}^*$. ECM degrades at rate ϕ_m^*.

Activation of latent TGF-β, via alternative sources, is assumed to occur basally (Burgess et al. 2016) at a constant rate κ_a^* in addition to mechanical activation of latent TGF-β (Wipff et al. 2007; Buscemi et al. 2011). Recall that ASM cell con-

traction mechanically activates latent TGF-β, via integrins (Tatler and Jenkins 2012), by unfolding the latent complex that is anchored to the ECM (providing resistance (Hinz 2015)) and that encapsulates latent TGF-β. Hence, both the contractile ASM and ECM are required for the mechanical activation of TGF-β (Tatler et al. 2011); however it is assumed that the process does not result in the loss of either constituent. Latent TGF-β is found in abundance (Annes et al. 2003) and therefore is not a limiting factor in the mechanical activation step. Activation of latent TGF-β in response to an external stimulus, $\hat{\kappa}_s^*(t^*)$, represents exposure to an irritant and mimics an asthmatic exacerbation. Experimentally, the stimulus may represent the administration of a contractile agonist such as methacholine (MCh) that is known to cause contraction of the ASM in lung-slice models (Tan and Sanderson 2014). Following the methods of Chernyavsky et al. (2014), we model this as a time-dependent function given by

$$\hat{\kappa}_s^*(t^*) = \frac{\kappa_s^*}{\sqrt{2\pi\nu^{*2}}} \exp\left[\frac{-(t^* - t_i^*)^2}{2\nu^{*2}}\right]. \tag{2.1.5}$$

The stimulation (possibly experimental challenge) occurs at time t_i^* for a duration of ν and at rate κ_s^*. Subsequent active TGF-β signalling pathways drive further mechanical activation of latent TGF-β via ASM contraction and is assumed to occur at rate $\hat{\kappa}_{ac}^*(a^*)$, as in (2.1.3). This contractile agonist effect of active TGF-β-induced mechanical activation generates a positive feedback loop. As reflected in (2.1.3), we assume that this process saturates so that the amount of achievable contraction of the ASM (in order to mechanically activate TGF-β) is physically limited. Active TGF-β is removed from the system at a rate ϕ_a^* due to natural degradation and binding to receptors that initiate other signalling pathways that are not modelled here.

2.1.2 Model refinement

In this section we refine our general model (2.1.1) to account for specific active TGF-β-receptor binding events that initiate particular cellular responses. We suggest that the rates (2.1.3) may be refined to indicate which cell receptors are required for the distinct cellular responses (*i.e.* which ASM phenotype expresses the required receptor and the availability of such receptor) by including

the combined density of either the proliferating or contractile ASM and active TGF-β. We assume that the receptors expressed by the proliferating and contractile ASM cells are limited so that the binding rate saturates with the combined density of proliferating or contractile ASM and active TGF-β. The refined ODE model is

$$\frac{\mathrm{d}p^*}{\mathrm{d}t^*} = \hat{\kappa}_p^*(p^*)p^*\left(1+\hat{\kappa}_{ap}^*(a^*,p^*)\right) + \kappa_{cp}^* c^* - \kappa_{pc}^* p^*, \tag{2.1.6a}$$

$$\frac{\mathrm{d}c^*}{\mathrm{d}t^*} = \kappa_{pc}^* p^* - \kappa_{cp}^* c^* - \hat{\phi}_c^*(m^*)c^*, \tag{2.1.6b}$$

$$\frac{\mathrm{d}a^*}{\mathrm{d}t^*} = \kappa_a^* + \left(\hat{\kappa}_s^*(t^*) + \hat{\kappa}_{ac}^*(a^*,c^*)\right)c^*m^* - \kappa_b^* a^*(p^*+c^*) - \phi_a^* a^*, \tag{2.1.6c}$$

$$\frac{\mathrm{d}m^*}{\mathrm{d}t^*} = \left(\kappa_{cm}^* + \hat{\kappa}_{acm}^*(a^*,c^*)\right)c^* + \left(\kappa_{pm}^* + \hat{\kappa}_{apm}^*(a^*,p^*)\right)p^* + \hat{\kappa}_e^*(a^*) - \phi_m^* m^*, \tag{2.1.6d}$$

where, the refined rates for TGF-β-induced ASM proliferation, $\hat{\kappa}_{ap}^*(a^*,p^*)$, and ECM secretion, $\hat{\kappa}_{apm}^*(a^*,p^*)$, are

$$\hat{\kappa}_i^*(a^*,p^*) = \frac{\kappa_i^*(a^*p^*)^{n_p}}{\tilde{\eta}_i^* + (a^*p^*)^{n_p}}, \qquad i \in \{ap, apm\}. \tag{2.1.7}$$

Here, $\hat{\kappa}_i^*$ is a function of the product a^*p^* to reflect that active TGF-β must bind to receptors expressed by the proliferating ASM cells in order to initiate the associated pathway (*e.g.* ASM proliferation). Likewise, the refined rates for active TGF-β-induced ASM contraction, $\hat{\kappa}_{ac}^*(a^*,c^*)$, and ECM secretion, $\hat{\kappa}_{acm}^*(a^*,c^*)$, are

$$\hat{\kappa}_i^*(a^*,c^*) = \frac{\kappa_i^*(a^*c^*)^{n_c}}{\tilde{\eta}_i^* + (a^*c^*)^{n_c}}, \qquad i \in \{ac, acm\}; \tag{2.1.8}$$

as above, the dependence on a^*c^* indicates that active TGF-β must bind to receptors expressed by the contractile ASM cells in order to initiate the associated pathway (*e.g.* ASM contraction). We assume that the receptors expressed by other surrounding cells (excluding ASM cells) are in abundance and thus, we refine the rate for active TGF-β-induced ECM secretion from external sources, $\hat{\kappa}_e^*(a^*)$, to

$$\hat{\kappa}_e^*(a^*) = \frac{\kappa_e^* a^{*n}}{\tilde{\eta}_e^* + a^{*n}}. \tag{2.1.9}$$

Furthermore, we include higher order saturation of ECM aided survival of the contractile ASM and refine $\hat{\phi}_c^*(m^*)$ to

$$\hat{\phi}_c^*(m^*) = \phi_c^* - \frac{\phi_{cm}^* m^{*n_m}}{\tilde{\eta}_{cm}^* + m^{*n_m}}. \tag{2.1.10}$$

The Hill coefficients n_p, n_c, n and n_m in (2.1.7) to (2.1.10) represent the order of saturation. Note that $\tilde{\eta}^*$ (in the refined model) and η^* (in the general model) have different dimensions (details in Table C.1 in Appendix C.1).

In addition to the natural degradation of active TGF-β, ϕ_a^*, we must account for removal of active TGF-β through binding to the receptors presented on both the proliferative and contractile ASM cells. Hence, we include the degrading term

$$\hat{\kappa}_b^*(a^*, p^*, c^*) = \kappa_b^* a^*(p^* + c^*), \tag{2.1.11}$$

that describes the rate of change in concentration of active TGF-β.

Our general and refined models, (2.1.1) and (2.1.6), respectively, are subject to the initial conditions:

$$p^*(0) = P^*, \qquad c^*(0) = C^*, \qquad a^*(0) = A^*, \qquad m^*(0) = M^*, \tag{2.1.12}$$

where $P^*, C^*, A^*, M^* > 0$.

2.1.3 Parameter choices

There is a lack of detailed experimental data to appropriately fit the vast number of parameters in our proposed models, (2.1.1) and (2.1.6). For example, the study of Bai et al. (2000) quantifies ASM mass evolution; however, this may not be entirely due to proliferation. Moreover, it is not clear whether parameters measured from *in vitro* experiments are an accurate reflection of those parameters *in vivo*. Therefore, we follow Baker et al. (2017) and choose an illustrative parameter set whereby comparable processes have similar rates. Where possible, we determine estimates for the order of magnitude of rates from the literature and our collaborator's knowledge (Tatler 2016). Baseline parameter values are given in Table C.2 in Appendix C.1.

2.1.4 Non-dimensionalisation

The rate of natural degradation of active TGF-β, ϕ_a^*, is one of the few known rates within each of the models and occurs on the order of minutes (Wakefield et al. 1990; Makinde et al. 2007). Hence, we non-dimensionalise time, t^*, relative to ϕ_a^* such that

$$t = t^* \phi_a^*. \tag{2.1.13}$$

We non-dimensionalise the density of proliferating ASM, p^*, contractile ASM, c^*, ECM, m^* and concentration of active TGF-β, a^*, relative to reference quantities, p_r^*, c_r^*, m_r^* and a_r^*, respectively, to obtain

$$p(t) = \frac{p^*(t^*)}{p_r^*}, \quad c(t) = \frac{c^*(t^*)}{c_r^*}, \quad a(t) = \frac{a^*(t^*)}{a_r^*}, \quad m(t) = \frac{m^*(t^*)}{m_r^*}. \tag{2.1.14}$$

The dimensionless version of the general ODE model (2.1.1) is given by

$$\frac{\mathrm{d}p}{\mathrm{d}t} = \kappa_p p \left(1 - \frac{p}{p_{max}}\right)\left(1 + \frac{\kappa_{ap} a}{\eta_{ap} + a}\right) + \frac{\kappa_{cp}\gamma_c}{\gamma_p} c - \kappa_{pc} p, \tag{2.1.15a}$$

$$\frac{\mathrm{d}c}{\mathrm{d}t} = \frac{\kappa_{pc}\gamma_p}{\gamma_c} p - \kappa_{cp} c - \left(\phi_c - \frac{\phi_{cm} m}{\eta_{cm} + m}\right) c, \tag{2.1.15b}$$

$$\frac{\mathrm{d}a}{\mathrm{d}t} = \kappa_a + \left(\frac{\kappa_s}{\nu} \exp\left[\frac{-(t - t_i)^2}{\nu^2}\right] + \frac{\kappa_{ac} a}{\eta_{ac} + a}\right) \frac{cm}{\gamma_a} - a, \tag{2.1.15c}$$

$$\begin{aligned}\frac{\mathrm{d}m}{\mathrm{d}t} = &\left(\kappa_{cm} + \frac{\kappa_{acm} a}{\eta_{acm} + a}\right)\gamma_c c + \left(\kappa_{pm} + \frac{\kappa_{apm} a}{\eta_{apm} + a}\right)\gamma_p p \\ &+ \frac{\kappa_e a}{\eta_e + a} - \phi_m m,\end{aligned} \tag{2.1.15d}$$

and the dimensionless version of the refined ODE model (2.1.6) is given by

$$\frac{\mathrm{d}p}{\mathrm{d}t} = \kappa_p p\left(1-\frac{p}{p_{max}}\right)\left(1+\frac{\kappa_{ap}(ap)^{n_p}}{\tilde{\eta}_{ap}+(ap)^{n_p}}\right)+\frac{\kappa_{cp}\gamma_c}{\gamma_p}c-\kappa_{pc}p, \tag{2.1.16a}$$

$$\frac{\mathrm{d}c}{\mathrm{d}t} = \frac{\kappa_{pc}\gamma_p}{\gamma_c}p-\kappa_{cp}c-\left(\phi_c-\frac{\phi_{cm}m^{n_m}}{\tilde{\eta}_{cm}+m^{n_m}}\right)c, \tag{2.1.16b}$$

$$\begin{aligned}\frac{\mathrm{d}a}{\mathrm{d}t} = {}& \kappa_a+\left(\frac{\kappa_s}{\nu}\exp\left[\frac{-(t-t_i)^2}{\nu^2}\right]+\frac{\kappa_{ac}(ac)^{n_c}}{\tilde{\eta}_{ac}+(ac)^{n_c}}\right)\frac{cm}{\gamma_a}\\ & -\kappa_b\left(\frac{\gamma_p}{\gamma_c}p+c\right)a-a,\end{aligned} \tag{2.1.16c}$$

$$\begin{aligned}\frac{\mathrm{d}m}{\mathrm{d}t} = {}& \left(\kappa_{cm}+\frac{\kappa_{acm}(ac)^{n_c}}{\tilde{\eta}_{acm}+(ac)^{n_c}}\right)\gamma_c c+\left(\kappa_{pm}+\frac{\kappa_{apm}(ap)^{n_p}}{\tilde{\eta}_{apm}+(ap)^{n_p}}\right)\gamma_p p\\ & +\frac{\kappa_e a^n}{\tilde{\eta}_e+a^n}-\phi_m m.\end{aligned} \tag{2.1.16d}$$

In (2.1.15) and (2.1.16), we introduce the parameters

$$\gamma_p = \frac{p_r^*}{m_r^*}, \qquad \gamma_c = \frac{c_r^*}{m_r^*}, \qquad \gamma_a = \frac{a_r^*}{m_r^*}, \tag{2.1.17}$$

which represent the ratio of the reference quantities of proliferating ASM, p_r^*, contractile ASM, c_r^*, and active TGF-β, a_r^*, to that of ECM, m_r^*, respectively. The non-dimensionalisation of the remaining parameters in the general model (2.1.15) and the refined model (2.1.16) are provided in Table C.1 in Appendix C.1.

Both of the dimensionless models, (2.1.15) and (2.1.16), are subject to the dimensionless initial conditions:

$$p(0) = P, \qquad c(0) = C, \qquad a(0) = A, \qquad m(0) = M, \tag{2.1.18}$$

where,

$$P = \frac{P^*}{p_r^*}, \qquad C = \frac{C^*}{c_r^*}, \qquad A = \frac{A^*}{a_r^*}, \qquad M = \frac{M^*}{m_r^*}. \tag{2.1.19}$$

2.2 Asymptotic reduction

Hereafter, we consider first order saturation of the Hill functions within the refined model (2.1.16), *i.e.* $n_p, n_c, n_m, n = 1$, and to permit analysis, we introduce a small parameter ε. Following discussions with Tatler (2016), we identify the fast and slow time scales associated with rapid signalling pathways and gradually evolving downstream effects. The basal non-mechanical activation of TGF-β, κ_a, ECM aided survival of contractile ASM, ϕ_{cm}, ECM secretion from the contractile ASM, κ_{cm}, ECM secretion from the contractile ASM induced by active TGF-β, κ_{acm}, and ECM secretion from other surrounding cells, κ_e, act on a slow timescale of hours to days, compared to the remaining rates within the systems that act over the order of minutes (Tatler 2016). Therefore, we choose to scale κ_a, ϕ_{cm}, κ_{cm}, κ_{acm} and κ_e with ε such that

$$\kappa_a = \varepsilon\tilde{\kappa}_a, \quad \phi_{cm} = \varepsilon\tilde{\phi}_{cm}, \quad \kappa_{cm} = \varepsilon\tilde{\kappa}_{cm}, \quad \kappa_{acm} = \varepsilon\tilde{\kappa}_{acm}, \quad \kappa_e = \varepsilon\tilde{\kappa}_e. \tag{2.2.1}$$

We proceed by expanding each of the variables via asymptotic series in ε such that

$$\begin{aligned} p(t) &= p^{(0)}(t) + \varepsilon p^{(1)}(t) + \mathcal{O}(\varepsilon^2), \\ c(t) &= c^{(0)}(t) + \varepsilon c^{(1)}(t) + \mathcal{O}(\varepsilon^2), \\ a(t) &= a^{(0)}(t) + \varepsilon a^{(1)}(t) + \mathcal{O}(\varepsilon^2), \\ m(t) &= m^{(0)}(t) + \varepsilon m^{(1)}(t) + \mathcal{O}(\varepsilon^2). \end{aligned} \tag{2.2.2}$$

Substituting the expansions (2.2.2) into both of the models, (2.1.15) and (2.1.16), we obtain the respective leading order systems.

At the leading order, $\mathcal{O}(1)$, the general model (2.1.15) reads

$$\frac{\mathrm{d}p^{(0)}}{\mathrm{d}t} = \kappa_p p^{(0)} \left(1 - \frac{p^{(0)}}{p_{max}}\right) \left(1 + \frac{\kappa_{ap} a^{(0)}}{\eta_{ap} + a^{(0)}}\right) + \frac{\kappa_{cp}\gamma_c}{\gamma_p} c^{(0)} - \kappa_{pc} p^{(0)}, \tag{2.2.3a}$$

$$\frac{\mathrm{d}c^{(0)}}{\mathrm{d}t} = \frac{\kappa_{pc}\gamma_p}{\gamma_c} p^{(0)} - \left(\kappa_{cp} + \phi_c\right) c^{(0)}, \tag{2.2.3b}$$

$$\frac{\mathrm{d}a^{(0)}}{\mathrm{d}t} = \left(\frac{\kappa_s}{\nu} \exp\left[\frac{-(t-t_i)^2}{\nu^2}\right] + \frac{\kappa_{ac} a^{(0)}}{\eta_{ac} + a^{(0)}}\right) \frac{c^{(0)} m^{(0)}}{\gamma_a} - a^{(0)}, \tag{2.2.3c}$$

$$\frac{\mathrm{d}m^{(0)}}{\mathrm{d}t} = \left(\kappa_{pm} + \frac{\kappa_{apm} a^{(0)}}{\eta_{apm} + a^{(0)}}\right) \gamma_p p^{(0)} - \phi_m m^{(0)}, \tag{2.2.3d}$$

and the refined model (2.1.16) reads

$$\begin{aligned}\frac{\mathrm{d}p^{(0)}}{\mathrm{d}t} = {} & \kappa_p p^{(0)} \left(1 - \frac{p^{(0)}}{p_{max}}\right) \left(1 + \frac{\kappa_{ap} a^{(0)} p^{(0)}}{\tilde{\eta}_{ap} + a^{(0)} p^{(0)}}\right) \\ & + \frac{\kappa_{cp}\gamma_c}{\gamma_p} c^{(0)} - \kappa_{pc} p^{(0)},\end{aligned} \tag{2.2.4a}$$

$$\frac{\mathrm{d}c^{(0)}}{\mathrm{d}t} = \frac{\kappa_{pc}\gamma_p}{\gamma_c} p^{(0)} - \left(\kappa_{cp} + \phi_c\right) c^{(0)}, \tag{2.2.4b}$$

$$\begin{aligned}\frac{\mathrm{d}a^{(0)}}{\mathrm{d}t} = {} & \left(\frac{\kappa_s}{\nu} \exp\left[\frac{-(t-t_i)^2}{\nu^2}\right] + \frac{\kappa_{ac} a^{(0)} c^{(0)}}{\tilde{\eta}_{ac} + a^{(0)} c^{(0)}}\right) \frac{c^{(0)} m^{(0)}}{\gamma_a} \\ & - \kappa_b \left(\frac{\gamma_p p^{(0)}}{\gamma_c} + c^{(0)}\right) - a^{(0)},\end{aligned} \tag{2.2.4c}$$

$$\frac{\mathrm{d}m^{(0)}}{\mathrm{d}t} = \left(\kappa_{pm} + \frac{\kappa_{apm} a^{(0)} p^{(0)}}{\tilde{\eta}_{apm} + a^{(0)} p^{(0)}}\right) \gamma_p p^{(0)} - \phi_m m^{(0)}. \tag{2.2.4d}$$

2.3 Stability analysis

In the absence of stimulation, *i.e.* $\kappa_s = 0$, we identify four possible non-negative steady states of the reduced systems (2.2.3) and (2.2.4). Hereafter, overbar indicates the steady state of each variable and subscript labels represent each steady state case.

Firstly, in both of the leading order models, (2.2.3) and (2.2.4), we identify the zero steady state

$$\left(\bar{p}_1^{(0)}, \bar{c}_1^{(0)}, \bar{a}_1^{(0)}, \bar{m}_1^{(0)}\right) = (0, 0, 0, 0)\,. \tag{2.3.1}$$

Secondly (and again in both (2.2.3) and (2.2.4)), we identify a state where the leading order concentration of active TGF-β is zero,

$$\left(\bar{p}_2^{(0)}, \bar{c}_2^{(0)}, \bar{a}_2^{(0)}, \bar{m}_2^{(0)}\right) = \left(\bar{p}_2^{(0)}, \bar{c}_2^{(0)}, 0, \bar{m}_2^{(0)}\right), \tag{2.3.2}$$

where,

$$\bar{p}_2^{(0)} = p_{max}\left(1 - \frac{\kappa_{pc}\phi_c}{\kappa_p\left(\kappa_{cp} + \phi_c\right)}\right), \tag{2.3.3a}$$

$$\bar{c}_2^{(0)} = \frac{\kappa_{pc}\gamma_p\bar{p}_2^{(0)}}{\gamma_c\left(\kappa_{cp} + \phi_c\right)}, \tag{2.3.3b}$$

$$\bar{m}_2^{(0)} = \frac{\kappa_{pm}\gamma_p\bar{p}_2^{(0)}}{\phi_m}. \tag{2.3.3c}$$

The steady state (2.3.2) is positive and thus, biologically relevant, for

$$\frac{\kappa_{pc}\phi_c}{\kappa_p(\phi_c + \kappa_{cp})} < 1. \tag{2.3.4}$$

Finally, we identify a further two positive steady states,

$$\left(\bar{p}_{3,4}^{(0)}, \bar{c}_{3,4}^{(0)}, \bar{a}_{3,4}^{(0)}, \bar{m}_{3,4}^{(0)}\right) > (0,0,0,0), \tag{2.3.5}$$

that are given by the intersection of the nullclines of the respective reduced systems, (2.2.3) and (2.2.4). In the leading order general model (2.2.3), the steady state solutions (2.3.5) are given by the intersections of the hypersurfaces:

$$\bar{p}_{3,4}^{(0)} = p_{max}\left(1 - \frac{\kappa_{pc}\phi_c}{\kappa_p(\phi_c + \kappa_{cp})}\left(\frac{\eta_{ap} + \bar{a}_{3,4}^{(0)}}{\eta_{ap} + (\kappa_{ap} + 1)\bar{a}_{3,4}^{(0)}}\right)\right), \tag{2.3.6a}$$

$$\bar{c}_{3,4}^{(0)} = \frac{\kappa_{pc}\gamma_p\bar{p}_{3,4}^{(0)}}{\gamma_c(\kappa_{cp} + \phi_c)}, \tag{2.3.6b}$$

$$\bar{a}_{3,4}^{(0)} = \frac{\kappa_{ac}\bar{c}_{3,4}^{(0)}\bar{m}_{3,4}^{(0)}}{\gamma_a} - \eta_{ac}, \tag{2.3.6c}$$

$$\bar{m}_{3,4}^{(0)} = \left(\kappa_{pm} + \frac{\kappa_{apm}\bar{a}_{3,4}^{(0)}}{\eta_{apm} + \bar{a}_{3,4}^{(0)}}\right)\frac{\gamma_p\bar{p}_{3,4}^{(0)}}{\phi_m}. \tag{2.3.6d}$$

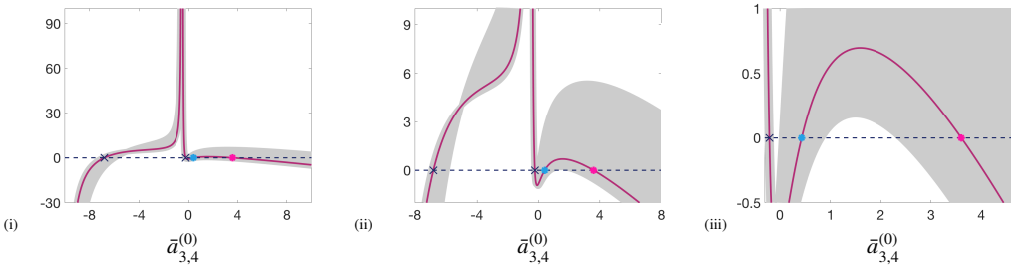

Figure 2.2: Equation (2.3.7) plotted as a function of $\bar{a}_{3,4}^{(0)}$ for various parameter values (grey regions) to illustrate the possible values of (2.3.5). Zoom increases from (i) to (iii). The pink line indicates baseline parameter values provided in Table C.2 in Appendix C.1. Intersections of the pink curve (or grey regions) with the dashed zero line provide values of the steady state $\bar{a}_{3,4}^{(0)}$ in (2.3.5), the blue dot indicates $\bar{a}_3^{(0)}$ and the pink dot indicates $\bar{a}_4^{(0)}$. The two x's indicate the additional solutions to (2.3.7) that are negative and therefore not biologically relevant.

Expressions (2.3.6) can be written in terms of the leading order steady state concentration of active TGF-β, $\bar{a}_{3,4}^{(0)}$, and thus, we rearrange (2.3.6) to obtain a nonlinear equation in $\bar{a}_{3,4}^{(0)}$,

$$0 = -\eta_{ac} - \bar{a}_{3,4}^{(0)} + \frac{\kappa_{ac}\kappa_{pc}\gamma_p^2 p_{max}^2}{\phi_m \gamma_a \gamma_c \left(\kappa_{cp} + \phi_c\right)} \left(1 - \frac{\kappa_{pc}\phi_c}{\kappa_p \left(\kappa_{cp} + \phi_c\right)} \times \left(\frac{\eta_{ap} + \bar{a}_{3,4}^{(0)}}{\eta_{ap} + \left(\kappa_{ap} + 1\right)\bar{a}_{3,4}^{(0)}}\right)\right)^2 \left(\kappa_{pm} + \frac{\kappa_{apm}\bar{a}_{3,4}^{(0)}}{\eta_{apm} + \bar{a}_{3,4}^{(0)}}\right). \tag{2.3.7}$$

Solutions to (2.3.7) provide (2.3.5). Given a range of suitable parameter estimates, we confirm numerically the existence of two positive solutions, $\bar{a}_3^{(0)}$ and $\bar{a}_4^{(0)}$ (Figure 2.2).

In the leading order refined model (2.2.4), the steady state solutions (2.3.5) are given by the intersections of the hypersurfaces:

$$\bar{p}_{3,4}^{(0)} = p_{max}\left(1 - \frac{\kappa_{pc}\phi_c}{\kappa_p(\phi_c + \lambda_{pc})}\left(\frac{\tilde{\eta}_{ap} + \bar{a}_{3,4}^{(0)}\bar{p}_{3,4}^{(0)}}{\tilde{\eta}_{ap} + (\kappa_{ap}+1)\bar{a}_{3,4}^{(0)}\bar{p}_{3,4}^{(0)}}\right)\right), \tag{2.3.8a}$$

$$\bar{c}_{3,4}^{(0)} = \frac{\kappa_{pc}\gamma_p\bar{p}_{3,4}^{(0)}}{\gamma_c(\kappa_{cp} + \phi_c)}, \tag{2.3.8b}$$

$$\begin{aligned}\bar{a}_{3,4}^{(0)} = \frac{\kappa_{pc}}{\kappa_{pc} + \kappa_b(\kappa_{cp} + \phi_c + \kappa_{pc})\bar{c}_{3,4}^{(0)}}\Bigg(&\frac{\kappa_{ac}\bar{c}_{3,4}^{(0)}\bar{m}_{3,4}^{(0)}}{\gamma_a} \\ &-\tilde{\eta}_{ac}\left(\frac{1}{\bar{c}_{3,4}^{(0)}} + \frac{\kappa_b(\kappa_{cp} + \phi_c + \kappa_{pc})}{\kappa_{pc}}\right)\Bigg),\end{aligned} \tag{2.3.8c}$$

$$\bar{m}_{3,4}^{(0)} = \left(\kappa_{pm} + \frac{\kappa_{apm}\bar{a}_{3,4}^{(0)}\bar{p}_{3,4}^{(0)}}{\tilde{\eta}_{apm} + \bar{a}_{3,4}^{(0)}\bar{p}_{3,4}^{(0)}}\right)\frac{\gamma_p\bar{p}_{3,4}^{(0)}}{\phi_m}. \tag{2.3.8d}$$

Compared to (2.3.6), expressions (2.3.8) do not reduce to explicit functions of a single variable. Instead, expressions (2.3.8) reduce to two implicit functions of two variables and thus, we proceed numerically to confirm the existence of two positive solutions, $\bar{a}_3^{(0)}$ and $\bar{a}_4^{(0)}$, for a range of suitable parameter estimates.

The stability of the leading order steady states is determined by the eigenvalues of the corresponding Jacobian matrix of (2.2.3) and (2.2.4). Below, we consider the leading order zero steady state (2.3.1), for which eigenvalues can be obtained analytically. The Jacobian matrix for both of the reduced systems (2.2.3) and (2.2.4) evaluated at (2.3.1), $\mathbf{J}_0$, is given by

$$\mathbf{J}_0 = \begin{bmatrix} -\kappa_{pc} + \kappa_p & \frac{\kappa_{cp}\gamma_c}{\gamma_p} & 0 & 0 \\ \frac{\kappa_{pc}\gamma_p}{\gamma_c} & -\kappa_{cp} - \phi_c & 0 & 0 \\ 0 & 0 & -1 & 0 \\ \kappa_{pm}\gamma_p & 0 & 0 & -\phi_m \end{bmatrix}. \tag{2.3.9}$$

Correspondingly, the eigenvalues, Λ_j for $j \in \{1, \ldots, 4\}$, of $\mathbf{J}_0$ are given by

$$\Lambda_1 = -1, \tag{2.3.10a}$$

$$\Lambda_2 = -\phi_m, \tag{2.3.10b}$$

$$\Lambda_3 = \frac{\kappa_p - \kappa_{cp} - \kappa_{pc} - \phi_c}{2} + \frac{1}{2}\left(\left(\kappa_p - \kappa_{cp} - \kappa_{pc} - \phi_c\right)^2 - 4\left(\phi_c\kappa_{pc} - \phi_c\kappa_p - \kappa_{cp}\kappa_p\right)\right)^{\frac{1}{2}}, \tag{2.3.10c}$$

$$\Lambda_4 = \frac{\kappa_p - \kappa_{cp} - \kappa_{pc} - \phi_c}{2} - \frac{1}{2}\left(\left(\kappa_p - \kappa_{cp} - \kappa_{pc} - \phi_c\right)^2 - 4\left(\phi_c\kappa_{pc} - \phi_c\kappa_p - \kappa_{cp}\kappa_p\right)\right)^{\frac{1}{2}}. \tag{2.3.10d}$$

The eigenvalue Λ_3 is positive for

$$\phi_c\kappa_{pc} - \phi_c\kappa_p - \kappa_{cp}\kappa_p < 0, \tag{2.3.11}$$

and thus, for this parameter restriction, the leading order zero steady state (2.3.1) is unstable. The inequality (2.3.11) may be rearranged to obtain (2.3.4) and hence, this stability condition coincides with the existence of the biologically relevant steady state (2.3.2). The rate of ASM phenotype switching from the proliferative to contractile state, κ_{pc}, and the rate of ASM proliferation, κ_p, are of similar magnitude and thus (2.3.11) is satisfied for biologically relevant parameters. Accordingly, we have located a transcritical bifurcation in the leading order zero steady state (2.3.1).

Guided by our findings at leading order in the reduced models, (2.2.3) and (2.2.4), we carry out a steady state stability analysis of the full general model (2.1.15) and the full refined model (2.1.16) in the dynamical systems software `XPPAUT`. The dimensionless parameters representing the rate of ASM proliferation, κ_p, phenotype switching from the proliferative to contractile phenotype, κ_{pc} and contractile ASM degradation, ϕ_c, (all relative to the rate of active TGF-β degradation) feature in the reduced restriction (2.3.4). We therefore investigate the stability and location of the steady states of the full models (2.1.15) and (2.1.16) as functions of these parameters (Figures 2.3 and 2.5, respectively).

There are many qualitative similarities between the bifurcation diagrams for the general model and those for the refined model; however, there are quantitative

differences between the two (*cf.* Figures 2.3, 2.5). We see that the values of the steady states for the active TGF-β concentration, $\bar{a}$, in the general model are larger than in the refined model. This may be expected as the removal of active TGF-β is reduced by neglecting specified binding events (*cf.* Figures 2.3, 2.5).

As previously identified in the reduced models (2.2.3) and (2.2.4), we observe regimes where there are up to four possible non-negative steady states, giving rise to a bi-stability (Figures 2.3, 2.5). Within the chosen parameter span of κ_p and κ_{pc}, we observe three distinct bifurcation points in the first two columns of Figures 2.3 and 2.5. Firstly, we see a transcritical bifurcation, secondly, we see a change in stability of the positive branch and finally, we see another change in stability that gives rise to a bi-stable regime. The two points of stability change along the branch indicate the upper and lower bound of a bi-stable region, respectively. In the reduced models, these observations correspond to the transcritical bifurcation in the leading order zero steady state (2.3.1) as the leading order steady state (2.3.2) becomes positive and stable by satisfying the parameter restriction (2.3.4). The leading order steady states (2.3.5) correspond to the upper and lower bound of a bi-stable region.

As outlined in Section 1.2, there is a correlation in the severity of asthma and the amount of active TGF-β present in the airways (Chen and Khalil 2006; Al Alawi et al. 2014). Within the bi-stable parameter regime, we associate the stable steady state where the concentration of active TGF-β remains very small with a healthy homeostatic state that maintains normal ASM and ECM accumulation. We associate the stable steady state where the concentration of active TGF-β is chronically elevated with a diseased state that results in excessive ASM and ECM accumulation. The unstable steady state located between the two acts as a transition threshold leading to irreversible airway alterations and asthma development. With reference to the bifurcation diagrams in Figures 2.3 and 2.5, the healthy steady state is located in the lower section of the stable branch, the transition steady state is located in the unstable section of the branch and the diseased steady state is located in the upper stable section of the branch.

For values of κ_p below the location of the transcritical bifurcation point, there are no biologically relevant steady states in either of the respective systems (*e.g.* Figures 2.3 (i), 2.5 (i)), suggesting that the proliferation rate must be large

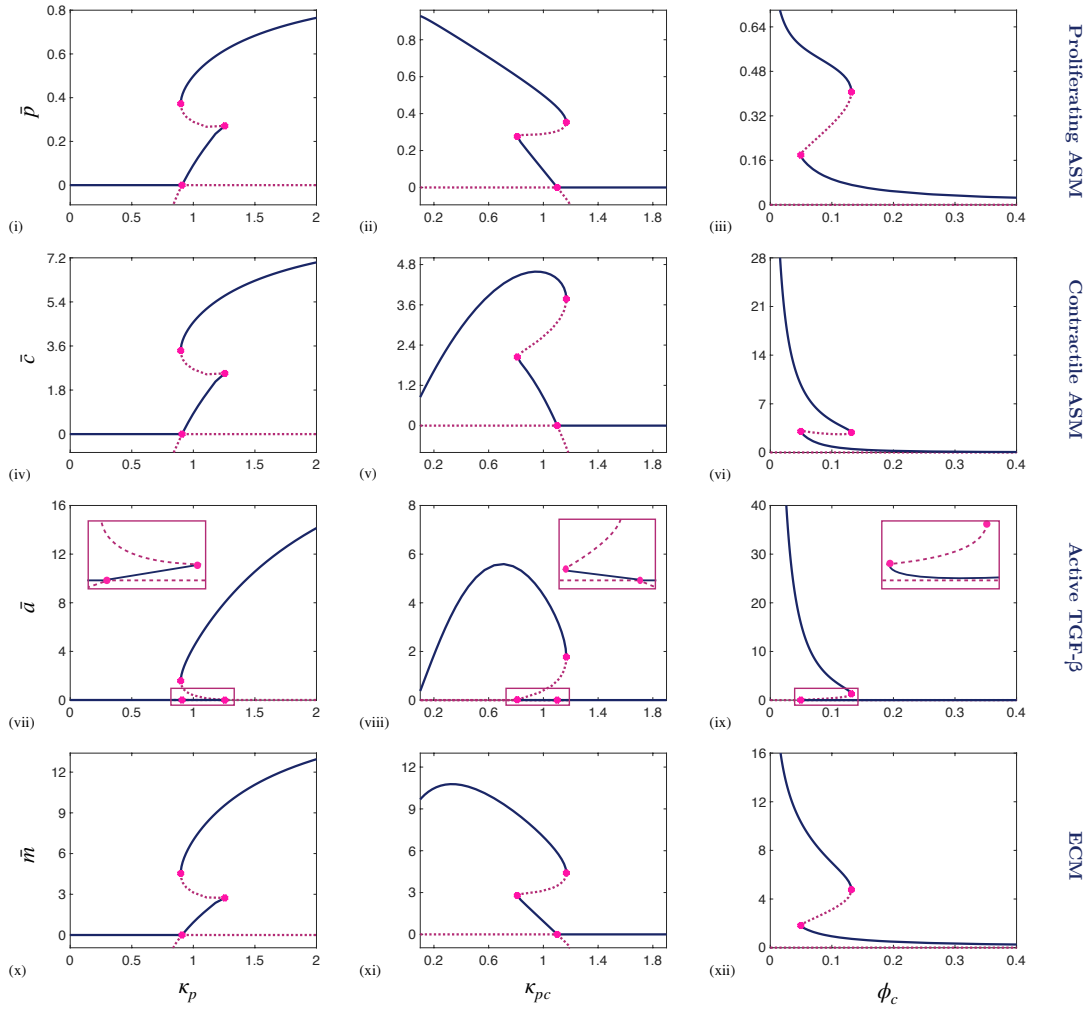

Figure 2.3: Bifurcation diagrams for κ_p, κ_{pc}, ϕ_c (1st, 2nd and 3rd column, respectively) in the general model (2.1.15). The parameter values are baseline values provided in Table C.2 in Appendix C.1.

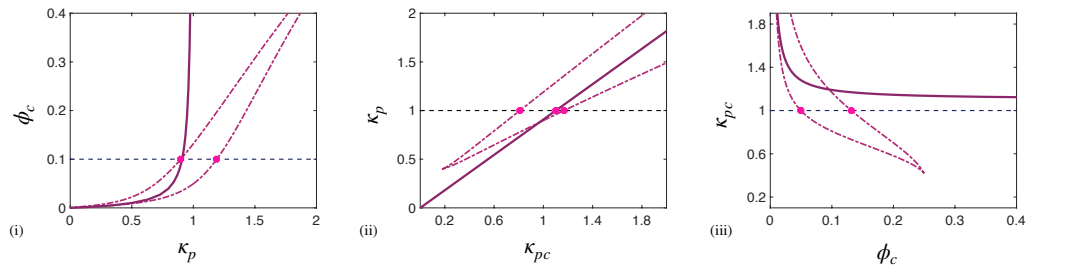

Figure 2.4: Two Parameter bifurcation diagrams for κ_p, κ_{pc}, ϕ_c in the general model (2.1.15). Solid lines track the transcritical branching point, pink dashed lines track the limit points defining the bi-stable regime, black dashed lines indicate a slice corresponding to Figure 2.3 and the pink dots represent the corresponding bifurcation points. The parameter values are baseline values provided in Table C.2 in Appendix C.1

enough to allow for sustainable growth of the ASM and ECM populations. For increasingly large κ_p, the bi-stable regime is surpassed and the elevated positive steady state becomes the only biologically relevant steady state (*e.g.* Figures 2.3 (iv), 2.5 (iv)). Intuitively, this steady state rises with increasing rate of ASM proliferation due to the accumulation of ASM which subsequently increases ECM secretion and causes further activation of TGF-β (*e.g.* Figures 2.3 (vii), 2.5 (vii)) that initiates a positive feedback loop.

On the other hand, there are no biologically relevant steady states in either of the respective systems for values of κ_{pc} above the transcritical bifurcation point (*e.g.* Figures 2.3 (i), 2.5 (i)). This indicates that the ASM phenotype switching rate from the proliferative to the contractile state must be small enough so that there is a sufficient amount of ASM cells in the proliferative state in order to sustain ASM growth. This acts in a similar manner to the proliferation rate being too low, whereby ECM secretion and TGF-β activation is hindered downstream. The stable steady state population of proliferating ASM increases as the switch rate continues to decrease; however, it is interesting to note that this corresponds to a decrease in the contractile ASM, ECM and active TGF-β quantities once a maximum is achieved (*e.g.* Figures 2.3 (viii), 2.5 (viii)). It appears that there is an optimum switch rate where there is sufficient proliferative ASM to increase growth and ECM secretion, yet allow for a large contractile ASM population that is necessary to mechanically activate TGF-β (*cf.* Figures 2.3 (ii), (v); 2.5 (ii), (v)).

The two bifurcation points, where there is a change in direction and stability of the positive stable branch, persist as we vary the rate of degradation of the contractile ASM, ϕ_c (*e.g.* Figures 2.3 (iii), 2.5 (iii)). For large values of ϕ_c there is a transcritical bifurcation, as observed in the other diagrams; however, we have restricted the range of ϕ_c that is displayed in the third column of Figures 2.3 and 2.5 in order to study the bi-stable regime of interest closely. Here, the lower region of the stable branch quickly reduces towards the the unstable steady state as ϕ_c increases. Whereas, there is a dramatic increases in the constituents' steady state value for very small values of ϕ_c (*e.g.* Figures 2.3 (vi), 2.5 (vi)). In this instance, it is clear that the reduced rate of degradation of contractile ASM does not sufficiently regulate the accumulation of ASM mass and as a result, causes excessive growth of the contractile ASM, ECM secretion and TGF-β

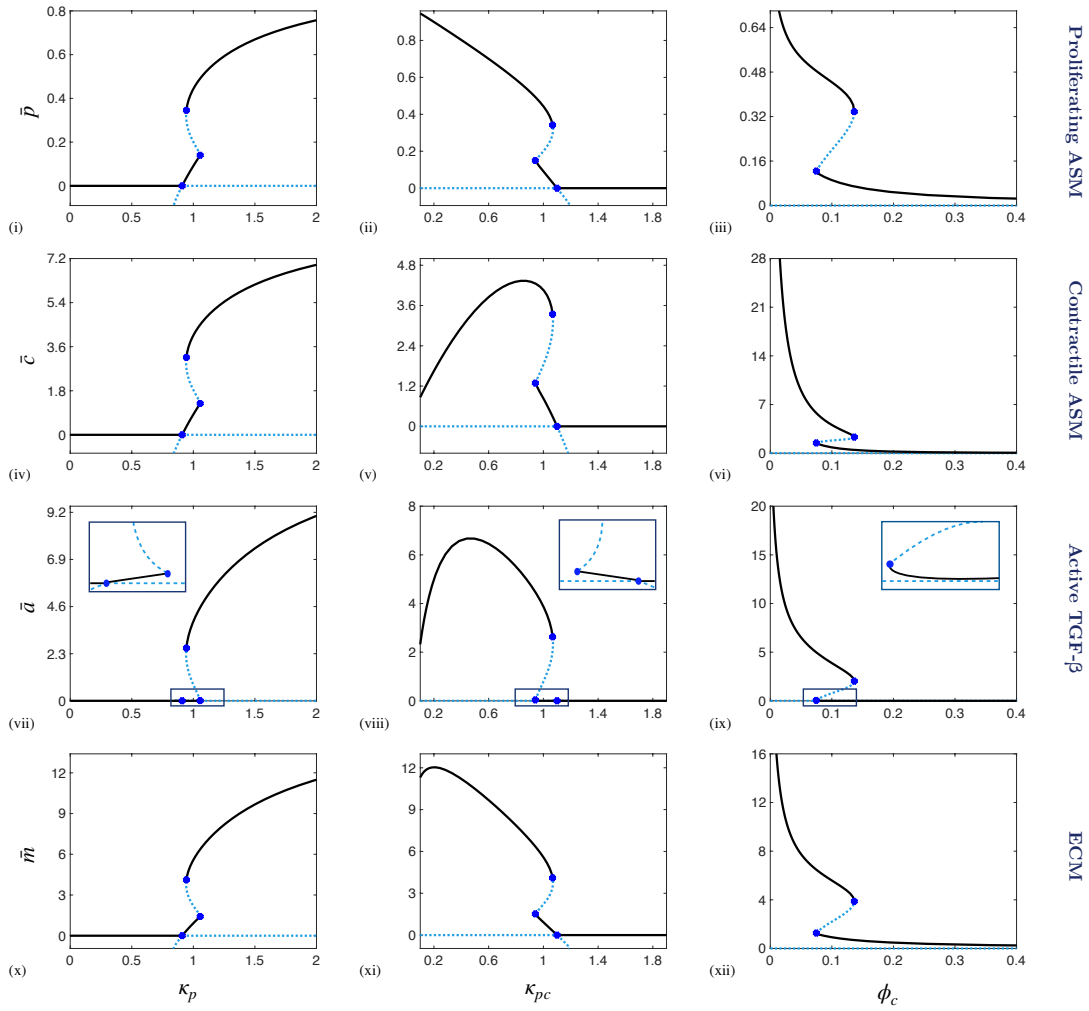

Figure 2.5: Bifurcation diagrams for κ_p, κ_{pc}, ϕ_c (1st, 2nd and 3rd column, respectively) in the refined model (2.1.16). The parameter values are baseline values provided in Table C.2 in Appendix C.1.

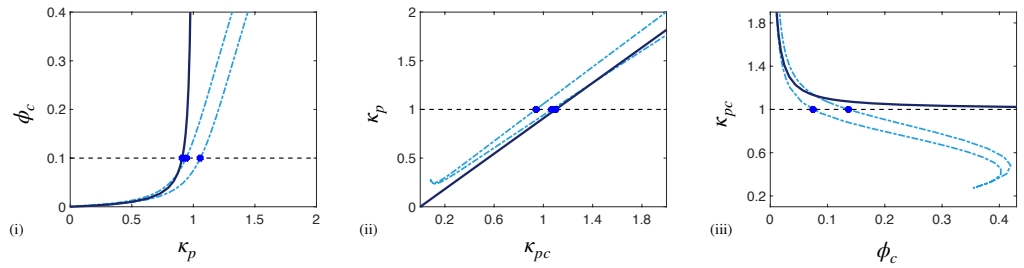

Figure 2.6: Two Parameter bifurcation diagrams for κ_p, κ_{pc}, ϕ_c in the refined model (2.1.16). Solid lines track the transcritical branching point, blue dashed lines track the limit points defining the bi-stable regime, black dashed lines indicate a slice corresponding to Figure 2.5 and the blue dots represent the corresponding bifurcation points. The parameter values are baseline values provided in Table C.2 in Appendix C.1.

activation (*e.g.* Figures 2.3 (xii), 2.5 (xii)).

In Figures 2.4 and 2.6 we track the motion of the bifurcation points (from the single parameter diagrams in Figures 2.3 and 2.5) in two dimensional parameter space to show the creation and destruction of the bi-stable regime. The two models display similar behaviour in two parameter space. Both regimes follow a similar trend; however, overall the bi-stable region is wider in the general model (2.1.15) than in the refined model (2.1.16), suggesting that the refined model is more sensitive to parameter variation (*cf.* Figures 2.3, 2.5).

In both models, there exists a combination of κ_p and κ_{pc} that leads to a transcritical bifurcation point and is displayed by the approximately linear correlation in Figures 2.4 (ii) and 2.6 (ii). Furthermore, this point appears as both parameters increase, demonstrating a positive relation between the proliferation rate of ASM and the switching rate of ASM phenotype from the proliferative to contractile state. In contrast, this bifurcation point does not exist for all values of ϕ_c, specifically for values of $\kappa_p > 1$ (Figures 2.4 (i), 2.6 (i)) and for values of $\kappa_{pc} < 1$ (Figures 2.4 (iii), 2.6 (iii)). For values of $\kappa_p > 1$ we note that only the bi-stable regime exists (Figures 2.4 (i), 2.6 (i)). Therefore, a balance is required between the rate of proliferation and degradation of the ASM in order to permit a bi-stable regime that exhibits a state of relatively low concentration of active TGF-β. As proliferation increases, so must the degradation of ASM to regulate the increased ASM mass, subsequent ECM secretion and TGF-β activation. We note that the path of the bi-stable region is steeper and narrower in the refined model than in the general model (*cf.* Figures 2.4 (i), 2.6 (i)).

For very small values of κ_{pc}, we see that there are no bifurcation points for any value of ϕ_c, meaning that there are no biologically relevant steady states in either of the respective systems (Figures 2.4 (iii), 2.6 (iii)). Therefore, when the ASM phenotype switching rate from the proliferative to contractile state is significantly small, there are no rates of contractile ASM degradation that permit a biologically relevant steady state. In this instance, there is so little contractile ASM, due to insignificant amounts being switched from the proliferative population, that the degradation of what remains does not make a significant difference to the overall dynamics of the system.

Similarly, for very small values of κ_p, we see that not all values of κ_{pc} permit a

bi-stable regime and the transcritical bifurcation is the only bifurcation point in the respective systems (Figures 2.4 (ii), 2.6 (ii)). Biologically, the amount of proliferating ASM that may be exchanged to the contractile state is considerably reduced, due to the decline in the production rate. Hence, any minor contribution from the proliferative population is deemed insignificant, irrespective of the switch rate, and does not alter the overall systems dynamics. We note that this critical value of κ_p is smaller in the refined model than in the general model (*cf.* Figures 2.6 (i), 2.4 (i)). The critical value of κ_{pc}, for which the bi-stable regime does not exist, is likewise significantly smaller in the refined model than in the general model (*cf.* Figures 2.6 (ii), 2.4 (ii)).

2.4 Unsteady numerical results

As outlined above, we associate the stable steady state where the concentration of active TGF-β remains very small with a healthy homeostatic state. We associate the stable steady state where the concentration of active TGF-β is chronically elevated with a diseased state. Finally, the unstable steady state located between the two acts as a transition threshold leading to irreversible airway alterations and asthma development. In this section, we initialise our ODE systems with the healthy steady state and demonstrate that in the presence of stimuli, $\hat{\kappa}_s(t)$, the healthy homeostatic state may be lost as the threshold over which irreversible airway alterations occur is surpassed, giving rise to the diseased state. Following the approach of Chernyavsky et al. (2014), here we simulate asthmatic exacerbations at multiple time points, t_i, in both the full general model (2.1.15) and the full refined model (2.1.16). We show the possible agonist-driven increase in the activation of TGF-β and the downstream consequences that may lead to airway remodelling in asthma.

2.4.1 Effect of increasing the number of stimuli

In this section we simulate recurrent challenges of contractile agonist, $\hat{\kappa}_s$ and increase the frequency of occurrence (Figure 2.7). For a low number of challenges, the systems return to the healthy homeostatic state following exposures (Figures 2.7 (i), (iv)). As the number of exposures increases, the concentration

of active TGF-β continues to climb (*e.g.* Figure 2.7 (v)). Subsequently, ASM and ECM mass increases and leads to further activation of TGF-β in a positive feedback loop. In this instance, the threshold for which the systems can return to the healthy state is surpassed and the irreversible changes to the overall dynamics lead to the diseased state. Once a high number of successive exposures occur, ASM and ECM accumulation appears to adapt to the newly adopted diseased regime and the relative amplitude of the perturbations decreases once a certain number of stimulations have been applied. This is somewhat clearer in the general model than in the refined model whereby the ASM mass, in both the proliferative and contractile form, have saturated at the diseased state and the relative amplitude of the perturbation from this state reduces at each exposure (Figures 2.7 (iii), (vi)).

Overall, the mass of each constituent in the general model increases more rapidly than in the refined model and is particularly noticeable when comparing Figures 2.7 (ii) and (v). Moreover, the general model gives rise to higher concentrations of active TGF-β at each given exposure to the stimulant. This is to be expected due to the reduced removal of active TGF-β from the system by ne-

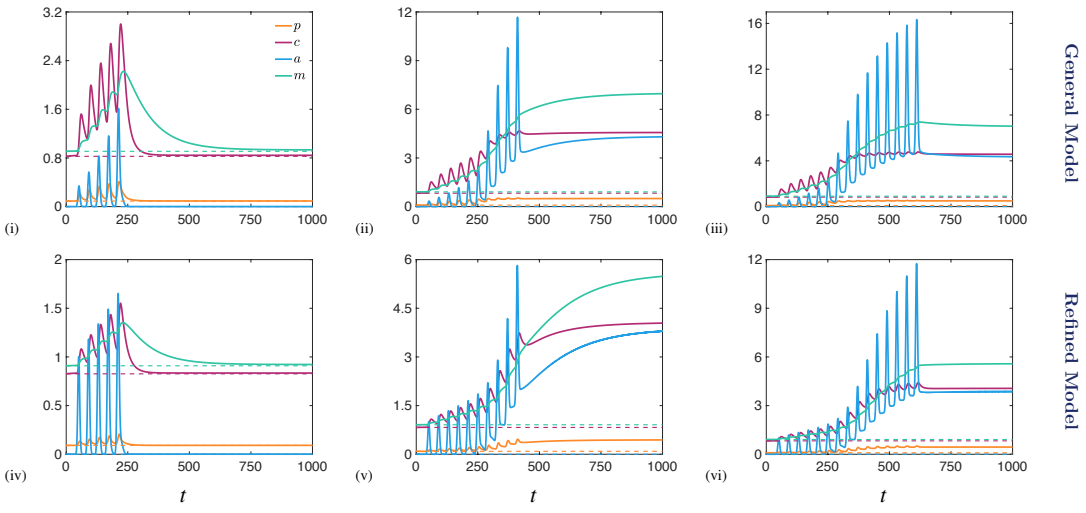

Figure 2.7: (i)–(iii) Results from the general model (2.1.15) and (iv)–(vi) results from the refined model (2.1.16) to illustrate the effect of increasing the number of stimuli driving TGF-β activation on the density of airway wall components. From right to left, the number of exposures are 5, 10 and 15. Dashed lines correspond to the healthy homeostatic state initial condition. Parameter values, selected within the bi-stable regime, are provided in Table C.3 in Appendix C.1.

glecting removal via specified binding events.

2.4.2 Effect of increasing the frequency of stimuli

In this section we simulate a fixed number of recurrent stimuli and reduce the period between exposures. When the stimulation occurs at a low frequency there is sufficient recovery time between exposures for the system to return the healthy homeostatic state (Figures 2.8 (i), (iv)). Adequate clearance of active TGF-β is hindered as the frequency increases (Figures 2.8 (iii), (vi)), and thus, the underlying mechanotransductive feedback loop of further TGF-β activation drives the system towards the diseased state.

Interestingly, the long-term dynamics in the general model differs to that in the refined model for a moderate frequency (*cf.* Figures 2.8 (ii), (v)). Here, neglecting TGF-β removal via specified binding events in the general model (2.1.15) leads to a persistent elevated concentration of active TGF-β that affects ASM and ECM accumulation downstream. Conversely, the removal due to binding events in the refined model (2.1.16) sufficiently reduces the concentration of

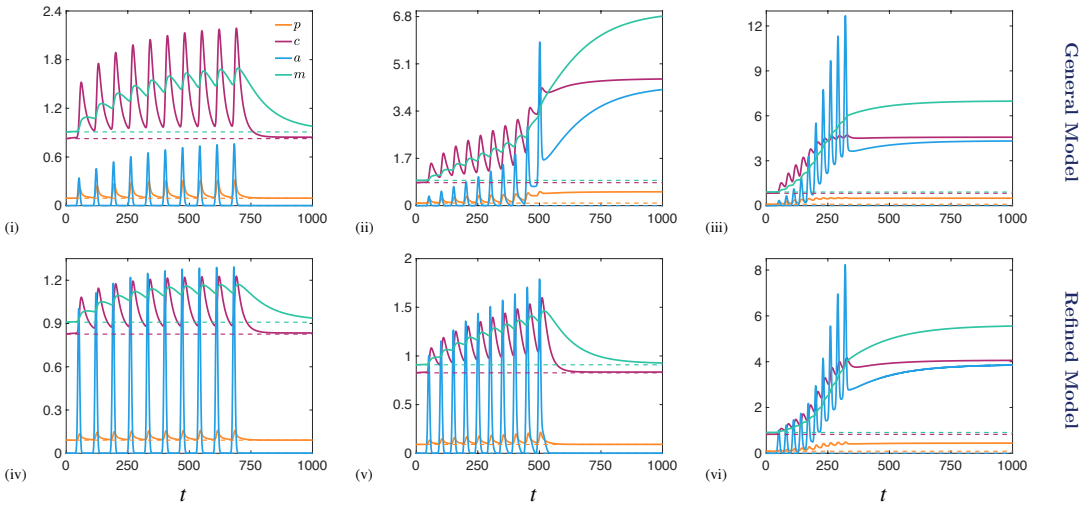

Figure 2.8: (i)–(iii) Results from the general model (2.1.15) and (iv)–(vi) results from the refined model (2.1.16) to illustrate the effect of increasing the frequency of stimuli driving TGF-β activation on the density of airway wall components. The frequency of exposures increase between plots from left to right. Dashed lines correspond to the healthy homeostatic state initial condition. Parameter values, selected within the bi-stable regime, are provided in Table C.3 in Appendix C.1.

active TGF-β which compensates for slightly more frequent exposures to the stimulant.

2.4.3 Effect of increasing the clearance rate of active TGF-β

In this section we simulate a fixed number of recurrent stimuli, occurring at the same frequency, and increase the rate of clearance of active TGF-β following exposure. As previously in the case of increasing stimulus frequency (Figure 2.8), we find that as the clearance reduces, the concentration of active TGF-β continues to rise and consequently re-establishes a new chronically elevated concentration. The persistent presence of active TGF-β, due to reduced clearance, affects the downstream dynamics and increases the amount of ASM and ECM (Figures 2.9 (i), (iv)). For moderate clearance, the disease state is established in the general model prior to that in the refined model and hence, there is visible accumulation of ASM and ECM following the final exacerbation (*cf.* Figures 2.9 (ii), (v)).

Interestingly, in the diseased cases, the refined model demonstrates that the ac-

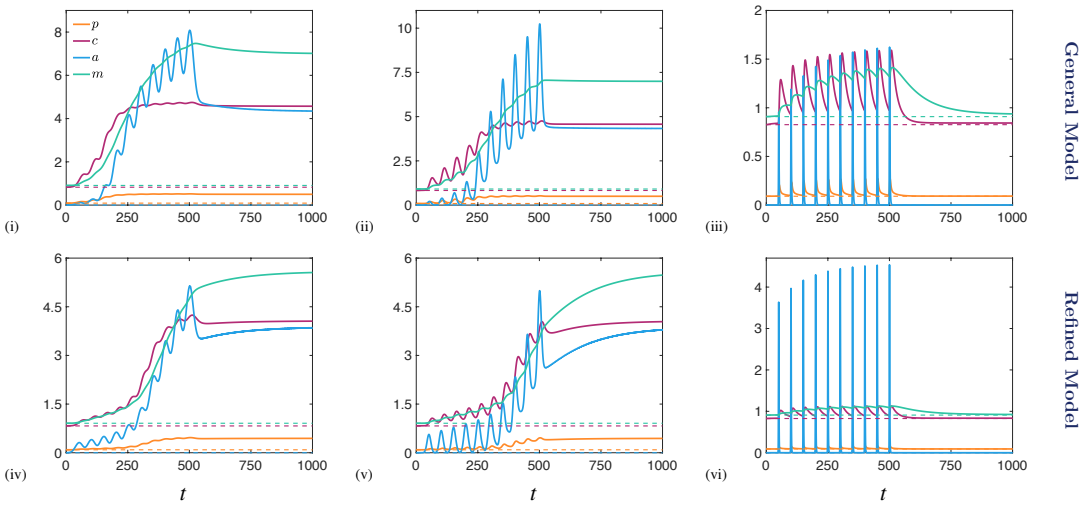

Figure 2.9: (i)–(iii) Results from the general model (2.1.15) and (iv)–(vi) results from the refined model (2.1.16) to illustrate the effect of increasing the clearance of active TGF-β, following stimuli, on the density of airway wall components. The clearance of active TGF-β increases between plots from left to right. Dashed lines correspond to the healthy homeostatic state initial condition. Parameter values, selected within the bi-stable regime, are provided in Table C.3 in Appendix C.1.

cumulation of ASM, ECM and active TGF-β reduces below the diseased steady state following each exacerbation and then proceeds to increase to adopt the diseased state. On the other hand, the general model shows that the ASM, ECM and active TGF-β accumulation simply reduce from the peak to the diseased steady state. This is evident for both slow clearance (*cf.* Figures 2.9 (iv), (i)) and for moderate clearance (*cf.* Figures 2.9 (v), (ii)).

A sufficient clearance rate allows for the system to return to the healthy homeostatic state in both the general and refined models. The accumulation of ASM, ECM and active TGF-β periodically rise and fall between the temporary peak and the healthy state following each exacerbation. Furthermore, the concentration of TGF-β activated immediately following exposure to the stimulant is less in Figures 2.9 (iii), (vi) than in the previous disease free cases shown above in Figures 2.7 and 2.8.

When the clearance of active TGF-β is sufficient the system appears to adapt to experiencing challenges and returns to the healthy state following each exposure. Moreover, the temporary increase in active TGF-β reaches a consistent maximum following exposure to the stimulant. This adaption process is similarly observed in the previous cases of the diseased state (*e.g.* Figure 2.7 (iii)).

2.4.4 Effect of increasing the strength of stimuli

In this section we simulate a fixed number of recurrent stimuli, occurring at the same frequency and with the same clearance rate and increase the amplitude of each exposure (*i.e.* increasing κ_s increases the strength of the stimulant). As expected, we see that when the strength of the stimulant is relatively low the long-term dynamics are unaffected by the temporary rise in ASM, ECM and active TGF-β accumulation (Figures 2.10 (i), (iv)). Although, the temporary rise in ASM and ECM is significantly higher in the general model than in the refined model (*cf.* Figures 2.10 (i), (iv)). Following a slightly increased strength of stimulant, we observe a slight delay in the refined model for the system to return from the temporary peak to the healthy steady state, despite the general model increasing to a higher temporary peak. This is highlighted by the accumulation of ASM and active TGF-β displayed in Figures 2.10 (ii) and (v).

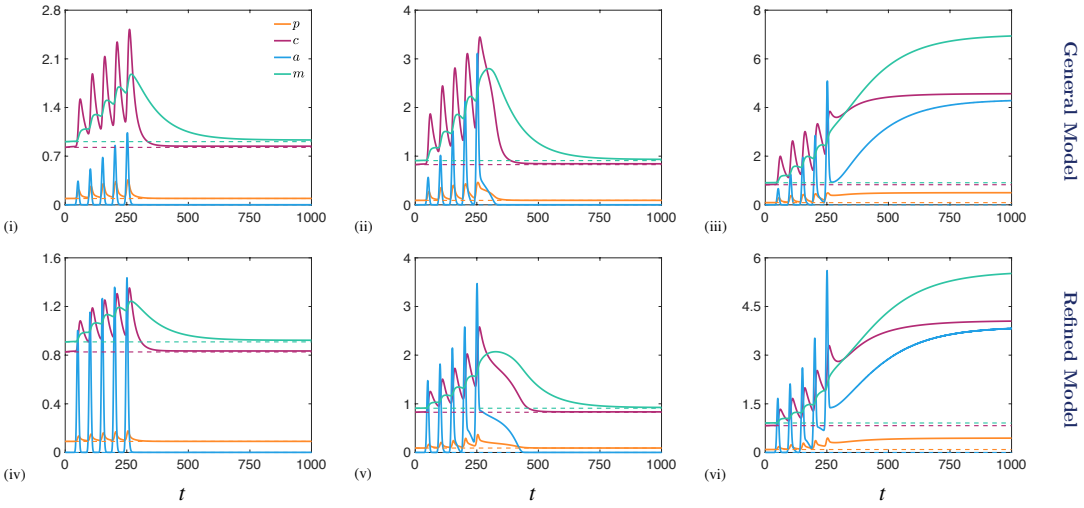

Figure 2.10: (i)–(iii) Results from the general model (2.1.15) and (iv)–(vi) results from the refined model (2.1.16) to illustrate the effect of increasing the strength of stimuli driving TGF-β activation on the density of airway wall components. The strength of the stimuli increases between plots from left to right. Dashed lines correspond to the healthy homeostatic state initial condition. Parameter values, selected within the bi-stable regime, are provided in Table C.3 in Appendix C.1.

Increasing the strength of the stimulant further changes the long-term dynamics and gives rise to the disease state (Figures 2.10 (iii), (vi)). We find that the models are very sensitive to the strength of the stimulant and that very little change is required in order to significantly alter the downstream dynamics. Here, the percentage increase in κ_s (the parameter representing the strength of the exacerbation) that is required to exhibit a significant change in the long-term behaviour is at least an order of magnitude smaller than in previous parameter explorations.

2.5 Summary

We have presented two ODE models that describe the interaction of ASM and ECM and the effect of TGF-β activation; a general case neglecting active TGF-β binding events and a refined model accounting for active TGF-β binding events, and have analysed the systems in parallel. To begin, we introduced suitable parameter scalings (based on estimates of timescales of interaction rates (Tatler

2016)) via a small parameter, ε, that allowed us to reduce both of our models to leading order systems. Subsequently, we determined the important parameters within the systems and performed steady state stability and bifurcations analysis. Thereafter, we identified parameter regimes that allowed for a bi-stable region and simulated the possible downstream effects of introducing an external stimulant, mimicking an asthmatic exacerbation. Results obtained in our bifurcation analysis demonstrate that the rate of ASM proliferation, degradation and phenotype switching from proliferative to contractile state dominate the long-term dynamics of the system. The ASM is the link between each of these factors and thus, our findings suggest that the ASM, in both a contractile and proliferative state, is a key component within the airway wall and is responsible for maintaining growth, ECM secretion and TGF-β mechanical activation. We have shown that a balance is required between these three important roles to allow for the overall system to exhibit a bi-stable regime. This bi-stable regime allows for both a steady state maintaining a relatively low concentration of active TGF-β, representing healthy homeostasis, and a relatively higher concentration of active TGF-β with accompanying increased ASM and ECM accumulation, representing diseased homeostasis.

Results obtained simulating an asthmatic exacerbation highlight the importance of the number, the strength, the frequency of occurrence and the clearance of active TGF-β following the exacerbation. We have observed that both an increased frequency of exposures to a stimulant and a reduced rate of clearance of active TGF-β following exposure increases the accumulation in ASM and ECM and alters the steady state of the systems in the long-term. This may be apparent in patients who experience regular exposures to an irritant and as a result, develop long-term irreversible airway remodelling. We have shown that allowing adequate recovery time or improving recovery time (*i.e.* reduced frequency and sufficient active TGF-β clearance) between successive exacerbations returns the healthy homeostatic state. Therefore, increasing the clearance of active TGF-β could be a possible method of asthma management or treatment.

Our findings are consistent with Chernyavsky et al. (2014) and Hill et al. (2018), who likewise explore airway remodelling in response to transient inflammatory or contractile agonist challenges. Similarly, we find that when the clearance of

active TGF-β is inefficient (*i.e.* the inflammation resolution speed is slow), a small number of exacerbation events may lead to significant airway remodelling that remains after the stimulant resides.

Chernyavsky et al. (2014) consider remodelling due to the growth of the ASM alone (ASM hyperplasia) and that the phenotype switching rate from the contractile to proliferative state is modulated by the inflammatory status (which changes in response to the stimulant). In contrast, we model the accumulation of ECM and active TGF-β accompanying ASM growth and consider a constant switch rate between the ASM sub-populations.

The morphoelastic model of Hill et al. (2018) reveals persistent ASM contraction in asthmatics via either a mechanotransductive feedback loop, insufficient clearance of contractile agonists, or a combination of the two. Our ODE model uncovers a bi-stable regime and highlights a threshold concentration of active TGF-β that once surpassed, leads to irreversible airway remodelling. Motivated by these findings, in the following chapters we turn our attention to a biomechanical approach and develop a tissue-level description of TGF-β activation in response to active contraction of the ASM and prescribed cyclic stretching. In later chapters, we revisit our ODE model representing the rate of change in concentration of active TGF-β (2.1.16c) in order to couple our biomechanical and dynamical descriptions.

CHAPTER 3

A Biomechanical Model of Lung-slice Stretching

In this chapter, we develop a mechanical description of the experimental PCLS stretching (Tatler 2016) outlined in Section 1.3.1. We use constrained mixture theory (Ateshian 2017) to model an airway within the PCLS as a saturated mixture of incompressible, fiber-reinforced, hyperelastic constituents comprising an active contractile ASM component, a nonlinear strain-stiffening ECM component and other passive (non-contributing) constituents (including water).

3.1 Continuum description of lung-slice tissue

The development of the proceeding biomechanical model is motivated by the PCLS stretching experiment outlined in Section 1.3.1 and aims to elucidate the potential mechanisms responsible for the mechanical activation of TGF-β in response to imposed stretch. Recall that TGF-β is stored in a latent complex that is anchored to the ECM and connected to the ASM via integrins (refer to Figure 1.2). Contraction of the ECM generates a mechanical force that strains the integrins due to resistance of the ECM. The resultant strain (transmitted via integrins) unfolds the latent complex and consequently activates TGF-β.

We represent a single airway within the PCLS as a cylinder, whose constituents are modelled via constrained mixture theory (Truesdell and Toupin 1960; Bowen 1976; Truesdell and Noll 1992; Ateshian 2017). The formulation for obtaining

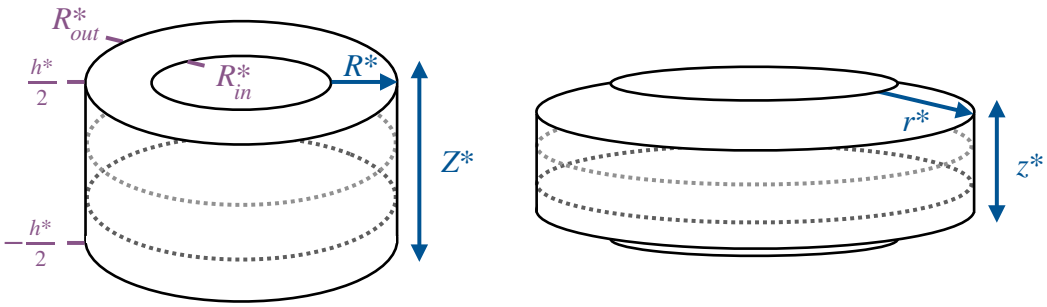

Figure 3.1: Dimensional undeformed reference configuration (3.1.3) (left) and deformed configuration (3.1.4) (right) to illustrate the geometry of an airway modelled within the PCLS. Dotted lines indicate the circumferential fibres representing the active ASM and passive ECM components.

the constitutive mechanical relation for this type of material is given in detail by Humphrey and Rajagopal (2002); Ateshian (2007); Ateshian and Ricken (2010). Specifically, we consider a saturated multiphase mixture of an active contractile ASM component and a strain-stiffening ECM component, each modelled as a nonlinear, incompressible, fibre-reinforced hyperelastic material (Holzapfel 2000), and other passive tissue components. We assume that the mechanical contributions of the contractile ASM and ECM dominate those of the other tissue components (such as water, that has no mechanical contribution to the tissue) and therefore we solely model the contractile ASM and ECM stress state alongside the corresponding overall tissue stress following deformation. Hereafter c and m subscripts denote the contractile ASM and ECM, respectively. The remaining components are grouped together and are collectively labelled with a subscript u.

Since the duration of the PCLS experiment of interest is significantly less than that of ASM growth or proliferation and ECM deposition (Tatler 2016), we assume that the apparent densities of the ASM and ECM are constant over the experimental time frame. Furthermore, we assume that there are no proliferating ASM cells at the start of the experiment and hence, absent for the entirety of the experiment. Correspondingly, the volumes fractions of contractile ASM and ECM are constant and denoted

$$\Phi_c = \frac{\bar{c}^*}{c^{*\mathrm{T}}}, \qquad \Phi_m = \frac{\bar{m}^*}{m^{*\mathrm{T}}}, \tag{3.1.1}$$

respectively, where $\bar{c}^*$ and $\bar{m}^*$ are the steady-state apparent densities and ${c^*}^{\mathrm{T}}$ and ${m^*}^{\mathrm{T}}$ denote the true densities of ASM and ECM respectively. The assumption of intrinsic incompressibility requires that there is no change in the apparent densities of the remaining constituents. Subsequently, we group all remaining constituents into a separate constant volume fraction Φ_u. Hence, saturation of the tissue demands

$$\sum_i \Phi_i = 1, \qquad i \in \{c, m, u\}. \tag{3.1.2}$$

Following the traditional continuum mechanics approach (Truesdell and Toupin 1960; Truesdell and Noll 1992; Holzapfel 2000) we assume that a common unstressed and unstrained reference configuration applies to each constituent in the airway, in which Lagrangian cylindrical coordinates (R^*, Θ, Z^*) describe the airway geometry:

$$R^*_{\mathrm{in}} \leq R^* \leq R^*_{\mathrm{out}}, \qquad 0 \leq \Theta \leq 2\pi, \qquad -\frac{h^*}{2} \leq Z^* \leq \frac{h^*}{2}, \tag{3.1.3}$$

and wherein asterisks denote dimensional quantities, R^*_{in} and R^*_{out} denotes the inner and outer radius and $h^*/2$ and $-h^*/2$ denotes the upper and lower surfaces of the undeformed airway, respectively (Figure 3.1).

Imposed stretching or contraction of the ASM causes a deformation described by the *deformed configuration* (r^*, θ, z^*). For simplicity, we consider an axisymmetric radial airway stretch, and further assume there is no torsion, so that the deformation is described by

$$r^* = r^*(R^*, Z^*), \qquad \theta = \Theta, \qquad z^* = z^*(R^*, Z^*). \tag{3.1.4}$$

The constituents within the tissue are constrained and therefore also deform axisymetrically according to (3.1.4). The undeformed reference configuration (3.1.3) and deformed configuration (3.1.4) are illustrated in Figure 3.1.

The deformation gradient tensor in cylindrical polars for the whole tissue, and

accounting for (3.1.4), (as defined in (1.5.2)) is given by

$$\mathbf{F} = \begin{pmatrix} \frac{\partial r^*}{\partial R^*} & 0 & \frac{\partial r^*}{\partial Z^*} \\ 0 & \frac{r^*}{R^*} & 0 \\ \frac{\partial z^*}{\partial R^*} & 0 & \frac{\partial z^*}{\partial Z^*} \end{pmatrix}, \tag{3.1.5}$$

and the corresponding Cauchy Green deformation tensors (as defined in (1.5.4)) are

$$\mathbf{B} = \begin{pmatrix} \left(\frac{\partial r^*}{\partial R^*}\right)^2 + \left(\frac{\partial r^*}{\partial Z^*}\right)^2 & 0 & \frac{\partial r^*}{\partial R^*}\frac{\partial z^*}{\partial R^*} + \frac{\partial r^*}{\partial Z^*}\frac{\partial z^*}{\partial Z^*} \\ 0 & \left(\frac{r^*}{R^*}\right)^2 & 0 \\ \frac{\partial r^*}{\partial R^*}\frac{\partial z^*}{\partial R^*} + \frac{\partial r^*}{\partial Z^*}\frac{\partial z^*}{\partial Z^*} & 0 & \left(\frac{\partial z^*}{\partial R^*}\right)^2 + \left(\frac{\partial z^*}{\partial Z^*}\right)^2 \end{pmatrix}, \tag{3.1.6}$$

$$\mathbf{C} = \begin{pmatrix} \left(\frac{\partial r^*}{\partial R^*}\right)^2 + \left(\frac{\partial z^*}{\partial R^*}\right)^2 & 0 & \frac{\partial r^*}{\partial R^*}\frac{\partial r^*}{\partial Z^*} + \frac{\partial z^*}{\partial R^*}\frac{\partial z^*}{\partial Z^*} \\ 0 & \left(\frac{r^*}{R^*}\right)^2 & 0 \\ \frac{\partial r^*}{\partial R^*}\frac{\partial r^*}{\partial Z^*} + \frac{\partial z^*}{\partial Z^*}\frac{\partial z^*}{\partial R^*} & 0 & \left(\frac{\partial r^*}{\partial Z^*}\right)^2 + \left(\frac{\partial z^*}{\partial Z^*}\right)^2 \end{pmatrix}. \tag{3.1.7}$$

Accordingly, the (required) principal invariants (as defined in (1.5.5)) are given by

$$I_1 = \left(\frac{\partial r^*}{\partial R^*}\right)^2 + \left(\frac{\partial r^*}{\partial Z^*}\right)^2 + \left(\frac{r^*}{R^*}\right)^2 + \left(\frac{\partial z^*}{\partial R^*}\right)^2 + \left(\frac{\partial z^*}{\partial Z^*}\right)^2, \tag{3.1.8a}$$

$$I_3 = \left(\frac{r^*}{R}\frac{\partial r^*}{\partial R^*}\frac{\partial z^*}{\partial Z^*} - \frac{r^*}{R}\frac{\partial r^*}{\partial Z^*}\frac{\partial z^*}{\partial R^*}\right)^2. \tag{3.1.8b}$$

Incompressibility is enforced by demanding $I_3 = 1$ (Ogden 2003) and hence, we take the positive square root of (3.1.8b) and rearrange to obtain

$$\frac{r^*}{R}\left(\frac{\partial r^*}{\partial R^*}\frac{\partial z^*}{\partial Z^*} - \frac{\partial r^*}{\partial Z^*}\frac{\partial z^*}{\partial R^*}\right) = 1. \tag{3.1.9}$$

Mechanical anisotropy is imparted to the airway via strain-stiffening of collagen fibres and contractile force generation of ASM bundles (Ogden 2003). ECM strain-stiffening occurs in the direction of the collagen fibre orientation and accounts for the recruitment of collagen fibres (from a crimped to uncrimped configuration) when stretched (Hiorns et al. 2014). Contractile force generation is

assumed to occur in the direction of the ASM bundle orientation and occurs in response to an exogenous agonist and active TGF-β signalling pathways. To describe this, we assume that the ASM and ECM constituents within the tissue are associated with a set of fibres, denoted $\mathbf{G}$, orientated circumferentially (Amrani and Panettieri 2003; Ijpma et al. 2017) with undeformed direction

$$\mathbf{G} = \mathbf{e}_\theta. \tag{3.1.10}$$

In the deformed configuration the fibres have direction

$$\mathbf{g} = \mathbf{F}\mathbf{G} \equiv \mathbf{F}_\theta. \tag{3.1.11}$$

The additional (required) deformation invariant (as defined in (1.5.8)) associated with this single family of fibres is given by

$$I_4 = \left(\frac{r^*}{R^*}\right)^2. \tag{3.1.12a}$$

3.1.1 Strain-energy functions

Under the above assumptions, the constitutive mechanical law for the airway wall is obtained following the additive approach of Ambrosi and Pezzuto (2012) by introducing an active component, W^*_{act}, to the passive isotropic, W^*_{iso}, and anisotropic, W^*_{ani}, components of the strain-energy function, W^* (see Section 1.5.2). As in (1.5.16), we follow Holzapfel et al. (2000) and define the strain-energy for the ASM and ECM within the tissue as

$$W_i{}^*(I_1, I_4) = W^*_{i\text{iso}}(I_1) + W^*_{i\text{ani}}(I_4) + W^*_{i\text{act}}(I_4), \qquad i \in \{c, m\}. \tag{3.1.13}$$

As previously noted, we assume that the constituents grouped within the volume fraction Φ_u do not have any mechanical contribution and thus

$$W_u{}^* = 0. \tag{3.1.14}$$

As a result, the strain-energy function for the whole tissue, W^*, is defined by the weighted addition of the strain-energy functions for ASM, $W_c{}^*$, and ECM,

${W_m}^*$, such that

$$W^*(I_1, I_4) = \Phi_c {W_c}^*(I_1, I_4) + \Phi_m {W_m}^*(I_1, I_4). \tag{3.1.15}$$

In (3.1.13) and (3.1.15), I_1 and I_4 denote the first and fourth principle invariants of the right Cauchy-Green deformation tensor, $\mathbf{B}$, and are defined in (3.1.8a) and (3.1.12a), respectively. Derivatives of the strain-energy functions with respect to the invariants I_1 and I_4 are defined in (1.5.18).

We assume that the isotropic response of the tissue is described via a Neo-Hookean material (see (1.5.11)), with passive isotropic stiffness ${\mu_c}^*$ and ${\mu_m}^*$ for the ASM and ECM, respectively. It is assumed that collagen fibres within the ECM do not store strain-energy when the airway is not inflated *i.e.* at low pressures, hence following Holzapfel et al. (2000) we associate an isotropic part of the ECM strain-energy function to the mechanical response of the non-collagenous matrix material. At high pressures the resistance of the tissue to stretch is almost entirely due to collagen fibres within the ECM, which is governed by an anisotropic function. To account for strain-stiffening, as in Hiorns et al. (2014), we employ the anisotropic model of Holzapfel et al. (2000) (see (1.5.17)) with the addition of a Heaviside function so that the collagen fibres are only recruited when stretched. There is no active force contribution from the ECM; however, we include an active component to the ASM strain-energy function. The form of the active component in the Cauchy stress tensor (denoted $\boldsymbol{\sigma}^*$ and defined below) follows the general form used in Ambrosi and Pezzuto (2012) (see (1.5.20)),

$$\boldsymbol{\sigma}^*_{c\,\text{act}} = \alpha^*(\mathbf{g} \otimes \mathbf{g}), \tag{3.1.16}$$

where $\mathbf{g}$ denotes the direction of the deformed fibres and α^* is the active contractile force generated by the ASM.

In view of the above, the strain-energy functions for the ASM and ECM components are given by

$${W_c}^*(I_1, I_4) = \frac{{\mu_c}^*}{2}(I_1 - 3) + \frac{\alpha^*}{2} I_4, \tag{3.1.17a}$$

$${W_m}^*(I_1, I_4) = \frac{{\mu_m}^*}{2}(I_1 - 3) + \frac{\omega^*}{2\zeta}\mathrm{H}(I_4 - 1)\left(\exp\left(\zeta(I_4 - 1)^2\right) - 1\right). \tag{3.1.17b}$$

The reference configuration is stressed in the presence of contractile force, *i.e.* $\alpha^* \neq 0$, and hence the active contribution in (3.1.17a) includes I_4 as opposed to $(I_4 - 1)$. For the undeformed reference configuration to be unstressed we require $\alpha^* = 0$. In (3.1.17b), $\omega^* > 0$ is a constant parameter defining the passive anisotropic stiffness and accounts for the density of the fibres in the matrix and $\zeta > 0$ is a dimensionless constant parameter defining the nonlinear increase in stiffness of the fibres as they deform (Hiorns et al. 2014). The strain-energy function for the whole tissue is given by (3.1.15).

Differentiating ${W_c}^*$ and ${W_m}^*$ with respect to the invariants I_1 and I_4 we have

$$W_{c1}^* = \frac{{\mu_c}^*}{2}, \tag{3.1.18a}$$

$$W_{c4}^* = \frac{\alpha^*}{2}, \tag{3.1.18b}$$

$$W_{m1}^* = \frac{{\mu_m}^*}{2}, \tag{3.1.18c}$$

$$\begin{aligned} W_{m4}^* = {} & \frac{\omega^*}{2\zeta}\delta(I_4 - 1)\left(\exp\left(\zeta(I_4 - 1)^2\right) - 1\right) \\ & + \omega^*(I_4 - 1)\mathrm{H}(I_4 - 1)\exp\left(\zeta(I_4 - 1)^2\right). \end{aligned} \tag{3.1.18d}$$

We note that $\delta(I_4 - 1) = 0$ for $I_4 \neq 1$ and $\exp\left(\zeta(I_4 - 1)^2\right) - 1 = 0$ for $I_4 = 1$, thus (3.1.18d) reduces to

$$W_{m4}^* = \omega^*(I_4 - 1)\mathrm{H}(I_4 - 1)\exp\left(\zeta(I_4 - 1)^2\right). \tag{3.1.19}$$

Hence, with (3.1.15), (3.1.18) and (3.1.19) we obtain the strain-energy function derivatives for the whole tissue,

$$W_1^* = \Phi_c\frac{{\mu_c}^*}{2} + \Phi_m\frac{{\mu_m}^*}{2}, \tag{3.1.20a}$$

$$W_4^* = \Phi_c\frac{\alpha^*}{2} + \Phi_m\omega^*(I_4 - 1)\mathrm{H}(I_4 - 1)\exp\left(\zeta(I_4 - 1)^2\right). \tag{3.1.20b}$$

3.1.2 Cauchy stress tensor

The Cauchy stress tensor (Ogden 2003) for the whole tissue, denoted $\boldsymbol{\sigma}^*$, satisfies

$$\boldsymbol{\sigma}^* = -\mathscr{P}^*\mathbf{I} + 2W_1^*\mathbf{B} + 2W_4^*\mathbf{g}\otimes\mathbf{g}. \tag{3.1.21}$$

Here, $\mathbf{I}$ is the identity matrix and the pressure $\mathscr{P}^*$ is included to enforce tissue incompressibility (Ogden 2003). $\mathbf{B}$ is the left Cauchy Green stress tensor, $\mathbf{g}$ denotes the direction of the deformed fibres and W_i^* for $j \in \{1,4\}$ are derivatives of the strain-energy function for the whole tissue, with respect to the first and fourth invariant, definitions and derivations of which are in the previous Section 3.1.

In view of equations (3.1.6), (3.1.11) and (3.1.21) we note that

$$\mathbf{g} \otimes \mathbf{g} = \begin{pmatrix} 0 & 0 & 0 \\ 0 & \left(\frac{r^*}{R^*}\right)^2 & 0 \\ 0 & 0 & 0 \end{pmatrix}. \tag{3.1.22}$$

Hence, the non-zero components of the Cauchy stress tensor (3.1.21) for the whole tissue are

$$\sigma_{rr}^* = -\mathscr{P}^* + 2W_1^* \left(\left(\frac{\partial r^*}{\partial R^*}\right)^2 + \left(\frac{\partial r^*}{\partial Z^*}\right)^2 \right), \tag{3.1.23a}$$

$$\sigma_{\theta\theta}^* = -\mathscr{P}^* + 2(W_1^* + W_4^*) \left(\frac{r^*}{R^*}\right)^2, \tag{3.1.23b}$$

$$\sigma_{zz}^* = -\mathscr{P}^* + 2W_1^* \left(\left(\frac{\partial z^*}{\partial R^*}\right)^2 + \left(\frac{\partial z^*}{\partial Z^*}\right)^2 \right), \tag{3.1.23c}$$

$$\sigma_{rz}^* = \sigma_{zr}^* = 2W_1^* \left(\frac{\partial r^*}{\partial R^*}\frac{\partial z^*}{\partial R^*} + \frac{\partial r^*}{\partial Z^*}\frac{\partial z^*}{\partial Z^*} \right). \tag{3.1.23d}$$

The tissue comprises three constituents with volume fractions Φ_c, Φ_m and Φ_u, and hence, the Cauchy stress tensor for the whole tissue is the weighted addition of the three constituents Cauchy stress tensors such that

$$\boldsymbol{\sigma}^* = \sum_i \Phi_i {\boldsymbol{\sigma}_i}^*, \qquad i \in \{c, m, u\}, \tag{3.1.24}$$

The Cauchy stress tensor for each constituent is defined by

$$\boldsymbol{\sigma}_c^* = -\mathscr{P}^*\mathbf{I} + 2W_{c1}^*\mathbf{B} + 2W_{c4}^*\mathbf{g}\otimes\mathbf{g}, \tag{3.1.25a}$$

$$\boldsymbol{\sigma}_m^* = -\mathscr{P}^*\mathbf{I} + 2W_{m1}^*\mathbf{B} + 2W_{m4}^*\mathbf{g}\otimes\mathbf{g}, \tag{3.1.25b}$$

$$\boldsymbol{\sigma}_u^* = -\mathscr{P}^*\mathbf{I}, \tag{3.1.25c}$$

whose components are given by (3.1.23) under the replacements $\sigma^* = \sigma_i^*$ and $W^* = W_i^*$ for $i \in \{c, m, u\}$.

3.1.3 von Mises stress

As summarised above (and explained in Section 1.1.4), TGF-β is mechanically activated by straining and unfolding the latent complex (encapsulating TGF-β) that is anchored to the ECM and connected to the ASM via integrins. Sufficient strain transmission, due to the constituents moving past one another (*e.g.* contraction of the ASM), is required to unfold the latent complex (refer to Figure 1.2). In the constrained mixture description of the PCLS, however, the constituents are constrained to undergo the same deformation as that of the whole tissue (3.1.4) (*i.e.* the relative velocity of each constituent remains the same at all times). Therefore, we represent the mechanical activation of TGF-β with the difference in the constituent stress state. We expect that contraction of the ASM, and similarly, stretch-induced strain-stiffening of the ECM generates a difference in the constituents' stress state and therefore drives the mechanical activation of TGF-β by unfolding the interconnecting latent complex.

In the absence of any strict rationale to use an individual Cauchy stress component, we use the von Mises stress which encompasses all of the Cauchy stress components (as defined in (1.5.25). In the following sections, $\sigma_{c\mathrm{VM}}^*$ and $\sigma_{m\mathrm{VM}}^*$ denotes the von Mises stress of the ASM and ECM, respectively. Furthermore, we define the absolute difference in the constituent von Mises stress as

$$\sigma_{\mathrm{dif}}^* = \left|\sigma_{c\mathrm{VM}}^* - \sigma_{m\mathrm{VM}}^*\right|. \tag{3.1.26}$$

3.1.4 Mechanical equilibrium

In mechanical equilibrium, and assuming there are no body forces on the tissue, the balance of linear momentum in (1.5.27) reduces to two equations,

$$\frac{\partial \sigma_{rr}^*}{\partial r^*} + \frac{\partial \sigma_{zr}^*}{\partial z^*} + \frac{1}{r^*}\left(\sigma_{rr}^* - \sigma_{\theta\theta}^*\right) = 0, \tag{3.1.27a}$$

$$\frac{\partial \sigma_{rz}^*}{\partial r^*} + \frac{\partial \sigma_{zz}^*}{\partial z^*} + \frac{1}{r^*}\sigma_{rz}^* = 0. \tag{3.1.27b}$$

Noting that

$$\frac{\partial}{\partial R^*} = \frac{\partial r^*}{\partial R^*}\frac{\partial}{\partial r^*} + \frac{\partial z^*}{\partial R^*}\frac{\partial}{\partial z^*}, \tag{3.1.28a}$$

$$\frac{\partial}{\partial Z^*} = \frac{\partial r^*}{\partial Z^*}\frac{\partial}{\partial r^*} + \frac{\partial z^*}{\partial Z^*}\frac{\partial}{\partial z^*}, \tag{3.1.28b}$$

we obtain

$$\frac{\partial}{\partial r^*} = \left(\frac{\partial r^*}{\partial R^*}\frac{\partial z^*}{\partial Z^*} - \frac{\partial r^*}{\partial Z^*}\frac{\partial z^*}{\partial R^*}\right)^{-1}\left(\frac{\partial z^*}{\partial Z^*}\frac{\partial}{\partial R^*} - \frac{\partial z^*}{\partial R^*}\frac{\partial}{\partial Z^*}\right), \tag{3.1.29a}$$

$$\frac{\partial}{\partial z^*} = \left(\frac{\partial r^*}{\partial R^*}\frac{\partial z^*}{\partial Z^*} - \frac{\partial r^*}{\partial Z^*}\frac{\partial z^*}{\partial R^*}\right)^{-1}\left(\frac{\partial r^*}{\partial R^*}\frac{\partial}{\partial Z^*} - \frac{\partial r^*}{\partial Z^*}\frac{\partial}{\partial R^*}\right). \tag{3.1.29b}$$

Using (3.1.29), we express (3.1.27) in terms of the undeformed reference configuration,

$$\begin{aligned}\frac{\partial r^*}{\partial R^*}\frac{\partial \sigma_{rz}^*}{\partial Z^*} - \frac{\partial r^*}{\partial Z^*}\frac{\partial \sigma_{rz}^*}{\partial R^*} + \frac{\partial z^*}{\partial Z^*}\frac{\partial \sigma_{rr}^*}{\partial R^*} - \frac{\partial z^*}{\partial R^*}\frac{\partial \sigma_{rr}^*}{\partial Z^*} \\ + \left(\frac{\partial r^*}{\partial R^*}\frac{\partial z^*}{\partial Z^*} - \frac{\partial r^*}{\partial Z^*}\frac{\partial z^*}{\partial R^*}\right)\left(\frac{\sigma_{rr}^* - \sigma_{\theta\theta}^*}{r^*}\right) = 0,\end{aligned} \tag{3.1.30a}$$

$$\begin{aligned}\frac{\partial r^*}{\partial R^*}\frac{\partial \sigma_{zz}^*}{\partial Z^*} - \frac{\partial r^*}{\partial Z^*}\frac{\partial \sigma_{zz}^*}{\partial R^*} + \frac{\partial z^*}{\partial Z^*}\frac{\partial \sigma_{rz}^*}{\partial R^*} - \frac{\partial z^*}{\partial R^*}\frac{\partial \sigma_{rz}^*}{\partial Z^*} \\ + \left(\frac{\partial r^*}{\partial R^*}\frac{\partial z^*}{\partial Z^*} - \frac{\partial r^*}{\partial Z^*}\frac{\partial z^*}{\partial R^*}\right)\frac{\sigma_{rz}^*}{r^*} = 0.\end{aligned} \tag{3.1.30b}$$

3.1.5 Boundary conditions

At the outer radius, we enforce a displacement boundary condition,

$$r^*\left(R_{\text{out}}^*, Z^*\right) = r_{\text{dis}}^*, \tag{3.1.31}$$

to describe the radial stretch of the airway due to the axisymetric stretch imposed on the PCLS via the BioFlex method, as outlined in Section 1.3.1 (see Figure 1.5). Furthermore, the upper, lower and inner surfaces of the tissue are traction-free such that

$$\boldsymbol{\sigma}^* \left(R^*, \tfrac{h^*}{2} \right) \mathbf{n}^*_{\text{up}} = \mathbf{0}, \tag{3.1.32a}$$

$$\boldsymbol{\sigma}^* \left(R^*, -\tfrac{h^*}{2} \right) \mathbf{n}^*_{\text{low}} = \mathbf{0}, \tag{3.1.32b}$$

$$\boldsymbol{\sigma}^* \left(R^*_{\text{in}}, Z^* \right) \mathbf{n}^*_{\text{in}} = \mathbf{0}, \tag{3.1.32c}$$

where the unit normals to the upper, $\mathbf{n}^*_{\text{up}}$, lower, $\mathbf{n}^*_{\text{low}}$, and inner, $\mathbf{n}^*_{\text{in}}$, surfaces in the reference configuration are given by:

at $Z^* = \frac{h^*}{2}$:

$$\mathbf{n}^*_{\text{up}} = \left(\left(-\frac{\partial z^*}{\partial R^*} \right)^2 + \left(\frac{\partial r^*}{\partial R^*} \right)^2 \right)^{-\frac{1}{2}} \cdot \left(-\frac{\partial z^*}{\partial R^*}, 0, \frac{\partial r^*}{\partial R^*} \right); \tag{3.1.33a}$$

at $Z^* = -\frac{h^*}{2}$:

$$\mathbf{n}^*_{\text{low}} = \left(\left(-\frac{\partial z^*}{\partial R^*} \right)^2 + \left(\frac{\partial r^*}{\partial R^*} \right)^2 \right)^{-\frac{1}{2}} \cdot \left(-\frac{\partial z^*}{\partial R^*}, 0, \frac{\partial r^*}{\partial R^*} \right); \tag{3.1.33b}$$

at $R^* = R^*_{\text{in}}$:

$$\mathbf{n}^*_{\text{in}} = \left(\left(-\frac{\partial z^*}{\partial Z^*} \right)^2 + \left(\frac{\partial r^*}{\partial Z^*} \right)^2 \right)^{-\frac{1}{2}} \cdot \left(-\frac{\partial z^*}{\partial Z^*}, 0, \frac{\partial r^*}{\partial Z^*} \right). \tag{3.1.33c}$$

3.1.6 Non-dimensionalisation

We non-dimensionalise the governing equations by introducing the following scalings

$$(r, R) = \frac{(r^*, R^*)}{R^*_{\text{out}}}, \qquad (z, Z) = \frac{(z^*, Z^*)}{h^*}, \tag{3.1.34}$$

so that the dimensionless undeformed reference configuration is given by

$$R_{\text{in}} \leq R \leq 1, \qquad 0 \leq \Theta \leq 2\pi, \qquad -\tfrac{1}{2} \leq Z \leq \tfrac{1}{2}, \tag{3.1.35}$$

and the deformed configuration is given by

$$r = r(R, Z), \qquad \theta = \Theta, \qquad z = z(R, Z), \tag{3.1.36}$$

wherein $R_{\text{in}} = R^*_{\text{in}}/R^*_{\text{out}}$ denotes the dimensionless inner radius. Of use in the sequel will be the aspect ratio of the undeformed airway, defined by $\varepsilon = h^*/R^*_{\text{out}}$.

The dimensionless components of the deformation gradient tensor (3.1.5) are given by

$$\mathbf{F} = \begin{pmatrix} \frac{\partial r}{\partial R} & 0 & \frac{1}{\varepsilon}\frac{\partial r}{\partial Z} \\ 0 & \frac{r}{R} & 0 \\ \varepsilon\frac{\partial z}{\partial R} & 0 & \frac{\partial z}{\partial Z} \end{pmatrix}, \tag{3.1.37}$$

and the dimensionless components of the corresponding Cauchy Green deformation tensors (3.1.6) are given by

$$\mathbf{B} = \begin{pmatrix} \left(\frac{\partial r}{\partial R}\right)^2 + \left(\frac{1}{\varepsilon}\frac{\partial r}{\partial Z}\right)^2 & 0 & \varepsilon\frac{\partial r}{\partial R}\frac{\partial z}{\partial R} + \frac{1}{\varepsilon}\frac{\partial r}{\partial Z}\frac{\partial z}{\partial Z} \\ 0 & \left(\frac{r}{R}\right)^2 & 0 \\ \varepsilon\frac{\partial r}{\partial R}\frac{\partial z}{\partial R} + \frac{1}{\varepsilon}\frac{\partial r}{\partial Z}\frac{\partial z}{\partial Z} & 0 & \left(\varepsilon\frac{\partial z}{\partial R}\right)^2 + \left(\frac{\partial z}{\partial Z}\right)^2 \end{pmatrix}, \tag{3.1.38}$$

$$\mathbf{C} = \begin{pmatrix} \left(\frac{\partial r}{\partial R}\right)^2 + \left(\varepsilon\frac{\partial z}{\partial R}\right)^2 & 0 & \frac{1}{\varepsilon}\frac{\partial r}{\partial R}\frac{\partial r}{\partial Z} + \varepsilon\frac{\partial z}{\partial R}\frac{\partial z}{\partial Z} \\ 0 & \left(\frac{r}{R}\right)^2 & 0 \\ \frac{1}{\varepsilon}\frac{\partial r}{\partial R}\frac{\partial r}{\partial Z} + \varepsilon\frac{\partial z}{\partial Z}\frac{\partial z}{\partial R} & 0 & \left(\frac{1}{\varepsilon}\frac{\partial r}{\partial Z}\right)^2 + \left(\frac{\partial z}{\partial Z}\right)^2 \end{pmatrix}. \tag{3.1.39}$$

We non-dimensionalise the strain-energy functions, W^*, pressure, $\mathscr{P}^*$, and the Cauchy stress, $\boldsymbol{\sigma}^*$, with the passive isotropic stiffness of the ASM, μ_c^*, such that

$$\begin{aligned} W &= \frac{W^*}{{\mu_c}^*}, & W_c &= \frac{{W_c}^*}{{\mu_c}^*}, & W_m &= \frac{{W_m}^*}{{\mu_c}^*}, & \mathscr{P} &= \frac{\mathscr{P}^*}{{\mu_c}^*}, \\ \boldsymbol{\sigma} &= \frac{\boldsymbol{\sigma}*}{{\mu_c}^*}, & \boldsymbol{\sigma}_c &= \frac{{\boldsymbol{\sigma}_c}^*}{{\mu_c}^*}, & \boldsymbol{\sigma}_m &= \frac{{\boldsymbol{\sigma}_m}^*}{{\mu_c}^*}, & \boldsymbol{\sigma}_u &= \frac{{\boldsymbol{\sigma}_u}^*}{{\mu_c}^*}. \end{aligned} \tag{3.1.40}$$

Under the above definitions, the dimensionless strain-energy functions for each constituent are

$$W_c = \frac{(I_1 - 3)}{2} + \frac{\alpha}{2} I_4, \tag{3.1.41a}$$

$$W_m = \mu \frac{(I_1 - 3)}{2} + \frac{\omega}{2} \mathrm{H}(I_4 - 1) \left(\exp\left(\zeta (I_4 - 1)^2 \right) - 1 \right), \tag{3.1.41b}$$

and hence, for the whole tissue

$$W = \Phi_c W_c + \Phi_m W_m, \tag{3.1.42}$$

where the dimensionless parameters μ, ω and α are defined by

$$\mu = \frac{{\mu_m}^*}{{\mu_c}^*}, \qquad \omega = \frac{\omega^*}{{\mu_c}^*}, \qquad \alpha = \frac{\alpha^*}{{\mu_c}^*}, \tag{3.1.43}$$

and the deformation invariant is

$$I_4 = \left(\frac{r}{R} \right)^2. \tag{3.1.44}$$

Derivatives of the dimensionless strain-energy functions for each of the constituents (3.1.41) in terms of the deformed radius, r, and undeformed radius, R, are

$$W_{c1} = \frac{1}{2}, \tag{3.1.45a}$$

$$W_{m1} = \frac{\mu}{2}, \tag{3.1.45b}$$

$$W_{c4} = \frac{\alpha}{2}, \tag{3.1.45c}$$

$$W_{m4} = \omega \left(\left(\frac{r}{R} \right)^2 - 1 \right) H \left(\left(\frac{r}{R} \right)^2 - 1 \right) \exp\left(\zeta \left(\left(\frac{r}{R} \right)^2 - 1 \right)^2 \right), \tag{3.1.45d}$$

and thus, for the whole tissue

$$W_1 = \Phi_c \frac{1}{2}, + \Phi_m \frac{\mu}{2}, \tag{3.1.46a}$$

$$W_4 = \Phi_c \frac{\alpha}{2} + \Phi_m \omega \left(\left(\frac{r}{R} \right)^2 - 1 \right) \times H \left(\left(\frac{r}{R} \right)^2 - 1 \right) \exp \left(\zeta \left(\left(\frac{r}{R} \right)^2 - 1 \right)^2 \right). \tag{3.1.46b}$$

The dimensionless Cauchy stress tensor for the whole tissue is

$$\boldsymbol{\sigma} = -\mathscr{P}\mathbf{I} + 2W_1\mathbf{B} + 2W_4\mathbf{g} \otimes \mathbf{g}, \tag{3.1.47}$$

where

$$\mathbf{g} \otimes \mathbf{g} = \begin{pmatrix} 0 & 0 & 0 \\ 0 & \left(\frac{r}{R}\right)^2 & 0 \\ 0 & 0 & 0 \end{pmatrix}. \tag{3.1.48}$$

Accordingly, the dimensionless Cauchy stress components for the whole tissue are

$$\sigma_{rr} = -\mathscr{P} + 2W_1 \left(\left(\frac{\partial r}{\partial R} \right)^2 + \frac{1}{\varepsilon^2} \left(\frac{\partial r}{\partial Z} \right)^2 \right), \tag{3.1.49a}$$

$$\sigma_{\theta\theta} = -\mathscr{P} + 2(W_1 + W_4) \left(\frac{r}{R} \right)^2, \tag{3.1.49b}$$

$$\sigma_{zz} = -\mathscr{P} + 2W_1 \left(\varepsilon^2 \left(\frac{\partial z}{\partial R} \right)^2 + \left(\frac{\partial z}{\partial Z} \right)^2 \right), \tag{3.1.49c}$$

$$\sigma_{rz} = \sigma_{zr} = 2W_1 \left(\varepsilon \frac{\partial r}{\partial R} \frac{\partial z}{\partial R} + \frac{1}{\varepsilon} \frac{\partial r}{\partial Z} \frac{\partial z}{\partial Z} \right). \tag{3.1.49d}$$

The dimensionless Cauchy stress tensor for the whole tissue is the weighted addition of the three dimensionless constituents Cauchy stress tensors such that

$$\boldsymbol{\sigma} = \sum_i \Phi_i \boldsymbol{\sigma}_i, \qquad i \in \{c, m, u\}, \tag{3.1.50}$$

and where the dimensionless Cauchy stress tensor for each constituent is

$$\boldsymbol{\sigma}_c = -\mathscr{P}\mathbf{I} + 2W_{c1}\mathbf{B} + 2W_{c4}\mathbf{g}\otimes\mathbf{g}, \tag{3.1.51a}$$

$$\boldsymbol{\sigma}_m = -\mathscr{P}\mathbf{I} + 2W_{m1}\mathbf{B} + 2W_{m4}\mathbf{g}\otimes\mathbf{g}, \tag{3.1.51b}$$

$$\boldsymbol{\sigma}_u = -\mathscr{P}\mathbf{I}, \tag{3.1.51c}$$

each with components of the exact form in (3.1.49) by allowing $\sigma = \sigma_i$ and $W = W_i$ for $i \in \{c, m, u\}$, as previously in Section 3.1.2.

The dimensionless von Mises stress for the ASM and ECM is given by

$$\sigma_{i\mathrm{VM}} = \frac{1}{\sqrt{2}}\Big((\sigma_{irr} - \sigma_{i\theta\theta})^2 + (\sigma_{i\theta\theta} - \sigma_{izz})^2 + (\sigma_{izz} - \sigma_{irr})^2 + 6\left({\sigma_{ir\theta}}^2 + {\sigma_{i\theta z}}^2 + {\sigma_{izr}}^2\right)\Big)^{\frac{1}{2}}, \qquad i \in \{c, m\}, \tag{3.1.52}$$

and the dimensionless difference in the constituent von Mises stress is

$$\sigma_{\mathrm{dif}} = \left|\sigma_{c\mathrm{VM}} - \sigma_{m\mathrm{VM}}\right|. \tag{3.1.53}$$

The dimensionless version of the linear momentum equations (3.1.30) reads

$$\frac{\partial r}{\partial R}\frac{\partial \sigma_{rz}}{\partial Z} - \frac{\partial r}{\partial Z}\frac{\partial \sigma_{rz}}{\partial R} + \varepsilon\left(\frac{\partial z}{\partial Z}\frac{\partial \sigma_{rr}}{\partial R} - \frac{\partial z}{\partial R}\frac{\partial \sigma_{rr}}{\partial Z}\right) + \varepsilon\left(\frac{\partial r}{\partial R}\frac{\partial z}{\partial Z} - \frac{\partial r}{\partial Z}\frac{\partial z}{\partial R}\right)\left(\frac{\sigma_{rr} - \sigma_{\theta\theta}}{r}\right) = 0, \tag{3.1.54a}$$

$$\frac{\partial r}{\partial R}\frac{\partial \sigma_{zz}}{\partial Z} - \frac{\partial r}{\partial Z}\frac{\partial \sigma_{zz}}{\partial R} + \varepsilon\left(\frac{\partial z}{\partial Z}\frac{\partial \sigma_{rz}}{\partial R} - \frac{\partial z}{\partial R}\frac{\partial \sigma_{rz}}{\partial Z}\right) + \varepsilon\left(\frac{\partial r}{\partial R}\frac{\partial z}{\partial Z} - \frac{\partial r}{\partial Z}\frac{\partial z}{\partial R}\right)\frac{\sigma_{rz}}{r} = 0, \tag{3.1.54b}$$

and by substituting (3.1.49) into (3.1.54), we express these linear momentum

equations in terms of the reference configuration,

$$\begin{aligned}
&\frac{\partial z}{\partial Z}\frac{\partial}{\partial R}\left[\left(\frac{\partial r}{\partial Z}\right)^2\right]-\frac{\partial z}{\partial R}\frac{\partial}{\partial Z}\left[\left(\frac{\partial r}{\partial Z}\right)^2\right]\\
&\quad+\frac{\partial r}{\partial R}\frac{\partial}{\partial Z}\left[\frac{\partial r}{\partial Z}\frac{\partial z}{\partial Z}\right]-\frac{\partial r}{\partial Z}\frac{\partial}{\partial R}\left[\frac{\partial r}{\partial Z}\frac{\partial z}{\partial Z}\right]\\
&\qquad+\frac{1}{r}\left(\frac{\partial r}{\partial R}\frac{\partial z}{\partial Z}-\frac{\partial r}{\partial Z}\frac{\partial z}{\partial R}\right)\left(\frac{\partial r}{\partial Z}\right)^2\\
&\quad+\varepsilon^2\frac{\partial z}{\partial Z}\frac{\partial}{\partial R}\left[\left(\frac{\partial r}{\partial R}\right)^2\right]-\varepsilon^2\frac{\partial z}{\partial R}\frac{\partial}{\partial Z}\left[\left(\frac{\partial r}{\partial R}\right)^2\right]\\
&\qquad+\varepsilon^2\frac{\partial r}{\partial R}\frac{\partial}{\partial Z}\left[\frac{\partial r}{\partial R}\frac{\partial z}{\partial R}\right]-\varepsilon^2\frac{\partial r}{\partial Z}\frac{\partial}{\partial R}\left[\frac{\partial r}{\partial R}\frac{\partial z}{\partial R}\right]\\
&\qquad\quad+\frac{\varepsilon^2}{2W_1}\frac{\partial z}{\partial R}\frac{\partial \mathscr{P}}{\partial Z}-\frac{\varepsilon^2}{2W_1}\frac{\partial z}{\partial Z}\frac{\partial \mathscr{P}}{\partial R}\\
&\qquad\quad+\frac{\varepsilon^2}{r}\left(\frac{\partial r}{\partial R}\frac{\partial z}{\partial Z}-\frac{\partial r}{\partial Z}\frac{\partial z}{\partial R}\right)\left(\frac{\partial r}{\partial R}\right)^2\\
&\qquad\quad-\frac{\varepsilon^2(W_1+W_4)r}{W_1R^2}\left(\frac{\partial r}{\partial R}\frac{\partial z}{\partial Z}-\frac{\partial r}{\partial Z}\frac{\partial z}{\partial R}\right)=0, \qquad (3.1.55a)\\
&\frac{\partial r}{\partial R}\frac{\partial}{\partial Z}\left[\left(\frac{\partial z}{\partial Z}\right)^2\right]-\frac{\partial r}{\partial Z}\frac{\partial}{\partial R}\left[\left(\frac{\partial z}{\partial Z}\right)^2\right]\\
&\quad+\frac{\partial z}{\partial Z}\frac{\partial}{\partial R}\left[\frac{\partial z}{\partial Z}\frac{\partial r}{\partial Z}\right]-\frac{\partial z}{\partial R}\frac{\partial}{\partial Z}\left[\frac{\partial z}{\partial Z}\frac{\partial r}{\partial Z}\right]\\
&\quad+\frac{1}{r}\left(\frac{\partial r}{\partial R}\frac{\partial z}{\partial Z}-\frac{\partial r}{\partial Z}\frac{\partial z}{\partial R}\right)\frac{\partial z}{\partial Z}\frac{\partial r}{\partial Z}+\frac{1}{2W_1}\frac{\partial r}{\partial Z}\frac{\partial \mathscr{P}}{\partial R}\\
&\qquad-\frac{1}{2W_1}\frac{\partial r}{\partial R}\frac{\partial \mathscr{P}}{\partial Z}+\varepsilon^2\frac{\partial r}{\partial R}\frac{\partial}{\partial Z}\left[\left(\frac{\partial z}{\partial R}\right)^2\right]\\
&\qquad-\varepsilon^2\frac{\partial r}{\partial Z}\frac{\partial}{\partial R}\left[\left(\frac{\partial z}{\partial R}\right)^2\right]+\varepsilon^2\frac{\partial z}{\partial Z}\frac{\partial}{\partial R}\left[\frac{\partial r}{\partial R}\frac{\partial z}{\partial R}\right]\\
&\quad-\varepsilon^2\frac{\partial z}{\partial R}\frac{\partial}{\partial Z}\left[\frac{\partial r}{\partial R}\frac{\partial z}{\partial R}\right]+\frac{\varepsilon^2}{r}\left(\frac{\partial r}{\partial R}\frac{\partial z}{\partial Z}-\frac{\partial r}{\partial Z}\frac{\partial z}{\partial R}\right)\frac{\partial r}{\partial R}\frac{\partial z}{\partial R}=0. \qquad (3.1.55b)
\end{aligned}$$

The dimensionless version of the incompressibility constraint (3.1.9) is

$$\frac{r}{R}\left(\frac{\partial r}{\partial R}\frac{\partial z}{\partial Z}-\frac{\partial r}{\partial Z}\frac{\partial z}{\partial R}\right)=1. \qquad (3.1.56)$$

The dimensionless displacement boundary condition, r_{dis}, at the dimensionless

outer radius, $R = 1$, is given by

$$r(1, Z) = r_{\text{dis}}, \tag{3.1.57}$$

and the dimensionless free boundary conditions at the dimensionless upper, $Z = \frac{1}{2}$, lower, $Z = -\frac{1}{2}$, and inner, $R = R_{\text{in}}$, surfaces of the PCLS are

$$\boldsymbol{\sigma}\left(R, \tfrac{1}{2}\right)\mathbf{n}_{\text{up}} = \mathbf{0}, \tag{3.1.58a}$$

$$\boldsymbol{\sigma}\left(R, -\tfrac{1}{2}\right)\mathbf{n}_{\text{low}} = \mathbf{0}, \tag{3.1.58b}$$

$$\boldsymbol{\sigma}\left(R_{\text{in}}, Z\right)\mathbf{n}_{\text{in}} = \mathbf{0}, \tag{3.1.58c}$$

where the dimensionless unit normals to the upper, $\mathbf{n}_{\text{up}}$, lower, $\mathbf{n}_{\text{low}}$, and inner, $\mathbf{n}_{\text{in}}$, surfaces in the reference configuration are given by:

at $Z = \frac{1}{2}$:

$$\mathbf{n}_{\text{up}} = \left(\left(-\frac{\partial z}{\partial R}\right)^2 + \left(\frac{\partial r}{\partial R}\right)^2\right)^{-\frac{1}{2}} \cdot \left(-\frac{\partial z}{\partial R}, 0, \frac{\partial r}{\partial R}\right); \tag{3.1.59a}$$

at $Z = -\frac{1}{2}$:

$$\mathbf{n}_{\text{low}} = \left(\left(-\frac{\partial z}{\partial R}\right)^2 + \left(\frac{\partial r}{\partial R}\right)^2\right)^{-\frac{1}{2}} \cdot \left(-\frac{\partial z}{\partial R}, 0, \frac{\partial r}{\partial R}\right); \tag{3.1.59b}$$

at $R = R_{\text{in}}$:

$$\mathbf{n}_{\text{in}} = \left(\left(-\frac{\partial z}{\partial Z}\right)^2 + \left(\frac{\partial r}{\partial Z}\right)^2\right)^{-\frac{1}{2}} \cdot \left(-\frac{\partial z}{\partial Z}, 0, \frac{\partial r}{\partial Z}\right). \tag{3.1.59c}$$

Substituting for $\mathbf{n}$ and σ from (3.1.59) and (3.1.49) respectively into the traction-free boundary conditions (3.1.58) gives:

at $Z = \pm\frac{1}{2}$:

$$\frac{\partial r}{\partial R}\frac{\partial r}{\partial Z}\frac{\partial z}{\partial Z} - \frac{\partial z}{\partial R}\left(\frac{\partial r}{\partial Z}\right)^2 + \frac{\varepsilon^2 \mathscr{P}}{2W_1} = 0, \tag{3.1.60a}$$

$$\frac{\partial r}{\partial R}\left(\frac{\partial z}{\partial Z}\right)^2 - \frac{\partial z}{\partial R}\frac{\partial r}{\partial Z}\frac{\partial z}{\partial Z} - \frac{\mathscr{P}}{2W_1}\frac{\partial r}{\partial R} = 0; \tag{3.1.60b}$$

at $R = R_{\text{in}}$:

$$\frac{\partial r}{\partial R}\frac{\partial r}{\partial Z}\frac{\partial z}{\partial R} - \frac{\partial z}{\partial Z}\left(\frac{\partial r}{\partial R}\right)^2 + \frac{\mathscr{P}}{2W_1}\frac{\partial z}{\partial Z} = 0, \tag{3.1.60c}$$

$$-\frac{\mathscr{P}}{2W_1}\frac{\partial r}{\partial Z} - \varepsilon^2\frac{\partial r}{\partial R}\frac{\partial z}{\partial R}\frac{\partial z}{\partial Z} + \varepsilon^2\frac{\partial r}{\partial Z}\left(\frac{\partial z}{\partial R}\right)^2 = 0. \tag{3.1.60d}$$

3.2 Numerical results

Numerical solutions to the full biomechanical model (that balances linear momentum (3.1.55) and satisfies tissue incompressibility (3.1.56), subject to the imposed radial stretch (3.1.57) at the outer radius, R_{out}, and the free boundary conditions (3.1.60) at the upper, lower and inner surfaces of the PCLS) are obtained via a finite element method, implemented in the software FEBio (Maas et al. 2012) (details in Appendix B.1). To confirm that our numerical results are correct, we carry out suitable mesh convergence tests by uniformly refining the mesh. We demonstrate that our results converge to a solution with increasing number of elements in Figure 3.2.

The L^2 norm of a $q \times s$ matrix $\mathbf{A}$ is defined as

$$\|\mathbf{A}\|_{L^2} = \left(\sum_{j=1}^{q}\sum_{k=1}^{s}|A_{jk}|^2\right)^{\frac{1}{2}}. \tag{3.2.1}$$

We use the L^2 norm (3.2.1) as a comparable measure in our mesh convergence tests in order to provide a global representation of the change in solution. In addition to the radial and axial deformation variables, r and z, we consider the von Mises stress, σ_{VM}, in order to provide an overall representation of the Cauchy Stress components. For consistency, $\|r(R,Z)\|_{L^2}$, $\|z(R,Z)\|_{L^2}$ and

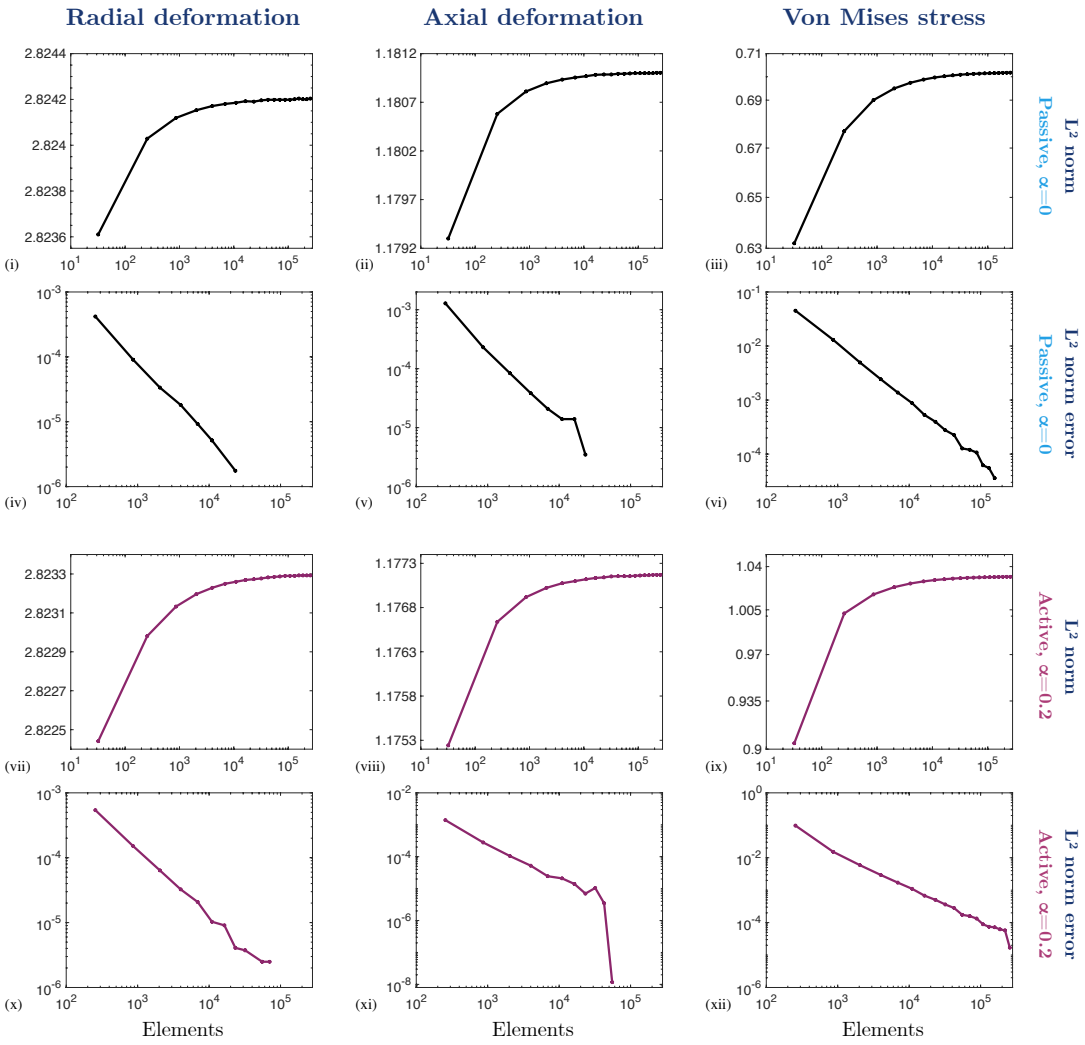

Figure 3.2: (i)–(iii) The L^2 norm (3.2.1) and (iv)–(vi) the L^2 norm error between iterations of mesh refinement (3.2.2) of the radial deformation, r, axial deformation, z, and von Mises stress, σ_{VM}, in the passive, $\alpha = 0$, case, plotted against the number of elements in the mesh. (vii)–(ix) The L^2 norm (3.2.1) and (x)–(xii) the L^2 norm error (3.2.2) of r, z and σ_{VM} in the active, $\alpha = 0.2$, case, plotted against the number of elements in the mesh. A fixed 5% stretch is applied with $\varepsilon = 1$ throughout and the remaining parameter values are in Table C.4 in Appendix C.2.

$\|\sigma_{\text{VM}}(R, Z)\|_{L^2}$ are evaluated at the nodal positions of the coarse mesh at each iteration and are plotted against the number of elements in the mesh to show that the solutions converge appropriately both in the passive and active contraction case (Figures 3.2 (i)–(iii) and (vii)–(ix), respectively).

Using (3.2.1), we define the L^2 norm error between iterations, n, as

$$\left| \|\mathbf{A}_n\|_{L^2} - \|\mathbf{A}_{n+1}\|_{L^2} \right|. \tag{3.2.2}$$

We show that the errors between iterations decay to zero in Figures 3.2 (iv)–(vi) and (x)–(xii), again in both the passive and active contraction case respectively. Note that we have carried out mesh convergence tests for $\varepsilon \in \{0.01, 0.1, 1\}$, with and without a prescribed stretch, but limit the results displayed in Figure 3.2 to $\varepsilon = 1$ with a 5% fixed stretch applied for concision. In the following simulations we use a mesh that is in the regime where the stress and deformation variables have reached a steady state and the error between mesh refinement iterations is sufficiently small.

3.2.1 Deformation and stresses in a thick lung-slice

In this section we consider $\varepsilon = 1$, meaning that the initial thickness of the PCLS, h^*, is equal to the undeformed outer radius, R^*_{out}. The behaviour of the non-zero Cauchy stress components, σ_{rr}, $\sigma_{\theta\theta}$, σ_{zz}, σ_{rz} and the displacements in the radial, r, and axial, z, directions in response to a 5% stretch applied at the outer radius of the PCLS are shown in Figure 3.3. Here, the presence of active contraction increases, from left to right, and is absent in the passive case.

In both the passive and active contraction cases we observe that the radial deformation, r, decays approximately linearly with undeformed radius, R, along the airway wall but remains uniform axially (Figures 3.3 (i)–(iii)). As required by the incompressibility of the material, the airway thins as it is stretched (Figures 3.3 (iv)–(vi)).

The mechanical stress within the tissue displays significant spatial heterogeneity (*e.g.* Figure 3.3 (xviii)). Moreover, we observe that while the deformation of the airway is qualitatively similar in the passive and active contraction cases (*cf.* Figures 3.3 (i), (iii)), there are distinct qualitative and quantitative differences in the stress state between these regimes (*cf.* Figures 3.3 (xvi), (xviii)). In particular, there is an increased and exaggerated heterogeneous stress distribution in the presence of active contraction. Furthermore, the axial dependence of these heterogeneous stress distributions increases with increased active contraction

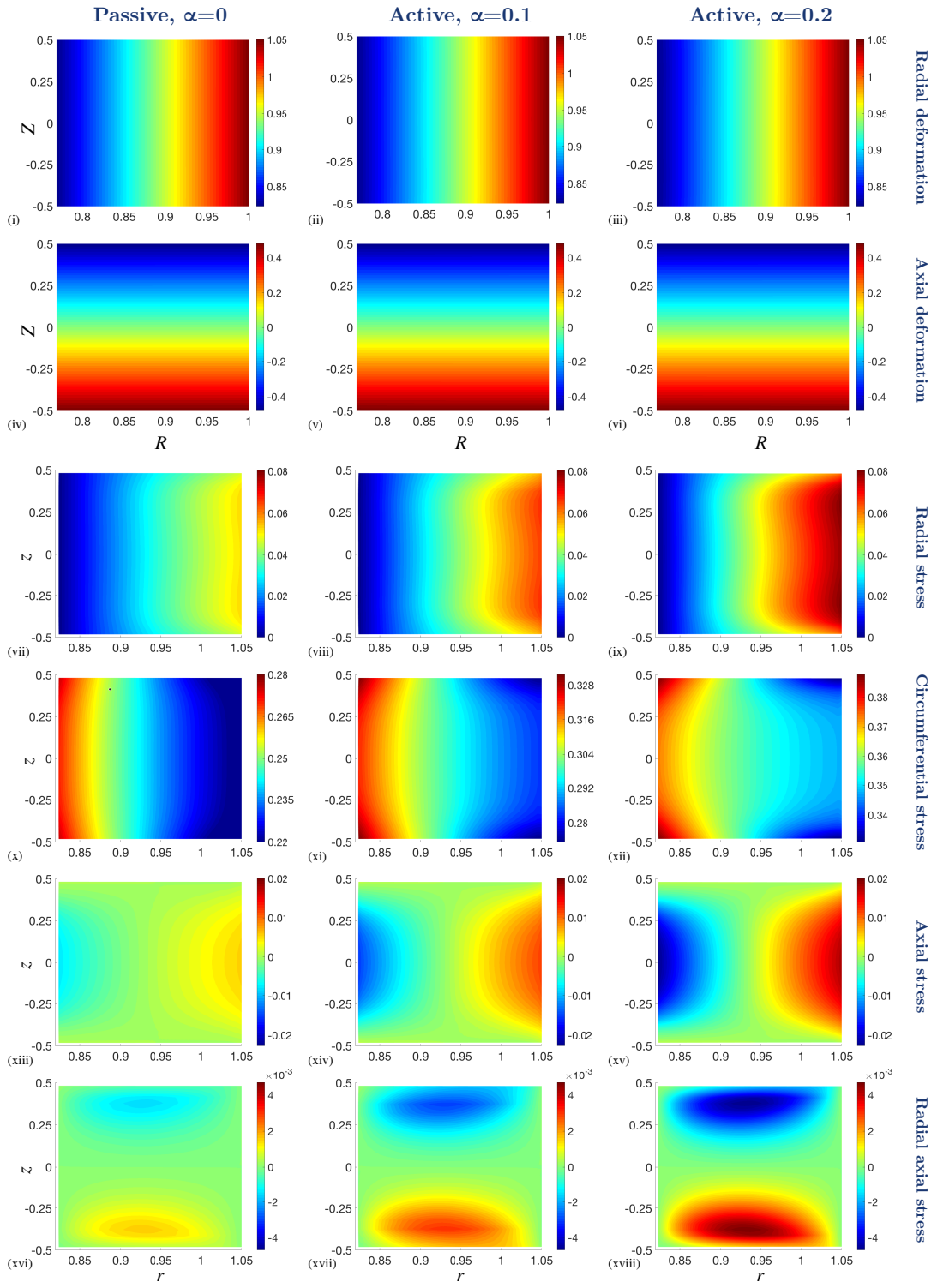

Figure 3.3: (i)–(iii) Radial deformation, r, and (iv)–(vi) axial deformation, z, plotted over the undeformed configuration, (R, Z). Cauchy stress components (vii)–(ix) σ_{rr}, (x)–(xii) $\sigma_{\theta\theta}$, (xiii)–(xv) σ_{zz} and (xvi)–(xviii) σ_{rz} plotted over the deformed configuration, (r, z). A 5% fixed stretch is applied in the passive, $\alpha = 0$, and active cases, $\alpha = 0.1$ and $\alpha = 0.2$, for $\varepsilon = 1$. Remaining parameter values are in Table C.4 in Appendix C.2.

and is highlighted by the circumferential stress distribution, $\sigma_{\theta\theta}$ (Figure 3.3 (xii)).

In each case we observe increased radial stress, σ_{rr}, at the outer boundary (in the direction of the prescribed stretch), whilst remaining approximately zero at the inner radius (Figures 3.3 (vii)–(ix)). Similarly, tissue contractility significantly influences the circumferential stress, $\sigma_{\theta\theta}$, as is to be expected, since the generated contractile stress acts in the direction of the circumferential fibres embedded in the airway (Figures 3.3 (x)–(xii)). Moreover, we see that the circumferential stress is higher at the inner radius than at the outer radius (Figures 3.3 (x)–(xii)).

The thinning and stretching of the PCLS under the imposed stretch is reflected in the distributions of the axial, σ_{zz}, and shear, σ_{rz}, stresses with an order of magnitude increase observed in the axial stress in the presence of contraction (Figures 3.3 (xiii)–(xviii)). The positive (tensile) axial stress at the outer radius and negative (compressive) axial stress at the inner radius reflects the relative thickening at the inner radius compared with that at the outer. The shear stress is positive at the lower surface and negative at the upper surface reflecting the relatively increased displacement of material radially and downward at the upper (and upward at the lower) surface.

3.2.2 Deformation and stresses in a thin lung-slice

The preceding results correspond to an airway of thickness comparable to its outer radius (in particular, we set $\varepsilon = 1$). The typical thickness for a PCLS is in the range of 100–250μm and a typical airway radius is in the range of 1–5mm, giving $0.02 < \varepsilon < 0.25$. Motivated by this, we investigate the dependence of the model behaviour on the PCLS thickness by varying the aspect ratio ε. We consider the passive, $\alpha = 0$, and active contraction case, $\alpha = 0.2$, in Figures 3.4 and 3.5. Here, we reduce ε from $\varepsilon = 1$ to $\varepsilon = 0.01$ in the direction of the black arrows. Note that the variables are plotted as a function of deformed radius at the undeformed axial centre of the PCLS, *i.e.* at $Z = 0$ (Figure 3.4). This is true in all cases bar the axial deformation, z, which we plot as a function of radius at the undeformed upper surface of the PCLS, *i.e.* at $Z = \frac{1}{2}$, in order to illustrate the thinning of the PCLS in response to stretch (Figures 3.4 (iii), (iv)).

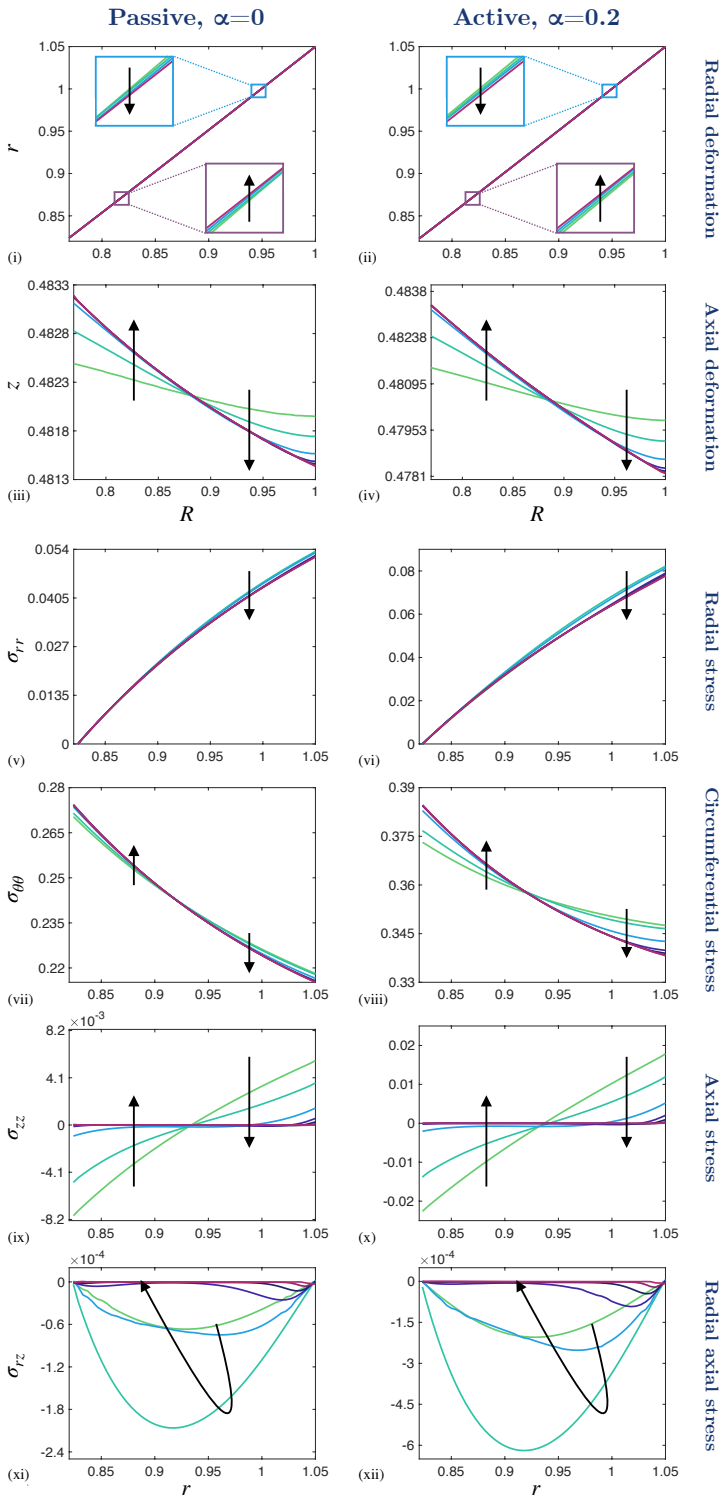

Figure 3.4: (i)–(ii) Radial deformation, $r(R,0)$, and (iii)–(iv) axial deformation, $z(R,\frac{1}{2})$, plotted over the undeformed radius, R. Cauchy stress components (v)–(vi) σ_{rr}, (vii)–(viii) $\sigma_{\theta\theta}$, (ix)–(x) σ_{zz} and (xi)–(xii) σ_{rz} plotted over the deformed radius, r, at $Z = 0$. A 5% fixed stretch is applied in the passive, $\alpha = 0$, and active contraction case, $\alpha = 0.2$. The aspect ratio decreases in direction of black arrows for $\varepsilon \in \{1, 0.5, 0.25, 0.1, 0.05, 0.025, 0.01\}$ and the remaining parameter values are in Table C.4 in Appendix C.2.

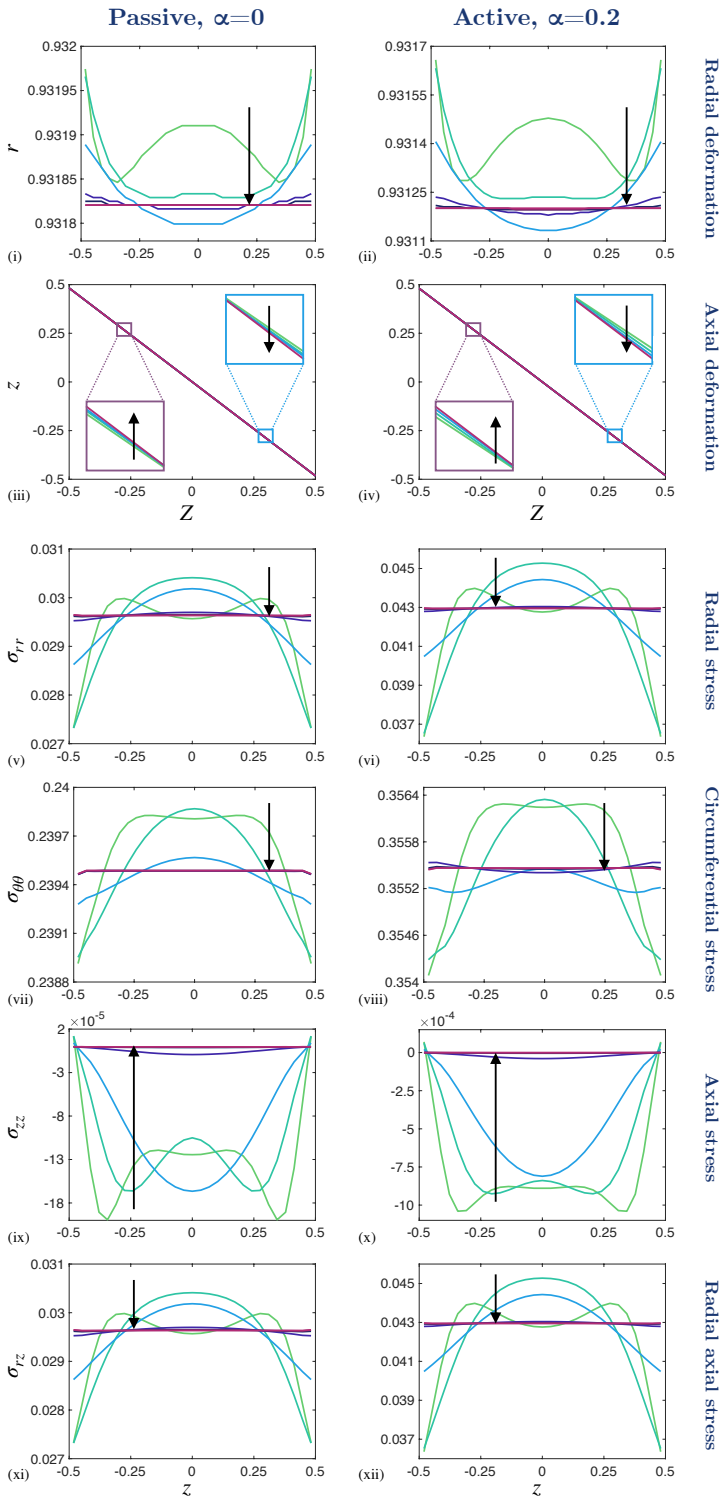

Figure 3.5: (i)–(ii) Radial deformation, r, and (iii)–(iv) axial deformation, z, plotted over the undeformed thickness, Z. Cauchy stress components (v)–(vi) σ_{rr}, (vii)–(viii) $\sigma_{\theta\theta}$, (ix)–(x) σ_{zz} and (xi)–(xii) σ_{rz} plotted over the deformed thickness, z, at $R = R_{\text{mid}}$. A 5% fixed stretch is applied in the passive, $\alpha = 0$, and active contraction case, $\alpha = 0.2$. The aspect ratio decreases in direction of black arrows for $\varepsilon \in \{1, 0.5, 0.25, 0.1, 0.05, 0.025, 0.01\}$ and the remaining parameter values are in Table C.4 in Appendix C.2.

The results illustrating axial dependence are all plotted over the thickness of the PCLS through the undeformed radial midpoint R_{mid} (Figure 3.5).

In both the passive and active contraction cases, the radial deformation at the axial centre line varies linearly with R and remains approximately invariant with ε (Figures 3.4 (i), (ii) inset highlighting the very slight variation with ε) and with correspondingly little change in the radial stress (Figures 3.4 (v), (vi)). Conversely, the near-uniform thinning of the airway, observed in Figures 3.3 (iii), (iv), becomes marginally more exaggerated as ε is reduced and the PCLS thins more at the outer radius than at the inner radius. Similarly, the circumferential stress increases at the inner radius and decreases at the outer radius as ε reduces (Figures 3.4 (vii), (viii)). On the other hand, we observe that the heterogeneous axial and shear stress distributions decay to zero in Figures 3.4 (ix)–(xii).

The deformation and stress variation through the axial thickness is shown in Figure 3.5. Here we observe only a weak dependence of the radial deformation and stresses on Z, that decays to uniformity with decreasing ε. In particular, the axial stress decays to zero with ε (Figures 3.5 (ix), (x)). In contrast, the axial deformation remains approximately linear in Z as ε decreases (Figures 3.5 (iii), (iv) inset highlighting the very slight variation with ε). In the active contraction case, the above described features persist, but the variations in deformation and associated stresses are exaggerated quantitatively (*cf.* Figures 3.4, 3.5).

3.3 Summary

In this chapter we have developed a biomechanical model of the PCLS stretching experiment performed by Tatler (2016) that is outlined in Section 1.3.1. Our biomechanical approach provides a description of the stresses generated in the PCLS due to airway deformation that are potentially responsible for the mechanical activation of TGF-β. In particular, in section 3.1.3, we presented a convenient representation for the mechanical activation of TGF-β by the means of the difference in constituent von Mises stress.

The PCLS tissue is described (in a cylindrical geometry) as an incompressible hyperelastic material comprising active ASM and passive ECM components

embedded with circumferential fibres. The governing equations satisfy tissue incompressibilty and the balance of linear momentum. The upper, lower and inner surfaces of the PCLS are modelled as traction-free boundaries, whereas a displacement is prescribed at the outer boundary to describe the performed stretching.

We simulated our model in the finite element software FEBio and performed suitable mesh convergence tests to show that our results converge to a solution. We observed the behaviour of the deformation and stresses in response to active contraction and prescribed stretch. Initially, we investigated the behaviour of a PCLS of equal thickness to the outer radius of the airway, *i.e.* $\varepsilon = 1$. Thereafter, we reduced the aspect ratio, ε, to demonstrate the dependence of the model behaviour on the PCLS thickness. Our key results highlight a very weak dependence of the radial deformation and stresses on Z that decay uniformly with decreasing ε and, importantly, in both the passive and active contraction cases. Furthermore, we have shown that the axial and shear stresses decay to zero across the radius (as well as thickness for the axial stress) for small ε. Guided by these observations, in the following chapter, we consider analytical simplifications of our model that allow for efficient parameter sweeps in order to investigate the effect of material properties on the mechanical activation of TGF-β.

CHAPTER 4

Biomechanical Model Approximations

Guided by the observations in Section 3.2.2, in this chapter we consider to separate analytical simplifications of the biomechanical model introduced in Chapter 3. Firstly, in Section 4.1, we adopt a membrane model, following Wong and Shield (1969), that allows reduction to one spatial dimension. Subsequently in Section 4.2, we consider an asymptotic approach to obtain a reduced model describing the leading order PCLS deformation in the thin-PCLS-limit. In Section 4.3, we address the suitability of each approximation by comparing them to the full biomechanical model simulated in FEBio (Maas et al. 2012).

4.1 Membrane approximation

In this section we simplify the biomechanical model (equations (3.1.55) and (3.1.56) with boundary conditions (3.1.57) and (3.1.60)) by assuming that the PCLS behaves as an elastic membrane, in which case we neglect Z dependence and set $z = Z$ so that there is no change in the axial thickness of the PCLS upon deformation. This membrane description has previously been used by Wong and Shield (1969) to approximate an axisymmetric stretch of an isotropic sheet; however, Wong and Shield (1969) find that the approximation breaks down when the sheet has an edge which is traction-free. The determinant of the deformation gradient approaches zero in the close vicinity of the traction-free edge and a singularity appears in the governing equations when the material is

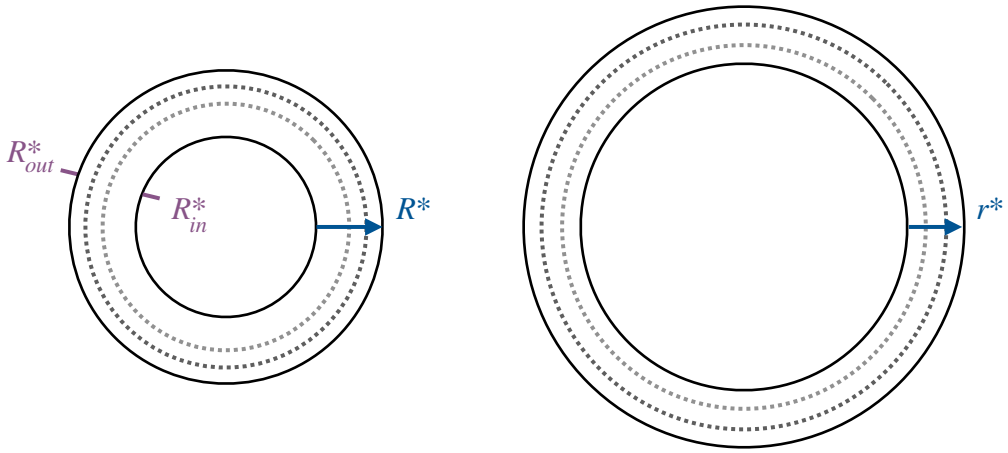

Figure 4.1: Dimensional undeformed (left) and deformed (right) configurations to illustrate the geometry of an airway modelled as a membrane within the PCLS (omitting Z dependence). Dotted lines indicate the circumferential fibres representing the active ASM and passive ECM components.

incompressible. Similarly, although we consider an anisotropic material with active contractile force generation, we find inconsistencies with the governing equations and the prescribed boundary conditions when the thickness of the PCLS is fixed. Specifically, the traction-free boundary conditions on the upper, lower and inner surfaces of the PCLS cannot be satisfied simultaneously, whilst preserving incompressibility, without the PCLS changing in thickness. Therefore, enforcing torsion free axisymmetry as previously, in this section we reduce the description of the PCLS to that in Figure 4.1 and consider the one-dimensional deformation $r = r(R)$. Consequently, we do not enforce the free boundary conditions on the upper and lower surfaces, (3.1.58a) and (3.1.58b). It should be noted that the membrane approximation is not a limiting case of the full PCLS model as $\varepsilon \to 0$, since we constrain Z to remain fixed.

4.1.1 Membrane governing equations

The deformation gradient tensor (3.1.37), and the corresponding Cauchy Green stress tensors (3.1.38) reduce to

$$\mathbf{F} = \begin{pmatrix} \frac{\mathrm{d}r}{\mathrm{d}R} & 0 \\ 0 & \frac{r}{R} \end{pmatrix}, \qquad \mathbf{B} = \mathbf{C} = \begin{pmatrix} \left(\frac{\mathrm{d}r}{\mathrm{d}R}\right)^2 & 0 \\ 0 & \left(\frac{r}{R}\right)^2 \end{pmatrix}. \tag{4.1.1}$$

Accordingly, the non-zero components of the Cauchy stress tensor for the whole tissue (3.1.49) reduce to

$$\sigma_{rr} = -\mathscr{P} + 2W_1 \left(\frac{R}{r}\right)^2, \tag{4.1.2a}$$

$$\sigma_{\theta\theta} = -\mathscr{P} + 2(W_1 + W_4) \left(\frac{r}{R}\right)^2, \tag{4.1.2b}$$

where, as previously, the Cauchy stress components for each constituent take the form (4.1.2), with $\sigma = \sigma_i$ and $W = W_i$ for $i \in \{c, m, u\}$. Again, note that axial dependence, Z, is neglected in this membrane approximation and therefore the Cauchy stress, $\boldsymbol{\sigma}$, and pressure, $\mathscr{P}$, are functions of radius, R, only.

Collecting the non-zero components of the dimensionless linear momentum equations (3.1.54) leaves

$$\frac{r}{R}\frac{\mathrm{d}\sigma_{rr}}{\mathrm{d}R} + \frac{1}{r}\left(\sigma_{rr} - \sigma_{\theta\theta}\right) = 0. \tag{4.1.3}$$

The dimensionless incompressibility constraint (3.1.56) reduces to

$$\frac{\mathrm{d}r}{\mathrm{d}R} = \frac{R}{r}, \tag{4.1.4}$$

the dimensionless displacement boundary condition at the outer radius (3.1.57) reduces to

$$r(1) = r_{\mathrm{dis}}, \tag{4.1.5}$$

and the dimensionless free boundary condition at the inner radius (3.1.58c) reduces to

$$\sigma_{rr}(R_{\mathrm{in}}) = 0. \tag{4.1.6}$$

We omit the dimensionless free boundary conditions on the upper and lower surfaces, (3.1.58a) and (3.1.58b), respectively.

Substituting (4.1.2) into (4.1.3) and then coupling with (4.1.4), we seek solutions to

$$\frac{\mathrm{d}r}{\mathrm{d}R} = \frac{R}{r}, \tag{4.1.7a}$$

$$\frac{\mathrm{d}\sigma_{rr}}{\mathrm{d}R} = \frac{2}{R}\left(W_1 + W_4 - \frac{W_1 R^4}{r^4}\right), \tag{4.1.7b}$$

subject to the boundary conditions at the outer radius (4.1.5) and the inner radius (4.1.6).

4.1.2 Analytical solutions

Integrating (4.1.7a) with respect to R, subject to the outer boundary condition (4.1.5), gives

$$r^2 = R^2 - 1 + {r_{\mathrm{dis}}}^2, \qquad R_{\mathrm{in}} \leq R \leq 1. \tag{4.1.8}$$

Subsequently, integrating (4.1.7b) with respect to R and applying the zero radial stress condition at the inner boundary (4.1.6) gives

$$\sigma_{rr} = \int_{R_{\mathrm{in}}}^{R} \frac{2}{R'}\left(W_1 + W_4 - \frac{W_1 R'^4}{r^4}\right)\mathrm{d}R'. \tag{4.1.9}$$

In order to obtain $\sigma_{\theta\theta}$ (4.1.2b), we require the pressure, $\mathscr{P}$; combining (4.1.2) and (4.1.9) provides

$$\mathscr{P} = 2\frac{W_1 R^2}{r^2} - \int_{R_{\mathrm{in}}}^{R} \frac{2}{R'}\left(W_1 + W_4 - \frac{W_1 R'^4}{r^4}\right)\mathrm{d}R', \tag{4.1.10}$$

and the constituent and total tissue stress follow directly.

4.2 Thin-PCLS-limit

In this section, motivated by the typical geometry of the PCLS (see Section 3.2.2), we consider the limit $0 < \varepsilon \ll 1$, so that the thickness of the PCLS is small in comparison to a typical airway radius (Figure 4.2). Correspondingly, and in view of our numerical results in Section 3.2.2 (in particular, Figure 3.5 where we observe r becomes independent of Z for $0 < \varepsilon \ll 1$), we seek expansions of the form

$$r = r^{(0)}(R) + \varepsilon r^{(1)}(R) + \varepsilon^2 r^{(2)}(R) + \mathcal{O}(\varepsilon^3), \tag{4.2.1a}$$

$$z = z^{(0)}(R,Z) + \varepsilon z^{(1)}(R,Z) + \varepsilon^2 z^{(2)}(R,Z) + \mathcal{O}(\varepsilon^3), \tag{4.2.1b}$$

$$\mathscr{P} = \mathscr{P}^{(0)}(R,Z) + \varepsilon \mathscr{P}^{(1)}(R,Z) + \varepsilon^2 \mathscr{P}^{(2)}(R,Z) + \mathcal{O}(\varepsilon^3), \tag{4.2.1c}$$

adopting corresponding notation for the strain-energy functions where necessary. We pause to highlight that the more general expansion, for which $r = r(R,Z)$ and the leading term for $\mathscr{P}$ is $\mathcal{O}(\varepsilon^{-2})$ (to obtain the proper leading order balance in the Cauchy stress) can be reduced to that shown in (4.2.1) (see Appendix B.3) and so we adopt this from the outset for brevity.

In the strain-energy function for the whole tissue, W (3.1.42), we assume that Φ_c, Φ_m, μ, ω, ζ and α all remain $\mathcal{O}(1)$ constants. Therefore, the derivative of the strain-energy function, with respect to the first invariant, W_1 (3.1.46a), is also $\mathcal{O}(1)$. The derivative with respect to the fourth invariant, W_4 (3.1.46b), however, depends upon the deformed radius, r. Therefore, using the asymptotic

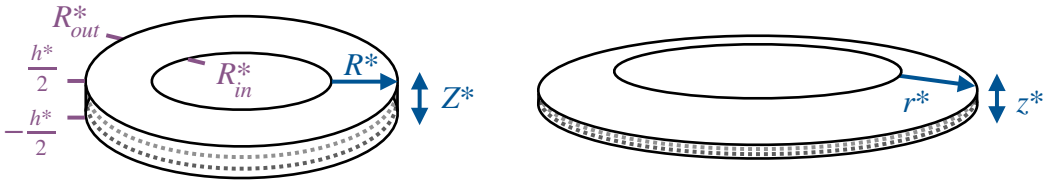

Figure 4.2: Dimensional undeformed (left) and deformed (right) configurations to illustrate the geometry of an airway modelled within the PCLS under the assumption that the outer radius of the airway within the PCLS is much larger than the initial thickness of the PCLS, *i.e.* $0 < \varepsilon \ll 1$. Dotted lines indicate the circumferential fibres representing the active ASM and passive ECM components.

expansions in (4.2.1a), the leading order terms in the derivative of the strain-energy function, with respect to the fourth invariant, for each constituent, W_{c4} and W_{m4} (3.1.45), are respectively

$$W_{c_4}^{(0)} = \frac{\alpha}{2}, \tag{4.2.2a}$$

$$\begin{aligned} W_{m_4}^{(0)} =& \omega \left(\left(\frac{r^{(0)}}{R} \right)^2 - 1 \right) \mathrm{H}\left(r^{(0)^2} - R^2 \right) \\ & \times \exp\left(\zeta \left(\left(\frac{r^{(0)}}{R} \right)^2 - 1 \right)^2 \right), \end{aligned} \tag{4.2.2b}$$

and correspondingly for the whole tissue

$$W_4^{(0)} = \Phi_c W_{c_4}^{(0)} + \Phi_m W_{m_4}^{(0)}. \tag{4.2.3}$$

4.2.1 Thin-PCLS-limit governing equations

At leading order, the governing equations (3.1.56) and (3.1.54) read

$$\frac{\mathrm{d}r^{(0)}}{\mathrm{d}R} \frac{\partial z^{(0)}}{\partial Z} = \frac{R}{r^{(0)}}, \tag{4.2.4a}$$

$$2 \frac{\mathrm{d}r^{(0)}}{\mathrm{d}R} \frac{\partial z^{(0)}}{\partial Z} \frac{\partial^2 z^{(0)}}{\partial Z^2} - \frac{\mathrm{d}r^{(0)}}{\mathrm{d}R} \frac{\partial \mathscr{P}^{(0)}}{\partial Z} = 0, \tag{4.2.4b}$$

subject to the displacement boundary condition at the outer radius (3.1.57),

$$r^{(0)}(1) = r_{\mathrm{dis}}, \tag{4.2.5}$$

and the following free boundary conditions at the upper, lower and inner surfaces of the PCLS (3.1.58):

at $Z = \pm\frac{1}{2}$:

$$\frac{\mathrm{d}r^{(0)}}{\mathrm{d}R} \left(\left(\frac{\partial z^{(0)}}{\partial Z} \right)^2 - \frac{\mathscr{P}^{(0)}}{2W_1} \right) = 0; \tag{4.2.6a}$$

at $R = R_{\text{in}}$:

$$\frac{\partial z^{(0)}}{\partial Z}\left(\left(\frac{\mathrm{d}r^{(0)}}{\mathrm{d}R}\right)^2 - \frac{\mathscr{P}^{(0)}}{2W_1}\right) = 0. \tag{4.2.6b}$$

Equation (4.2.4a) and the boundary conditions (4.2.6a) provide

$$z^{(0)} = \lambda_z^{(0)}(R)Z, \tag{4.2.7}$$

where the arbitrary function of R arising from the integration of (4.2.4a) vanishes due to axial symmetry in $z^{(0)}$ about the axial centre line, $Z = 0$. Furthermore, the equation (4.2.6b) requires $\mathscr{P}^{(0)} = \mathscr{P}^{(0)}(R)$. In view of which, together with the boundary conditions (4.2.6), we obtain:

$$\mathscr{P}^{(0)}(R) = 2W_1{\lambda_z^{(0)}}^2(R), \tag{4.2.8a}$$

$$\lambda_z^{(0)}(R_{\text{in}}) = \sqrt{\frac{R_{\text{in}}}{r^{(0)}(R_{\text{in}})}}. \tag{4.2.8b}$$

At $\mathcal{O}(\varepsilon)$ the linear momentum equations (3.1.54) read

$$\frac{\mathrm{d}r^{(0)}}{\mathrm{d}R}\left(\frac{\partial z^{(0)}}{\partial Z}\frac{\partial^2 z^{(1)}}{\partial Z^2} - \frac{1}{4W_1}\frac{\partial \mathscr{P}^{(1)}}{\partial Z}\right) = 0, \tag{4.2.9}$$

and the boundary conditions (3.1.57) and (3.1.60) provide

$$r^{(1)}(1) = 0, \tag{4.2.10a}$$

at $Z = \pm\frac{1}{2}$:

$$\frac{\mathrm{d}r^{(0)}}{\mathrm{d}R}\left(\frac{\partial z^{(0)}}{\partial Z}\frac{\partial z^{(1)}}{\partial Z} - \frac{\mathscr{P}^{(1)}}{4W_1}\right) = 0, \tag{4.2.10b}$$

at $Z = \pm\frac{1}{2}$:

$$\frac{\partial z^{(0)}}{\partial Z}\left(\frac{\mathrm{d}r^{(0)}}{\mathrm{d}R}\frac{\mathrm{d}r^{(1)}}{\mathrm{d}R} - \frac{\mathscr{P}^{(1)}}{4W_1}\right) = 0, \tag{4.2.10c}$$

Equation (4.2.10c) holds for all Z; however, all other terms except $\mathscr{P}^{(1)}$ are independent of Z. We hence conclude, $\mathscr{P}^{(1)}(R)$. In view of which, the boundary conditions (4.2.10b) and (4.2.10c) provide

$$\mathscr{P}^{(1)}(R) = 4W_1 \frac{\partial z^{(0)}}{\partial Z}\frac{\partial z^{(1)}}{\partial Z}, \tag{4.2.11a}$$

$$\mathscr{P}^{(1)}(R_{\text{in}}) = 4W_1 \left.\frac{\mathrm{d}r^{(0)}}{\mathrm{d}R}\right|_{R=R_{\text{in}}} \left.\frac{\mathrm{d}r^{(1)}}{\mathrm{d}R}\right|_{R=R_{\text{in}}}. \tag{4.2.11b}$$

To summarise, we have reduced the problem to two leading order variables; the radial deformation, $r^{(0)}(R)$, and the axial stretch, $\lambda_z^{(0)}(R)$, and obtained the governing equation (4.2.4a) and the boundary conditions (4.2.8b) and (4.2.5). However, we require a second governing equation to determine the two unknows, $r^{(0)}(R)$ and $\lambda_z^{(0)}(R)$. Therefore, we consider the $\mathcal{O}(\varepsilon^2)$ momentum equations (3.1.54) which read

$$\begin{aligned}\left(\frac{\partial^2 z^{(0)}}{\partial R \partial Z} + \frac{R}{{r^{(0)}}^2}\right)\left(\frac{\mathrm{d}r^{(0)}}{\mathrm{d}R}\right)^2 - \frac{1}{2W_1}\frac{\partial z^{(0)}}{\partial Z}\frac{\mathrm{d}\mathscr{P}^{(0)}}{\mathrm{d}R} \\ -\frac{W_1 + W_4^{(0)}}{W_1 R} + 2\left(\frac{\partial z^{(0)}}{\partial Z}\right)^{-1}\left(\frac{R}{{r^{(0)}}^2} - \right. \\ \left. \frac{R^2}{{r^{(0)}}^3}\frac{\mathrm{d}r^{(0)}}{\mathrm{d}R} - \frac{R}{r^{(0)}}\frac{\mathrm{d}r^{(0)}}{\mathrm{d}R}\frac{\partial^2 z^{(0)}}{\partial R \partial Z}\right) = 0,\end{aligned} \tag{4.2.12a}$$

$$\begin{aligned}\frac{\mathrm{d}r^{(0)}}{\mathrm{d}R}\left(-\frac{1}{2W_1}\frac{\partial \mathscr{P}^{(2)}}{\mathrm{d}Z} + 2\frac{\partial z^{(0)}}{\partial Z}\frac{\partial^2 z^{(2)}}{\partial Z^2} + \frac{\partial z^{(0)}}{\partial R}\frac{\partial^2 z^{(0)}}{\partial R^2}\right. \\ \left. + \frac{\partial z^{(0)}}{\partial R}\frac{\partial^2 z^{(0)}}{\partial R \partial Z} + \frac{1}{r^{(0)}}\frac{\mathrm{d}r^{(0)}}{\mathrm{d}R}\frac{\partial z^{(0)}}{\partial Z}\frac{\partial z^{(0)}}{\partial R}\right) + \frac{\partial z^{(0)}}{\partial Z}\frac{\partial z^{(0)}}{\partial R}\frac{\mathrm{d}^2 r^{(0)}}{\mathrm{d}R^2} = 0.\end{aligned} \tag{4.2.12b}$$

Equation (4.2.12a) closes the leading order problem. Equation (4.2.12b) introduces higher order terms which are not of interest for the leading order problem and is therefore not needed here.

Substituting (4.2.7) and (4.2.8a) into (4.2.12a) provides an equation for $\lambda_z^{(0)}$ and

hence, together with (4.2.4a), we obtain the following pair of coupled ODEs:

$$\frac{\mathrm{d}r^{(0)}}{\mathrm{d}R} = \frac{R}{r^{(0)}{\lambda_z}^{(0)}}, \tag{4.2.13a}$$

$$\begin{aligned}\frac{\mathrm{d}{\lambda_z}^{(0)}}{\mathrm{d}R} = \frac{R}{R^2 + 2{r^{(0)}}^2{\lambda_z^{(0)}}^4}\Bigg(2{\lambda_z}^{(0)} - \frac{R^2}{{r^{(0)}}^2} \\ - \left(1 + \frac{W_4^{(0)}}{W_1}\right)\frac{{r^{(0)}}^2{\lambda_z^{(0)}}^2}{R^2}\Bigg).\end{aligned} \tag{4.2.13b}$$

Together with the boundary condition (4.2.5) and the relation (4.2.5), this provides a boundary value problem that describes the leading order radial and axial deformation, and from which the leading order Cauchy stress components for the whole tissue and each of the constituents follow directly. We note that the boundary condition (4.2.8b) on $\lambda_z^{(0)}$ is posed at the (unknown) deformed inner radius. We therefore solve (4.2.13) numerically by treating $r^{(0)}(R_{\mathrm{in}})$ as a shooting parameter and seek the solution set $r^{(0)}$, $\lambda_z^{(0)}$ and R_{in} that satisfies (4.2.13), (4.2.5) and (4.2.8b) (details in Appendix B.2.1).

4.3 Suitability of approximations

In this section we compare numerical simulations of the full model with those of the membrane model and the thin-PCLS-limit model to demonstrate their validity. To recap, the governing equations of the full model are

$$\begin{aligned}&\frac{\partial z}{\partial Z}\frac{\partial}{\partial R}\left[\left(\frac{\partial r}{\partial Z}\right)^2\right] - \frac{\partial z}{\partial R}\frac{\partial}{\partial Z}\left[\left(\frac{\partial r}{\partial Z}\right)^2\right] \\ &\quad + \frac{\partial r}{\partial R}\frac{\partial}{\partial Z}\left[\frac{\partial r}{\partial Z}\frac{\partial z}{\partial Z}\right] - \frac{\partial r}{\partial Z}\frac{\partial}{\partial R}\left[\frac{\partial r}{\partial Z}\frac{\partial z}{\partial Z}\right] \\ &\quad\quad + \frac{1}{r}\left(\frac{\partial r}{\partial R}\frac{\partial z}{\partial Z} - \frac{\partial r}{\partial Z}\frac{\partial z}{\partial R}\right)\left(\frac{\partial r}{\partial Z}\right)^2 \\ &\quad + \varepsilon^2\frac{\partial z}{\partial Z}\frac{\partial}{\partial R}\left[\left(\frac{\partial r}{\partial R}\right)^2\right] - \varepsilon^2\frac{\partial z}{\partial R}\frac{\partial}{\partial Z}\left[\left(\frac{\partial r}{\partial R}\right)^2\right] \\ &\quad\quad + \varepsilon^2\frac{\partial r}{\partial R}\frac{\partial}{\partial Z}\left[\frac{\partial r}{\partial R}\frac{\partial z}{\partial R}\right] - \varepsilon^2\frac{\partial r}{\partial Z}\frac{\partial}{\partial R}\left[\frac{\partial r}{\partial R}\frac{\partial z}{\partial R}\right] \\ &\quad\quad\quad + \frac{\varepsilon^2}{2W_1}\frac{\partial z}{\partial R}\frac{\partial \mathscr{P}}{\partial Z} - \frac{\varepsilon^2}{2W_1}\frac{\partial z}{\partial Z}\frac{\partial \mathscr{P}}{\partial R}\end{aligned}$$

$$
\begin{aligned}
&+\frac{\varepsilon^2}{r}\left(\frac{\partial r}{\partial R}\frac{\partial z}{\partial Z}-\frac{\partial r}{\partial Z}\frac{\partial z}{\partial R}\right)\left(\frac{\partial r}{\partial R}\right)^2\\
&-\frac{\varepsilon^2(W_1+W_4)r}{W_1R^2}\left(\frac{\partial r}{\partial R}\frac{\partial z}{\partial Z}-\frac{\partial r}{\partial Z}\frac{\partial z}{\partial R}\right)=0, \qquad (4.3.1a)\\
&\frac{\partial r}{\partial R}\frac{\partial}{\partial Z}\left[\left(\frac{\partial z}{\partial Z}\right)^2\right]-\frac{\partial r}{\partial Z}\frac{\partial}{\partial R}\left[\left(\frac{\partial z}{\partial Z}\right)^2\right]\\
&+\frac{\partial z}{\partial Z}\frac{\partial}{\partial R}\left[\frac{\partial z}{\partial Z}\frac{\partial r}{\partial Z}\right]-\frac{\partial z}{\partial R}\frac{\partial}{\partial Z}\left[\frac{\partial z}{\partial Z}\frac{\partial r}{\partial Z}\right]\\
&+\frac{1}{r}\left(\frac{\partial r}{\partial R}\frac{\partial z}{\partial Z}-\frac{\partial r}{\partial Z}\frac{\partial z}{\partial R}\right)\frac{\partial z}{\partial Z}\frac{\partial r}{\partial Z}+\frac{1}{2W_1}\frac{\partial r}{\partial Z}\frac{\partial \mathscr{P}}{\partial R}\\
&-\frac{1}{2W_1}\frac{\partial r}{\partial R}\frac{\partial \mathscr{P}}{\partial Z}+\varepsilon^2\frac{\partial r}{\partial R}\frac{\partial}{\partial Z}\left[\left(\frac{\partial z}{\partial R}\right)^2\right]\\
&-\varepsilon^2\frac{\partial r}{\partial Z}\frac{\partial}{\partial R}\left[\left(\frac{\partial z}{\partial R}\right)^2\right]+\varepsilon^2\frac{\partial z}{\partial Z}\frac{\partial}{\partial R}\left[\frac{\partial r}{\partial R}\frac{\partial z}{\partial R}\right]\\
&-\varepsilon^2\frac{\partial z}{\partial R}\frac{\partial}{\partial Z}\left[\frac{\partial r}{\partial R}\frac{\partial z}{\partial R}\right]+\frac{\varepsilon^2}{r}\left(\frac{\partial r}{\partial R}\frac{\partial z}{\partial Z}-\frac{\partial r}{\partial Z}\frac{\partial z}{\partial R}\right)\frac{\partial r}{\partial R}\frac{\partial z}{\partial R}=0, \qquad (4.3.1b)\\
&\frac{r}{R}\left(\frac{\partial r}{\partial R}\frac{\partial z}{\partial Z}-\frac{\partial r}{\partial Z}\frac{\partial z}{\partial R}\right)=1, \qquad (4.3.1c)
\end{aligned}
$$

subject to the boundary conditions

$$
r(1,Z)=r_{\text{dis}}, \qquad (4.3.2a)
$$

at $Z=\pm\frac{1}{2}$:

$$
\begin{aligned}
&\frac{\partial r}{\partial R}\frac{\partial r}{\partial Z}\frac{\partial z}{\partial Z}-\frac{\partial z}{\partial R}\left(\frac{\partial r}{\partial Z}\right)^2+\frac{\varepsilon^2\mathscr{P}}{2W_1}=0, \qquad (4.3.2b)\\
&\frac{\partial r}{\partial R}\left(\frac{\partial z}{\partial Z}\right)^2-\frac{\partial z}{\partial R}\frac{\partial r}{\partial Z}\frac{\partial z}{\partial Z}-\frac{\mathscr{P}}{2W_1}\frac{\partial r}{\partial R}=0; \qquad (4.3.2c)
\end{aligned}
$$

at $R=R_{\text{in}}$:

$$
\begin{aligned}
&\frac{\partial r}{\partial R}\frac{\partial r}{\partial Z}\frac{\partial z}{\partial R}-\frac{\partial z}{\partial Z}\left(\frac{\partial r}{\partial R}\right)^2+\frac{\mathscr{P}}{2W_1}\frac{\partial z}{\partial Z}=0, \qquad (4.3.2d)\\
&-\frac{\mathscr{P}}{2W_1}\frac{\partial r}{\partial Z}-\varepsilon^2\frac{\partial r}{\partial R}\frac{\partial z}{\partial R}\frac{\partial z}{\partial Z}+\varepsilon^2\frac{\partial r}{\partial Z}\left(\frac{\partial z}{\partial R}\right)^2=0, \qquad (4.3.2e)
\end{aligned}
$$

and where derivatives of the strain-energy function, W, in terms of the deformed radius, r, and undeformed radius, R, are

$$W_1 = \Phi_c \frac{1}{2}, + \Phi_m \frac{\mu}{2}, \tag{4.3.3a}$$

$$\begin{aligned} W_4 = \Phi_c \frac{\alpha}{2} + \Phi_m \omega \left(\left(\frac{r}{R} \right)^2 - 1 \right) \\ \times H \left(\left(\frac{r}{R} \right)^2 - 1 \right) \exp \left(\zeta \left(\left(\frac{r}{R} \right)^2 - 1 \right)^2 \right). \end{aligned} \tag{4.3.3b}$$

The membrane model solves

$$\frac{\mathrm{d}r}{\mathrm{d}R} = \frac{R}{r}, \tag{4.3.4a}$$

$$\frac{\mathrm{d}\sigma_{rr}}{\mathrm{d}R} = \frac{2}{R} \left(W_1 + W_4 - \frac{W_1 R^4}{r^4} \right), \tag{4.3.4b}$$

subject to the boundary conditions

$$r(1) = r_{\mathrm{dis}}, \tag{4.3.5}$$

$$\sigma_{rr}(R_{\mathrm{in}}) = 0. \tag{4.3.6}$$

Finally, the thin-PCLS-limit model solves the coupled ODEs

$$\frac{\mathrm{d}r^{(0)}}{\mathrm{d}R} = \frac{R}{r^{(0)} {\lambda_z}^{(0)}}, \tag{4.3.7a}$$

$$\begin{aligned} \frac{\mathrm{d}{\lambda_z}^{(0)}}{\mathrm{d}R} = \frac{R}{R^2 + 2 {r^{(0)}}^2 {\lambda_z^{(0)}}^4} \left(2 {\lambda_z}^{(0)} - \frac{R^2}{{r^{(0)}}^2} \right. \\ \left. - \left(1 + \frac{W_4^{(0)}}{W_1} \right) \frac{{r^{(0)}}^2 {\lambda_z^{(0)}}^2}{R^2} \right), \end{aligned} \tag{4.3.7b}$$

subject to the boundary conditions

$$r^{(0)}(1) = r_{\mathrm{dis}}, \tag{4.3.8}$$

$$\lambda_z^{(0)}(R_{\mathrm{in}}) = \sqrt{\frac{R_{\mathrm{in}}}{r^{(0)}(R_{\mathrm{in}})}}, \tag{4.3.9}$$

where the leading order derivative of strain-energy function with respect to the fourth invariant, $W_4^{(0)}$, in terms of the leading order deformed radius, $r^{(0)}$, and

undeformed radius, R, is

$$W_4^{(0)} = \Phi_c \frac{\alpha}{2} + \Phi_m \omega \left(\left(\frac{r^{(0)}}{R} \right)^2 - 1 \right) \mathrm{H}\left({r^{(0)}}^2 - R^2 \right) \tag{4.3.10}$$

$$\times \exp\left(\zeta \left(\left(\frac{r^{(0)}}{R} \right)^2 - 1 \right)^2 \right). \tag{4.3.11}$$

We plot the radial deformation, r, axial deformation, z, and the corresponding stresses, $\boldsymbol{\sigma}$, obtained in all three models, both in the presence and absence of active contractile force in Figure 4.3. Results from the full and thin-PCLS models in Figure 4.3 are plotted as functions of radius at the undeformed axial centre line, *i.e.* at $Z = 0$, apart from the axial deformation, z, which we plot as a function of radius at the undeformed upper surface of the PCLS, *i.e.* at $Z = \pm\frac{1}{2}$, in order to illustrate the thinning of the PCLS in response to stretch. Those from the membrane case, however, do not depend on Z; for illustrative purposes, we plot z fixed at $Z = \pm\frac{1}{2}$ in order to emphasise the thinning of the PCLS (relative to the reference configuration) that is displayed by the full and thin-PCLS models.

We find that, despite its relative mathematical and computational simplicity, the thin-PCLS-limit provides an excellent approximation to the full model, showing good quantitative agreement in all variables. In contrast, the membrane model is unable to replicate the full model behaviour. The one-dimensional geometry of the membrane approximation constrains the inner radius of the membrane to deform corresponding to the displaced outer boundary in order to preserve incompressibility. As a result, we observe an increased radial deformation and elevated radial and circumferential stress in the membrane approximation compared to the thin-PCLS-limit approximation and the full model (Figures 4.3 (i)–(ii), (v)–(viii), respectively). Whereas, the thickness of the PCLS in both the full model and the thin-PCLS-limit allows the generated stresses to be absorbed by the axial deformation (Figures 4.3 (iii), (iv)). Hence, the thin-PCLS-limit provides a more realistic representation of the full problem (for small ε) than the membrane.

Active contraction accentuates the radial deformation of the PCLS and the thic-

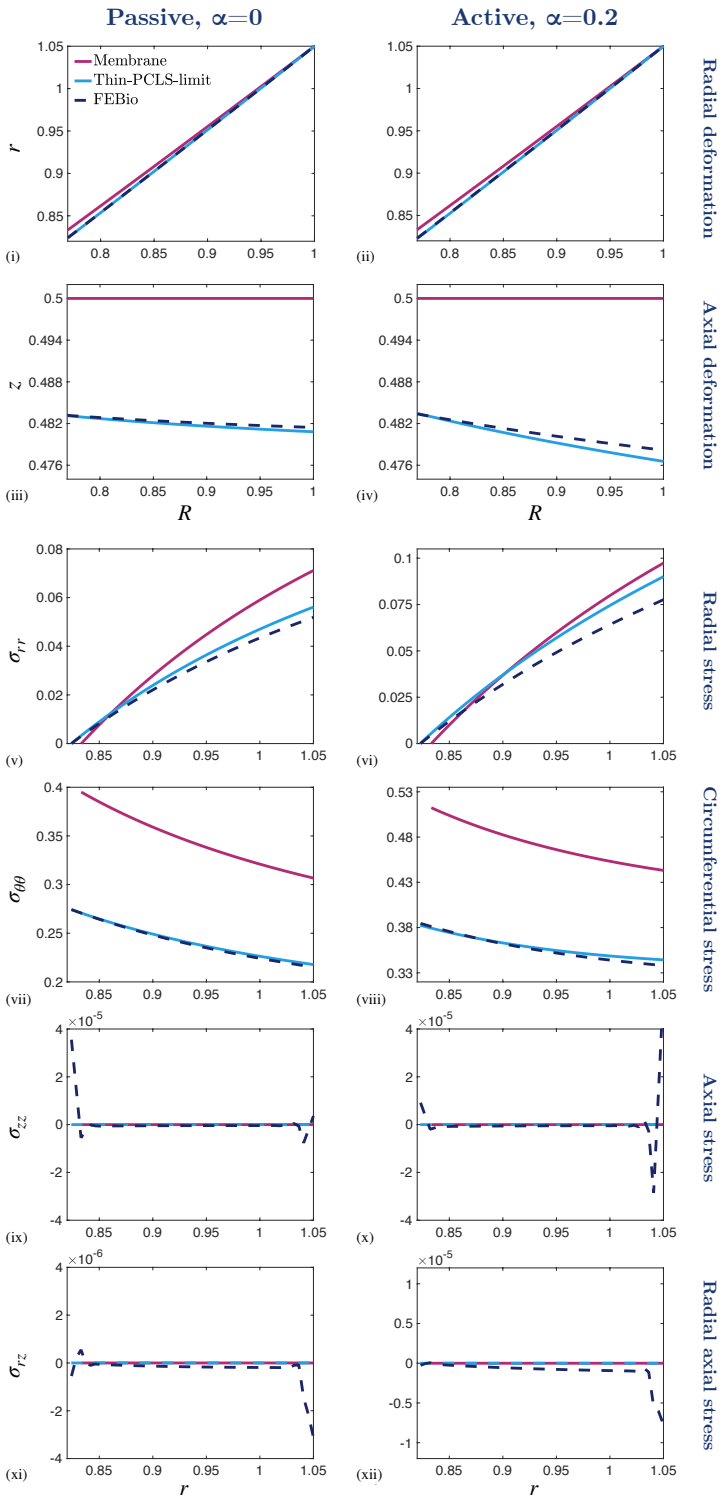

Figure 4.3: Radial displacement, r, axial displacement, z, and Cauchy stress components, $\boldsymbol{\sigma}$, plotted as functions of undeformed radius, R, and deformed radius, r, at the undeformed centre of the PCLS ($Z = 0$), respectively. A 5% fixed stretch is applied to the PCLS in the passive, $\alpha = 0$, (1^{st} column) and active, $\alpha = 0.2$, (2^{nd} column) case. The aspect ratio $\varepsilon = 0.01$ throughout and the remaining parameter values are provided in Table C.4 in Appendix C.2.

kness of the PCLS decreases accordingly in order to maintain tissue incompressibility (*cf.* Figures 4.3 (iii), (iv)). This feature is only observed in the full model and the thin-PCLS-limit. Further contraction-induced deformation is not permitted in the membrane approximation due to the one-dimensional geometry and incompressibility constraint, and as a result, active contraction simply increases the stress generated in the membrane. Hence, there are significant qualitative and quantitative differences observed in the stress distributions of the two approximations and only the thin-PCLS-limit provides a suitable approximation to the full model.

The full model exhibits rapid variation in the axial and shear stress components near the inner and outer airway radii (Figures 4.3 (ix), (xii)). However, this (small-amplitude) boundary layer behaviour in the axial and shear stress components near the airway boundaries (that is evident in the full model) is not captured by either of the simple models. Therefore, a boundary layer analysis of these features forms a natural future extension of this work.

4.4 Thin-PCLS-limit parameter exploration

In the preceding numerical experiments, our parameter choices follow that of Hill et al. (2018) or are estimated from the literature and by our collaborators (Tatler 2016). The parameter values are provided in Table C.5 in Appendix C.2. In this section we take advantage of the computational tractability of our reduced model (4.2.13) to explore the influence of the airway's mechanical properties on the model behaviour, and in particular, examine differences in the constituents' stresses that cause TGF-β activation. Such parameter searches are computationally prohibitive in the full model.

In Section 3.1.3, we proposed that the difference in constituent von Mises stress is a convenient way to represent the mechanical activation of TGF-β (given that we are using constrained mixture theory). Hence, in this section we present example simulations showing the constituents' von Mises stress; as well as the deformation variables and associated tissue stress components. In the following chapter, the difference in constituent von Mises stress is a crucial quantity for our model development.

4.4.1 Effect of increasing imposed stretch amplitude

The effect of the imposed radial displacement on the constituent stress, in the absence of contraction, is illustrated in Figures 4.4 and 4.5. Here, we increase the fixed stretch applied from 0% (unstretched) to 20%. Over this range, we observe a significant increase in stress heterogeneity, with high radial (circumferential) stresses evident at the outer (inner) airway wall (Figure 4.4).

For both the ASM and ECM components, we see that the distribution of the von Mises stress follows that of the circumferential stress since the contributions from the circumferential stress dominate those from the radial stress (*cf.* Figures 4.4 (x), (xiii) and (xvi) for example). This is to be expected in the passive case due to the strain-stiffening of the ECM that occurs in direction of the circumferential fibres when stretched. However, we see that increasing the stiffness of ECM relative to that of ASM (μ) dramatically alters the distribution of the constituent radial stress (*cf.* Figures 4.4 (i), (iii) and (x), (xii)) and consequently, the absolute difference in constituent von Mises stress (*cf.* Figures 4.5 (iv), (vi)).

As the imposed radial stretch is increased from zero, the axial deformation becomes less uniform across the airway thickness (Figures 4.5 (i)–(iii)). Moreover, we observe that the heterogeneity of the axial thinning with increasing stretch is exaggerated with ECM compliance (*cf.* Figures 4.9 (i), (iii)). This suggests that the stiffness of the ECM provides resistance to the imposed stretch across the airway wall, in addition to the associated strain-stiffening. As a result, the profile of the PCLS is more uniform for stiff ECM and thicker (thinner) at the inner (outer) radius for compliant ECM.

The stiffness of the ECM in the PCLS also has strong implications on the difference in constituent von Mises stress. When the ECM is relatively compliant, the stress state of the ASM is higher than that of the ECM for small stretches (due to the passive isotropic material properties, *i.e.* μ) (*cf.* Figures 4.4 (x), (xvi)). However, strain-stiffening of the ECM occurs exponentially with stretch (refer to the strain-energy function for the ECM in (3.1.41b)) and as a result, the stress state of the ECM increases more significantly with stretch than that of the ASM. Therefore, we observe the difference in constituent von Mises stress initially decrease with stretch, before increasing as ECM dominates at high amplitudes

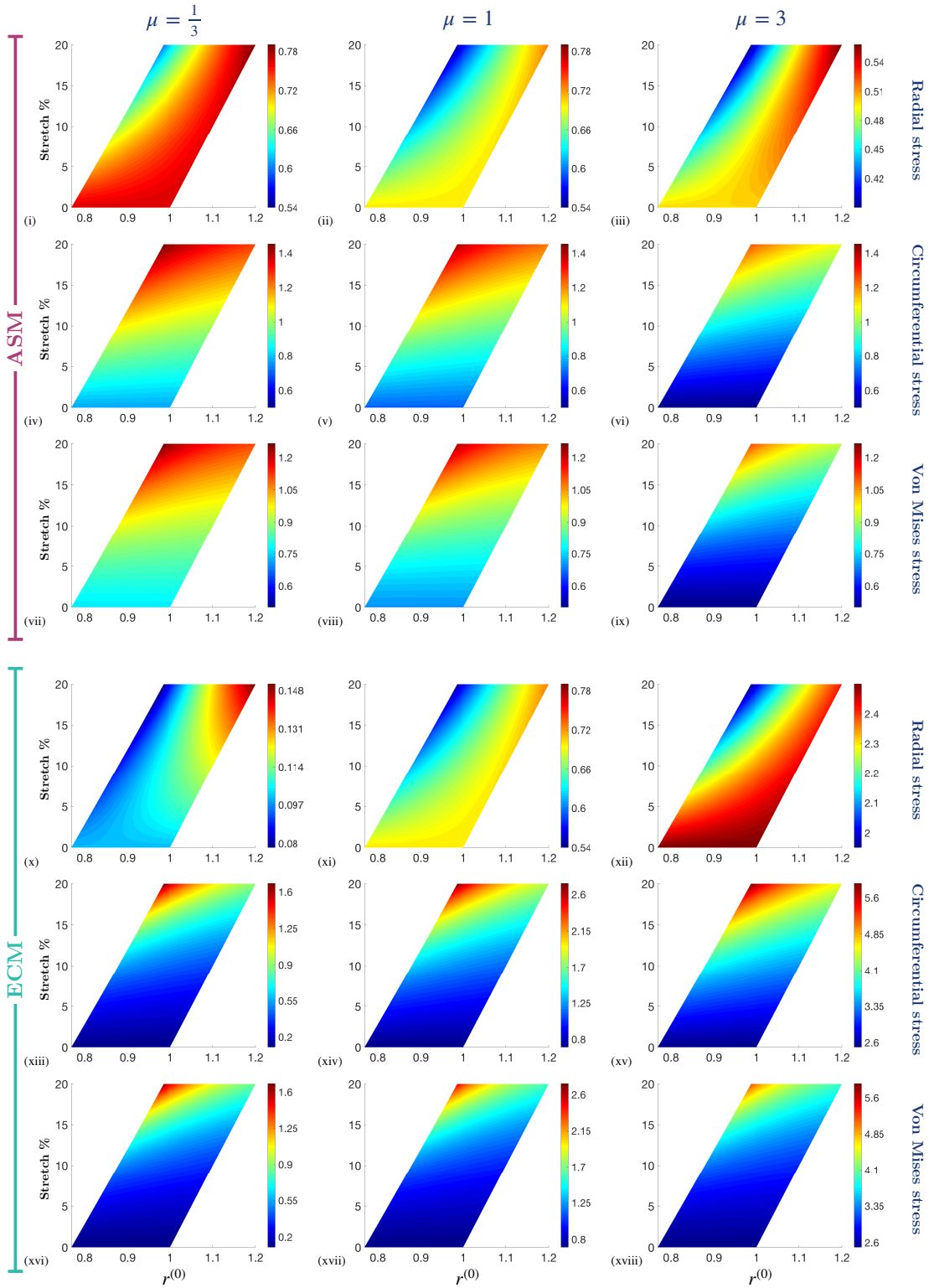

Figure 4.4: Effect of stretch on constituent stress components, $\boldsymbol{\sigma}_c$ and $\boldsymbol{\sigma}_m$, as a function of deformed radius, $r^{(0)}$, for different stiffnesses of ECM relative to that of ASM, μ. Simulated parameter values are provided in Table C.5 in Appendix C.2.

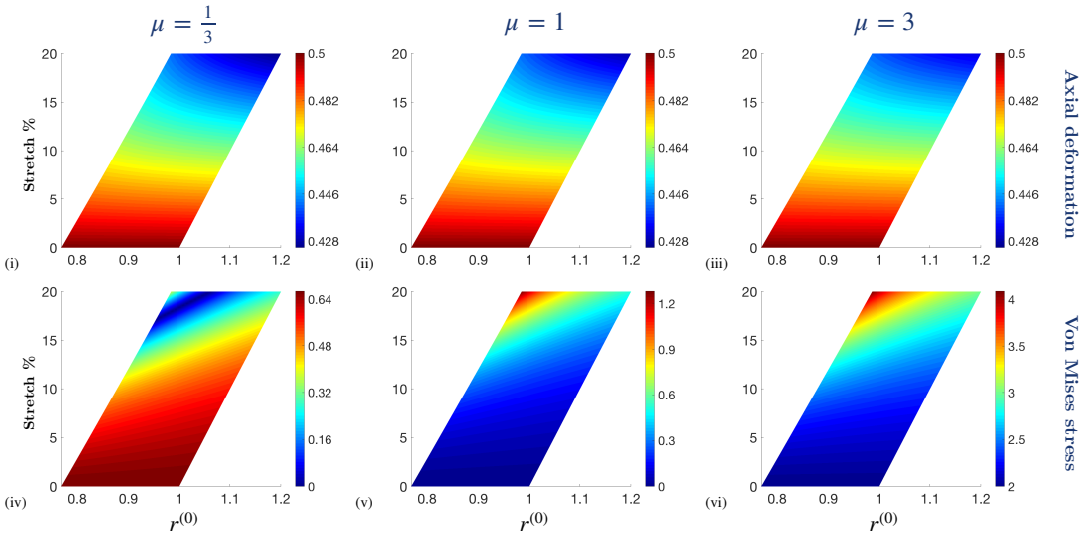

Figure 4.5: Effect of stretch on the axial deformation at the upper surface, $z^{(0)}(R, \frac{1}{2})$, and the absolute difference in constituent von Mises stress, σ_{dif} (3.1.53), as a function of deformed radius, $r^{(0)}$, for different stiffnesses of ECM relative to that of ASM, μ. Simulated parameter values are provided in Table C.5 in Appendix C.2.

of imposed stretch (Figure 4.5 (iv)). Conversely, when the ECM is of equal stiffness or stiffer than the ASM, the difference in constituent stress increases with stretch (Figures 4.5 (v), (vi)). In the following sections we investigate if such features persist in the presence of contractile force generated by the ASM.

4.4.2 Effect of increasing smooth muscle contraction

The influence of ASM contractility on the airway constituent stress and deformation, at fixed imposed stretch, is illustrated in Figures 4.6 and 4.7. As expected, increasing the contractile force generation of the ASM leads to significant radial contraction of the airway, and associated resistance to axial thinning at the inner radius (Figures 4.7 (i)–(iii)). Correspondingly, we observe elevated and increasingly non-uniform radial stress of the ASM and ECM constituents in Figures 4.6 (i)–(iii) and (x)–(xii), respectively.

In general, the stress distributions are qualitatively similar, with a small stress increase at a larger fixed stretch. The circumferential stress, and correspondingly the von Mises stress, of the ECM are exceptions to this general observation and display significantly different heterogeneous distributions for each

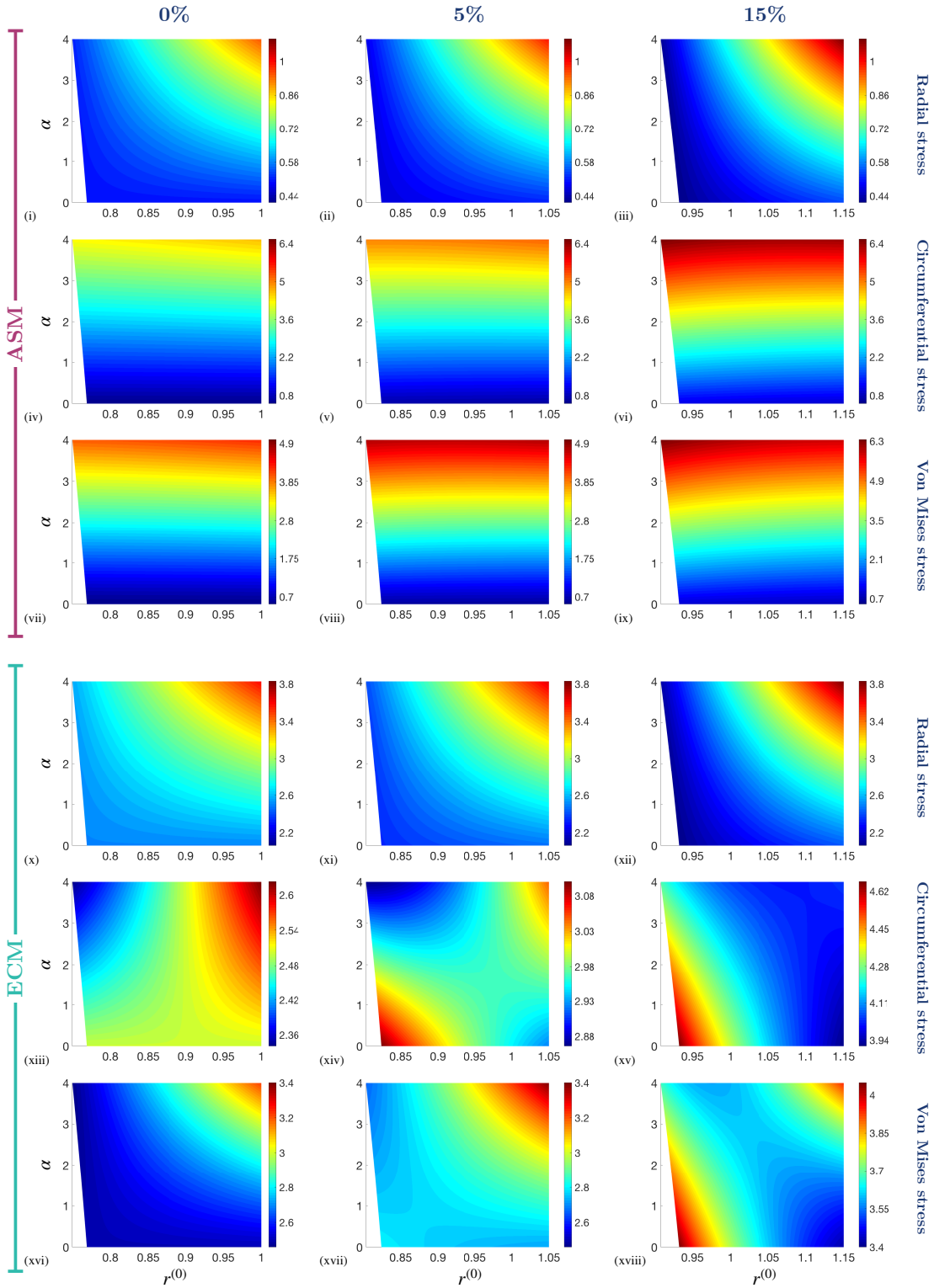

Figure 4.6: Effect of constant contraction, α, on constituent stress components, $\boldsymbol{\sigma}_c$ and $\boldsymbol{\sigma}_m$, as a function of deformed radius, $r^{(0)}$, in the presence and absence of fixed stretch. Simulated parameter values are provided in Table C.5 in Appendix C.2.

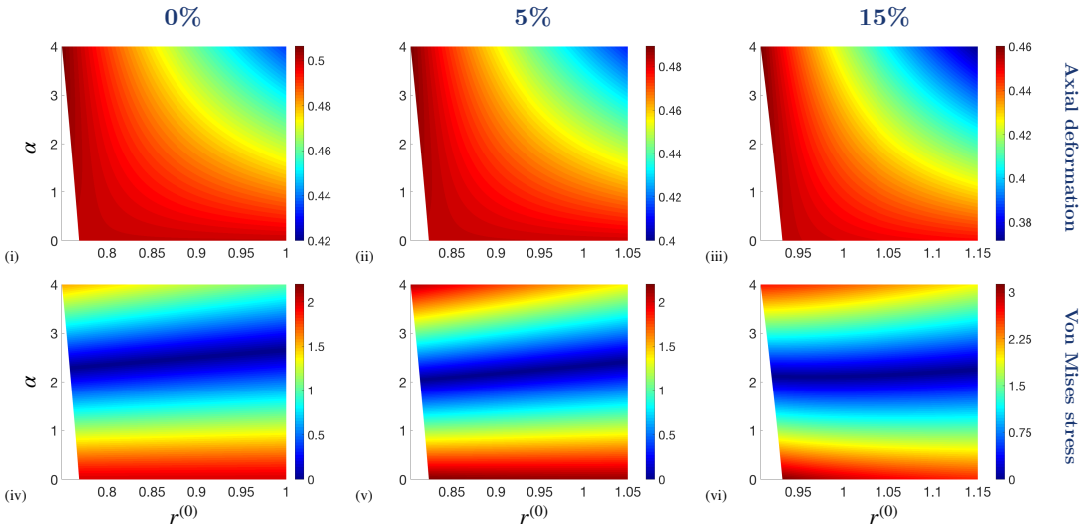

Figure 4.7: Effect of constant contraction, α, on the axial deformation at the upper surface, $z^{(0)}(R, \frac{1}{2})$, and the absolute difference in constituent von Mises stress, σ_{dif} (3.1.53), as a function of deformed radius, $r^{(0)}$, in the presence and absence of fixed stretch. Simulated parameter values are provided in Table C.5 in Appendix C.2.

imposed fixed stretch (*cf.* Figures 4.6 (xiii), (xiv) and (xv)). More specifically, in the absence of stretch, the circumferential stress of the ECM is maximal at the outer radius when the contractility of the ASM is high (Figure 4.6 (xiii)). Whereas in the the presence of a 15% stretch, the circumferential stress of the ECM is maximal at the inner radius and when there is no contractile force generated by the ASM (Figure 4.6 (xiii)). The evident transition between these two modes is observed in Figure 4.6 (xiv).

Unlike our previous observations for increasing stretch in Figure 4.4, we see that increasing the contractile force generated by the ASM leads to comparable radial and circumferential stress components of the ECM (Figure 4.6). As a result, features of both the radial and circumferential components are captured in the von Mises stress distribution of the ECM (*e.g.* Figures 4.6 (xii), (xv) and (xviii)). We see that the difference in the constituent von Mises stress initially decreases as contraction of the ASM increases (Figures 4.7 (iv)–(vi)). Here, the increasing contractile force generation by the ASM and the stiff (strain-stiffened when stretched) ECM means that the constituents become comparably stressed. The von Mises stress of the ASM and ECM then equalises before the difference in constituent von Mises stress begins to increase with contraction of the ASM (Figures 4.7 (iv)–(vi)). This observation holds in each instance of imposed

stretch, and is exaggerated with increasing stretch (*cf.* Figures 4.7 (iv), (vi)).

Our results suggest that, in order to activate TGF-β efficiently, the ASM may act in one of two ways: firstly as a (relatively) passive component, to allow for the difference in constituent von Mises stress to be driven by the stiffness and additional strain-stiffening of the ECM with imposed stretch, and secondly, as a highly contracted component in order to dominate over the stress contributions of the stiffened ECM. In light of such findings, we move on to investigate the effect of increasing the isotropic stiffness of the ECM in the presence of contractile force generated by the ASM.

4.4.3 Effect of increasing extracellular matrix isotopic stiffness

The influence of constituent stiffness on the airway wall stress and deformation, at fixed imposed stretch, is illustrated in Figures 4.8 and 4.9. The ratio of the passive isotropic stiffness of ECM to that of the ASM is given by μ. The ECM is more compliant than the ASM for $\mu < 1$, stiffer than the ASM for $\mu > 1$, and the same stiffness as the ASM for $\mu = 1$. In this section, we increase μ in the presence of a constant active contractile force generated by the ASM, α.

When the ECM is more compliant than the ASM ($\mu < 1$) we observe a slight reduction in radial contraction compared to the case for which the ECM stiffness exceeds that of the ASM ($\mu > 1$). Correspondingly, there is an increased resistance to axial thinning with increasing μ observed in Figures 4.9 (i)–(iii). As a result, we see that the magnitude of the stress components of the ASM decrease with increasing μ (due to the decreased radial contraction), whilst the magnitude of the stress components of the ECM increase with increasing μ (*cf.* Figures 4.8 (v), (xiv)). These observations persist and are emphasised under the application of fixed stretch (due to additional strain-stiffening of the ECM when stretched).

In general, we see that the stress distributions of the ASM display greater non-uniformity across the airway radius than that of the ECM, particularly when stretched. For example, the von Mises stress (predominately influenced by the circumferential stress) of the ASM and ECM differ significantly (*cf.* Figures 4.8 (ix), (xviii)). As the stiffness of the ECM increases, the von Mises stress of the

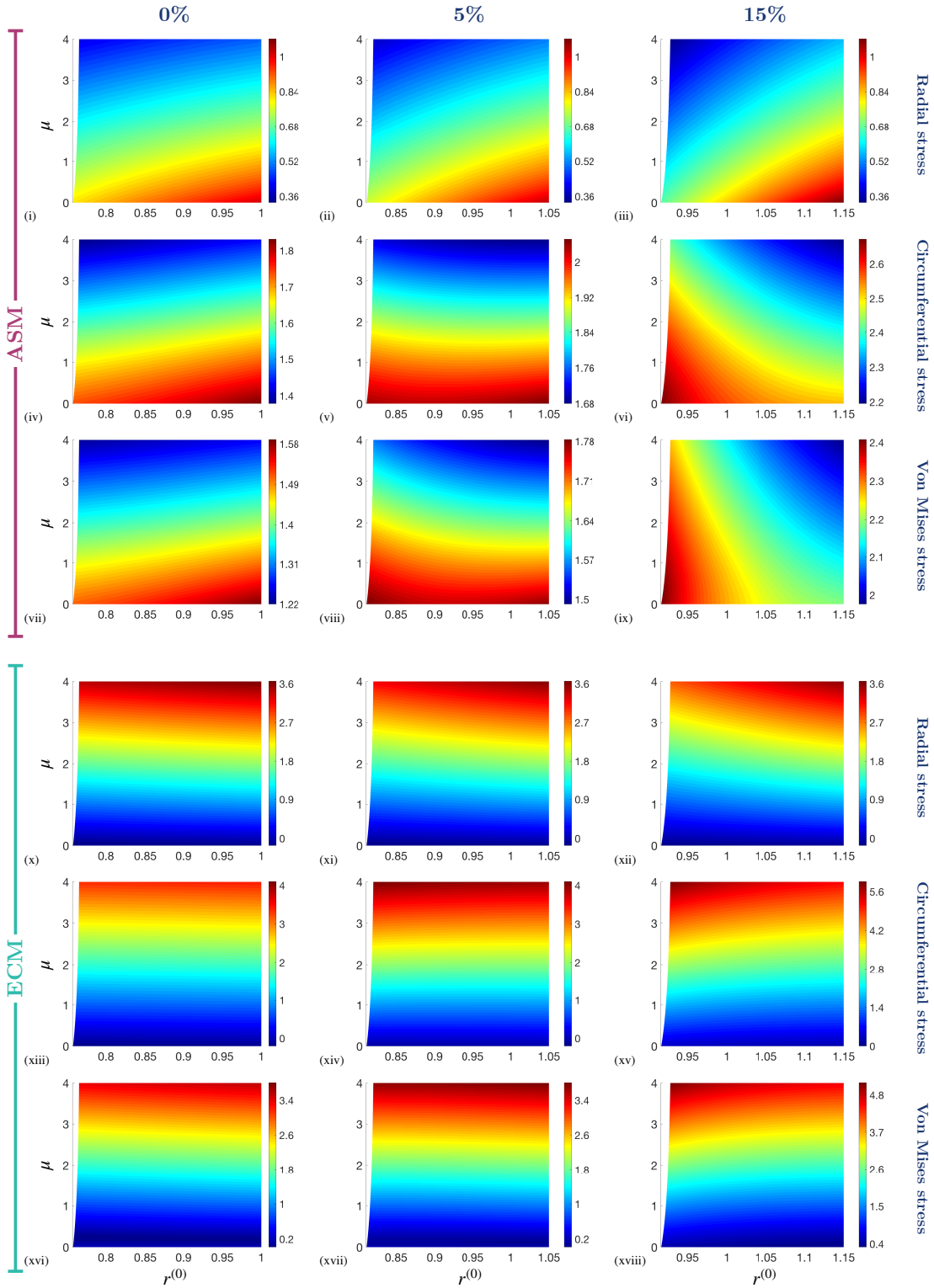

Figure 4.8: Effect of the stiffness of ECM relative to that of ASM, μ, on constituent stress components, $\boldsymbol{\sigma}_c$ and $\boldsymbol{\sigma}_m$, as a function of deformed radius, $r^{(0)}$, in the presence and absence of fixed stretch. Simulated parameter values are provided in Table C.5 in Appendix C.2.

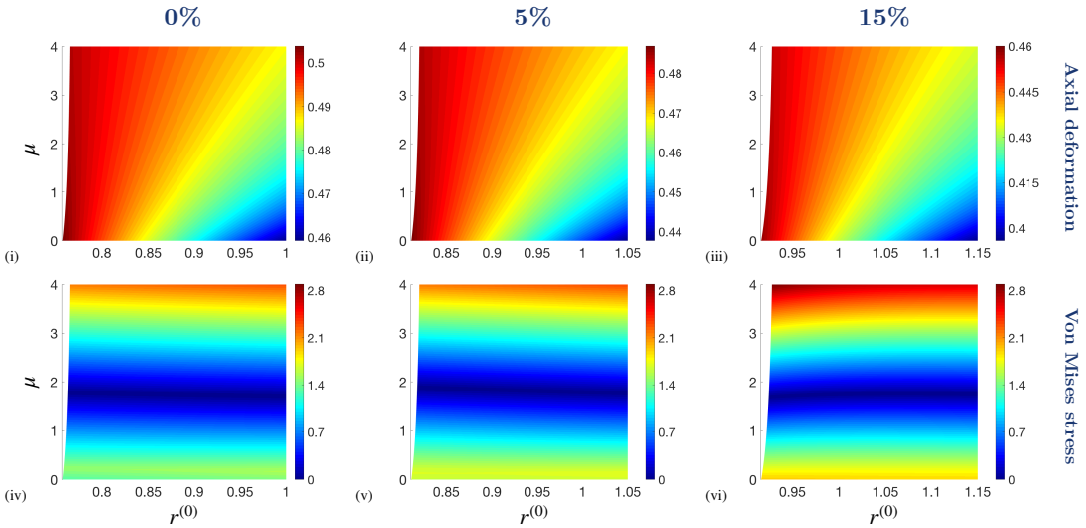

Figure 4.9: Effect of the stiffness of ECM relative to that of ASM, μ, on axial deformation, z, and the absolute difference in constituent von Mises stress, σ_{dif} (3.1.53), as a function of deformed radius, $r^{(0)}$, in the presence and absence of fixed stretch. Simulated parameter values are provided in Table C.5 in Appendix C.2.

ASM remains higher at the outer radius than at the inner radius in the absence of stretch (Figure 4.8 (vii)). In the presence of a 15% amplitude stretch, however, the von Mises stress of the ASM varies significantly across the airway wall and is higher at the inner radius than at the outer radius (Figure 4.8 (ix)). Therefore, imposed stretch induces a dramatic change in the distribution of the von Mises stress of the ASM and the apparent transition between these two extremes is observed in Figure 4.8 (viii). This behaviour is similar to that exhibited by the ECM when increasing the contractile force generated by the ASM in Figures 4.6 (xiii)–(xviii).

As a result, we see a larger difference in constituent von Mises stress with increasing μ when stretched (Figure 4.9 (vi)). Note that the von Mises stress of the ASM is not equal to that of the ECM at $\mu = 1$ (despite having the same isotropic stiffness) due to the active contractile force generated by the ASM. Therefore, we see that the absolute difference in constituent von Mises stress initially decreases with increasing μ as the ECM and the ASM become comparably stressed. Once equalised, the difference in constituent von Mises stress increases with μ (Figures 4.9 (iv)–(vi)). Therefore, consistent with that in Section 1.1.4 (*i.e.* inline with experimental intuition), our findings suggest that in the presence of contractile force generated by the ASM, the ECM is required

to be sufficiently stiff in order to mechanically activate TGF-β. Moreover, imposed stretch enhances the mechanical activation of TGF-β due to the increased strain-stiffening of ECM that extenuates the difference in the constituents von Mises stress.

4.5 Summary

In this chapter we have presented two reductions of the full model of the experimentally stretched PCLS that was introduced in Chapter 3 (that balances linear momentum (3.1.55) and satisfies tissue incompressibility (3.1.56), subject to the imposed radial stretch (3.1.57) at the outer radius, R_{out}, and the free boundary conditions (3.1.60) at the upper, lower and inner surfaces of the PCLS). Initially, we adopted a membrane representation (where axial variation is neglected *a priori*, and the PCLS thickness remains unchanged upon deformation). Secondly, and in view of the typical dimensions of the PCLS and numerical evidence, we considered an asymptotic reduction, appropriate for the limit in which the PCLS thickness is much smaller than the typical airway radius (*i.e.* $0 < \varepsilon \ll 1$), and in which we are able to retain a description of the radial and axial airway deformation and the associated stresses. In each case, the model reduces to one spatial dimension; the membrane model admits analytical solutions, while in thin-PCLS-limit we obtain a pair of coupled nonlinear ODEs describing the deformation, numerical solutions to which are obtained via a shooting method.

An axisymmetric radial stretch of a circular isotropic sheet has previously been modelled by Yang (1967) by assuming the deformation, $r = r(R)$, $z = \lambda(R)Z$ *a priori*. In Section 4.2, we have shown that the form of this deformation is revealed at leading order in the (active anisotropic) thin-PCLS-limit via asymptotic expansions and supported by numerical evidence provided in Section 3.2.2 and Appendix B.3.

In Section 4.3, we assessed the applicability of each approximation and found that the membrane model is unable to capture the full model behaviour, but that the asymptotically-reduced model provides an excellent approximation to the full model for suitable regimes (*i.e.* $\varepsilon = 0.01$), at reduced computational

cost. Moreover, in Section 3.2.2 and in particular, Figure 3.5, we observed that the stress distributions become approximately uniform for $\varepsilon \leq 0.05$. This suggests that the approximate bound on the aspect ratio in the thin-PCLS model is $\varepsilon = 0.05$. The typical aspect ratio of the PCLS is $0.02 < \varepsilon < 0.25$ and thus, the thin-PCLS model provides a reasonable approximation to the full model. Many important features of the full model are not captured by the membrane approximation. The one-dimensional geometry of the membrane, together with tissue incompressibility, constrains the inner radius to deform according to the stretch imposed at the outer radius. As a result, ASM induced-contraction of the inner radius is not permitted and stresses are simply elevated in the membrane. Conversely, the thin-PCLS-limit replicates the behaviour observed in the full model and thins axially (more so at the outer radius than inner radius) in the presence of stretch and active contractile force to preserve incompressibility. Correspondingly, the magnitude of the stress is reduced and absorbed by the deformation of the PCLS.

The computational tractability of our thin-PCLS-limit approximation allowed us to efficiently explore the effects of material parameter variation on the constituent stress and tissue deformation. We have observed that an imposed stretch increases both the radial and axial deformation of the PCLS, and as a result, the heterogeneity of the stresses within. Furthermore, increased contraction of ASM leads to significant radial contraction of the airway and corresponding axial thinning. Conversely, increased stiffness of ECM relative to that of ASM reduces radial contraction and increases resistance to the associated axial thinning.

In the constrained mixture description of the PCLS the constituents are constrained to undergo the same deformation as that of the whole tissue (*i.e.* the relative velocity of each constituent remains the same at all times). Therefore, in Section 3.1.3 we proposed that the difference in constituent von Mises stress provides a convenient way to represent the mechanical activation of TGF-β, whereby a sufficiently large difference in the constituents von Mises stress is required to unfold the latent complex (that is anchored between the two constituents via integrins) and subsequently activate TGF-β (refer to Figure 1.2). In the absence of any strict rationale to use an individual Cauchy stress component, we chose to use the von Mises stress, which encompasses all of the Cauchy

stress components, as this provides an overall representation of the constituent stress state. Our key results have demonstrated that increased deformation, ASM contraction and ECM stiffness generate a significant qualitative and quantitative difference in the constituents von Mises stress. Importantly, we have observed that as the contraction of the ASM or stiffness of the ECM is increased, the absolute difference in constituent von Mises stress initially decays to zero and then increases. This reveals values of ECM stiffness and ASM contractility for which the constituents are comparably stressed. Once these values are surpassed, the difference in constituent von Mises stress continues to increase, for either increased ASM contraction or increased ECM stiffness. These key features have the potential to initiate a positive mechanotransductive feedback loop of TGF-β activation, leading to airway remodelling in the asthmatic airway, and motivates our model development. Therefore, in the following chapter we couple our biomechanical models of the PCLS stretching experiment to our dynamical ODE model of TGF-β activation (introduced in Chapter 2) to investigate the activation of TGF-β due to mechanical feedback.

CHAPTER 5

A Model of TGF-β Activation Coupled to Biomechanical Descriptions of Stretched Lung-slices

In this chapter we couple the biomechanical descriptions of the PCLS stretching experiment (developed in Chapters 3 and 4) to a simplified version of the dynamical ODE model of TGF-β activation (developed in Chapter 2) to investigate the mechanotransductive feedback loop of TGF-β activation. Specifically, we model active TGF-β mediated contraction of the ASM and the subsequent change in mechanical properties of the PCLS as activation of TGF-β progresses. The dynamical model in Chapter 2 describes the time-dependent subcellular signalling pathways that lead to the activation of TGF-β. The full biomechanical model and asymptotic approximation in Chapters 3 and 4, on the other hand, describe the spatially-dependent stress-induced mechanical activation of TGF-β due to deformation. Therefore, prior to coupling, we refine each model to allow for spatiotemporal dependence of active TGF-β.

5.1 Model development

In this chapter, we develop the single ODE (2.1.6c), that describes the rate of change in concentration of active TGF-β, a^*, and that accounts for specific TGF-β-receptor binding events that initiate specific cellular responses. To recap, basal activation of TGF-β occurs at rate κ_a^*. Mechanical activation of TGF-β occurs due to contraction of the contractile ASM, c^*, and resistance of the ECM, m^*. ASM contraction is stimulated by the contractile agonist $\hat{\kappa}_s^*(t^*)$, and is up-regulated by activated TGF-β signalling pathways at rate $\hat{\kappa}_{ac}^*(a^*, c^*)$. Active TGF-$\beta$ is removed from the system due to binding to the proliferating ASM, p^*, and contractile ASM, c^*, at rate κ_b^*. Finally, natural degradation of active TGF-β occurs at rate ϕ_a^*.

We want to couple the biomechanical description of the stretched PCLS to the mechanical activation of TGF-β. As outlined in Section 1.1.4, deformation of the constituents (*e.g.* contraction of the ASM) mechanically activates TGF-β by straining and unfolding the interconnecting latent complex. However, the biomechanical model is formulated using constrained mixture theory and consequently, the PCLS constituents are constrained to deform following that of the whole tissue at all times (*i.e.* the relative velocity of each constituent is the same at all times). Therefore, as outlined in Section 3.1.3, we propose use of the difference in constituent von Mises stress, σ_{dif}^* (3.1.26), as a convenient way to represent the mechanical activation of TGF-β.

Differences in the constituent von Mises stress, determined by the biomechanical model, emerge as a result of ASM contraction induced by both a contractile agonist and active TGF-β signalling (following suitable refinement in the next section) and therefore provide an appropriate replacement for $\hat{\kappa}_s^*(t^*)$ and $\hat{\kappa}_{ac}^*(a^*)$ in (2.1.6c). Again, following Baker et al. (2017), we assume that the stress-induced mechanical activation of TGF-β, $\hat{\kappa}_m^*(\sigma_{\text{dif}}^*)$, is limited and takes the form of a saturating Hill function,

$$\hat{\kappa}_m^*(\sigma_{\text{dif}}^*) = \frac{\kappa_m^* \left|\sigma_{\text{dif}}^*\right|^{n_{\text{VM}}}}{{\eta^*}_{\text{VM}}^{n_{\text{VM}}} + \left|\sigma_{\text{dif}}^*\right|^{n_{\text{VM}}}}. \tag{5.1.1}$$

Here, we use the absolute value of the difference in constituent von Mises stress,

σ^*_{dif}, to ensure that $\hat{\kappa}^*_m \geq 0$. Furthermore, we chose n_{VM} sufficiently large to resemble a threshold over which TGF-β is mechanically activated (*i.e.* the threshold of strain that the latent complex may withstand, as outlined in Section 1.1.4). The constant κ^*_m denotes the maximum rate of mechanical activation of TGF-β.

As noted in Section 3.1, the re-generation timescale of constituents within the PCLS is longer than the duration of the experiment (Tatler 2016), and accordingly, we assume that there is no ASM growth or ECM secretion during the performed stretching. Therefore, both the contractile ASM and ECM apparent densities, $\bar{c}^*$ and $\bar{m}^*$, respectively, remain constant throughout the experiment. Again, as in Section 3.1, we assume that there are no proliferating ASM cells *i.e.* $p^* = 0$.

The equation governing the activation of TGF-β in place of (2.1.6c) is then:

$$\frac{\partial a^*}{\partial t^*} = \kappa^*_a + \hat{\kappa}^*_m(\sigma^*_{\text{dif}})\bar{c}^*\bar{m}^* - \kappa^*_b\bar{c}^*a^* - \phi^*_a a^*. \tag{5.1.2}$$

Active TGF-β very rapidly binds to many TGF-β-specific receptors that are expressed on multiple cells in the PCLS tissue and hence, we assume that there is no active TGF-β in the PCLS at the start of the experiment. Therefore, (5.1.2) is subject to the initial condition

$$a^*(R^*, Z^*, 0) = 0. \tag{5.1.3}$$

We redefine the constant α^* in the active component of the ASM strain-energy function, W^*_c (3.1.17a), that represents the force generation by the ASM during contraction, as

$$\alpha^* = \alpha^*_s + \hat{\alpha}^*_{ac}(a^*). \tag{5.1.4}$$

The constant α^*_s represents the contractile force generated by the ASM when exposed to an exogenous agonist, *e.g.* methacholine (MCh). The function $\hat{\alpha}^*_{ac}(a^*)$ represents the contractile force induced by endogenously activated TGF-β, a^*. As previously, we assume that $\hat{\alpha}^*_{ac}(a^*)$ is limited and takes the form of a saturating Hill function,

$$\hat{\alpha}^*_{ac}(a^*) = \frac{\alpha^*_{ac}a^*}{\eta^* + a^*}, \tag{5.1.5}$$

where the constant α^*_{ac} denotes the maximum TGF-β induced contractile force

that can be generated by the ASM. Following Hiorns et al. (2014), we assume that α^* (5.1.4) remains independent of the invariant I_4. The isotropic and anisotropic components of the strain-energy functions for the ASM and ECM therefore remain unchanged, as in (3.1.17), and the existing formulation of the full biomechanical model (Section 3.1) and thin-PCLS approximation (Section 4.2) are unchanged.

Previously we applied a fixed stretch to the PCLS (denoted r^*_{dis} in (3.1.31) in Section 3.1.5). In this chapter we impose cyclic stretching to the outer boundary to mimic the experimental protocol (see Section 1.3.1) so that

$$\hat{r}^*_{\text{dis}}(t^*) = R^*_{\text{out}} + r^*_{\text{dis}} \sin^2(\psi^* t^*). \tag{5.1.6}$$

Here, the amplitude of the cyclic stretch is r^*_{dis} and the frequency is ψ^*. Note that in the absence of cyclic stretching, *i.e.* $r^*_{\text{dis}} = 0$, the outer boundary is fixed at the undeformed radius R^*_{out}.

5.1.1 Non-dimensionalisation

The scalings for the dynamical model and the biomechanical model follow those of Sections 2.1.4 and 3.1.6, respectively, with exception of the following variables:

$$\begin{aligned} \kappa_m &= \frac{\kappa^*_m \phi^{*2}_a}{\kappa^*_a}, & \kappa_b &= \kappa^*_b \phi^*_a, & a &= \frac{a^*}{a^*_r}, \\ \eta_{\text{VM}} &= \frac{\eta^*_{\text{VM}}}{\mu^*_c}, & \eta &= \frac{\eta^* \phi^* a}{\kappa^*_a}, & a^*_r &= \frac{\kappa^*_a}{\phi^*_a}, \end{aligned} \tag{5.1.7}$$

where, κ^*_m denotes the rate of mechanical activation of TGF-β, κ^*_b, the rate of active TGF-β-receptor binding, η^*_{VM}, the threshold over which TGF-β is mechanically activated, η^*, the threshold over which contractile force generated by the ASM saturates and μ^*_c, the isotropic stiffness of the ASM, as in (3.1.17). We choose the reference concentration of active TGF-β, a^*_r, to be the ratio of basal activation of TGF-β, κ^*_a, and the natural degradation of active TGF-β, ϕ^*_a, to reduce the number of rate parameters in the coupled model (5.1.2). There-

fore, the dimensionless version of the coupled model (5.1.2) is

$$\frac{\partial a}{\partial t} = 1 + \hat{\kappa}_m(\sigma_{\text{dif}})\Phi_c\Phi_m - (\kappa_b\Phi_c + 1)a, \tag{5.1.8}$$

where the dimensionless function

$$\hat{\kappa}_m(\sigma_{\text{dif}}) = \frac{\kappa_m|\sigma_{\text{dif}}|^{n_{\text{VM}}}}{\eta_{\text{VM}}^{n_{\text{VM}}} + |\sigma_{\text{dif}}|^{n_{\text{VM}}}}, \tag{5.1.9}$$

represents the mechanical activation of TGF-β and the dimensionless function

$$\alpha = \alpha_s + \hat{\alpha}_{ac}(a), \tag{5.1.10}$$

represents contractile force density generated by ASM, where α_s represents the contractile force generated by the ASM when exposed to MCh and the function $\hat{\alpha}_{ac}(a)$, given by

$$\hat{\alpha}_{ac}(a) = \frac{\alpha_{ac}a}{\eta + a} \tag{5.1.11}$$

represents the contractile force induced by endogenously activated TGF-β, a. The dimensionless version of the time dependent outer boundary condition is

$$\hat{r}_{\text{dis}}(t) = R_{\text{out}} + r_{\text{dis}}\sin^2(\psi t), \tag{5.1.12}$$

where the frequency of the performed cyclic stretching, ψ^*, is non-dimensionalised via $\psi = \frac{\psi^*}{\phi_a^*}$, and finally, the dimensionless initial condition is

$$a(R, Z, 0) = 0. \tag{5.1.13}$$

In the following we consider two coupled cases; one in which the activation of TGF-β is coupled to the full biomechanical model and the second coupled to the thin-PCLS-limit approximation. The proceeding descriptions summarise the two dimensionless coupled models.

The difference in constituent von Mises stress is determined in each of the respective biomechanical descriptions of the stretched PCLS to obtain the rate of mechanical activation of TGF-β, $\hat{\kappa}_m$ (5.1.9). The concentration of active TGF-β is determined by the dynamical model (5.1.8) which induces contraction of the ASM in the respective PCLS descriptions via α (5.1.11). For the full coupled

model (full model), we solve (3.1.55) and (3.1.56), subject to the free boundary conditions (3.1.58), and the imposed stretch (5.1.12) at the outer radius, R_{out}, to obtain the constituent von Mises stresses. In the thin-PCLS-limit coupled model (thin-PCLS model), stresses are obtained by solving the coupled ODES (4.2.13), subject to the imposed stretch (5.1.12) at the outer radius, R_{out}, and by shooting for a solution that satisfies the constraint (4.2.8b) at the inner radius, R_{in}.

Initially, in the reference configuration, the PCLS is at rest due to the absence of imposed stretch and ASM contraction. The rate of activation of TGF-β is initially at baseline. The prescribed cyclic stretching is applied to the PCLS in this state. The PCLS deforms due to the contractile force generated by the ASM (in response to active TGF-β) and the imposed stretch (that leads to strain-stiffening of the ECM). As a result, there is a difference in the constituent von Mises stress. This leads to the mechanical activation of TGF-β (once the stress threshold over which TGF-β is mechanically activated is surpassed) and gives rise to a positive mechanotransductive feedback loop. Subsequently, we expect to observe further contraction of the ASM and modification in the material properties of the PCLS tissue that are mediated by active TGF-β signalling pathways.

5.2 Numerical results

The thin-PCLS-limit provides a suitable and, importantly, a computationally tractable approximation to the full biomechanical model for $\varepsilon = 0.01$ (see Section 4.3). In this section we simulate the full model and the thin-PCLS model and compare the behaviour of the two for $\varepsilon = 0.01$. In order to couple the dynamical description of TGF-β activation (that is simulated in Matlab), and the full biomechanial description of the stretched PCLS (that is simulated in FEBio) efficiently, we have developed multiple bespoke codes; full details are provided in Appendices B.1 and B.2 for the full and the thin-PCLS couplings, respectively.

FEBio does not currently support spatially-dependent contractile force. Therefore, in order to couple the full biomechanical model (simulated in FEBio) we use

$$\hat{\alpha}_{ac}(\tilde{a}) = \frac{\alpha_{ac}\tilde{a}}{\eta + \tilde{a}}, \tag{5.2.1}$$

instead of (5.1.11), where $\tilde{a}$ indicates the averaged concentration of active TGF-β in the PCLS at time t. Accordingly, we use (5.2.1) in (5.1.10) in the thin-PCLS when comparing the two coupled models. Spatially-dependent contractile force, however, can be accounted for in the thin-PCLS model, demonstrating another computational advantage over the full model. Hereafter, we refer to the functions (5.2.1) and (5.1.11) as averaged contractile force and spatial contractile force generated by the ASM, respectively. Furthermore, in this chapter we do do not consider exposure to an exogenous agonist and therefore, we set $\alpha_s = 0$ in (5.1.10) to closely examine the effect of endogenously activated TGF-β-induced contraction of the ASM.

It should be noted that the radial uniformity of the averaged contractile force (5.2.1) does not imply radial uniformity of the concentration of active TGFβ across the airway wall due to the heterogeneity of the constituent von Mises stress (that persists in the absence and presence of a constant contractile force generated by the ASM) that drives the mechanical activation of TGF-β. Therefore, in the following section that considers spatially-independent contractile force generated by the ASM, we may still expect to observe radial variation in the concentration of active TGF-β. In the section thereafter, however, we illustrate the importance of including the spatial-dependence of ASM contractility in mechanotransductive feedback.

5.2.1 Spatially-independent ASM contractile force

In this section we consider the consequence of the contractile force (5.2.1) that is determined by the averaged concentration of active TGF-β in the PCLS at time t. The effect of cyclic stretch on the activation of TGF-β within the PCLS is illustrated in Figure 5.1. Here, the concentration of active TGF-β, a, is plotted as a function of time, t, and deformed radius, r, (and equivalently $r^{(0)}$ for the thin-PCLS model) at the undeformed centre of the PCLS ($Z = 0$). This provides

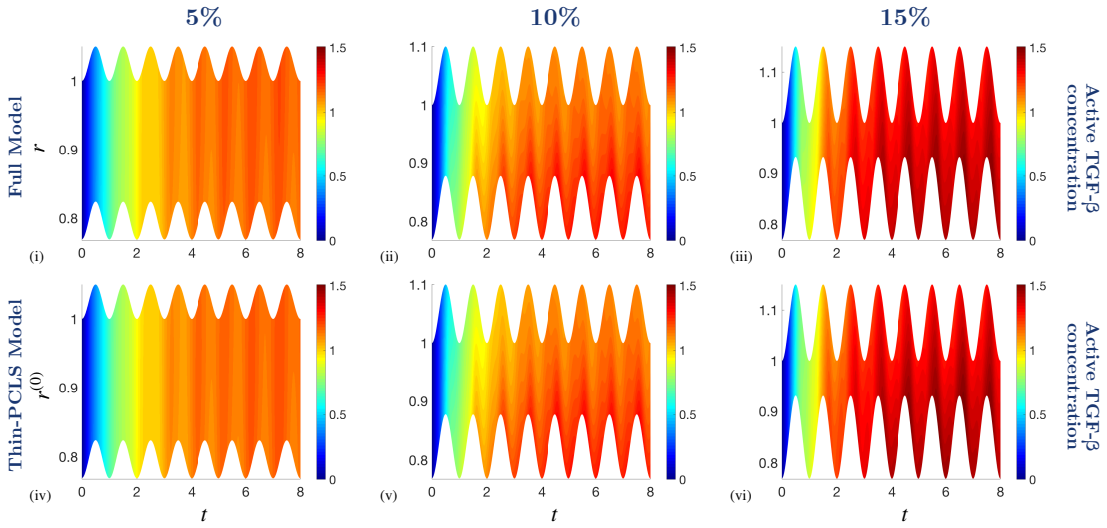

Figure 5.1: Concentration of active TGF-β, a, in the (i)–(iii) full model and (iv)–(vi) thin-PCLS model, plotted as a function of time, t, and deformed radius, r, (and equivalently $r^{(0)}$ for the thin-PCLS model) at the undeformed centre of the PCLS ($Z = 0$) for increased amplitude of cyclic stretch, 5% (1$^{\text{st}}$ column), 10% (2$^{\text{nd}}$ column) and 15% (3$^{\text{rd}}$ column), and averaged contractile force of the ASM (5.2.1). The aspect ratio $\varepsilon = 0.01$ and the remaining parameter values are in Table C.6 in Appendix C.3.

an example cross section through the PCLS. Recall that the stresses do not vary axially in the thin-PCLS model (see Section 4.2) and, for the value of $\varepsilon = 0.01$ used here, the stresses show only a very weak axial dependence in the full model (see Section 3.2.2). Therefore, the example cross section through the PCLS illustrates the overall distribution of active TGF-β (Figure 5.1).

As expected, due to the the agreement of the un-coupled versions (see Section 4.3), the behaviour of the thin-PCLS model replicates that of the full model (Figure 5.1). Therefore, the following observations are applicable to both the full model (Figures 5.1 (i)–(iii)) and thin-PCLS model (Figures 5.1 (iv)–(vi)).

Increasing the amplitude of imposed cyclic stretch increases the concentration of active TGF-β (*cf.* Figures 5.1 (i), (iii)). Moreover, 5%, 10% and 15% amplitude stretches give rises to qualitatively and quantitatively different distributions of active TGF-β during the imposed cyclic stretching (*cf.* Figures 5.2 (i), (ii), (iii)). As highlighted previously, we observe that the heterogeneous distribution of the difference in constituent von Mises stress (despite the radially uniform averaged contractile force (5.2.1)) introduces radial dependence to the concentration of active TGF-β (*e.g.* Figures 5.2 (i)–(iii)). For a 5% imposed cyclic stretch

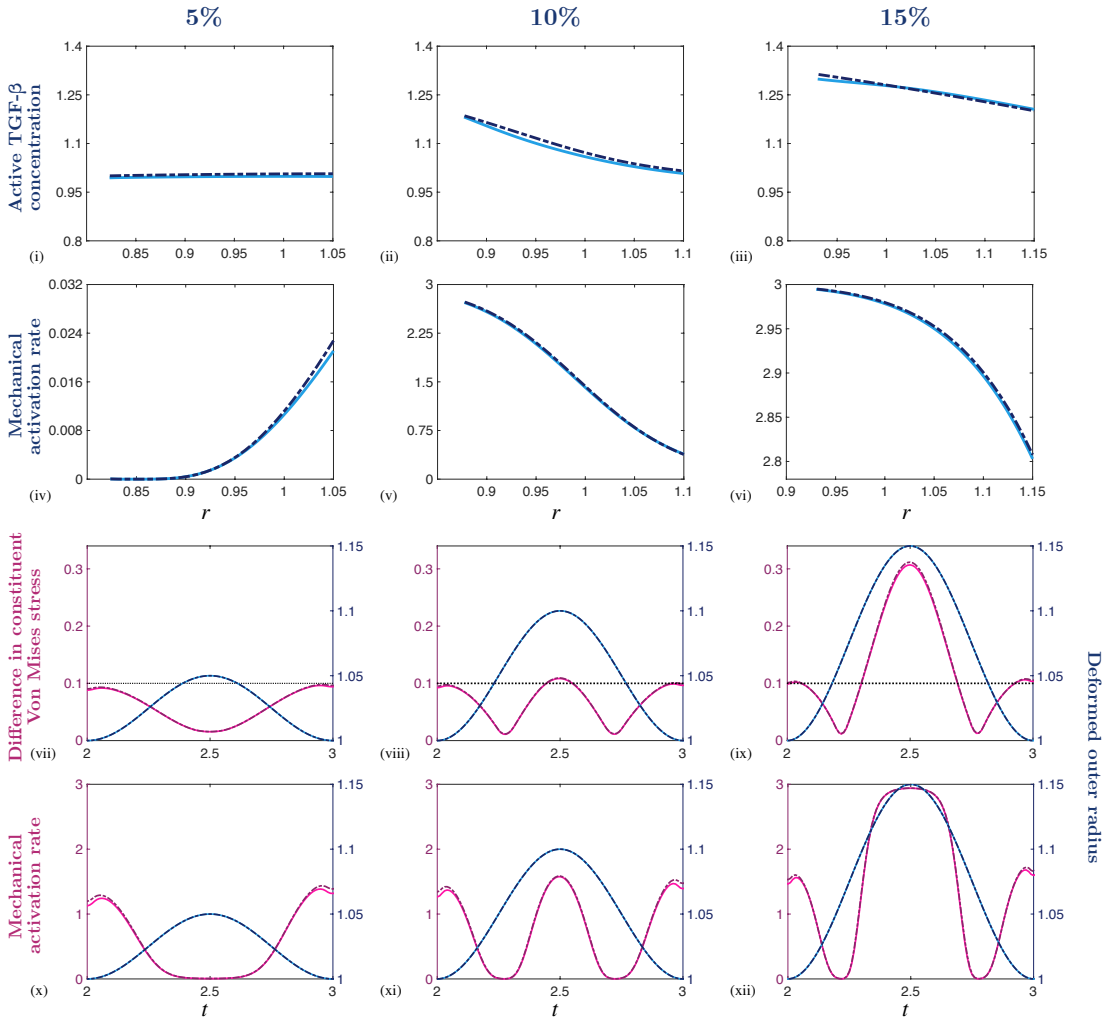

Figure 5.2: Examples corresponding to the results in Figure 5.1 of the effect of 5% (1st column), 10% (2nd column) and 15% (3rd column) cyclic stretch and averaged contractile force (5.2.1) on the mechanical activation of TGF-β. Dashed lines indicate the results obtained in the full model and solid lines indicate the results obtained in the thin-PCLS model. (i)–(iii) Concentration of active TGF-β, a, and (iv)–(vi) the rate of mechanical activation of TGF-β, $\hat{\kappa}_m$, plotted as functions of deformed radius, r, at the maximum of the example cycle (time $t = 2.5$). (vii)–(ix) The averaged (across the airway wall) absolute difference in constituent von Mises stress (pink lines), the threshold over which TGF-β is mechanically activated (black dotted line) and the deformed outer radius (blue lines) plotted as functions of time, t, over an example stretch cycle. (x)–(xii) The averaged (across the airway wall) rate of mechanical activation of TGF-β (pink lines) and the deformed outer radius (blue lines) plotted as functions of time, t, over an example stretch cycle. The aspect ratio $\varepsilon = 0.01$ throughout and the remaining parameter values are in Table C.6 in Appendix C.3.

we see that the concentration of active TGF-β remains uniform across the radius (Figure 5.1 (i), Figure 5.2 (i)), whilst increasing the stretch amplitude to 10% and 15% increases the radial heterogeneity (Figures 5.1 (ii)–(ii), Figures 5.2 (ii)–(iii)). Moreover, the concentration of active TGF-β builds up at the inner radius over time and particularly in the presence of stretch.

It appears that the periodic relaxation phases of the cyclic stretch (*i.e.* temporarily returning to the reference configuration) allows for slight clearance of active TGF-β with each cycle. As a result we observe the concentration of active TGF-β reach a dynamic equilibrium (Figure 5.1) with a (dimensional) time period of 3 minutes 20 seconds (reflective of the frequency of the imposed cyclic stretching at 0.3Hz) that is equivalent to 1 dimensionless time-step. As the imposed cyclic stretch temporarily decreases, both dynamical and mechanical factors contribute to the decay of TGF-β. This includes TGF-β-receptor binding, natural degradation and a reduction in the mechanical activation of TGF-β.

Increasing the amplitude of cyclic stretch imposes a greater deformation on the PCLS and as a result, generates a larger difference in the constituent von Mises stress (due to increased strain-stiffening of the ECM) that drives the mechanical activation of TGF-β. Hence, the stress threshold over which TGF-β is mechanically activated is surpassed significantly due to a 15% amplitude stretch compared to a 5% amplitude stretch. This is observed when comparing the concentration of active TGF-β at the dimensionless time $t = 2.5$ (which corresponds to a dimensional time of 8 minutes 20 seconds) in Figures 5.1 (i) and (iii). This suggests that increased amplitude of stretch (*i.e.* deformation of the PCLS) initiates a positive mechanotransductive feedback loop, thereby increasing the concentration of active TGF-β.

In order to assess the mechanotransductive feedback loop further, we examine the behaviour of the difference in constituent von Mises stress, and the subsequent rate of mechanical activation of TGF-β, over the dimensionless time-frame $t \in [2, 3]$ (Figures 5.2 (vii)–(xii)), and in particular, at the maximum of the imposed stretch at the dimensionless time $t = 2.5$ (Figures 5.2 (i)–(vi)). This selected time-frame provides an example of a complete cycle of imposed stretch during the experiment and, as above, is highlighted as a crucial transition period of TGF-β activation.

For 10% and 15% amplitude stretches, we observe that the maximal difference in constituent von Mises stress occurs at the maximum of the imposed stretch, *i.e.* at the dimensionless time $t = 2.5$ (Figures 5.2 (vii)–(ix)). In this case, the difference in constituent von Mises stress is predominantly driven by the associated strain-stiffening of the ECM. We observe that the difference in constituent von Mises stress decreases as the stretch decreases; however, when the stretch is sufficiently small (mid cycle) the contractile force generated by the ASM dominates over the strain-stiffening of the ECM and as a result, drives a difference in the constituent von Mises stress once more. Therefore, we see that there are two peaks in the difference in constituent von Mises stress; one due to maximal strain-stiffening of the ECM at the maximum of the imposed stretch, and a second due to the contractile force generated by the ASM at the minimum of imposed stretch (Figures 5.2 (vii)–(ix)).

Interestingly, we observe that there is only one peak in the difference in constituent von Mises stress and the rate of mechanical activation of TGF-β in the case of 5% amplitude stretching, as opposed to two in the cases of 10% and 15% amplitude stretching (*cf.* Figures 5.2 (vii)–(ix)). In the 5% case, the constituents are comparably stressed due to the contractile force generated by the ASM and the amount of strain-stiffening of the ECM that is associated with a 5% amplitude stretch (Figure 5.2 (vii)). As a result, the singular peak occurs at the minimum of the imposed stretched when ECM strain-stiffening reduces and ASM contractile force contributions dominate. At the maximum of the 5% imposed stretch, the difference in constituent von Mises stress is not sufficient to surpass the threshold over which TGF-β is mechanically activated. Conversely, ECM strain-stiffening is significant at 15% amplitude stretch and as a result, leads to a dramatic increase in the rate of mechanical activation of TGF-β and hence, the resultant concentration of active TGF-β (*cf.* Figures 5.2, 1$^{\text{st}}$ and 3$^{\text{rd}}$ column). Moreover, we observe that the rate of mechanical activation of TGF-β has a steep profile for 15% amplitude stretching which resembles the sigmoid representation in (5.1.9).

5.2.2 Spatially-dependent ASM contractile force

Simulations of the full model in FEBio are currently limited to those that consider (uniform) averaged contractile force of the ASM. The thin-PCLS model, on the other hand, is capable of accommodating spatially-dependent contractile force generated by the ASM and that is induced by the concentration of active TGF-β. In Section 5.2.1 we demonstrated that the thin-PCLS model well approximates that observed in the full model. Therefore, in this section, we exploit the thin-PCLS model to investigate the spatial-dependence of mechanotranductive feedback via (5.1.11).

The outer radius of the PCLS is fixed without stretch in Figures 5.3 (i)–(iii) and the amplitude of cyclic stretch increases in 5% increments in subsequent rows to 20%. As previously, we see that the concentration of active TGF-β increases with increased amplitude of cyclic stretch. Moreover, the difference in constituent von Mises stress increases with increased amplitude of cyclic stretch and surpasses the threshold, over which TGF-β is mechanically activated, efficiently (*cf.* Figures 5.3 (iv), (xiii)). We observe that radial contraction of the airway occurs continuously in the absence of stretch (Figures 5.3 (i)–(iii)) and intermittently in the presence of cyclic stretch, due to the prescribed deformation (Figures 5.3 (iv)–(xv)). Moreover, the extent to which the airway radially contracts saturates as the contractile force generated by the ASM reaches the maximum, α_{ac}, as TGF-β activation progresses.

Stark differences emerge between the instances of averaged contractile force and spatial contractile force as the concentration of active TGF-β rises (*cf.* Figure 5.3, 1$^{\text{st}}$ and 2$^{\text{nd}}$ column). For example, in the absence of stretch, spatial contractile force results in a higher concentration of active TGF-β at the inner radius than the outer radius (Figure 5.3 (ii)), whereas averaged contractile force distributes the concentration of active TGF-β more uniformly across the airway wall (Figure 5.3 (i)).

To emphasise the difference in the evolving distributions of active TGF-β, we plot the concentration of active TGF-β over the deformed radius, r, at two time points (Figures 5.3, 3$^{\text{rd}}$ column). Here, the two selected time points correspond to a maximum (indicated by dotted lines) and minimum (indicated by solid

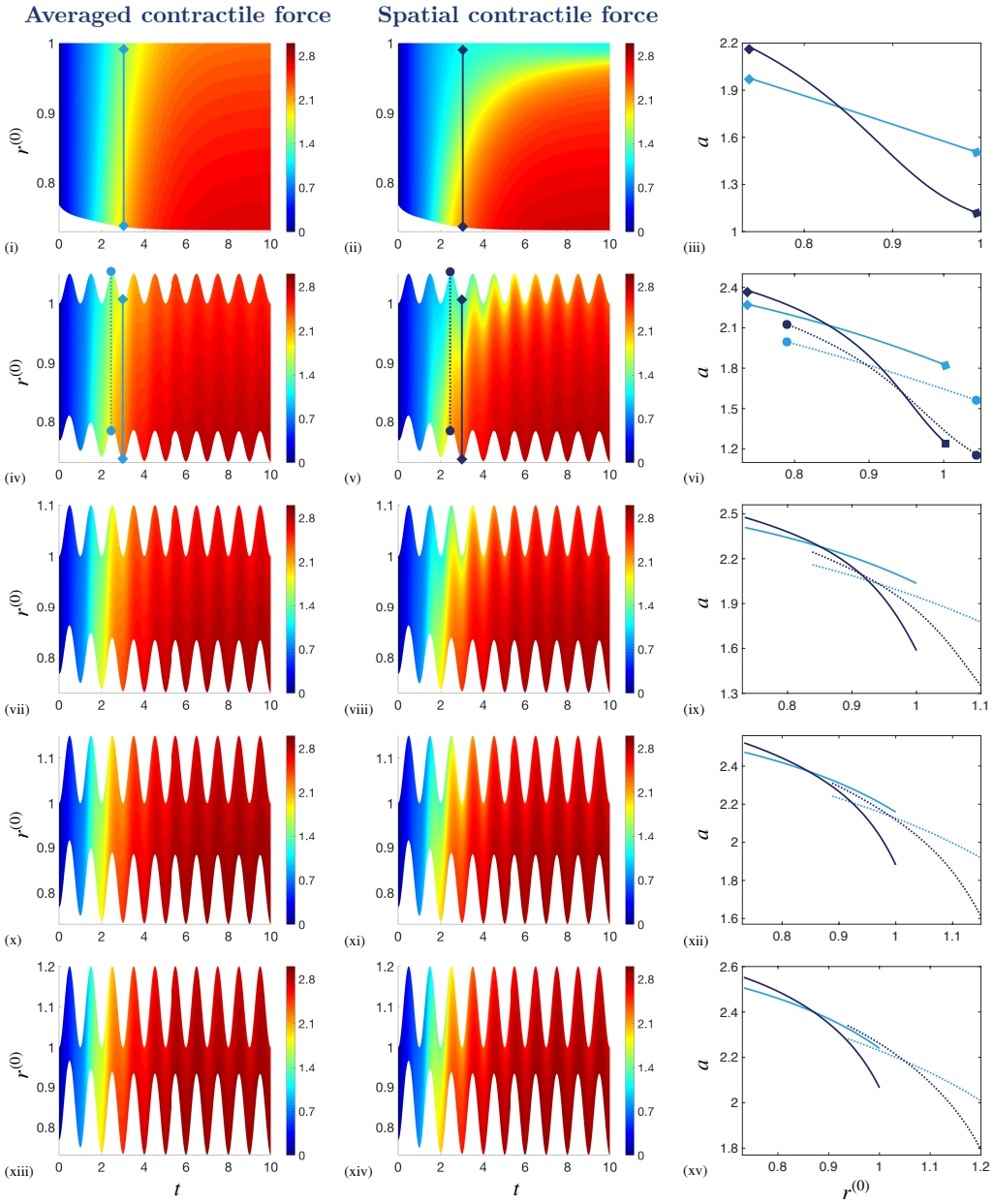

Figure 5.3: Concentration of active TGF-β, a, in the thin-PCLS model plotted as a function of time, t, and deformed radius, $r^{(0)}$, for averaged contractile force (5.2.1) (1$^{\text{st}}$ column) and for spatial contractile force (5.1.11) (2$^{\text{nd}}$ column). The 3$^{\text{rd}}$ column illustrates the distribution of active TGF-β over the deformed radius $r^{(0)}$ at $t = 2.5$ (dotted lines) and at $t = 3$ (solid lines). The light blue lines correspond to the 1$^{\text{st}}$ column and the dark blue lines correspond to the 1$^{\text{st}}$ column. The amplitude of cyclic stretch increases in 5% increments from (i)–(iii) 0%, to (xiii)–(xv) 20%. The aspect ratio $\varepsilon = 0.01$ and the remaining parameter values are in Table C.6 in Appendix C.3.

lines) of the imposed cyclic stretch and are chosen to highlight the TGF-β activation threshold. As expected, we see that the averaged contractile force minimises the variation of active TGF-β across the radius. For example, at $t = 3$ in the absence of cyclic stretching, we observe that averaged contractile force generation results in a linearly increasing concentration of active TGF-β from the outer to inner radius, whereas spatial contractile force gives rise to a nonlinear distribution of active TGF-β (Figure 5.3 (iii)). Similarly, at $t = 2.5$ in the cyclically stretched case, spatial contractile force generation leads to elevated concentrations of active TGF-β at the inner radius and reduced concentrations at the outer radius, compared to those in the case of averaged contraction (*e.g.* Figure 5.3 (vi)). These results reflect the mechanical feedback mechanisms responsible for TGF-β-induced contractile force generation across the airway wall that we shall investigate further.

Increasing the threshold over which active TGF-β induces contraction of the ASM, η, results in a delay in the mechanical activation of TGF-β via mechanotransductive feedback (Figure 5.4). Again, averaged contractile force and spatial contractile force lead to significantly different distributions of active TGF-β across the airway wall and the extent to which these differ is exaggerated for increased η (*cf.* Figures 5.3 and 5.4).

The concentration of active TGF-β is far higher at the inner radius than at the outer radius in the case of spatial contractile force (Figures 5.4, 2^{nd} column). This suggests that the heterogeneity of the contractile force generated by the ASM is strongly influenced by the rising concentrations of active TGF-β across the airway wall (*e.g.* Figure 5.4 (xi)). Here, the increasing concentration of active TGF-β at the inner radius initiates a mechanotranductive feedback loop (via ASM contractile force) that further elevates the concentration of active TGF-β. Conversely, the concentration of active TGF-β at the outer radius is not sufficient to surpass the required threshold that initiates contraction of the ASM (*e.g.* Figure 5.4 (xi)). As a consequence, the mechanical activation of TGF-β is hindered and the low concentration of active TGF-β persists. In these regions the basal activation, mechanical activation and degradation of TGF-β are balanced and thus, the reduced concentration of active TGF-β is maintained. These interesting features are absent for averaged contractile force (*cf.* Figures 5.4 (x), (xi)).

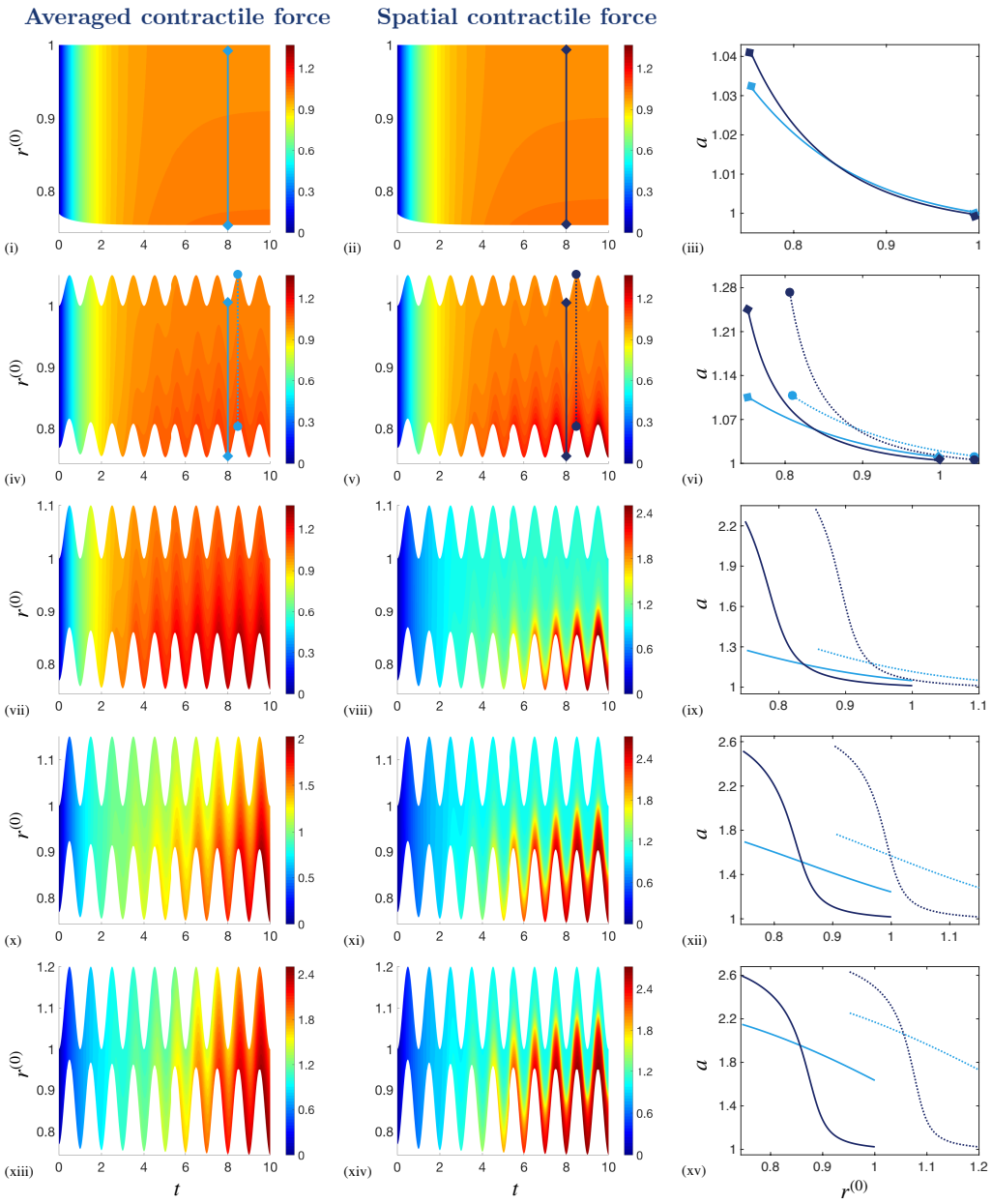

Figure 5.4: The effect of increased contractile force generation threshold, η, on the concentration of active TGF-β, a, in the thin-PCLS model plotted as a function of time, t, and deformed radius, $r^{(0)}$, for averaged contractile force (5.2.1) (1$^{\text{st}}$ column) and for spatial contractile force (5.1.11) (2$^{\text{nd}}$ column). The 3$^{\text{rd}}$ column illustrates the distribution of active TGF-β over the deformed radius $r^{(0)}$ at $t = 8$ (solid lines) and at $t = 8.5$ (dotted lines). The light blue lines correspond to the 1$^{\text{st}}$column and the dark blue lines correspond to the 1$^{\text{st}}$ column. The amplitude of cyclic stretch increases in 5% increments from (i)–(iii) 0% (xiii)–(xv) to 20%. The aspect ratio $\varepsilon = 0.01$ and the remaining parameter values are in Table C.6 in Appendix C.3.

In order to highlight the importance of accounting for the spatial-dependence of ASM contractility, and illustrate the downstream effects of averaged contraction for increased η, we plot the concentration of active TGF-β at a maximum and minimum of the imposed cyclic stretch over the deformed radius (Figures 5.4, 3rd column). Here we see that the extrema in the active TGF-β concentration, observed in the case of spatial contractile force, are significantly reduced due to averaging (*e.g.* Figure 5.4 (xii)). Increasing the amplitude of cyclic stretch exaggerates these observations, where the concentration of active TGF-β displays a sigmoid profile (reflecting the stress threshold leading to the mechanical activation of TGF-β) across the the airway wall (Figure 5.4 (xv)).

5.3 Summary

In this chapter we have coupled our dynamical model, describing the change in concentration of active TGF-β, and our biomechanical descriptions of TGF-β activation in a cyclically stretched PCLS. Our results reveal a positive mechanotransductive feedback loop, whereby active TGF-β-induced constituent stress differences cause further TGF-β activation. In particular, TGF-β activation induces contraction of the ASM and prescribed cyclic stretch causes strain-stiffening of the ECM fibres. This leads to an increased difference in the constituent von Mises stress that subsequently up-regulates the mechanical activation of TGF-β.

Our results demonstrate that increasing the amplitude of imposed cyclic stretch increases the concentration of active TGF-β. The contractile force generated by the ASM saturates at the inner radius as the concentration of active TGF-β rises. As a result, the rate of mechanical activation of TGF-β is up-regulated at the inner radius (due to the increased difference in constituent von Mises stress) which correspondingly, leads to elevated concentrations of active TGF-β. This may be observed in the asthmatic airway, where elevated ASM contractility (bronchoconstriction) narrows the airway and subsequently mechanically activates TGF-β.

Investigating the spatial variation of the contractile force generated by the ASM is only computationally tractable in our thin-PCLS model. Our results show

that including the spatial-dependence of ASM contractility is of vital importance in order to understand how the distribution of active TGF-β, and hence the contraction of ASM, may increase in the airway wall. We aim to provide insight into the mechanisms that may be responsible for the mechanical activation of TGF-β in the stretched PCLS that is observed experimentally. Moreover, we aim to gain an understanding of how the mechanical activation of TGF-β is linked to airway remodelling in asthma via mechanotrandsuctive feedback. Therefore, in the following chapter we exploit the thin-PCLS model to compare simulated results against experimentally obtained data.

CHAPTER 6

Comparison to Experimental Data

In this chapter we compare experimental data obtained by Tatler (2016; 2019) in the human PCLS and in the mouse PCLS (outlined in Sections 1.3.1 and 1.3.2, respectively) to results obtained via the thin-PCLS model (accounting for spatially-dependent contractile force). Importantly, in this chapter the thin-PCLS model explains potential mechanisms responsible for the mechanical activation of TGF-β in the stretched PCLS that is observed experimentally.

6.1 Cyclically stretched human lung-slices

Human PCLS are obtained from the healthy regions of lung tissue from cancer resections in non-asthmatic donors (details in Appendix A.2). Stretch is applied cyclically, in the form of a sine wave with a 15% amplitude and 0.3Hz frequency, for 24 hours (Tatler 2016) (via the Bioflex method illustrated in Figure 1.5). The amount of PSmad2 (proteins that are the main signal transducers for receptors of TGF-β and therefore an indicator of the amount of activated TGF-β) is quantified using a Phospho-Smad2 (S245/250/255) ELISA Kit at the end of the experiment ($t^* = 24$ hours) and indicates the noncumulative activity of TGF-β within the PCLS (Tatler 2016). The PSmad2 signalling activity following cyclic stretching of the PCLS is quantified in Figure 6.1 (i). The percentage increase in PSmad2 signalling activity in the stretched case, relative to the unstretched case, is illustrated in Figure 6.1 (ii). Results, for each of the three donors, indicate that TGF-β activation is increased in the cyclically stretched case compared to the unstretched case.

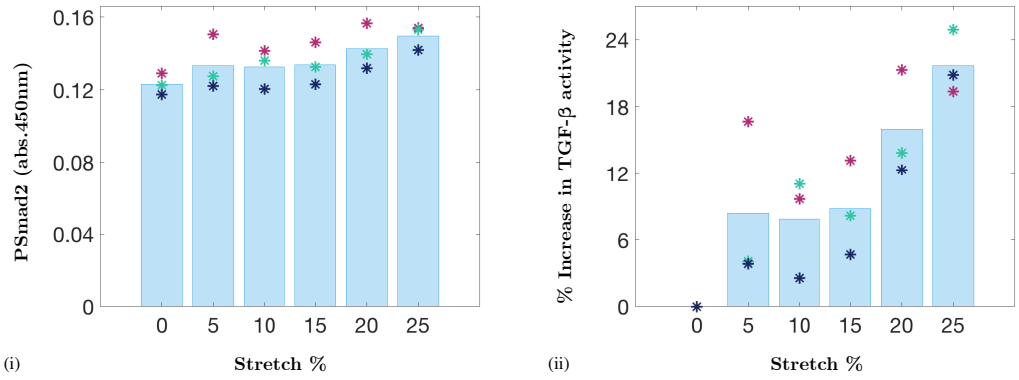

Figure 6.1: Experimental data, obtained by Tatler (2016), corresponding to the human PCLS stretching experiment outlined in Section 1.3.1. (i) TGF-β activity quantified via PSmad2 activity and (ii) percentage change in TGF-β activity relative to the unstretched human PCLS, plotted against the amplitude of cyclic stretch (%). Stars indicate the results for the three different human donors. The bars are the averaged results across the three human donors.

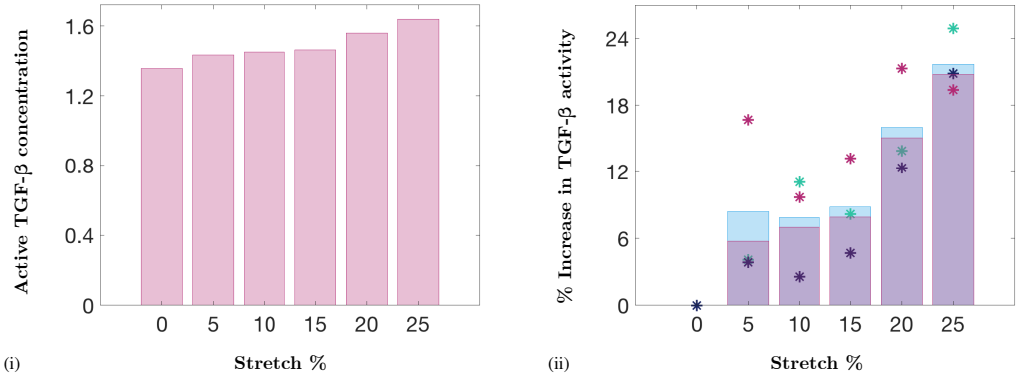

Figure 6.2: Simulated results obtained via the thin-PCLS model. (i) Concentration of active TGF-β, a, plotted against the amplitude of cyclic stretch (%). (ii) Comparison of the percentage change in TGF-β activity, relative to the unstretched PCLS, to the experimental results in Figure 6.1. Purple bars indicate simulated results, blue bars indicate experimental results and the stars indicate experimental results for the three different human donors. The blue bars are the averaged experimental results across the three human donors. Simulated parameter values are provided in Table C.7 in Appendix C.3.

The experimental data indicates a significant increase in the activity of TGF-β with the application of stretch (5%, 10% and 15% stretches) that increases further for high amplitude stretching (20% and 25% stretches) (Figure 6.1). In-

terestingly, the average activity of TGF-β is very similar for 5%, 10% and 15% amplitude cyclic stretches; however, the activity of TGF-β fluctuates between the three donors for stretches of these amplitudes (Figure 6.1). On the other hand, there is a clear positive trend in the activity of TGF-β, for both the individual donors and overall average, from the 15% to 25% amplitude stretches.

For comparative purposes, we display the noncumulative concentration of active TGF-β obtained via the spatially-dependent thin-PCLS model at $t = 432$ (equivalently $t^* = 24$ hours) in Figure 6.2; however, we restrict results displayed in Figure 6.3 (containing functions plotted over the deformed radius and time) to $t = 10$ (equivalently $t^* \approx 33$ minutes) in order to observe the qualitative behaviour in complete cycles of the stretching performed at 0.3 Hz. Similar to the results in the previous chapter, we observe that the concentration of active TGF-β reaches a dynamic equilibrium (as cell signalling pathways and mechanical activation balance) before the end of the experiment which justifies the selected time-frame. Furthermore, in this experiment, the PCLS are not exposed to an exogenous agonist, *i.e.* no methacholine (MCh) challenges. Accordingly, we set $\alpha_s = 0$ in (5.1.10) in this section.

Consistent with previous results in Chapter 5, we likewise find that increasing the amplitude of imposed cyclic stretch in the simulation increases the concentration of active TGF-β in the PCLS and, importantly, resembles the experimentally observed behaviour (Figure 6.2). We display the concentration of active TGF-β for each of the amplitudes of imposed stretch (Figure 6.2 (i)) alongside the percentage increase in the concentration of active TGF-β relative to the unstretched case, which provides a direct comparison to the experimental data and shows that our results are in agreement qualitatively (Figure 6.2 (ii)).

In order to understand the experimentally observed behaviour we investigate the spatio-temporal distributions of active TGF-β, and the associated feedback mechanism, during the imposed cyclic stretching. The distribution of the concentration of TGF-β that is activated during the cyclic stretching, a, is illustrated as a function of deformed radius, r, and time, t, in Figures 6.3, 1$^{\text{st}}$ column. The corresponding contractile force generated by the ASM, α (5.1.10), and the mechanical activation of TGF-β, $\hat{\kappa}_m$ (5.1.9), is illustrated in Figures 6.3, 2$^{\text{nd}}$ and 3$^{\text{rd}}$ column, respectively. We see that both the rate of mechanical activation of

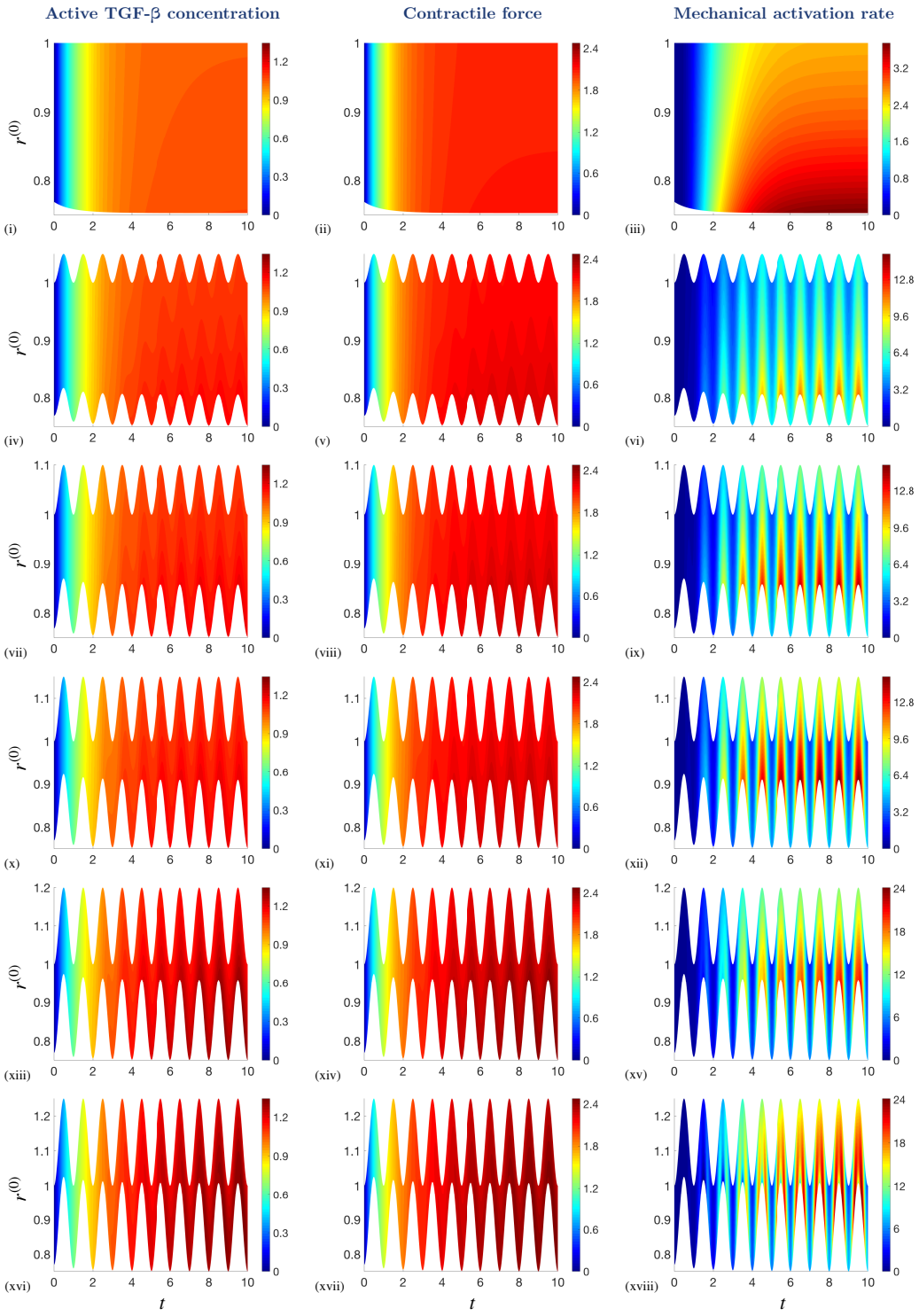

Figure 6.3: Concentration of active TGF-β, a, (1st column) contractile force generated by the ASM, α (5.1.10), (2nd column) and rate of mechanical activation of TGF-β, $\hat{\kappa}_m$ (5.1.9), (3rd column) plotted as functions of time, t, and deformed radius, $r^{(0)}$. Stretch amplitude increases from unstretched (0%) in the 1st row to 25% in the 6th row. Simulated parameter values are provided in Table C.7 in Appendix C.3.

TGF-β and the contractile force generated by the ASM reach a dynamic equilibrium that is reflected in the distribution of active TGF-β. Moreover, the rate of mechanical activation of TGF-β and contractile force generated by the ASM build up at the inner radius and correspondingly, leads to an elevated concentration of active TGF-β at the inner radius that is emphasised with stretch amplitude (*cf.* Figures 6.3 (iv)–(vi), (xvi)–(xviii)). This suggests that imposed cyclic stretching generates a large difference in the constituent von Mises stress, σ_{dif}, and as a result, the threshold over which TGF-β is mechanically activated, η_{VM}, is surpassed sufficiently, initiating a positive feedback loop that allows the concentration of active TGF-β to rise.

In general, the rate of mechanical activation of TGF-β increases significantly for the higher amplitude stretches, 20% and 25% (Figures 6.3 (xv), (xviii)). There is a moderate response for the lower amplitude stretches, 5%, 10% and 15% (Figures 6.3 (vi), (ix), (xii)), and a very small response for the unstretched case (Figure 6.3 (ii)). Thus, it appears that there are two possible thresholds leading to an increase in the activation of TGF-β; one which acts upon the application of stretch, and a second that acts for high amplitude cyclic stretching. To investigate this further, we plot the maximum and the minimum values of the rate of mechanical activation of TGF-β, $\hat{\kappa}_m$ (5.1.9), and the contractile force generated by the ASM, α (5.1.10), for each amplitude of cyclic stretch in Figure 6.4.

Interestingly, we see that ASM contractile force generation saturates prior to the rate of mechanical activation of TGF-β (Figure 6.4). As expected, in the 0 – 5% regime, there is a dramatic increase in both the rate of mechanical activation of TGF-β and the contractile force generated by the ASM due to the application of stretch and subsequent active TGF-β-induced signalling. In the 5 – 15% regime, the contractile force generated by the ASM rises, whilst the rate of mechanical activation of TGF-β is unchanged (*i.e.* the difference in constituent von Mises stress is comparable for the 5%, 10% and 15% amplitude stretches), whereas in the 20 – 25% regime, the rate of mechanical activation of TGF-β continues to climb (*i.e.* the difference in constituent von Mises stress increases for 20% and 25% amplitude stretches) as the contractile force generated by the ASM saturates (Figure 6.4).

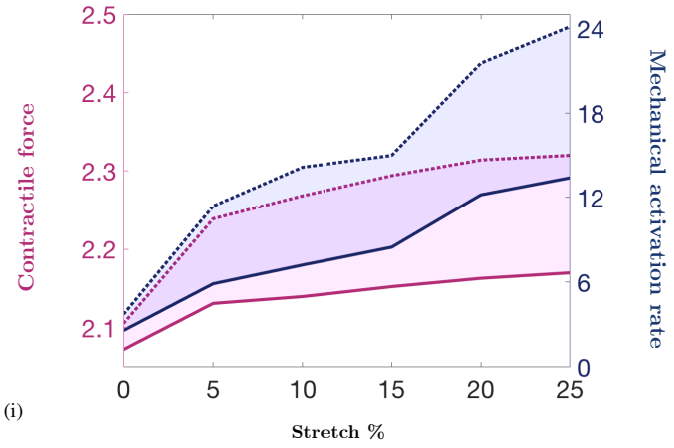

Figure 6.4: Maximum (dotted lines) and minimum values of the contractile force generated by the ASM, α (5.1.10), (pink) and the rate of mechanical activation of TGF-β, $\hat{\kappa}_m$ (5.1.9), (dark blue) corresponding to the results in Figures 6.2 and 6.3, plotted against the amplitude of cyclic stretch (%). Parameter values correspond to those in Figures 6.2 and 6.3 and are provided in Table C.6 in Appendix C.3.

The thin-PCLS model developed in Chapter 5 elucidates the potential mechanisms responsible for the mechanical activation of TGF-β in the stretched PCLS that is observed experimentally. Specifically, the difference in constituent von Mises stress, which represents the unfolding of the latent TGF-β complex in the mechanical activation of TGF-β (see Section 1.1.4), provides a possible explanation as to why the concentration of active TGF-β is elevated for higher amplitudes of imposed cyclic stretch and reduced (and alike) for lower amplitudes of imposed cyclic stretch.

Strain-stiffening of the ECM increases with increased amplitude of cyclic stretching and as a result, increases the von Mises stress of the ECM (*e.g.* previously observed in the passive case in Figures 4.4 (xvi)–(xviii)). Similarly, the von Mises stress of the ASM increases as contractile force generation, induced by active TGF-β signalling pathways, increases (*e.g.* previously observed as constant contractile force increases in Figures 4.6 (x)–(xii)). The von Mises stress of the increasingly strain-stiffened ECM (associated with imposed stretch) and increasingly contracted ASM (as TGF-β progresses) must therefore be comparable for imposed cyclic stretches of amplitudes 5%, 10% and 15%, and hence, the rate of mechanical activation of TGF-β is similar for these stretch amplitudes (Figure 6.4).

For high amplitude stretching (20% and 25% amplitudes), however, contractile force saturates (physically limited), whilst the strain-stiffening of the ECM continues to rise, which increases the difference in constituent von Mises stress. This explanation is supported by our previous parameter explorations in Section 4.4, in particular, where we observe an increase in the difference in constituent von Mises stress (that is higher at the inner radius than the outer radius) for increasingly large stretches (imposed stretch amplitude $\geq 15\%$ in Figure 4.5 (v)) and regions of parameter space where the ECM and ASM are comparably stressed as contractile force increases in the presence of stretch (Figure 4.7 (vi)). Further support for this explanation is provided in the previous chapter, specifically Section 5.2.2, where we investigate the effect of spatially-dependent contractile force generated by the ASM and witness an exaggerated mechnotransductive feedback loop of TGF-β activation at the inner radius that is absent at the outer radius (*e.g.* Figure 5.4 (xiv)).

6.2 Chronic ovalbumin-challenged mouse model

As outlined in Section 1.3.2, ovalbumin (OVA)-induced experimental asthma in the mouse shares many of the characteristics of allergic asthma in humans (described in Section 1.2). Furthermore, the effects of bronchoconstriction (significant narrowing of the airways) in asthma may be examined by exposing PCLS to an exogenous contractile agonist, MCh.

As described in Section 1.3.2, Brook et al. (2019) quantify the airway size and the ASM and collagen (major ECM component) airway fractions for prepared and stained mouse PCLS obtained via a chronic OVA-challenged mouse model. Hereafter, saline refers to normal airway tissue, whereas OVA refers to asthmatic airway tissue. According to the experimental data provided by Brook et al. (2019), the volume fractions of ASM and ECM are $\Phi_c = 0.0754$ and $\Phi_m = 0.1084$ in the saline PCLS, and $\Phi_c = 0.1346$ and $\Phi_m = 0.1654$ in the OVA PCLS, respectively. Therefore the approximate increase in ASM volume fraction is 78.5% and in ECM volume fraction is 52.6% in the OVA PCLS compared to the saline PCLS, demonstrating the significant airway remodelling generated by OVA challenge.

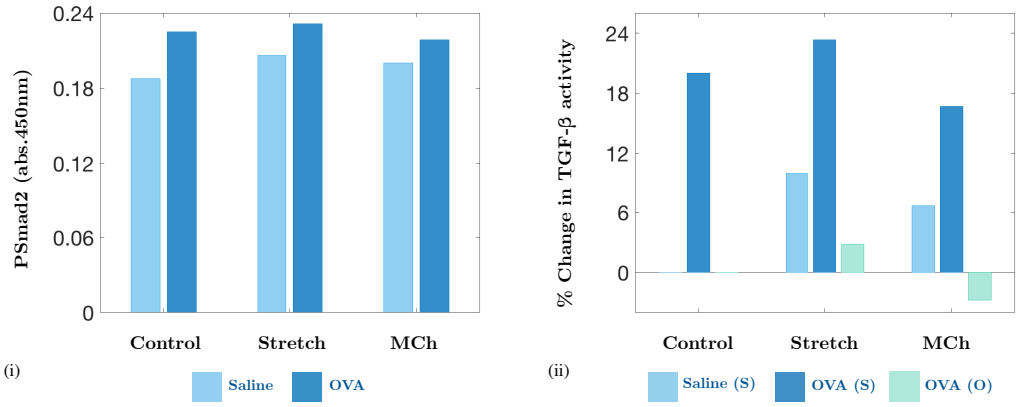

Figure 6.5: Experimental data, obtained by Tatler (2019), corresponding to the OVA-challenged mouse PCLS experiments outlined in Section 1.3.2. (i) The effect of cyclic stretch and MCh on TGF-β activity in mouse PCLS (quantified via PSmad2 activity) in the saline (light blue) and OVA (dark blue) case. (ii) Percentage change in TGF-β activity relative to saline control (S) and OVA control (O).

In the chronic OVA-challenged mouse study of Brook et al. (2019), Tatler (2019) performed additional experiments to asses the effect of increased ASM and ECM mass, ASM contraction, and cyclic stretch on the activity of TGF-β in the remodelled mouse PCLS. To do so, Tatler (2019) quantified PSmad2 activity in the cyclically stretched PCLS from OVA- and MCh-challenged cases compared to the saline (and OVA) controls, respectively. The activity of PSmad2 in each case is displayed in Figure 6.5 (i). The corresponding percentage change in each case, relative to the saline and OVA control, is displayed in Figure 6.5 (ii). Here, control indicates that the saline and OVA PCLS are unstretched and absent (untreated) of exogenous contractile agonist, MCh. Stretch indicates that the saline and OVA PCLS are cyclically stretched with amplitude of 15% in the absence of MCh. Finally, MCh indicates that the saline and OVA PCLS are unstretched and administered MCh to induce significant airway narrowing. The experimental results show that TGF-β activity is increased due to OVA-induced airway remodelling, MCh challenges and cyclic stretch, relative to the saline control. Interestingly, TGF-β activity in the OVA PCLS is increased due to cyclic stretch yet reduced due to MCh challenges, relative to the OVA control.

In order to investigate the experimentally observed behaviour, in this section we use the thin-PCLS model to simulate the additional experiments performed

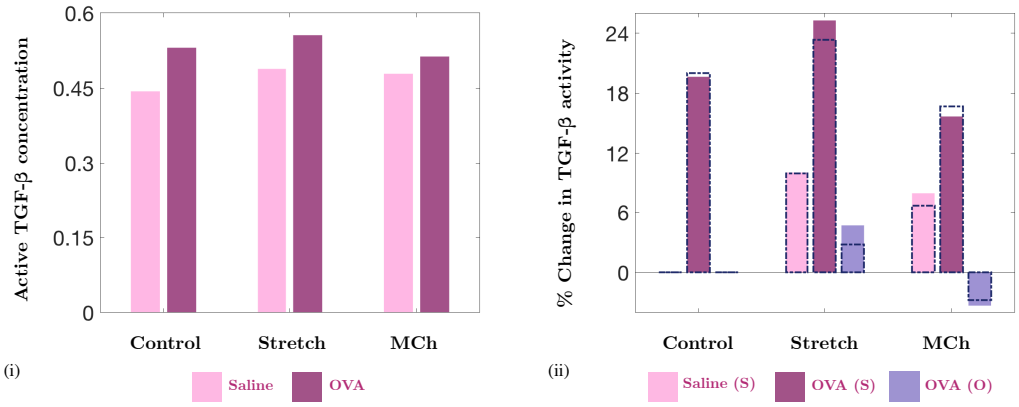

Figure 6.6: Simulated results obtained via the thin-PCLS model. (i) The effect of cyclic stretch and MCh-challenge on the concentration of active TGF-β in the saline mouse PCLS (light pink) and OVA mouse PCLS (dark pink). (ii) Comparison of the percentage change in the concentration of active TGF-β relative to saline control (S) and OVA control (O) to the experimental data obtained by Tatler (2019) in Figure 6.5, where dashed lines indicate the experimentally observed percentage change in TGF-β activity (quantified via PSmad2 activity). Simulated parameter values are provided in Table C.7 in Appendix C.3.

by Tatler (2019) in the mouse PCLS and compare the simulated results to the experimental data thereafter. Accordingly, we use the respective volume fractions of ASM and ECM provided by Brook et al. (2019). Moreover, in this section, we assume that the stiffness of the ECM, relative to that of the ASM, is $\mu = 1$ in the saline PCLS and $\mu = 3$ in the OVA PCLS (resembling the stiffened remodelled airway, as outlined in Section 1.2.3). Where applicable (*i.e.* in the MCh challenged PCLS), we consider the exogenous-induced contraction of the ASM, $\alpha \neq 0$ (5.1.10). Furthermore, it should be noted that the typical thickness of the airway wall in a mouse is approximately 50μm, which is significantly lower than in human and hence, the geometry of the PCLS in this section differs to that in Section 6.1 (*cf.* Figures 6.3, 6.7).

As previously in Section 6.1, we display the concentration of active TGF-β for each case (Figure 6.6 (i)) alongside the percentage change in the concentration of active TGF-β relative to the saline and OVA controls, which provides a direct comparison to the experimental data and shows that our results resemble the experimentally observed behaviour (Figure 6.6 (ii)). As expected (given our previous results in Section 6.1 and more generally in Chapter 5), we see that

imposed cyclic stretch increases the concentration of active TGF-β compared to the unstretched case (Figure 6.6). Moreover, this observation holds in both the saline and OVA cases.

In order to understand how each of these experimental factors may influence the activation of TGF-β, we plot the concentration of active TGF-β, a, the rate of mechanical activation of TGF-β, $\hat{\kappa}_m$ (5.1.9), and the effective mechanical activation of TGF-β, $\Phi_c\Phi_m\hat{\kappa}_m$ in (5.1.8), as functions of deformed radius, r, and time, t, in Figures 6.7, 1$^{\text{st}}$, 2$^{\text{nd}}$ and 3$^{\text{rd}}$ column, respectively.

Importantly, OVA challenges increase the area fraction of ECM and ASM, and as a result, we see that the effective mechanical activation of TGF-β, $\Phi_c\Phi_m\hat{\kappa}_m$, is significantly higher in the OVA PCLS than in the saline PCLS (*cf.* Figures 6.7 (iii), (xii)), despite the lower rate of mechanical activation of TGF-β, $\hat{\kappa}_m$ (*cf.* Figures 6.7 (ii), (xi)). The volume fractions of the constituents are much greater in the OVA PCLS than in the saline PCLS, and therefore enhance the rate of mechanical activation of TGF-β. Correspondingly, there is an increase in the concentration of active TGF-β in the OVA PCLS over the saline PCLS (*cf.* Figures 6.7 (i), (x)). Relative to the saline control, imposed cyclic stretch has a greater effect on the activation of TGF-β in the OVA PCLS than in the saline PCLS, due to the increased ECM mass contributing to the associated strain-stiffening that drives a larger difference in the consituent von Mises stress (*cf.* Figures 6.7 (i), (iv) and (i), (xiii) respectively; see also Figure 6.6). Relative to the respective controls (*i.e.* stretched OVA PCLS relative to OVA control and stretched saline PCLS relative to saline control), however, there is a larger increase in the activation of TGF-β in the stretched saline PCLS than in the stretched OVA PCLS (*cf.* Figures 6.7 (i), (iv) and (x), (xii) respectively; see also Figure 6.6). The OVA PCLS is stiffer than the saline PCLS (as a result of OVA-induced remodelling) and hence, the additional strain-stiffening of the ECM with imposed stretch is more significant in the saline PCLS than in the OVA PCLS.

Similarly, relative to the saline control, MCh challenges have a greater impact on the activation of TGF-β in the OVA PCLS than in the saline PCLS due to the increased ASM mass generating contractile force that drives a larger difference in the constituent von Mises stress (*cf.* Figures 6.7 (i), (vii) and (i), (xvi), respectively; see also Figure 6.6). Conversely, relative to the respective controls,

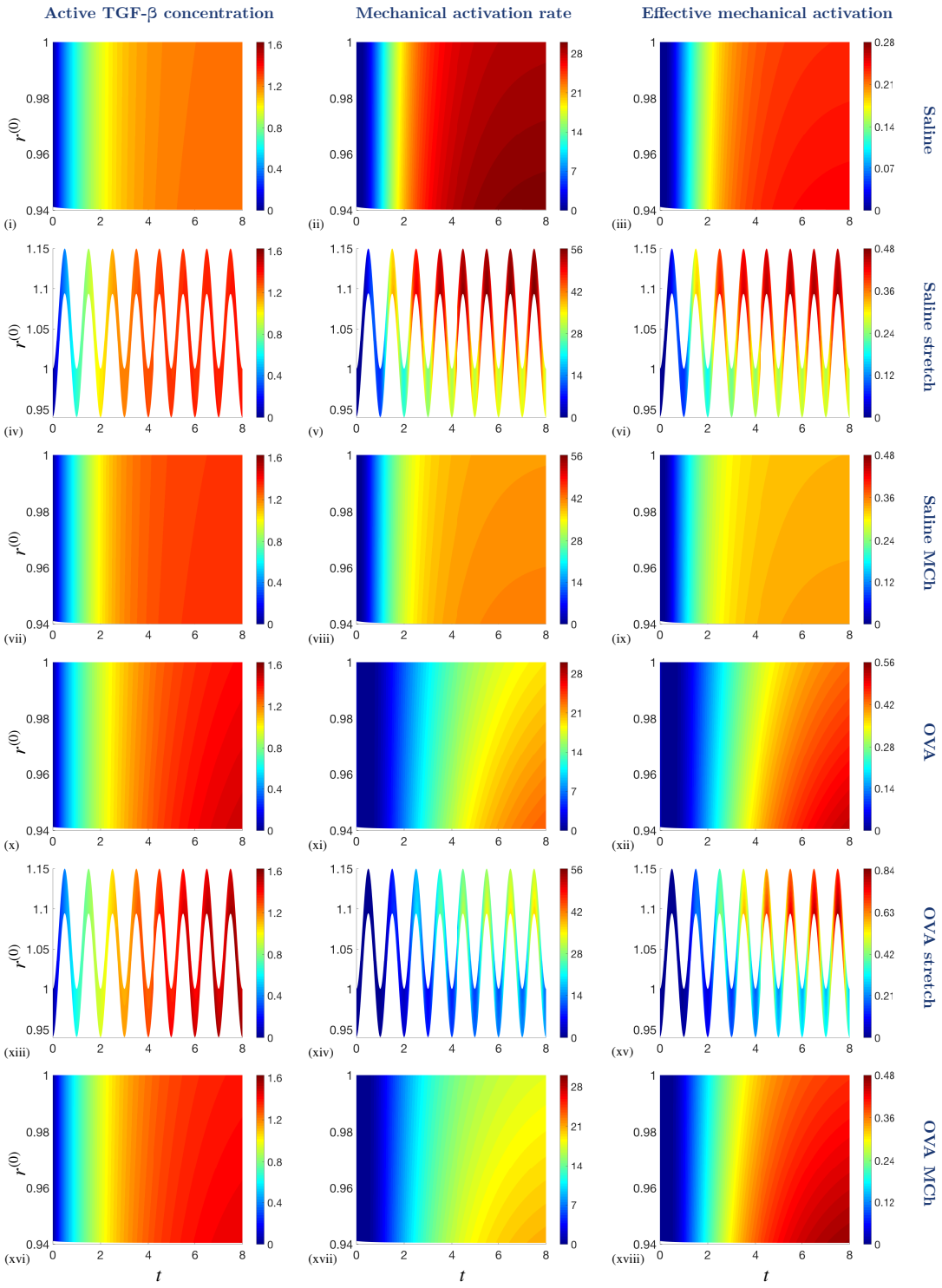

Figure 6.7: Concentration of active TGF-β, a, (1st column), rate of mechanical activation, $\hat{\kappa}_m$ (5.1.9), (2nd column) and the effective mechanical activation of TGF-β, $\Phi_c\Phi_m\hat{\kappa}_m$ in (5.1.8), (3rd column) plotted as functions of time, t, and deformed radius, $r^{(0)}$. Results correspond to those in Figure 6.6 for the (i)–(ix) saline and (x)–(xviii) OVA-challenged mouse PCLS. Simulated parameter values are provided in Table C.7 in Appendix C.3.

MCh challenges have a negative effect on the activation of TGF-β in the OVA PCLS due to the increased ASM mass generating contractile force alongside the stiffer ECM (*cf.* Figures 6.7 (i), (vii) and (x), (xvi), respectively; see also Figure 6.6). We have uncovered similar findings in Section 6.1, where we have observed that an increase in ASM contractile force, concurrent with ECM strain-stiffening, leads to comparably stressed constituents, a decrease in the difference in constituent von Mises stress and an overall reduction in the rate of mechanical activation of TGF-β.

Although our results resemble the experimentally observed behaviour in Figure 6.6 (ii), the thin-PCLS model may not be appropriate for investigating highly contracted ASM in the mouse PCLS. Experimentally, exposure to MCh causes exaggerated narrowing of the airway, which is not visible in the thin-PCLS model results (*cf.* Figures 6.7 (i), (vii)). The radial thickness of the mouse airway wall is very small and hence, the geometry of the mouse airway in the thin-PCLS model consists of very little tissue axially and radially (refer to Figure 4.2). Extreme contraction of the airway, however, requires significant axial thinning of the PCLS in order to preserve incompressibility. Therefore, the thin-PCLS model cannot replicate the significant radial contraction of the mouse airway, that is observed experimentally, due to the lack of deformable PCLS tissue.

6.3 Summary

In this chapter we have compared the data obtained in two separate series of experiments to results obtained via the thin-PCLS model. Firstly, in Section 6.1, comparisons were made to the data obtained in the cyclically stretched human PCLS and secondly, in Section 6.2, to the data obtained in the OVA-induced asthma mouse PCLS.

Our results in Section 6.1 successfully replicate the qualitative behaviour of the experimental observations in the human PCLS, whereby the concentration of active TGF-β increases with increased amplitude of imposed cyclic stretch (Tatler 2016). Moreover, we have observed that there are two possible thresholds leading to the increase in the mechanical activation of TGF-β; one which acts upon the application of stretch, and a second which acts for high amplitude

stretching. Though much greater than that in the unstretched PCLS, the difference in constituent von Mises stress is similar for stretches with an amplitude of 5%, 10% and 15%. This is due to the increasingly contracted ASM (as TGF-β progresses) and increasingly strain-stiffened ECM (associated with imposed stretch). As a result, the rate of mechanical activation of TGF-β and the subsequent concentration of active TGF-β is similar for these amplitude stretches. On the other hand, for stretches with an amplitude of 20% and 25%, we have demonstrated that the contractile force generated by the ASM saturates prior to the saturation of the rate of mechanical activation of TGF-β. Consequently, the exponential strain-stiffening of the ECM at high amplitude stretching drives differences in the constituent von Mises stress. As a result, the rate of mechanical activation of TGF-β increases for high amplitude stretching and ultimately gives rise to high concentration of active TGF-β. Therefore, we have revealed a potential mechanism that is responsible for the increase in the concentration of active TGF-β in the human PCLS in response to imposed stretch.

Our results in Section 6.2 resemble the experimentally observed change in the concentration of active TGF-β in the OVA-induced asthma mouse PCLS (Tatler 2019). The volume fractions of the constituents in the mouse PCLS were provided by Brook et al. (2019) and informed the thin-PCLS model. The results of the thin-PCLS model were then compared to the PSmad2 signalling activity data collected in the mouse PCLS by Tatler (2019). We have observed that increased ASM and ECM mass, imposed cyclic stretch and MCh challenge increases the concentration of active TGF-β in the mouse PCLS, relative to the saline control. However, relative to the respective control groups, imposed stretch gives rise to a more significant increase in the concentration of active TGF-β in the saline PCLS (relative to the saline control) compared to that in the OVA PCLS (relative to the OVA control). Moreover, we have observed that MCh challenge in the OVA PCLS decreases the mechanical activation of TGF-β relative to the OVA control. Our results suggest that the stiff ECM in the OVA PCLS influences the difference in the constituent von Mises stress in two ways; firstly during imposed stretch where ECM strain-stiffening is consequently not as significant in the stiff OVA PCLS than in the saline PCLS, and secondly during MCh challenge where increased contraction of the ASM leads to comparably stressed constituents and reduces the mechanical activation of TGF-β.

Despite agreement experimental results, however, we note that the thin-PCLS model may not be an appropriate representation of the mouse PCLS to examine significant contraction of the airway induced by an exogenous contractile agonist (*i.e.* MCh). Realistically, in the absence of imposed stretch, the outer radius of the airway wall should be relatively free to move as it is tethered to a more compliant, compressible parenchyma, which would require imposition of a stress free boundary condition instead of a displacement condition that is imposed. Therefore, further investigations should consider a stress condition at the outer radius, to allow the thin geometry of the mouse PCLS to narrow radially to a greater extent in the presence of high contractile force.

In this chapter, we have shown that the thin-PCLS model, and in particular the representation of the mechanical activation of TGF-β via the difference in constituent von Mises stress, may explain the underlying mechanisms for the mechanical activation of TGF-β that is observed experimentally. Specifically, we have demonstrated that when the constituents are comparably stressed (*i.e.* the difference in constituent von Mises stress is near zero), the mechanical activation of TGF-β is inhibited and represents insufficient strain transmission between the constituents, via the interconnecting integrins, that consequently does not unfold the latent complex encapsulating TGF-β. Furthermore, our results obtained in this chapter are supported by our observations in the parameter explorations in Section 4.4 and our mechanotransductive feedback investigations in Section 5.2.2.

CHAPTER 7

Conclusions

Despite its prevalence in the population, the causes of asthma remain poorly understood; in particular, the feedback mechanisms linking inflammation, bronchoconstriction and cytokine activation are yet to be elucidated. To help address this, we coupled subcellular mechanotransductive signalling pathways to nonlinear airway biomechanics and investigated the cell-mediated activation of TGF-β. In this chapter we summarise our main findings and suggest future investigations.

Our asymptotic reduction and findings in Chapter 2 suggest that a balance is required between the rate of ASM proliferation, degradation and phenotype switching to allow for a bi-stable regime where there are two positive steady states; one with a low concentration of active TGF-β and the other with a high concentration of active TGF-β (and as a result, increased ASM and ECM density). We associate the former with a healthy homeostatic state and the latter with a diseased (asthmatic) state. During an asthmatic exacerbation, simulation results demonstrate that the frequency of exposures to a stimulant and the clearance of active TGF-β following the exacerbation are critical determinants of disease development, whereby loss of the healthy homeostatic state results in excessive contraction of the ASM and accumulation of ECM, further up-regulating TGF-β production through a positive mechanotranductive feedback loop. Our results suggest that patients who are regularly exposed to an irritant experience worsening symptoms and develop long-term irreversible airway remodelling. We have shown that allowing adequate recovery time or improving recovery time (*i.e.* reduced frequency and sufficient active TGF-β

clearance) between successive exacerbations returns the healthy homeostatic state. Therefore, increasing the clearance of active TGF-β could be a possible method of asthma management or treatment.

Thereafter, in Chapter 3, we developed a nonlinear fibre-reinforced biomechanical model of an airway in PCLS, an *ex vivo* assay widely used for studying asthmatic airway biomechanics, that accommodates agonist-induced ASM contractility and ECM strain-stiffening. Direct numerical simulation of the full model (by means of the FEBio software) reveals the internal stress state of an axisymmetric airway within a PCLS under imposed deformation, and highlights the distinct qualitative and quantitative differences induced by ASM contractility. Such information is of key importance in interpreting PCLS experiments, and in particular those that seek to understand the feedback mechanisms linking inflammation, airway mechanics and TGF-β activation. However, the computational complexity of this model precludes thorough investigation of the parameter space, or mathematical analysis. To address this, in Chapter 4, we considered two reductions of the full model. First, we adopted a membrane representation (where axial variation is neglected *a priori*, and the PCLS thickness remains unchanged upon deformation). Secondly, and in view of the typical dimensions of the PCLS and numerical evidence, we considered an asymptotic reduction, appropriate for the limit in which the PCLS thickness is much smaller than the typical airway radius, and in which we are able to retain a description of the radial and axial airway deformation and the associated stresses. In each case, we reduced the model to calculations in one spatial dimension; the membrane model admits analytical solutions, while in thin-PCLS-limit the model reduces to a pair of coupled nonlinear ODEs describing the deformation, numerical solutions to which are obtained via a shooting method. We find that the membrane model is unable to capture the full model behaviour, but that the asymptotically-reduced model provides an excellent approximation to the full model, at reduced computational cost.

The computational tractability of our thin-PCLS-limit approximation allowed us to efficiently explore the effects of material parameter variation on the stress and tissue deformation that leads to the mechanical activation of TGF-β. Importantly, we revealed regimes where the constituents are comparably stressed due to ECM stiffness and ASM contractility. Uncovering these parameter regimes

helped us to interpret our subsequent results where we coupled the dynamical model, describing the change in concentration of active TGF-β, to the biomechanical descriptions of TGF-β activation in a cyclically stretched PCLS to investigate the cell-mediated activation of TGF-β.

Simulations in Chapter 5 uncover a positive mechanotransductive feedback loop: TGF-β activation induces contraction of the ASM and prescribed cyclic stretch causes strain-stiffening of the ECM fibres that increases the difference in the constituent von Mises stress, which up-regulates the mechanical activation of TGF-β. Furthermore, our results demonstrate that including the spatial-dependence of ASM-generated contractile force is of vital importance in order to understand how the concentration of active TGF-β, and hence the amount of contractile force generated by the ASM, may increase in the airway wall. Crucially, our computationally tractable model allows for comprehensive investigation of the mechanisms underpinning pro-remodelling and contractile cytokine activation in asthmatic airways, a key aspect of the pathogenesis and presentation of asthma, that has only recently received attention.

Comparisons were made between simulation results and experimental data obtained from both cyclically stretched human PCLS as well as ovalbumin (OVA)-induced asthma mouse PCLS in Chapter 6. In both cases our results successfully replicated the qualitative behaviour of the experimental observations. Moreover, our model reveals a potential mechanism that is responsible for the increase in the concentration of active TGF-β in the human PCLS in response to imposed stretch. Though much greater than that in the unstretched PCLS, the difference in constituent von Mises stress, and hence, the concentration of active TGF-β is similar for low amplitude stretches due to the increasingly contracted ASM (as TGF-β progresses) and increasingly strain-stiffened ECM (associated with imposed stretch). In contrast, for high amplitude stretches, we have demonstrated that the contractile force generated by the ASM saturates prior to the saturation of the rate of mechanical activation of TGF-β, and consequently, the exponential strain-stiffening of the ECM drives significant differences in the constituent von Mises stress. As a result, the rate of mechanical activation of TGF-β increases for high amplitude stretching and ultimately gives rise to high concentration of active TGF-β.

Our results suggest that the stiff ECM in the OVA-challenged mouse PCLS influences the difference in the constituent von Mises stress in two ways; firstly during imposed stretch where ECM strain-stiffening is consequently not as significant in the stiff OVA PCLS than in the saline PCLS, and secondly during methacholine (MCh) challenge where increased contraction of the ASM leads to comparably stressed constituents and reduces the mechanical activation of TGF-β. Despite agreement with experimental results, however, the thin-PCLS model may not be an appropriate representation of the mouse PCLS to examine significant contraction of the airway induced by MCh. Realistically, in the absence of imposed stretch, the outer radius of the airway wall should be relatively free to move as if it is tethered to a more compliant, compressible parenchyma, which would require imposition of a stress boundary condition instead of a displacement condition that is imposed. Therefore, further investigations should consider a stress condition at the outer radius, to allow the thin geometry of the mouse PCLS to narrow radially to a greater extent in the presence of high contractile force. A stress boundary condition at the outer radius should be easy to impose computationally but would require asymptotic reformulation in the thin-PCLS model in Chapter 4.

Exaggerated contraction of ASM and elevated concentrations of active TGF-β in the airway are both associated with asthma. Our results suggest that contraction of the ASM, induced by active TGF-β signalling pathways, generates a difference in the stress states of the airway wall constituents and consequently initiates a positive mechanotransductive feedback loop of TGF-β activation. In the presence of low to moderate amplitude stretching of the airway, however, the constituents in the airway wall are comparably stressed and the concentration of TGF-β is moderate. The imposed stretch of the airway may represent deep inspirations that temporarily alleviate bronchconstriction in the healthy airway. Using the thin-PCLS model, future work could focus on investigating the link between the amount of contractile force generated by the ASM and the amplitude of imposed stretch, and associated strain-stiffening of the ECM, to examine the effect of deep inspirations on the mechanical activation of TGF-β that could potentially limit airway remodelling. To do so, a detailed parameter fitting with experimental data would be required.

Undertaking parameterisation and model calibration would be the primary fo-

cus of future work. Moreover, validation of the thin-PCLS model would be required once spatial-dependence of contractile force is facilitated in FEBio. In addition, as the PCLS thickness is reduced, we observe rapid variations in the axial and shear stress components near the inner and outer airway radii that are not captured by the thin-PCLS (or membrane) model; a boundary layer analysis of these features forms a natural extension of this work.

Other important future considerations include developing our thin-PCLS model to accommodate, for example, spatially-dependent airway composition data and (or) the influence of the concentration of active TGF-β on the stiffness of the ECM relative the the ASM. Both advancements exploit the computational tractability and flexibility of the thin-PCLS model. The former would involve refining the volume fractions of the ECM and ASM to functions of radius according to the data provided by Brook et al. (2019), which details the distribution of the ECM and ASM across the airway of OVA-challenged mice PCLS. This would be of particular interest due to the build up of ASM contractile force, and subsequently elevated concentration of active TGF-β, at the inner radius of the airway that we have observed in our simulations. The latter would involve refining the parameter μ to a function of active TGF-β concentration using the same approach as the refinement of α (that defines the TGF-β-induced contractile force generated by the ASM) in Section 5.1. We expect to observe another mechnotransductive feedback loop, whereby the TGF-β-induced increase in ECM stiffness may up-regulate the mechanical activation of TGF-β.

A current limitation of the thin-PCLS model is the constrained mixture theory representation of the mechanical activation of TGF-β. The constrained mixture theory framework means that we cannot consider the different strain rates of the two constituents and that it is necessary to consider the difference in the constituent stresses. A more realistic representation of the cell-mediated activation of TGF-β would account for the constituents moving past one another. It could be that the differing strain rate is important in the mechanical activation of TGF-β but it is not possible to investigate this with a constrained mixture. Therefore, more advanced considerations include unconstrained multiphase solid mechanics and airway constituent growth. Given that the timescale of PCLS experiments is too short to replicate the behaviour *in vivo*, future work could also consider coupling the full dynamical model (that describes the rate

of change in density of the airway wall constituents) to an intact airway model in order to investigate the mechanisms underlying cell-mediated activation of TGF-β *in vivo*. This coupling would require significant development; firstly, a multiplicative decomposition of the deformation tensor in the biomechanical model (into an elastic and growth part) would need to be accounted for, and secondly, a stress boundary condition would need to be applied at the outer radius of an airway in plane strain.

In light of our suggestions for model developments, future experiments that aim to quantify the stiffness of ECM in response to dose dependent treatments of TGF-β, and likewise, those that aim to quantify the concentration of active TGF-β for various cultured stiffnesses would be extremely beneficial for model parameterisation and validation. Experimental data collected by Ramis and Tatler (2019) quantifies the rate of ASM proliferation in response to ECM stiffness in order to investigate their hypothesis that the micro-environment within a stiffer airway affects the phenotype of ASM and initiates asthma development. Human ASM cells, collected from the healthy bronchial tissue of three donors, were cultivated for a week in hydro-gels of different stiffnesses and the Psmad2 signalling activity was quantified to indicate the cell volume increase and the rate of ASM proliferation in response to the different matrix stiffnesses. A hydro-gel that was the same stiffness as the ASM cells was used to replicate the physiological healthy airway, and hydro-gels that were 6 times and 12 times stiffer than the ASM cells were used to resemble the pathological airway. The results of Ramis and Tatler (2019) demonstrate that the increased stiffness of the micro-environment increases PSmad2 activity and hence the rate of proliferation of the ASM. The described data would be crucial for parameterisation and validation of a model that couples the full dynamical system to an intact airway model. Ultimately, this proposed model may be used for further investigations, elucidating the multiple underlying mechanotransductive feedback mechanisms linking cell-mediated TGF-β activation and the accumulation of remodelled airway wall constituents in the asthmatic airways *in vivo*.

APPENDIX A

Biology

A.1 Terminology

Table A.1: Table of biological acronymns introduced in Chapter 1.

Acronym	Description
TGF-β	Transforming growth factor β
ASM	Airway smooth muscle
ECM	Extracellular matrix
LLC	Large latent complex
LAP	Latency associated protein
LTBP	Latent TGF-β binding protein
PCLS	Precision-cut lung-slice
MCh	Methacholine
OVA	Ovalbumin

A.2 Experimental protocol used to prepare human lung-slices

Details for the method used to obtain human PCLS provided by Tatler (2016).

Materials:

- DMEM + 2% L-Glut + 4% P/S + 4% Amphotericin
- Hanks balanced salt solution (HBSS)
- 24 well TC treated plates
- Autoclaved 2% low melting point agarose
- Vibratome (Leica VT1200S)
- Superglue
- Ice
- Angled scissors
- Scalpels
- Razor blade
- Hot block

Method:

1. Melt the 2% agarose by heating to over 65°C.
2. Chill HBSS on ice.
3. Reduce temperature to 41-42°C and maintain temperature, do not allow to cool as this will set the agarose.
4. Place lung tissue into 10cm petri dish containing chilled HBSS on ice.
5. Using a 21g needle and 10ml Syringe inject ∼20ml (may need more or less depending on size of tissue) 2% agarose into the pleura to inflate the tissue (inject at different sites but not too many as tissue will not inflate).
6. Transfer into 50ml falcon containing ice cold HBSS and incubate on ice for at least 2 hours to allow the agarose to set.
7. Set up the vibratome:
   i Fill the buffer tray with ice cold HBSS.
   ii Add ice to the ice bath.
   iii Fix the razor blade into position.
   iv Vibratome settings: 250um slice thickness, speed between 0.5 and

1mm/s amplitude 1.5mm.

8. In a petri dish cut the lung tissue using a scalpel to create a flat edge.
9. Using the superglue stick the cut lung tissue to the specimen holder.
10. Secure specimen holder to the vibratome.
11. Adjust the height of the blade and the distance to cut according to the tissue.
12. Start cutting slices. Use angled scissors to prevent tissue slices from folding back on themselves whist being cut and use these to transfer the slices into a falcon containing DMEM + 2% L-Glut + 4% P/S + 4% Amphotericin (make sure that there is no superglue on the slices)
13. Use a scalpel to remove the tissue from specimen holder and repeat steps 7-12 until all of the tissue has been sliced.
14. Incubate the PCLS over night at 37°C in DMEM + 2% L-Glut + 4% P/S + 4% Amphotericin.
15. The following morning plate the PCLS in to 24 well plates, 1 PCLS / well.
16. Alternatively cryopreserve the PCLS in FCS + 10% DMSO (n=6 PCLS per vial) using Mr Frosty boxes.

APPENDIX B

Biomechanical Models

B.1 Full model numerics

The following sections outline the numerical simulations of the full bioechanical model in the uncoupled (developed in Chapter 3) and coupled (Chapter 5) case.

B.1.1 Uncoupled simulation

In this section we describe the steps taken and the scripts used to simulate the full biomechanical model developed in Chapter 3.

First steps taken in the finite element software suite PreView (complementary to FEBio (Maas et al. 2012)):

- Dimensional geometry of the PCLS created (see Figure 3.1).
- Appropriate size of mesh (of hexahedral elements) chosen (refer to Figure 3.2).
- Material properties of the PCLS selected (and listed as the named options in PreView): *Uncoupled solid mixture* comprising
  - *Mooney-Rivlin* (reduced to Neo Hookean as in 1.5.11) components corresponding to W^*_{iso} in (3.1.17).
  - *fiber with exponential-power law (uncoupled formulation)* component corresponding to W^*_{mani} in (3.1.17b).
  - *uncoupled prescribed uniaxial active contraction* component correspond-

ing to W^*_{mact} in (3.1.17a).

- Meshed geometry of the PCLS exported to `PCLS.feb`.

Hereafter, our simulations run entirely from our single Matlab script that exploits `system` calls to FEBio. Steps taken in our Matlab script:

1. Dimensional material parameters determined.
2. `PCLS.feb` imported via `xml2struct.m` (Falkena 2019).
3. Outer boundary nodes identified within stored structure and converted from Cartesian to cylindrical co-ordinates via `cart2pol`.
4. Axisymmetrical displacement prescribed and applied to outer boundary nodes to determine the outer boundary conditions.
5. Outer boundary conditions converted to Cartesian co-ordinates (for compatibility with FEBio).
6. Single node at $Z = 0$ fixed with zero axial displacement to avoid obtaining a constant displacement solution.
7. Fibre orientation defined.
8. New text script, `PCLSNew.feb`, created via `fopen` and `fprintf` in the same format as `PCLS.feb` with chosen material parameter values, updated outer boundary conditions, embedded fibres and updated *logfile* of chosen outputs.
9. `PCLSNew.feb` solved in FEBio via Matlab `system` call.
10. Deformed nodal position, element centroid position and element Cauchy stress components at the element centroid position outputted in separate text files.
11. Output files imported into Matlab via customised import scripts.
12. Data converted from Cartesian to cylindrical co-ordinates via `cart2pol`, non-dimensionalised and expressed in the undeformed configuration, (R, Z).
13. Element centroid data projected (interpolated) to the nodal positions and saved.

B.1.2 Coupled simulation

In this section we describe the steps taken in FEBio and the scripts used to simulate the full coupled biomechanical model developed in Chapter 5.

The first steps are taken in PreView as in Section B.1.1. Thereafter, our simulations run entirely from our single Matlab script that makes multiple `system` calls to FEBio. Steps taken in our Matlab script:

1. Dimensionless rate parameters chosen, time span chosen and active TGF-β concentration initialised as in (5.1.13).
2. Stretch determined for $t = 0$ in (5.1.12).
3. ASM contraction determined given the current concentration of active TGF-β via (5.1.10) with (5.2.1).
4. Difference in constituent von Mises stress determined via steps 1–13 in Section B.1.1.
5. Mechanical activation of TGF-β, $\hat{\kappa}_m(\sigma_{\text{diff}})$, determined via (5.1.9).
6. `ode45` used to solve (5.1.8).
7. Steps 2–5 repeated for each time-step in 6 (replacing $t = 0$ with the current time-step).

It should be noted that FEBio requires dimensional parameters (SI units), whilst the dynamical model is dimensionless. Therefore, we highlight steps 1 and 12 in Section B.1.1 that correctly dimensionalises and non-dimensionalises quantities so that the parameters are consistent and importantly, compatible in both the dynamical model and biomechanical model coupling in 7 in Section B.1.2; however, this increases the number of calculations at each time-step.

B.2 Thin-PCLS-limit model numerics

Simulations of the thin-PCLS model are significantly less computationally expensive than those in the full model above, and thus the thin-PCLS model provides a tractable method to complete parameter sweeps. Furthermore, such simulations do not require any additional software packages (*i.e.* FEBio) beyond those available in Matlab.

Similar to the thin-PCLS model, shell theories seek to reduce the deformation governing equations. However, shell theories are applicable for radially thin-walled tissues and the thin-PCLS model reduction is applicable in the axially thin limit. Typically shell theories are used to model non-axisymmetry, growth and buckling, which involves an effective stiffness that results in greater resistance to tissue extension than bending. Conversely, the effective stiffness of the PCLS tissue results in greater resistance to bending than extension or compression. We are not aware of any axisymmetrically stretched thin shell reductions that numerically solve the deformation governing equations via the shooting method described below.

B.2.1 Uncoupled simulation

Simulations run efficiently from a single Matlab script. Steps taken in our Matlab script:

1. Dimensionless parameters specified.
2. Boundary value problem defined for the coupled ODES (4.2.13), subject to the imposed fixed stretch at the outer radius (4.2.5), using `bvp4c`.
3. Shoot for solution to (4.2.13) that satisfies the relation (4.2.8b) via `fsolve`.
4. Leading order deformation obtained. Cauchy stress components and constituent von Mises stresses follow directly.

Parameter sweeps (for example, in Section 4.4) are carried out by simply repeating steps 2–4 above in a `for` loop over the chosen parameter span.

B.2.2 Coupled simulation

Again, simulations run from a single Matlab script. Steps taken in our Matlab script:

1. Dimensionless parameters specified, time span chosen and active TGF-β concentration initialised as in (5.1.13).
2. Stretch determined for $t = 0$ in (5.1.12).
3. ASM contraction determined given the current concentration of active TGF-β (as a function of undeformed radius, R, via `polyfit`, required by the `bvp4c` syntax) via (5.1.10).
4. Boundary value problem defined for the coupled ODES (4.2.13), subject to the imposed fixed stretch at the outer radius, using `bvp4c`.
5. Shoot for solution to (4.2.13) that satisfies the relation (4.2.8b) via the efficient algorithm `fsolve`.
6. Leading order deformation obtained. Cauchy stress components and constituent von Mises stresses follow directly. Difference in constituent von Mises stress determined.
7. Mechanical activation of TGF-β, $\hat{\kappa}_m(\sigma_{\text{diff}})$, determined via (5.1.9).
8. `ode45` used to solve (5.1.8).
9. Steps 2–7 repeated for each time-step in 8 (replacing $t = 0$ with the current time-step).

It should be noted that `polyfit` in step 3 is required to represent spatial variation of (5.1.11) in `bvp4c`. In the instance of averaged contraction (5.2.1) (*i.e.* comparisons to the full model) it is not needed and as a result, the overall run time of these simulations is much reduced.

B.3 Thin-PCLS-limit model reduction

Guided by the numerical evidence (provided in Section 3.2.2 and below), in this section we demonstrate that the general expansions, for which $r = r(R, Z)$ and the leading order term for $\mathscr{P}$ is $\mathcal{O}(\varepsilon^{-2})$ (to obtain a proper leading order balance in the Cauchy stress) can be reduced to that shown in (4.2.1).

The general asymptotic expansions for each of the deformation variables are as follows,

$$r = r^{(0)}(R, Z) + \varepsilon r^{(1)}(R, Z) + \varepsilon^2 r^{(2)}(R, Z) + \mathcal{O}(\varepsilon^3), \tag{B.3.1a}$$

$$z = z^{(0)}(R, Z) + \varepsilon z^{(1)}(R, Z) + \varepsilon^2 z^{(2)}(R, Z) + \mathcal{O}(\varepsilon^3), \tag{B.3.1b}$$

$$\begin{aligned}\mathscr{P} = \varepsilon^{-2}\mathscr{P}^{(-2)}(R, Z) + \varepsilon^{-1}\mathscr{P}^{(-1)}(R, Z) + \mathscr{P}^{(0)}(R, Z) \\ + \varepsilon\mathscr{P}^{(1)}(R, Z) + \varepsilon^2\mathscr{P}^{(2)}(R, Z) + \mathcal{O}(\varepsilon^3).\end{aligned} \tag{B.3.1c}$$

As outlined in Section 4.2, we assume that Φ_c, Φ_m, μ, ω, ζ and α are all $\mathcal{O}(1)$ constants in the strain energy-function for the whole tissue, W (3.1.42). Therefore, the following derivatives of the strain-energy functions are $\mathcal{O}(1)$ constants: W_{c1} (3.1.45a), W_{m1} (3.1.45b) and W_1 (3.1.46a). The derivative of the strain-energy function with respect to the fourth invariant, W_4 (3.1.46b), is a function of radius, r. Therefore, using the asymptotic expansions (B.3.1) and expanding for small ε in (3.1.45d), we obtain the leading order terms in the derivative of the strain energy-function, with respect to the fourth invariant, for the ASM, W_{c4}, and the ECM, W_{m4}, as previously in (4.2.2) and correspondingly for the whole tissue, $W_4^{(0)}$ (4.2.3).

At the next order, $\mathcal{O}(\varepsilon)$, we obtain

$$W_{c_4}^{(1)} = 0, \tag{B.3.2a}$$

$$\begin{aligned} W_{m_4}^{(1)} = {} & \omega \exp\left(\zeta\left(\left(\frac{r^{(0)}}{R}\right)^2 - 1\right)^2\right) \\ & \times \left(\frac{2r^{(0)}r^{(1)}}{R^2}\mathrm{H}\left({r^{(0)}}^2 - R^2\right) + \left(\left(\frac{r^{(0)}}{R}\right)^2 - 1\right)\mathrm{H}\left(\frac{2r^{(0)}r^{(1)}}{R^2}\right)\right) \\ & + \omega \exp\left(\zeta\left(\left(\frac{r^{(0)}}{R}\right)^2 - 1\right)^2\right) \\ & \times 4\zeta\left(\frac{{r^{(0)}}^3 r^{(1)}}{R^4} - \frac{r^{(0)}r^{(1)}}{R^2}\right)\left(\left(\frac{r^{(0)}}{R}\right)^2 - 1\right)\mathrm{H}\left({r^{(0)}}^2 - R^2\right), \end{aligned} \tag{B.3.2b}$$

and correspondingly for the whole tissue,

$$W_4^{(1)} = \Phi_c W_{c_4}^{(1)} + \Phi_m W_{m_4}^{(1)}, \tag{B.3.3}$$

where, as previously, the notation $W_{i_4}^{(k)}$ for $i \in \{c, m\}$ refers to the $\mathcal{O}(\epsilon^k)$ term in (3.1.45c) and (3.1.45d).

B.3.1 Governing equations

Using the expansions (B.3.1) and expanding for small ε in (3.1.55)), at the leading order, $\mathcal{O}(\varepsilon^{-2})$, the governing equations (3.1.55) read

$$\frac{\partial r^{(0)}}{\partial Z}\frac{\partial \mathscr{P}^{(-2)}}{\partial R} - \frac{\partial r^{(0)}}{\partial R}\frac{\partial \mathscr{P}^{(-2)}}{\partial Z} = 0, \tag{B.3.4}$$

subject to the following free boundary conditions at the upper, lower and inner surfaces of the PCLS (3.1.58):

at $Z = \pm\frac{1}{2}$:

$$\frac{\partial r^{(0)}}{\partial R}\mathscr{P}^{(-2)} = 0, \tag{B.3.5a}$$

at $R = R_{\text{in}}$:

$$\frac{\partial z^{(0)}}{\partial Z}\mathscr{P}^{(-2)} = 0, \tag{B.3.5b}$$

$$\frac{\partial r^{(0)}}{\partial Z}\mathscr{P}^{(-2)} = 0. \tag{B.3.5c}$$

At the next order, $\mathcal{O}(\varepsilon^{-1})$, the governing equations (3.1.55) read

$$\frac{\partial r^{(1)}}{\partial Z}\frac{\partial \mathscr{P}^{(-2)}}{\partial R} + \frac{\partial r^{(0)}}{\partial Z}\frac{\partial \mathscr{P}^{(-1)}}{\partial R} - \frac{\partial r^{(1)}}{\partial R}\frac{\partial \mathscr{P}^{(-2)}}{\partial Z} - \frac{\partial r^{(0)}}{\partial R}\frac{\partial \mathscr{P}^{(-1)}}{\partial Z} = 0, \tag{B.3.6}$$

subject to the free boundary conditions (3.1.58):

at $Z = \pm\frac{1}{2}$:

$$\frac{\partial r^{(1)}}{\partial R}\mathscr{P}^{(-2)} + \frac{\partial r^{(0)}}{\partial R}\mathscr{P}^{(-1)} = 0, \tag{B.3.7a}$$

at $R = R_{\text{in}}$:

$$\frac{\partial z^{(1)}}{\partial Z}\mathscr{P}^{(-2)} + \frac{\partial z^{(0)}}{\partial Z}\mathscr{P}^{(-1)} = 0, \tag{B.3.7b}$$

$$\frac{\partial r^{(1)}}{\partial Z}\mathscr{P}^{(-2)} + \frac{\partial r^{(0)}}{\partial Z}\mathscr{P}^{(-1)} = 0. \tag{B.3.7c}$$

A solution to (B.3.4) that satisfies the free boundary conditions (B.3.5) is $\mathscr{P}^{(-2)} = 0$, and thus, a solution to (B.3.6) that satisfies the boundary conditions (B.3.7) is $\mathscr{P}^{(-1)} = 0$. This solution is consistent with our numerical solution obtained in FEBio in Section 3.2 (*e.g.* Figure 3.3), where the pressure is an $\mathcal{O}(1)$ quantity, *i.e.* where $\mathscr{P}^{(0)}$ is the leading order term. Subsequently, at $\mathcal{O}(1)$, the governing

equations (3.1.56) and (3.1.55) read

$$\frac{\partial r^{(0)}}{\partial R}\frac{\partial z^{(0)}}{\partial Z} - \frac{\partial r^{(0)}}{\partial Z}\frac{\partial z^{(0)}}{\partial R} - \frac{R}{r^{(0)}} = 0, \tag{B.3.8a}$$

$$\begin{aligned}\frac{R}{r^{(0)}}\frac{\partial^2 r^{(0)}}{\partial Z^2} + \frac{\partial r^{(0)}}{\partial Z}\Bigg(&\frac{\partial r^{(0)}}{\partial R}\frac{\partial^2 z^{(0)}}{\partial Z^2} - \frac{\partial z^{(0)}}{\partial R}\frac{\partial^2 r^{(0)}}{\partial Z^2} \\ &- \frac{\partial r^{(0)}}{\partial Z}\frac{\partial^2 z^{(0)}}{\partial R\partial Z} + \frac{\partial z^{(0)}}{\partial Z}\frac{\partial^2 r^{(0)}}{\partial R\partial Z} + \frac{\partial r^{(0)}}{\partial Z}\frac{R}{{r^{(0)}}^2}\Bigg) = 0,\end{aligned} \tag{B.3.8b}$$

$$\begin{aligned}\frac{2R}{r^{(0)}}\frac{\partial^2 z^{(0)}}{\partial Z^2} + \left(\frac{\partial z^{(0)}}{\partial Z}\right)^2\frac{\partial^2 r^{(0)}}{\partial R\partial Z} - \frac{\partial z^{(0)}}{\partial R}\frac{\partial z^{(0)}}{\partial Z}\frac{\partial^2 r^{(0)}}{\partial Z^2} \\ - \frac{1}{2W_1}\frac{\partial r^{(0)}}{\partial R}\frac{\partial \mathscr{P}^{(0)}}{\partial Z} + \frac{\partial r^{(0)}}{\partial Z}\Bigg(\frac{\partial z^{(0)}}{\partial R}\frac{\partial^2 z^{(0)}}{\partial Z^2} \\ - \frac{\partial z^{(0)}}{\partial Z}\frac{\partial^2 z^{(0)}}{\partial R\partial Z} + \frac{R}{{r^{(0)}}^2}\frac{\partial z^{(0)}}{\partial Z} + \frac{1}{2W_1}\frac{\partial \mathscr{P}^{(0)}}{\partial R}\Bigg) = 0,\end{aligned} \tag{B.3.8c}$$

subject to the displacement boundary condition at the outer radius (3.1.57),

$$r^{(0)}(1, Z) = r_{\text{dis}}, \tag{B.3.9}$$

and the free boundary conditions (3.1.58):

at $Z = \pm\frac{1}{2}$:

$$\frac{\partial r^{(0)}}{\partial R}\frac{\partial r^{(0)}}{\partial Z}\frac{\partial z^{(0)}}{\partial Z} - \frac{\partial z^{(0)}}{\partial R}\left(\frac{\partial r^{(0)}}{\partial Z}\right)^2 = 0, \tag{B.3.10a}$$

$$\frac{\partial r^{(0)}}{\partial R}\left(\frac{\partial z^{(0)}}{\partial Z}\right)^2 - \frac{\partial z^{(0)}}{\partial R}\frac{\partial r^{(0)}}{\partial Z}\frac{\partial z^{(0)}}{\partial Z} - \frac{\mathscr{P}^{(0)}(R, \frac{1}{2})}{2W_1}\frac{\partial r^{(0)}}{\partial R} = 0, \tag{B.3.10b}$$

at $R = R_{\text{in}}$:

$$\frac{\partial r^{(0)}}{\partial R}\frac{\partial r^{(0)}}{\partial Z}\frac{\partial z^{(0)}}{\partial R} - \frac{\partial z^{(0)}}{\partial Z}\left(\frac{\partial r^{(0)}}{\partial R}\right)^2 + \frac{\mathscr{P}^{(0)}}{2W_1}\frac{\partial z^{(0)}}{\partial Z} = 0, \tag{B.3.10c}$$

$$\frac{\mathscr{P}^{(0)}}{2W_1}\frac{\partial r^{(0)}}{\partial Z} = 0. \tag{B.3.10d}$$

We seek to obtain (4.2.4) which requires $r^{(0)}(R)$. We note that $r^{(0)}(R)$ is a solution to (B.3.8) that satisfies the displacement boundary condition (B.3.9) and the free boundary conditions (B.3.10). Moreover, numerical evidence provided in Figures B.1 1st column (illustrating the effect of reducing the aspect ration, ε, on the first derivative of the radial deformation, r, with respect to Z) shows that the dependence of r on Z is very weak. In view of this, we relegate Z dependence to the next order, and the governing equations (B.3.8) reduce to

$$\frac{\mathrm{d}r^{(0)}}{\mathrm{d}R}\frac{\partial z^{(0)}}{\partial Z} = \frac{R}{r^{(0)}}, \tag{B.3.11a}$$

$$2\frac{\mathrm{d}r^{(0)}}{\mathrm{d}R}\frac{\partial z^{(0)}}{\partial Z}\frac{\partial^2 z^{(0)}}{\partial Z^2} - \frac{1}{2W_1}\frac{\mathrm{d}r^{(0)}}{\partial R}\frac{\partial \mathscr{P}^{(0)}}{\partial Z} = 0, \tag{B.3.11b}$$

and the free boundary conditions (B.3.10) reduce to:

at $Z = \pm\frac{1}{2}$:

$$\frac{\mathrm{d}r^{(0)}}{\mathrm{d}R}\left(\frac{\partial z^{(0)}}{\partial Z}\right)^2 - \frac{\mathscr{P}^{(0)}}{2W_1}\frac{\mathrm{d}r^{(0)}}{\mathrm{d}R} = 0, \tag{B.3.12a}$$

at $R = R_{\mathrm{in}}$:

$$-\left(\frac{\mathrm{d}r^{(0)}}{\mathrm{d}R}\right)^2\frac{\partial z^{(0)}}{\partial Z} + \frac{\mathscr{P}^{(0)}}{2W_1}\frac{\partial z^{(0)}}{\partial Z} = 0. \tag{B.3.12b}$$

as previously in Section 4.2.1.

From (B.3.11a), we note that

$$\frac{\mathrm{d}r^{(0)}}{\mathrm{d}R} \neq 0, \qquad \frac{\partial z^{(0)}}{\partial Z} \neq 0, \tag{B.3.13}$$

and rearrange the reduced boundary conditions (B.3.12) to obtain

$$\mathscr{P}^{(0)}(R,\tfrac{1}{2}) = 2\mathrm{W}_1 \left(\frac{\partial z^{(0)}}{\partial Z}\bigg|_{Z=\frac{1}{2}} \right)^2, \tag{B.3.14a}$$

$$\mathscr{P}^{(0)}(R,-\tfrac{1}{2}) = 2\mathrm{W}_1 \left(\frac{\partial z^{(0)}}{\partial Z}\bigg|_{Z=-\frac{1}{2}} \right)^2, \tag{B.3.14b}$$

$$\mathscr{P}^{(0)}(R_{\mathrm{in}},Z) = 2\mathrm{W}_1 \left(\frac{\mathrm{d}r^{(0)}}{\mathrm{d}R}\bigg|_{R=R_{\mathrm{in}}} \right)^2. \tag{B.3.14c}$$

The boundary condition (B.3.14c) holds for all Z; however, $r^{(0)}$ is independent of Z, and therefore $\mathscr{P}^{(0)}(R)$. Subsequently, the $\mathcal{O}(1)$ governing equations (B.3.11) reduce to

$$\frac{\mathrm{d}r^{(0)}}{\mathrm{d}R}\frac{\partial z^{(0)}}{\partial Z} = \frac{R}{r^{(0)}}, \tag{B.3.15a}$$

$$\frac{\partial^2 z^{(0)}}{\partial Z^2} = 0, \tag{B.3.15b}$$

and provide

$$z^{(0)} = \lambda_z^{(0)}(R)Z, \tag{B.3.16}$$

where the arbitrary function of R arising from the integration of (B.3.23) vanishes due to axial symmetry in $z^{(0)}$ about the axial centre line, $Z = 0$, as previously in (4.2.7). Substituting (B.3.16) into (B.3.14) and (B.3.15) we obtain

$$\mathscr{P}^{(0)}(R) = 2\mathrm{W}_1 \lambda_z^{(0)}(R)^2, \tag{B.3.17a}$$

$$\lambda_z^{(0)}(R_{\mathrm{in}})^2 = \frac{R_{\mathrm{in}}}{r^{(0)}(R_{\mathrm{in}})}, \tag{B.3.17b}$$

as previously in (4.2.8).

So far we have demonstrated that $r^{(0)}(R)$ and $\mathscr{P}^{(0)}$ are appropriate leading order approximations in (4.2.1); we now show that $r^{(1)}(R)$ and $\mathscr{P}^{(1)}(R)$ follow.

Using the preceding information, and in particular (B.3.13), at $\mathcal{O}(\varepsilon)$ the govern-

ing equations read

$$\frac{r^{(1)}}{r^{(0)}} + \frac{r^{(0)}}{R}\left(\frac{\partial r^{(1)}}{\partial R}\frac{\partial z^{(0)}}{\partial Z} + \frac{\mathrm{d}r^{(0)}}{\mathrm{d}R}\frac{\partial z^{(1)}}{\partial Z} - \frac{\partial r^{(1)}}{\partial Z}\frac{\partial z^{(0)}}{\partial R}\right) = 0, \tag{B.3.18a}$$

$$\frac{\partial^2 r^{(1)}}{\partial Z^2} = 0, \tag{B.3.18b}$$

$$\begin{aligned} &2\frac{\mathrm{d}r^{(0)}}{\mathrm{d}R}\frac{\partial z^{(0)}}{\partial Z}\frac{\partial^2 z^{(1)}}{\partial Z^2} - \frac{\partial r^{(1)}}{\partial Z}\frac{\partial z^{(0)}}{\partial Z}\frac{\partial^2 z^{(0)}}{\partial R \partial Z} \\ &+\left(\frac{\partial z^{(0)}}{\partial Z}\right)^2\frac{\partial^2 r^{(1)}}{\partial R \partial Z} + \frac{1}{r^{(0)}}\left(\frac{\partial z^{(0)}}{\partial Z}\right)^2\frac{\partial r^{(1)}}{\partial Z}\frac{\mathrm{d}r^{(0)}}{\mathrm{d}R} \\ &+\frac{1}{2W_1}\left(\frac{\partial r^{(1)}}{\partial Z}\frac{\mathrm{d}\mathscr{P}^{(0)}}{\mathrm{d}R} - \frac{\mathrm{d}r^{(0)}}{\mathrm{d}R}\frac{\partial \mathscr{P}^{(1)}}{\partial Z}\right) = 0, \end{aligned} \tag{B.3.18c}$$

subject to the displacement boundary condition at the outer radius (3.1.57),

$$r^{(1)}(1, Z) = 0, \tag{B.3.19}$$

and the free boundary conditions (3.1.58):

at $Z = \pm\frac{1}{2}$:

$$\frac{\partial r^{(1)}}{\partial Z} = 0, \tag{B.3.20a}$$

$$\begin{aligned} &\left(\frac{\partial z^{(0)}}{\partial Z}\right)^2\frac{\partial r^{(1)}}{\partial R} + 2\frac{\mathrm{d}r^{(0)}}{\mathrm{d}R}\frac{\partial z^{(0)}}{\partial Z}\frac{\partial z^{(1)}}{\partial Z} - \frac{\partial z^{(0)}}{\partial Z}\frac{\partial z^{(0)}}{\partial R}\frac{\partial r^{(1)}}{\partial Z} \\ &-\frac{\mathscr{P}^{(0)}}{2W_1}\frac{\partial r^{(1)}}{\partial R} - \frac{\mathscr{P}^{(1)}}{2W_1}\frac{\mathrm{d}r^{(0)}}{\mathrm{d}R} = 0, \end{aligned} \tag{B.3.20b}$$

at $R = R_{\mathrm{in}}$:

$$\begin{aligned} &\frac{\mathrm{d}r^{(0)}}{\mathrm{d}R}\frac{\partial r^{(1)}}{\partial Z}\frac{\partial z^{(0)}}{\partial R} - \left(\frac{\mathrm{d}r^{(0)}}{\mathrm{d}R}\right)^2\frac{\partial z^{(1)}}{\partial Z} \\ &-2\frac{\mathrm{d}r^{(0)}}{\mathrm{d}R}\frac{\partial r^{(1)}}{\partial R}\frac{\partial z^{(0)}}{\partial Z} + \frac{\mathscr{P}^{(0)}(R_{\mathrm{in}})}{2W_1}\frac{\partial z^{(1)}}{\partial Z} + \frac{\mathscr{P}^{(1)}}{2W_1}\frac{\partial z^{(0)}}{\partial Z} = 0. \end{aligned} \tag{B.3.20c}$$

The $\mathcal{O}(\varepsilon)$ governing equation (B.3.18b) together with the boundary condition (B.3.20a) provides $r^{(1)}(R)$, and hence, the $\mathcal{O}(\varepsilon)$ governing equations (B.3.18)

reduce to

$$\frac{r^{(1)}}{r^{(0)}} + \frac{r^{(0)}}{R}\left(\frac{\partial r^{(1)}}{\partial R}\frac{\partial z^{(0)}}{\partial Z} + \frac{\mathrm{d}r^{(0)}}{\mathrm{d}R}\frac{\partial z^{(1)}}{\partial Z} - \frac{\partial r^{(1)}}{\partial Z}\frac{\partial z^{(0)}}{\partial R}\right) = 0, \tag{B.3.21a}$$

$$2\frac{\partial z^{(0)}}{\partial Z}\frac{\partial^2 z^{(1)}}{\partial Z^2} - \frac{1}{2W_1}\frac{\partial \mathscr{P}^{(1)}}{\partial Z} = 0, \tag{B.3.21b}$$

and, using (B.3.17), reduces the $\mathcal{O}(\varepsilon)$ free boundary conditions (B.3.20) to

at $Z = \pm\frac{1}{2}$:

$$\left(\frac{\partial z^{(0)}}{\partial Z}\right)^2 \frac{\mathrm{d}r^{(1)}}{\mathrm{d}R} - \frac{\mathscr{P}^{(0)}}{2W_1}\frac{\mathrm{d}r^{(1)}}{\mathrm{d}R} - \frac{\mathscr{P}^{(1)}}{2W_1}\frac{\mathrm{d}r^{(0)}}{\mathrm{d}R} = 0, \tag{B.3.22a}$$

at $R = R_{\text{in}}$:

$$-2\frac{\mathrm{d}r^{(0)}}{\mathrm{d}R}\frac{\mathrm{d}r^{(1)}}{\mathrm{d}R}\frac{\partial z^{(0)}}{\partial Z} + \frac{\mathscr{P}^{(1)}}{2W_1}\frac{\partial z^{(0)}}{\partial Z} = 0. \tag{B.3.22b}$$

The free boundary condition (B.3.22b) holds for all Z; however, all terms except $\mathscr{P}^{(1)}$ are independent of Z. Therefore, we conclude, $\mathscr{P}^{(1)}(R)$. Subsequently, the $\mathcal{O}(\varepsilon)$ governing equations (B.3.21) reduce to

$$\frac{r^{(1)}}{r^{(0)}} + \frac{r^{(0)}}{R}\left(\frac{\partial r^{(1)}}{\partial R}\frac{\partial z^{(0)}}{\partial Z} + \frac{\mathrm{d}r^{(0)}}{\mathrm{d}R}\frac{\partial z^{(1)}}{\partial Z} - \frac{\partial r^{(1)}}{\partial Z}\frac{\partial z^{(0)}}{\partial R}\right) = 0, \tag{B.3.23a}$$

$$\frac{\partial^2 z^{(1)}}{\partial Z^2} = 0, \tag{B.3.23b}$$

and provide

$$z^{(1)} = \lambda_z^{(1)}(R)Z, \tag{B.3.24}$$

where, again, the arbitrary function of R arising from the integration of (B.3.23b) vanishes due to the symmetry in $z^{(0)}$ about the axial centre line, $Z = 0$. Substituting (B.3.16) and (B.3.24) into the free boundary conditions (B.3.22) we obtain

$$\mathscr{P}^{(1)} = 4W_1\lambda_z^{(0)}(R)\lambda_z^{(1)}(R), \tag{B.3.25a}$$

$$\lambda_z^{(0)^3}(R_{\text{in}})\lambda_z^{(1)}(R_{\text{in}}) = -\frac{4W_1R_{\text{in}}^2}{r^{(0)^2}(R_{\text{in}})}\left(\frac{r^{(1)^2}(R_{\text{in}})}{r^{(0)^2}(R_{\text{in}})} - \frac{\lambda_z^{(1)^2}(R_{\text{in}})}{\lambda_z^{(0)^2}(R_{\text{in}})}\right). \tag{B.3.25b}$$

To summarise, we have reduced the problem to two leading order variables; the radial deformation, $r^{(0)}(R)$, and the axial stretch, $\lambda_z^{(0)}(R)$. The governing equations together with the free surface boundary conditions up to $\mathcal{O}(1)$ provide the pressure $\mathscr{P}^{(0)}(R)$ in terms of $r^{(0)}(R)$ and $\lambda_z^{(0)}(R)$. The leading order governing equations enforce incompressibility (B.3.15a) subject to the displacement boundary condition at the outer radius (B.3.9) and the free surface boundary conditions via a relation at the inner radius in (B.3.17b). The governing equations together with the free surface boundary conditions up to $\mathcal{O}(\varepsilon)$ provide $z^{(1)} = \lambda_z^{(1)}(R)Z$ in (B.3.24) and $\mathscr{P}^{(1)}(R)$ in (B.3.25a); however, we require a leading order equation that governs the balance of linear momentum to determine the two unknows, $r^{(0)}(R)$ and $\lambda_z^{(0)}(R)$. Therefore, at $\mathcal{O}(\varepsilon^2)$ the linear momentum equations read

$$\begin{aligned}
&\frac{R}{r^{(0)}}\frac{\partial^2 r^{(2)}}{\partial Z^2} + \left(\frac{\partial^2 z^{(0)}}{\partial R\partial Z} + \frac{R}{r^{(0)^2}}\right)\left(\frac{\mathrm{d}r^{(0)}}{\mathrm{d}R}\right)^2 \\
&\qquad - \frac{1}{2W_1}\frac{\partial z^{(0)}}{\partial Z}\frac{\mathrm{d}\mathscr{P}^{(0)}}{\mathrm{d}R} - \frac{W_1 + W_4^{(0)}}{W_1 R} \\
&+2\left(\frac{\partial z^{(0)}}{\partial Z}\right)^{-1}\left(\frac{R}{r^{(0)^2}} - \frac{R^2}{r^{(0)^3}}\frac{\mathrm{d}r^{(0)}}{\mathrm{d}R} - \frac{R}{r^{(0)}}\frac{\mathrm{d}r^{(0)}}{\mathrm{d}R}\frac{\partial^2 z^{(0)}}{\partial R\partial Z}\right) = 0,
\end{aligned} \tag{B.3.26a}$$

$$\begin{aligned}
&\frac{1}{2W_1}\left(\frac{\partial r^{(2)}}{\partial Z}\frac{\mathrm{d}\mathscr{P}^{(0)}}{\mathrm{d}R} - \frac{\partial \mathscr{P}^{(2)}}{\mathrm{d}Z}\frac{\mathrm{d}r^{(0)}}{\mathrm{d}R}\right) \\
&+2\frac{\mathrm{d}r^{(0)}}{\mathrm{d}R}\frac{\partial z^{(0)}}{\partial Z}\frac{\partial^2 z^{(2)}}{\partial Z^2} - \frac{\partial z^{(0)}}{\partial R}\frac{\partial z^{(0)}}{\partial Z}\frac{\partial^2 r^{(2)}}{\partial Z^2} \\
&+\frac{\mathrm{d}r^{(0)}}{\mathrm{d}R}\frac{\partial z^{(0)}}{\partial R}\frac{\partial^2 z^{(0)}}{\partial R^2} - \frac{\partial r^{(2)}}{\partial Z}\frac{\partial z^{(0)}}{\partial Z}\frac{\partial^2 z^{(0)}}{\partial R\partial Z} \\
&+\left(\frac{\partial z^{(0)}}{\partial Z}\right)^2\frac{\partial^2 r^{(2)}}{\partial R\partial Z} + \frac{\partial z^{(0)}}{\partial Z}\frac{\partial z^{(0)}}{\partial R}\frac{\mathrm{d}^2 r^{(0)}}{\mathrm{d}R^2} + \frac{\mathrm{d}r^{(0)}}{\mathrm{d}R}\frac{\partial z^{(0)}}{\partial R}\frac{\partial^2 z^{(0)}}{\partial R\partial Z} \\
&+\frac{1}{r^{(0)}}\left(\frac{\mathrm{d}r^{(0)}}{\mathrm{d}R}\right)^2\frac{\partial z^{(0)}}{\partial Z}\frac{\partial z^{(0)}}{\partial R} + \frac{1}{r^{(0)}}\left(\frac{\partial z^{(0)}}{\partial Z}\right)^2\frac{\mathrm{d}r^{(0)}}{\mathrm{d}R}\frac{\partial r^{(2)}}{\partial Z} = 0.
\end{aligned} \tag{B.3.26b}$$

Using (B.3.26a), we seek to obtain (4.2.12) in order to close the leading order problem. As previously, equation (B.3.26b) introduces higher order terms (*i.e.* $z^{(2)}$ and $\mathscr{P}^{(2)}$) which are not of interest for the leading order problem and is therefore not needed here.

Numerical evidence provided in Figures B.1, 2$^{\text{nd}}$ column shows that the dependence of r on Z is weak and importantly, that $\frac{\partial^2 r}{\partial Z^2}$ is much smaller than the other leading order quantities in (B.3.26a). As a result, the remaining $\mathcal{O}(1)$ terms in (B.3.26a) dominate to reveal (4.2.12). Moreover, for $\varepsilon = 0.01$, Figures B.1 (xi) and (xii) suggest that $r^{(2)} = r^{(2)}(R)$ and support our expansions in (4.2.1). Subsequently, substituting (B.3.16) and (B.3.17a) into (B.3.26a) provides an equation for $\lambda_z^{(0)}$ and hence, together with (B.3.15a), we obtain the pair of coupled ODEs (4.2.13). As outlined in Section 4.2.1, The coupled ODEs (4.2.13) together with the boundary condition (B.3.9) and the relation (B.3.25b) provides a boundary value problem that describes the leading order radial and axial deformation, and from which the leading order Cauchy stress components for the whole tissue and each of the constituents follow directly. We note that the boundary condition (B.3.25b) on $\lambda_z^{(0)}$ is posed at the (unknown) deformed inner radius. We therefore solve (4.2.13) numerically by treating $r^{(0)}(R_{\text{in}})$ as a shooting parameter and seek the solution set $r^{(0)}$, $\lambda_z^{(0)}$ and R_{in} that satisfies (4.2.13), (B.3.9) and (B.3.25b).

In summary, we have demonstrated that the full biomechanical model of the PCLS (Section 3.1) may be suitably reduced in the thin-PCLS-limit (Section 4.2) via the asymptotic expansions (4.2.1) to obtain a leading order boundary value problem.

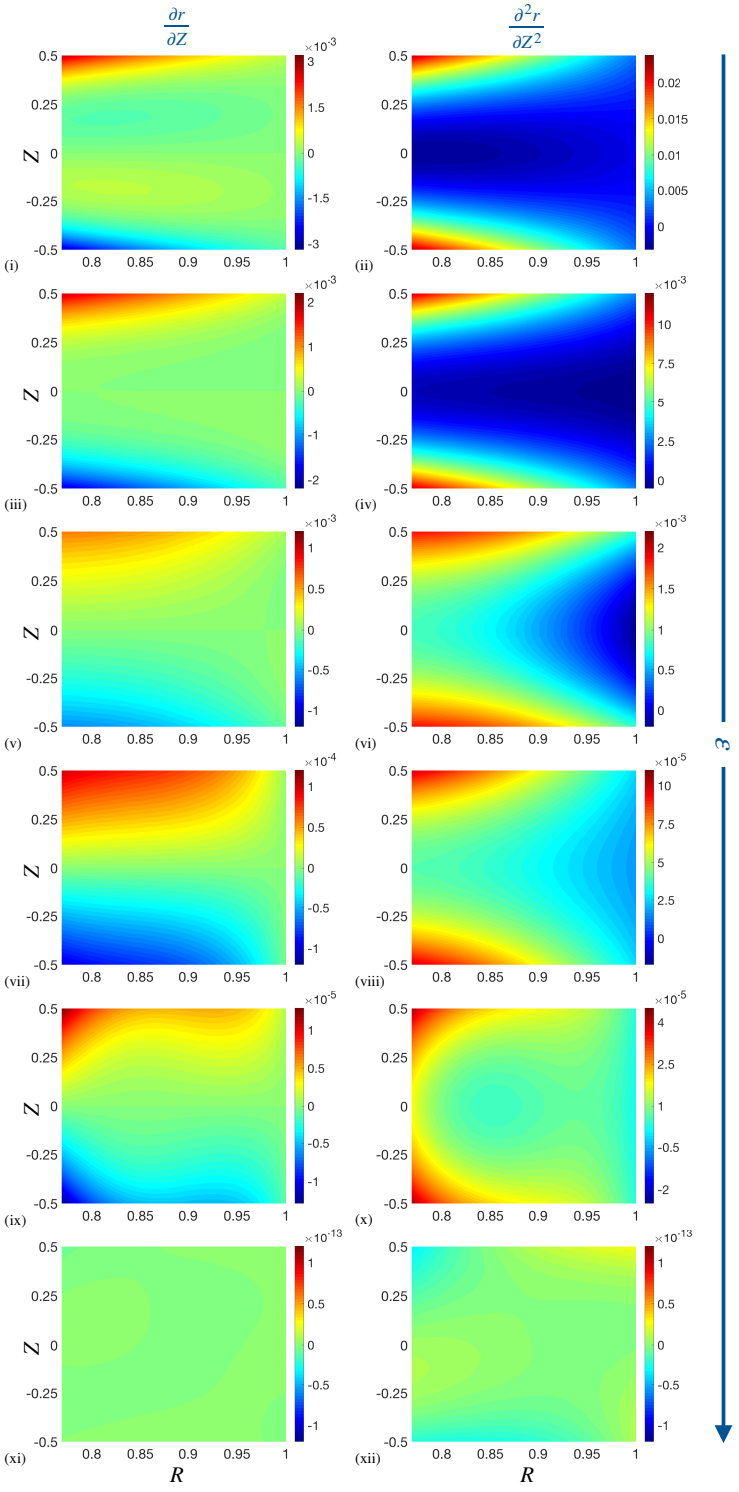

Figure B.1: The effect of reducing the aspect ratio, ε, on the first derivative (1st column) and second derivative (2nd column) of the radial deformation r with respect to Z, in the passive case, $\alpha = 0$, and under the application of a 5% fixed stretch. Results plotted in the undeformed reference configuration (R, Z). ε decreases in the direction of the arrow for $\varepsilon \in \{1, 0.5, 0.25, 0.1, 0.025, 0.01\}$. The remaining parameter values are provided in Table C.4 in Appendix C.2.

APPENDIX C

Parameter Values

C.1 Dynamical models

Tables of parameter values corresponding to the dynamical models developed in Chapter 2.

Table C.1: Table of parameters in the general ODE model (2.1.1) and the refined model (2.1.6), including the dimension, biological description and the corresponding dimensionless parameters in the dimensionless models 2.1.15 and 2.1.16. Those after the dotted line are specific to the refined ODE model (2.1.6).

Parameter	Dimension	Description	Dimensionless
p_r^*	$\frac{N}{L^3}$	Reference number of proliferating ASM cells per unit volume of tissue.	
c_r^*	$\frac{N}{L^3}$	Reference number of contractile ASM cells per unit volume of tissue.	
a_r^*	$\frac{N}{L^3}$	Reference number of active TGF-β molecules per unit volume of tissue.	

Table C.1: Table of parameters in the general ODE model (2.1.1) and the refined model (2.1.6), including the dimension, biological description and the corresponding dimensionless parameters in the dimensionless models 2.1.15 and 2.1.16. Those after the dotted line are specific to the refined ODE model (2.1.6) (continued).

Parameter	Dimension	Description	Dimensionless
m_r^*	$\frac{N}{L^3}$	Reference number of ECM proteins per unit volume of tissue.	
p^*	$\frac{N}{L^3}$	Number of proliferating ASM cells per unit volume of tissue.	$p = \frac{p^*}{p_r^*}$
c^*	$\frac{N}{L^3}$	Number of contractile ASM cells per unit volume of tissue.	$c = \frac{c^*}{c_r^*}$
a^*	$\frac{N}{L^3}$	Number of active TGF-β molecules per unit volume of tissue.	$a = \frac{a^*}{a_r^*}$
m^*	$\frac{N}{L^3}$	Number of ECM proteins per unit volume of tissue.	$m = \frac{m^*}{m_r^*}$
P^*	$\frac{N}{L^3}$	Initial number of proliferating ASM cells per unit volume of tissue.	$P = \frac{P^*}{p_r^*}$
C^*	$\frac{N}{L^3}$	Initial number of contractile ASM cells per unit volume of tissue.	$C = \frac{C^*}{c_r^*}$
A^*	$\frac{N}{L^3}$	Initial number of active TGF-β molecules per unit volume of tissue.	$A = \frac{A^*}{a_r^*}$
M^*	$\frac{N}{L^3}$	Initial number of ECM proteins per unit volume of tissue.	$M = \frac{M^*}{m_r^*}$

Table C.1: Table of parameters in the general ODE model (2.1.1) and the refined model (2.1.6), including the dimension, biological description and the corresponding dimensionless parameters in the dimensionless models 2.1.15 and 2.1.16. Those after the dotted line are specific to the refined ODE model (2.1.6) (continued).

Parameter	Dimension	Description	Dimensionless
p^*_{max}	$\frac{N}{L^3}$	Maximum number of proliferating ASM cells per unit volume of tissue.	$p_{max} = \frac{p^*_{max}}{p^*_r}$
γ_a	1	Ratio of reference TGF-β concentration and reference ECM density.	$\gamma_a = \frac{a^*_r}{m^*_r}$
γ_p	1	Ratio of reference proliferating ASM and reference ECM density.	$\gamma_p = \frac{p^*_r}{m^*_r}$
γ_c	1	Ratio of reference contractile ASM and reference ECM density.	$\gamma_c = \frac{c^*_r}{m^*_r}$
t^*	T	Time.	$t = \phi^*_a t^*$
t^*_i	T	Time of stimulus.	$t_i = \phi^*_a t^*_i$
ν^*	T	Duration of stimulus.	$\nu = \sqrt{2}\phi^*_a \nu^*$
ϕ^*_a	$\frac{1}{T}$	Rate of active TGF-β degradation.	$1 = \frac{\phi^*_a}{\phi^*_a}$
ϕ^*_c	$\frac{1}{T}$	Rate of contractile ASM apoptosis.	$\phi_c = \frac{\phi^*_c}{\phi^*_a}$
ϕ^*_{cm}	$\frac{1}{T}$	Rate of ECM aided contractile ASM survival.	$\phi_{cm} = \frac{\phi^*_{cm}}{\phi^*_a}$
ϕ^*_m	$\frac{1}{T}$	Rate of ECM degradation.	$\phi_m = \frac{\phi^*_m}{\phi^*_a}$
κ^*_p	$\frac{1}{T}$	Rate of ASM proliferation.	$\kappa_p = \frac{\kappa^*_p}{\phi^*_a}$

Table C.1: Table of parameters in the general ODE model (2.1.1) and the refined model (2.1.6), including the dimension, biological description and the corresponding dimensionless parameters in the dimensionless models 2.1.15 and 2.1.16. Those after the dotted line are specific to the refined ODE model (2.1.6) (continued).

Parameter	Dimension	Description	Dimensionless
κ_{ap}^*	1	Rate of TGF-β induced ASM proliferation.	$\kappa_{ap} = \kappa_{ap}^*$
κ_{cp}^*	$\frac{1}{T}$	Rate of switch from contractile ASM phenotype to proliferative ASM phenotype.	$\kappa_{cp} = \frac{\kappa_{cp}^*}{\phi_a^*}$
κ_{pc}^*	$\frac{1}{T}$	Rate of switch from proliferative ASM phenotype to contractile ASM phenotype.	$\kappa_{pc} = \frac{\kappa_{pc}^*}{\phi_a^*}$
κ_a^*	$\frac{N}{L^3 T}$	Rate of basal TGF-β activation.	$\kappa_a = \frac{\kappa_a^*}{\phi_a^* a_r^*}$
κ_s^*	$\frac{L^3}{N}$	Rate of stimulus induced TGF-β mechanical activation.	$\kappa_s = \frac{\kappa_s^* c_r^*}{\sqrt{\pi}}$
κ_{ac}^*	$\frac{L^3}{NT}$	Rate of TGF-β induced TGF-β mechanical activation.	$\kappa_{ac} = \frac{\kappa_{ac}^* c_r^*}{\phi_a^*}$
κ_{cm}^*	$\frac{1}{T}$	Rate of ECM secretion from contractile ASM.	$\kappa_{cm} = \frac{\kappa_{cm}^*}{\phi_a^*}$
κ_{acm}^*	$\frac{1}{T}$	Rate of TGF-β induced ECM secretion from contractile ASM.	$\kappa_{acm} = \frac{\kappa_{acm}^*}{\phi_a^*}$
κ_{pm}^*	$\frac{1}{T}$	Rate of ECM secretion from proliferating ASM.	$\kappa_{pm} = \frac{\kappa_{pm}^*}{\phi_a^*}$
κ_{apm}^*	$\frac{1}{T}$	Rate of TGF-β induced ECM secretion from proliferating ASM.	$\kappa_{apm} = \frac{\kappa_{apm}^*}{\phi_a^*}$

Table C.1: Table of parameters in the general ODE model (2.1.1) and the refined model (2.1.6), including the dimension, biological description and the corresponding dimensionless parameters in the dimensionless models 2.1.15 and 2.1.16. Those after the dotted line are specific to the refined ODE model (2.1.6) (continued).

Parameter	Dimension	Description	Dimensionless
κ_e^*	$\frac{N}{L^3T}$	Rate of TGF-β induced ECM deposition from alternative sources.	$\kappa_e = \frac{\kappa_e^*}{\phi_a^* m_r^*}$
η_{ap}^*	$\frac{N}{L^3}$	Disassociation constant.	$\eta_{ap} = \frac{\eta_{ap}^*}{a_r^*}$
η_{cm}^*	$\frac{N}{L^3}$	Disassociation constant.	$\eta_{cm} = \frac{\eta_{cm}^*}{m_r^*}$
η_{ac}^*	$\frac{N}{L^3}$	Disassociation constant.	$\eta_{ac} = \frac{\eta_{ac}^*}{a_r^*}$
η_{acm}^*	$\frac{N}{L^3}$	Disassociation constant.	$\eta_{acm} = \frac{\eta_{acm}^*}{a_r^*}$
η_{apm}^*	$\frac{N}{L^3}$	Disassociation constant.	$\eta_{apm} = \frac{\eta_{apm}^*}{a_r^*}$
η_e^*	$\frac{N}{L^3}$	Disassociation constant.	$\eta_e = \frac{\eta_e^*}{a_r^*}$
n_p	1	Hill Coefficient for active TGF-β binding to proliferating ASM receptor.	n_p
n_c	1	Hill Coefficient for active TGF-β binding to contractile ASM receptor.	n_c
n_m	1	Hill Coefficient for ECM aided contractile ASM survival.	n_m
n	1	Hill Coefficient for active TGF-β induced ECM deposition from alternative sources.	n

Table C.1: Table of parameters in the general ODE model (2.1.1) and the refined model (2.1.6), including the dimension, biological description and the corresponding dimensionless parameters in the dimensionless models 2.1.15 and 2.1.16. Those after the dotted line are specific to the refined ODE model (2.1.6) (continued).

Parameter	Dimension	Description	Dimensionless
$\tilde{\eta}^*_{ap}$	$(\frac{N^2}{L^6})^{n_p}$	Disassociation constant.	$\tilde{\eta}_{ap} = \frac{\tilde{\eta}_{ap}}{(a^*_r p^*_r)^{n_p}}$
$\tilde{\eta}^*_{apm}$	$(\frac{N^2}{L^6})^{n_p}$	Disassociation constant.	$\tilde{\eta}_{apm} = \frac{\tilde{\eta^*}_{apm}}{(a^*_r p^*_r)^{n_p}}$
$\tilde{\eta}^*_{ac}$	$(\frac{N^2}{L^6})^{n_c}$	Disassociation constant.	$\tilde{\eta}_{ac} = \frac{\tilde{\eta}^*_{ac}}{(a^*_r c^*_r)^{n_c}}$
$\tilde{\eta}^*_{acm}$	$(\frac{N^2}{L^6})^{n_c}$	Disassociation constant.	$\tilde{\eta}_{acm} = \frac{\tilde{\eta}^*_{acm}}{(a^*_r c^*_r)^{n_c}}$
$\tilde{\eta}^*_{cm}$	$(\frac{N}{L^3})^{n_m}$	Disassociation constant.	$\tilde{\eta}_{cm} = \frac{\tilde{\eta}^*_{cm}}{(m^*_r)^{n_m}}$
$\tilde{\eta}^*_{e}$	$(\frac{N}{L^3})^{n}$	Disassociation constant.	$\tilde{\eta}_{e} = \frac{\tilde{\eta}^*_{e}}{(a^*_r)^{n}}$
κ^*_b	$\frac{L^3}{NT}$	Rate of Active TGF-β binding to a receptor presented on proliferating or contractile ASM.	$\kappa_b = \frac{\kappa^*_b c^*_r}{\phi^*_a}$

Table C.2: Table of dimensionless baseline parameter values for the general ODE model (2.1.15) and the refined ODE model (2.1.16). Those in the final column are specific to the refined ODE model (2.1.16).

Parameter	Baseline	Parameter	Baseline	Parameter	Baseline
t	1000	p_{max}	1	n_p	1
ϕ_c	0.1	γ_p	1	n_c	1
ϕ_m	0.01	γ_a	0.06	n_m	1
ϕ_{cm}	0.001	γ_c	1	n	1
κ_p	1	κ_{ap}	1	$\tilde{\eta}_{ap}$	1
κ_{cp}	0.01	κ_{pc}	1	$\tilde{\eta}_{apm}$	10
κ_a	0.001	κ_{ac}	0.01	$\tilde{\eta}_{ac}$	1
κ_{apm}	0.1	κ_{pm}	0.1	$\tilde{\eta}_{acm}$	1
κ_{acm}	0.001	κ_{cm}	0.0001	$\tilde{\eta}_{cm}$	1
κ_e	0.001	η_e	1	$\tilde{\eta}_e$	1
η_{ap}	1	η_{cm}	1	κ_b	1
η_{ac}	1	η_{acm}	1	γ_a	0.01
η_{apm}	10				

Table C.3: Table of dimensionless parameter values for the general ODE model (2.1.15) and the refined ODE model (2.1.16) used to produce Figures 2.7 – 2.10. The remaining parameter values are baseline values, as provided in Table C.2.

	Parameter		
Figure 2.7	t_i	ν	κ_s
(i) (iv)	50:40:250	5	0.1
(ii) (v)	50:40:450	5	0.1
(iii) (vi)	50:40:650	5	0.1
Figure 2.8			
(i) (iv)	50:70:750	5	0.1
(ii) (v)	50:50:550	5	0.1
(iii) (vi)	50:30:350	5	0.1
Figure 2.9			
(i) (iv)	50:50:550	20	0.1
(ii) (v)	50:50:550	10	0.1
(iii) (vi)	50:50:550	1	0.1
Figure 2.10			
(i) (iv)	50:50:300	5	0.1
(ii) (v)	50:50:300	5	0.15
(iii) (vi)	50:50:300	5	0.17

C.2 Biomechanical models

Tables of parameter values corresponding to the biomechanical models developed in Chapters 3 and 4.

Table C.4: Table of dimensionless parameter values used in Sections 3.2 and 4.3. Dashes denote the given baseline value. Where multiple values are given, the value used for each plot in the figure is specified in the figure's legend. Where ranges of parameter values are given, the parameter is varied and takes values in the range that are specified in the figure's legend.

		Figures				
Parameter	**Baseline**	3.2	3.3	3.4 and 3.5	4.3	B.1
R_{in}	0.7692	-	-	-	-	-
R_{out}	1	-	-	-	-	-
r_{dis}	1.05	-	-	-	-	-
ε	1	-	-	$0.01 \leq \varepsilon \leq 1$	0.01	$0.01 \leq \varepsilon \leq 1$
Φ_c	0.5	-	-	-	-	-
Φ_m	0.5	-	-	-	-	-
Φ_u	0	-	-	-	-	-
ω	0.3492	-	-	-	-	-
ζ	1.48	-	-	-	-	-
μ	1	-	-	-	-	-
α	$\{0, 0.2\}$	-	$\{0, 0.1, 0.2\}$	-	-	0

Table C.5: Table of dimensionless parameter values used in the thin-PCLS-limit model in Section 4.4. Dashes denote the given baseline value. Where multiple values are given, the value used for each plot in the figure is specified in the figure's legend. Where ranges of parameter values are given, the parameter is varied and takes all values in the range.

		Figures		
Parameter	**Baseline**	4.4 and 4.5	4.6 and 4.7	4.8 and 4.9
R_{in}	0.7692	-	-	-
R_{out}	1	-	-	-
r_{dis}	$\{1, 1.05, 1.15\}$	$1 \leq r_{\text{dis}} \leq 1.2$	-	-
Φ_c	0.2	-	-	-
Φ_m	0.1	-	-	-
Φ_u	0.7	-	-	-
ω	0.3492	-	-	-
ζ	1.48	-	-	-
μ	$\{\frac{1}{3}, 1, 3\}$	-	3	$0 \leq \mu \leq 4$
α	0	-	$0 \leq \alpha \leq 4$	1

C.3 Coupled models

Tables of parameter values corresponding to the coupled models developed in Chapter 5.

Table C.6: Table of dimensionless parameter values used in the coupled models in Section 5.2. Dashes denote the given baseline value. Where multiple values are given, the value used for each plot in the figure is specified in the figure's legend.

		Figures		
Parameter	**Baseline**	5.1 and 5.2	5.3	5.4
R_{in}	0.7692	-	-	-
R_{out}	1	-	-	-
r_{dis}	$\{1, 1.05, 1.1, 1.15, 1.2\}$	$\{1.05, 1.1, 1.15\}$	-	-
ψ	π	-	-	-
ε	0.01	-	-	-
Φ_c	0.2	0.5	-	-
Φ_m	0.1	0.5	-	-
Φ_u	0.7	0	-	-
ω	0.3492	-	-	-
ζ	1.48	-	-	-
μ	1	-	3	3
κ_b	0.0138	-	-	-
κ_m	3	-	100	100
n_{VM}	4	-	-	-
η_{VM}	0.1	-	2.6591	2.6591
α_s	0	-	-	-
α_{ac}	0.2	-	10	10
η	1	-	-	2

Table C.7: Table of dimensionless parameter values used in the coupled models in Section 5.2. Dashes denote the given baseline value. Where multiple values are given, the value used for each plot in the figure is specified in the figure's legend.

	Figures	
Parameter	6.2, 6.3 and 6.4	6.6 and 6.7
R_{in}	0.7692	0.9412
R_{out}	1	-
r_{dis}	$\{1, 1.05, 1.1, 1.15, 1.2, 1.25\}$	1.15
ψ	π	-
ε	0.01	-
Φ_c	0.2	$\{0.0754, 0.1346\}$
Φ_m	0.1	$\{0.1084, 0.1654\}$
Φ_u	0.7	$\{0.8162, 0.7\}$
ω	0.3492	-
ζ	1.48	-
μ	1	$\{1, 2.28\}$
κ_b	0.0138	-
κ_m	43	80
n_{VM}	4	-
η_{VM}	3.1623	4
α_s	0	$\{0, 0.46\}$
α_{ac}	8	7
η	3	1

References

R. Abe, S. C. Donnelly, T. Peng, R. Bucala, and C. N. Metz. Peripheral blood fibrocytes: Differentiation pathway and migration to wound sites. *The Journal of Immunology*, 166(12):7556–7562, 2001.

D. A. Affonce and K. R. Lutchen. New perspectives on the mechanical basis for airway hyperreactivity and airway hypersensitivity in asthma. *Journal of Applied Physiology*, 101(6):1710–1719, 2006.

M. Al Alawi, T. Hassan, and S. H. Chotirmall. Transforming growth factor β and severe asthma: a perfect storm. *Respiratory Medicine*, 108:1409–1423, 2014.

M. Alrifai, L. M. Marsh, T. Dicke, A. Kiliç, M. L. Conrad, H. Renz, and H. Garn. Compartmental and temporal dynamics of chronic inflammation and airway remodelling in a chronic asthma mouse model. *PLoS ONE*, 9(1):85839, 2014.

D. Ambrosi and S. Pezzuto. Active stress vs. active strain in mechanobiology: constitutive issues. *Journal of Elasticity*, 107:199–212, 2012.

S. D. Amin, A. Majumdar, U. Frey, and B. Suki. Modeling the dynamics of airway constriction: effects of agonist transport and binding. *Journal of Applied Physiology*, 109(2):553–563, 2010.

Y. Amrani and R. A. Panettieri. Airway smooth muscle: contraction and beyond. *The International Journal of Biochemistry & Cell Biology*, 35(3):272–276, 2003.

S. S. An, R. E. Laudadio, J. Lai, R. A. Rogers, and J. J. Fredberg. Stiffness changes in cultured airway smooth muscle cells. *American Journal of Physiology - Cell Physiology*, 283:792–801, 2002.

R. C. Anafi and T. A. Wilson. Airway stability and heterogeneity in the constricted lung. *Journal of Applied Physiology*, 91(3):1185–1192, 2001.

J. P. Annes, J. S. Munger, and D. B. Rifkin. Making sense of latent TGF-β activation. *Journal of Cell Science*, 116(2), 2003.

J. P. Annes, Y. Chen, J. S. Munger, and D. B. Rifkin. Integrin mediated activation of latent TGF-β requires the latent TGF-β binding protein-1. *The Journal of Cell Biology*, 165(5):723–734, 2004.

Y. Aschner and G. P. Downey. Transforming growth factor-β: master regulator of the respiratory system in health and disease. *American Journal of Respiratory Cell and Molecular Biology*, 54(5):647–655, 2016.

R. K. Assoian, A. Komoriya, C. A. Meyers, D. M. Miller, and M. B. Sporn. Transforming growth factor-β in human platelets. *The Journal of biological chemistry*, 258(11):7155–7160, 1983.

G. A. Ateshian. On the theory of reactive mixtures for modeling biological growth. *Biomechanics and Modeling in Mechanobiology*, 6(6), 2007.

G. A. Ateshian. Mixture Theory for Modeling Biological Tissues: Illustrations from Articular Cartilage. In G. A. Holzapfel and R. W. Ogden, editors, *Biomechanics: Trends in Modeling and Simulation*, pages 1–51. Springer International Publishing, 2017.

G. A. Ateshian and T. Ricken. Multigenerational interstitial growth of biological tissues. *Biomechanics and Modeling in Mechanobiology*, 9(6):689–702, 2010.

T. R. Bai, J. Cooper, T. Koelmeyer, P. D. Paré, and T. D. Weir. The effect of age and duration of disease on airway structure in fatal asthma. *American Journal of Respiratory and Critical Care Medicine*, 162:663–669, 2000.

M. Baker, B. S. Brook, and M. R. Owen. Mathematical modelling of cytokines, MMPs and fibronectin fragments in osteoarthritic cartilage. *Journal of Mathematical Biology*, 75(4):1–40, 2017.

K. E. Barrett, S. M. Barman, S. Boitano, and H. L. Brooks. *Ganongs Review of Medical Physiology*. McGraw-Hill Medical, 23rd edition, 2009.

J. H. T. Bates and A. M. Lauzon. Modeling the oscillation dynamics of activated airway smooth muscle strips. *American Journal of Physiology-Lung Cellular and Molecular Physiology*, 289(5):849–855, 2005.

J. H. T. Bates and A. M. Lauzon. Parenchymal tethering, airway wall stiffness, and the dynamics of bronchoconstriction. *Journal of Applied Physiology*, 102 (5):1912–1920, 2007.

J. H. T. Bates, S. R. Bullimore, A. Z. Politi, J. Sneyd, R. C. Anafi, and A. M. Lauzon. Transient oscillatory force-length behavior of activated airway smooth muscle. *American Journal of Physiology - Lung Cellular and Molecular Physiology*, 297:362–372, 2009.

L. Benayoun, A. Druilhe, M. C. Dombret, M. Aubier, and M. Pretolani. Airway structural alterations selectively associated with severe asthma. *American Journal of Respiratory and Critical Care Medicine*, 167(10):1360–1368, 2003.

J. K. Bentley and M. B. Hershenson. Airway smooth muscle growth in asthma: proliferation, hypertrophy, and migration. *Proceedings of the American Thoracic Society*, 5(1):89–96, 2008.

R. Berair, R. Saunders, and C. E. Brightling. Origins of increased airway smooth muscle mass in asthma. *BMC Medicine*, 11(145), 2013.

C. Bergeron, W. Al Ramli, and Q. A. Hamid. Remodeling in Asthma. *Proceedings of the American Thoracic Society*, 6(3):301–305, 2009.

M. Böl, A. Schmitz, G. Nowak, and T. Siebert. A three-dimensional chemo-mechanical continuum model for smooth muscle contraction. *Journal of the Mechanical Behavior of Biomedical Materials*, 13:215–229, 2012.

A. J. Booth, R. Hadley, A. M. Cornett, A. A. Dreffs, S. A. Matthes, J. L. Tsui, K. Weiss, J. C. Horowitz, V. F. Fiore, T. H. Barker, B. B. Moore, F. J. Martinez, L. E. Niklason, and E. S. White. Acellular normal and fibrotic human lung matrices as a culture system for in vitro investigation. *American Journal of Respiratory and Critical Care Medicine*, 186(9):866–876, 2012.

Y. Bossé, P. D. Paré, C. Y. Seow, and J. Hogg. Airway wall remodeling in asthma: from the epithelial layer to the adventitia. *Current Allergy and Asthma Reports*, 8:357–366, 2008.

Y. Bossé, L. Y. M. Chin, P. D. Paré, and C. Y. Seow. Adaptation of airway smooth muscle to basal tone. *American Journal of Respiratory Cell and Molecular Biology*, 40(1):13–18, 2009.

J. Bousquet, P. K. Jeffery, W. W. Busse, M. Johnson, and A. M. Vignola. Asthma: from bronchoconstriction to airways inflammation and remodeling. *American Journal of Respiratory and Critical Care Medicine*, 161:1720–1745, 2000.

R. M. Bowen. *Theory of Mixtures*. Academic Press, New York, NY, 1976.

B. J. Breen, G. M. Donovan, J. Sneyd, and M. H. Tawhai. Quantifying parenchymal tethering in a finite element simulation of a human lung slice under bronchoconstriction. *Respiratory Physiology and Neurobiology*, 183(2):85–90, 2012.

C. E. Brightling, S. Gupta, S. Gonem, and S. Siddiqui. Lung damage and airway remodelling in severe asthma. *Clinical & Experimental Allergy*, 42(5):638–649, 2012.

B. S. Brook. Emergence of airway smooth muscle mechanical behavior through dynamic reorganization of contractile units and force transmission pathways. *Journal of Applied Physiology*, 116(8):980–997, 2014.

B. S. Brook and O. E. Jensen. The role of contractile unit reorganization in force generation in airway smooth muscle. *Mathematical Medicine and Biology*, 31 (2):99–124, 2014.

B. S. Brook, S. E. Peel, I. P. Hall, A. Z. Politi, J. Sneyd, Y. Bai, M. J. Sanderson, and O. E. Jensen. A biomechanical model of agonist-initiated contraction in the asthmatic airway. *Respiratory Physiology & Neurobiology*, 170:44–58, 2010.

B. S. Brook, C. J. Philp, M. R. Hill, A. Bullock, B. Liu, A. Habgood, A. E. John, R. J. Middlewick, K. E. Stephenson, A. T. Goodwin, J. Nadal, R. Hall, C. K. Billington, A. L. Tatler, R. D. O'Dea, and S. R. Johnson. A novel, comprehensive method to study murine airway remodeling reveals differential smooth muscle and collagen increases in large and small airways. In *American Journal of Respiratory and Critical Care Medicine 2019*, page 199:A5889. American Thoracic Society, 2019.

P. J. Brown, H. W. Greville, and K. E. Finucane. Asthma and irreversible airflow obstruction. *Thorax*, 39(2):131–136, 1984.

M. Brumen, A. S. Fajmut, A. Dobovišek, D. Dobovišek, and E. Roux. Mathematical modelling of Ca 2+ oscillations in airway smooth muscle cells. *Journal of Biological Physics*, 31:515–524, 2005.

S. R. Bullimore, S. Siddiqui, G. M. Donovan, J. G. Martin, J. Sneyd, J. H. T. Bates, and A. M. Lauzon. Could an increase in airway smooth muscle shortening velocity cause airway hyperresponsiveness? *American Journal of Physiology - Lung Cellular and Molecular Physiology*, 300(1), 2011.

J. K. Burgess, T. Mauad, G. Tjin, J. C. Karlsson, and G. Westergren Thorsson. The extracellular matrix - the under-recognised element in lung disease? *The Journal of Pathology*, 240(4):397–409, 2016.

L. Buscemi, D. Ramonet, F. Klingberg, A. Formey, J. Smith Clerc, J. J. Meister, and B. Hinz. The single-molecule mechanics of the latent TGF-β1 complex. *Current Biology*, 21(24):2046–2054, 2011.

V. Chan, J. K. Burgess, J. C. Ratoff, B. J. O'Connor, A. Greenough, T. H. Lee, and S. J. Hirst. Extracellular matrix regulates enhanced eotaxin expression in asthmatic airway smooth muscle cells. *American Journal of Respiratory and Critical Care Medicine*, 174:379–385, 2006.

G. Chen and N. Khalil. TGF-β1 increases proliferation of airway smooth muscle cells by phosphorylation of map kinases. *Respiratory research*, 7(1):2, 2006.

W. Cheng, K. Yan, L. Y. Xie, F. Chen, H. C. Yu, Y. X. Huang, and C. X. Dang. MiR-143-3p controls TGF-β1-induced cell proliferation and extracellular matrix production in airway smooth muscle via negative regulation of the nuclear factor of activated T cells 1. *Molecular immunology*, 78:133–139, 2016.

I. L. Chernyavsky, H. Croisier, L. A. C. Chapman, L. S. Kimpton, J. E. Hiorns, B. S. Brook, O. E. Jensen, C. K. Billington, I. P. Hall, and S. R. Johnson. The role of inflammation resolution speed in airway smooth muscle mass accumulation in asthma: insight from a theoretical model. *PLoS ONE*, 9(3):1–10, 2014.

A. Coccarelli, D. H. Edwards, A. Aggarwal, P. Nithiarasu, and D. Parthimos. A multiscale active structural model of the arterial wall accounting for smooth muscle dynamics. *Journal of the Royal Society, Interface*, 15(139):20170732, 2018.

H. Croisier, X. Tan, J. F. Perez Zoghbi, M. J. Sanderson, J. Sneyd, and B. S. Brook. Activation of store-operated calcium entry in airway smooth muscle cells: insight from a mathematical model. *PloS one*, 8(7), 2013.

M. J. Crowe, T. Doetschman, and D. G. Greenhalgh. Delayed wound healing in immunodeficient TGF-β1 knockout mice. *Journal of Investigative Dermatology*, 115:3–11, 2000.

R. Derynck and Y. E. Zhang. Smad-dependent and smad-independent pathways in TGF-β family signalling. *Nature*, 425:577–584, 2003.

G. M. Donovan. Multiscale mathematical models of airway constriction and disease. *Pulmonary Pharmacology & Therapeutics*, 24(5):533–539, 2011.

DoveMed, 2018. URL `https://www.dovemed.com/diseases-conditions/asthma-adults/`.

M. Ebina, H. Yaegashi, R. Chiba, T. Takahashi, M. Motomiya, and M. Tanemura. Hyperreactive site in the airway tree of asthmatic patients revealed by thickening of bronchial muscles: a morphometric study. *American Review of Respiratory Disease*, 141(5):1327–1332, 1990.

M. Eskandari and E. Kuhl. Systems biology and mechanics of growth. *WIREs Systems Biology and Medicine*, 7(6):401–412, 2015.

M. Eskandari, W. G. Kuschner, and E. Kuhl. Patient-Specific Airway Wall Remodeling in Chronic Lung Disease. *Annals of Biomedical Engineering*, 43(10): 2538–2551, 2015.

W. Falkena. xml2struct. *MATLAB Central File Exchange*, 2019. URL `https://www.mathworks.com/matlabcentral/fileexchange/28518-xml2struct`.

Forum of International Respiratory Societies. *The Global Impact of Respiratory Disease*. European Respiratory Society, Sheffield, 2nd edition, 2017. ISBN 9781849840880.

A. M. Freyer, S. R. Johnson, and I. P. Hall. Effects of growth factors and extracellular matrix on survival of human airway smooth muscle cells. *American Journal of Respiratory Cell and Molecular Biology*, 25:569–576, 2001.

A. R. Froese, C. Shimbori, P.-S. Bellaye, M. Inman, S. Obex, S. Fatima, G. Jenkins, J. Gauldie, K. Ask, and M. Kolb. Stretch-induced activation of transforming growth factor-β 1 in pulmonary fibrosis. *American Journal of Respiratory and Critical Care Medicine*, 194(1):84–96, 2016.

Y. C. Fung. *Biomechanics: mechanical properties of living tissues*. Springer, New York, NY, 1993.

T. C. Gasser, R. W. Ogden, and G. A. Holzapfel. Hyperelastic modelling of arterial layers with distributed collagen fibre orientations. *Journal of The Royal Society Interface*, 3:15–35, 2006.

P. O. Girodet, A. Ozier, I. Bara, J. M. Tunon de Lara, R. Marthan, and P. Berger. Airway remodeling in asthma: new mechanisms and potential for pharmacological intervention. *Pharmacology and Therapeutics*, 130(3):325–337, 2011.

P. E. Gleizes, J. S. Munger, I. Nunes, J. G. Harpel, R. Mazzieri, I. Noguera, and D. B. Rifkin. TGF-β latency: biological significance and mechanisms of activation. *Stem Cells*, 15(3):190–197, 1997.

A. M. Goldsmith, J. K. Bentley, L. Zhou, Y. Jia, K. N. Bitar, D. C. Fingar, and M. B. Hershenson. Transforming growth factor-β induces airway smooth muscle hypertrophy. *American Journal of Respiratory Cell and Molecular Biology*, 34: 247–254, 2006.

C. L. Grainge, L. C. K. Lau, J. A. Ward, V. Dulay, G. Lahiff, S. Wilson, S. Holgate, D. E. Davies, and P. H. Howarth. Effect of bronchoconstriction on airway remodeling in asthma. *The New England Journal of Medicine*, 364(21):2006–2015, 2011.

T. Haberichter, E. Roux, M. Marhl, and J. P. Mazat. The influence of different InsP 3 receptor isoforms on Ca 2 + signaling in tracheal smooth muscle cells. *Bioelectrochemistry*, 57:129–138, 2002.

M. R. Hill, X. Duan, G. A. Gibson, S. Watkins, and A. M. Robertson. A theoretical and non-destructive experimental approach for direct inclusion of measured collagen orientation and recruitment into mechanical models of the artery wall. *Journal of Biomechanics*, 45(5):762–771, 2012.

M. R. Hill, C. J. Philp, C. K. Billington, A. L. Tatler, S. R. Johnson, R. D. O'Dea, and B. S. Brook. A theoretical model of inflammation- and mechanotransduction-driven asthmatic airway remodelling. *Biomechanics and Modeling in Mechanobiology*, 17(5):1451–1470, 2018.

B. Hinz. The extracellular matrix and transforming growth factor-β1: tale of a strained relationship. *Matrix Biology*, 47:54–65, 2015.

J. E. Hiorns. *Mathematical modelling and imaging of asthmatic airways*. PhD thesis, The University of Nottingham, 2014.

J. E. Hiorns, O. E. Jensen, and B. S. Brook. Nonlinear compliance modulates dynamic bronchoconstriction in a multiscale airway model. *Biophysical Journal*, 107:3030–3042, 2014.

S. T. Holgate and R. Polosa. Treatment strategies for allergy and asthma. *Nature Reviews Immunology*, 8(3):218–230, 2008.

G. A. Holzapfel. *Nonlinear Solid Mechanics : A Continuum Approach for Engineering*. Wiley, 2000. ISBN 0471823198.

G. A. Holzapfel and R. W. Ogden. Constitutive modelling of arteries. *Proceedings of the Royal Society*, 466:1551–1597, 2010.

G. A. Holzapfel, T. C. Gasser, and R. W. Ogden. A new constitutive framework for arterial wall mechanics and a comparative study of material models. *Journal of Elasticity*, 61:1–48, 2000.

J. D. Humphrey. *Cardiovascular Solid Mechanics: Cells, Tissues, and Organs*. Springer Science & Business Media, 2002. ISBN 9781441928979.

J. D. Humphrey and K. R. Rajagopal. A constrained mixture model for growth and remodelling of soft tissues. *Mathematical Models and Methods in Applied Sciences*, 12(3), 2002.

G. Ijpma, A. Panariti, A. M. Lauzon, and J. G. Martin. Directional preference of airway smooth muscle mass increase in human asthmatic airways. *American Journal of Physiology - Lung Cellular and Molecular Physiology*, 312(6):845–854, 2017.

L. Irons, M. R. Owen, R. D. O'Dea, and B. S. Brook. Effect of loading history on airway smooth muscle cell-matrix adhesions. *Biophysical Journal*, 114(11): 2679–2690, 2018.

S. Ito, A. Majumdar, H. Kume, K. Shimokata, K. Naruse, K. R. Lutchen, D. Stamenović, and B. Suki. Viscoelastic and dynamic nonlinear properties of airway smooth muscle tissue: roles of mechanical force and the cytoskeleton. *American Journal of Physiology-Lung Cellular and Molecular Physiology*, 290(6): 1227–1237, 2006.

S. Itoh, M. Thorikay, M. Kowanetz, A. Moustakas, F. Itoh, C. H. Heldin, and P. Ten Dijke. Elucidation of Smad requirement in transforming growth factor-β type I receptor-induced responses. *Journal of Biological Chemistry*, 278(6): 3751–3761, 2003.

A. Januskevicius, S. Vaitkiene, R. Gosens, I. Janulaityte, D. Hoppenot, R. Sakalauskas, K. Malakauskas, L. F. Keglowich, P. Borger, S. S. Possa, D. C. Doeing, J. Solway, M. L. Fajt, S. E. Wenzel, A. J. Halayko, S. Holgate, J. Bousquet, K. Kumawat, T. Koopmans, R. Gosens, B. Yeganeh, A. L. James, R. Halwani, K. Kumawat, P. R. A. Johnson, H. Clevers, C. Logan, R. Nusse, H. A. Baarsma, M. Konigshoff, R. Gosens, B. G. J. Dekkers, K. Kumawat, R. Gosens, S. R. White, N. Krug, J. Bousquet, J. K. Bentley, M. B. Hershenson, M. Kato, S. S. Possa, F. Taki, J. M. Hughes, S. Sur, J. Mattes, B. Lamkhioued, L. Lintomen, A. B. Kay, S. Phipps, D. S. Robinson, R. T. Moon, S. Sokol, D. F. Choy, and L. Liu. Eosinophils enhance WNT-5a and TGF-β1 genes expression in airway smooth muscle cells and promote their proliferation by increased extracellular matrix proteins production in asthma. *BMC Pulmonary Medicine*, 16(1):94, 2016.

P. K. Jeffery. Remodeling in asthma and chronic obstructive lung disease. *American Journal of Respiratory and Critical Care Medicine*, 164:28–38, 2001.

S. Jianbing, X. Sufang, W. Ling, W. Jingyuan, and Z. Jing. Analysis of the nonlinear elastic response of rubber membrane with embedded circular rigid inclusion. *Journal of Theoretical and Applied Mechanics*, 45(3):23–36, 2015.

P. R. A. Johnson, M. Roth, M. Tamm, J. M. Hughes, Q. Ge, G. King, J. K. Burgess, and J. L. Black. Airway smooth muscle cell proliferation is increased in

asthma. *American Journal of Respiratory and Critical Care Medicine : An Official Journal of the American Thoracic Society, Medical Section of the American Lung Association*, 164(3):474–477, 2001.

P. R. A. Johnson, J. K. Burgess, P. A. Underwood, W. Au, M. H. Poniris, M. Tamm, Q. Ge, M. Roth, and J. L. Black. Extracellular matrix proteins modulate asthmatic airway smooth muscle cell proliferation via an autocrine mechanism. *Journal of Allergy and Clinical Immunology*, 113(4):690–696, 2004.

L. Jolly, A. Stavrou, G. Vanderstoken, V. A. Meliopoulos, A. Habgood, A. L. Tatler, J. Porte, A. J. Knox, P. H. Weinreb, S. M. Violette, T. Hussell, M. Kolb, M. R. Stampfli, S. Schultz Cherry, and G. Jenkins. Influenza promotes collagen deposition via $\alpha v\beta 6$ integrin-mediated transforming growth factor β activation. *The Journal of biological chemistry*, 289(51):35246–63, 2014.

V. Kaartinen, J. W. Voncken, C. Shuler, D. Warburton, D. Bu, N. Heisterkamp, and J. Groffen. Abnormal lung development and cleft palate in mice lacking TGF-$\beta 3$ indicates defects of epithelial-mesenchymal interaction. *Nature Genetics*, 11(4):415–421, 1995.

K. E. Kadler, D. F. Holmes, J. A. Trotter, and J. A. Chapman. Collagen fibril formation. *Biochemical Journal*, 316:1–11, 1996.

P. Kanchanawong, G. Shtengel, A. M. Pasapera, E. B. Ramko, M. W. Davidson, H. F. Hess, and C. M. Waterman. Nanoscale architecture of integrin-based cell adhesions. *Nature*, 468(7323):580–584, 2010.

H. H. Kariyawasam, M. Aizen, J. Barkans, D. S. Robinson, and A. B. Kay. Remodeling and airway hyperresponsiveness but not cellular inflammation persist after allergen challenge in asthma. *American Journal of Respiratory and Critical Care Medicine*, 175(9):896–904, 2007.

D. Kaur, F. Hollins, R. Saunders, L. Woodman, A. Sutcliffe, G. Cruse, P. Bradding, and C. E. Brightling. Airway smooth muscle proliferation and survival is not modulated by mast cells. *Clinical and experimental allergy : Journal of the British Society for Allergy and Clinical Immunology*, 40(2):279–88, 2010.

J. Keski-Oja, K. Koli, and H. von Melchner. TGF-β activation by traction? *Trends in Cell Biology*, 14(12):657–659, 2004.

N. Khalil, Y. D. Xu, R. O'Connor, and V. Duronio. Proliferation of pulmonary interstitial fibroblasts is mediated by transforming growth factor-β1-induced release of extracellular fibroblast growth factor-2 and phosphorylation of p38 MAPK and JNK. *Journal of Biological Chemistry*, 280(52):43000–43009, 2005.

M. A. Khan. Dynamics of airway response in lung microsections: a tool for studying airway-extra cellular matrix interactions. *Journal of Biomedical Science*, 23(1):43, 2016.

M. A. Khan, R. Ellis, M. D. Inman, J. H. T Bates, M. J. Sanderson, and L. J. Janssen. Influence of airway wall stiffness and parenchymal tethering on the dynamics of bronchoconstriction. *American Journal of Physiology - Lung Cellular and Molecular Physiology*, 299(1):98–108, 2010.

D. Y. Kim, E. Y. Kwon, G. U. Hong, Y. S. Lee, S. H. Lee, and J. Y. Ro. Cigarette smoke exacerbates mouse allergic asthma through smad proteins expressed in mast cells. *Respiratory research*, 12:49, 2011.

G. G. King, P. D. Paré, and C. Y. Seow. The mechanics of exaggerated airway narrowing in asthma: The role of smooth muscle. *Respiration Physiology*, 118 (1):1–13, 1999.

L. E. M. Kistemaker, I. S. T. Bos, M. H. Menzen, H. Maarsingh, H. Meurs, and R. Gosens. Combination therapy of tiotropium and ciclesonide attenuates airway inflammation and remodeling in a guinea pig model of chronic asthma. *Respiratory Research*, 17(1):1–10, 2016.

K. Koli, M. Hyytiäinen, M. J. Ryynänen, and J. Keski-Oja. Sequential deposition of latent TGF-β binding proteins (LTBPs) during formation of the extracellular matrix in human lung fibroblasts. *Experimental Cell Research*, 310(2): 370–382, 2005.

M. Kroon and G. A. Holzapfel. A new constitutive model for multi-layered collagenous tissues. *Journal of Biomechanics*, 41(12):2766–2771, 2008.

K. H. Kuo, A. M. Herrera, and C. Y. Seow. Ultrastructure of airway smooth muscle. *Respiratory Physiology & Neurobiology*, 137(2-3):197–208, 2003.

R. K. Lambert and T. A. Wilson. Smooth muscle dynamics and maximal expiratory flow in asthma. *Journal of Applied Physiology*, 99:1885–1890, 2005.

R. K. Lambert, T. A. Wilson, R. E. Hyatt, and J. R. Rodarte. A computational model for expiratory flow. *Journal of Applied Physiology*, 52(1):44–56, 1982.

R. K. Lambert, B. R. Wiggs, K. Kuwano, J. Hogg, P. D. Pare, and P. D. Pare. Functional significance of increased airway smooth muscle in asthma and COPD. *Journal of A*, 74(6):2771–2781, 1993.

R. K. Lambert, S. L. Codd, M. R. Alley, and R. J. Pack. Physical determinants of bronchial mucosal folding. *Journal of Applied Physiology*, 77(3):1206–1216, 1994.

N. Laping, E. Grygielko, A. Mathur, S. Butter, J. Bomberger, C. Tweed, W. Martin, J. Fornwald, R. Lehr, J. Harling, L. Gaster, J. F. Callahan, and B. A. Olson. Inhibition of transforming growth factor (TGF)-β1-induced extracellular matrix with a novel inhibitor of the TGF-β type I receptor kinase activity: SB-431542. *Molecular Pharmacology*, 62(1):58–64, 2002.

J. Latourelle, B. Fabry, and J. J. Fredberg. Dynamic equilibration of airway smooth muscle contraction during physiological loading. *Journal of Applied Physiology*, 92(2):771–779, 2002.

T. L. Lavoie, M. L. Dowell, O. J. Lakser, W. T. Gerthoffer, J. J. Fredberg, C. Y. Seow, R. W. Mitchell, and J. Solway. Disrupting actin-myosin-actin connectivity in airway smooth muscle as a treatment for asthma? *Proceedings of the American Thoracic Society*, 6(3):295–300, 2009.

M. Leclere, A. Lavoie-Lamoureux, P. Joubert, F. Relave, E. L. Setlakwe, G. Beauchamp, C. Couture, J. G. Martin, and J. P. Lavoie. Corticosteroids and antigen avoidance decrease airway smooth muscle mass in an equine asthma model. *American Journal of Respiratory Cell and Molecular Biology*, 47 (5):589–596, 2012.

S. K. Leivonen, L. Häkkinen, D. Liu, and V. M. Kähäri. Smad3 and extracellular signal-regulated kinase 1/2 coordinately mediate transforming growth factor-β-induced expression of connective tissue growth factor in human fibroblasts. *Journal of Investigative Dermatology*, 124:1162–1169, 2005.

B. León. T cells in allergic asthma: key players beyond the Th2 pathway. *Current Allergy and Asthma Reports*, 17(7):43, 2017.

J. J. Letterio and A. B. Roberts. Regulation of Immune Responses by TGF-β. *Annual Review of Immunology*, 16:137–61, 1998.

B. Li, Y.-P. Cao, X.-Q. Feng, and W. Yu. Mucosal wrinkling in animal antra induced by volumetric growth. *Applied Physics Letters*, 98(153701), 2011.

M. Li and Y. X. Shang. Ultrastructural changes in rat airway epithelium in asthmatic airway remodeling. *Pathology Research and Practice*, 210(12):1038–1042, 2014.

Z. Li, J. A. Dranoff, E. P. Chan, M. Uemura, J. Sévigny, and R. G. Wells. Transforming growth factor-β and substrate stiffness regulate portal fibroblast activation in culture. *Hepatology*, 46(4):1246–1256, 2007.

D. M. L. Lilburn, A. L. Tatler, J. S. Six, C. Lesbats, A. Habgood, J. Porte, T. Hughes Riley, D. E. Shaw, G. Jenkins, and T. Meersmann. Investigating lung responses with functional hyperpolarized xenon-129 MRI in an ex vivo rat model of asthma. *Magnetic Resonance in Medicine*, 76(4):1224–1235, 2016.

T. Liu. A constitutive model for cytoskeletal contractility of smooth muscle cells. *Proceedings of the Royal Society A: Mathematical, Physical and Engineering Sciences*, 470(2164), 2014.

B. Ma and K. R. Lutchen. An anatomically based hybrid computational model of the human lung and its application to low frequency oscillatory mechanics. *Annals of Biomedical Engineering*, 34(11):1691–1704, 2006.

S. A. Maas, B. J. Ellis, G. A. Ateshian, and J. A. Weiss. FEBio: Finite Elements for Biomechanics. *Journal of Biomechanical Engineering*, 134(1):011005–0110101, 2012.

T. Makinde, R. F. Murphy, and D. K. Agrawal. The regulatory role of TGF-β in airway remodeling in asthma. *Immunology and cell biology*, 85(5):348–56, 2007.

T. Mauad, E. H. Bel, and P. J. Sterk. Asthma therapy and airway remodeling. *Journal of Allergy and Clinical Immunology*, 120(5):997–1009, 2007.

S. J. McMillan and C. M. Lloyd. Prolonged allergen challenge in mice leads to persistent airway remodelling. *Clinical and Experimental Allergy*, 34(3):497–507, 2004.

M. A. Memon, M. D. Anway, T. R. Covert, M. Uzumcu, and M. K. Skinner. Transforming growth factor beta (TGF-β1, TGF-β2 and TGF-β3) null-mutant phenotypes in embryonic gonadal development. *Molecular and Cellular Endocrinology*, 294(1-2):70–80, 2008.

R. R. Mercer and J. D. Crapo. Spatial distribution of collagen and elastin fibers in the lungs. *Journal of Applied Physiology*, 69(2):756–765, 1990.

S. M. Mijailovich, J. P. Butler, and J. J. Fredberg. Perturbed equilibria of myosin binding in airway smooth muscle: bond-length distributions, mechanics, and ATP metabolism. *Biophysical Journal*, 79:2667–2681, 2000.

M. Mooney. A theory of large elastic deformation. *Journal of Applied Physics*, 11 (9):582–592, 1940.

M. Morioka, H. Parameswaran, K. Naruse, M. Kondo, M. Sokabe, Y. Hasegawa, B. Suki, and S. Ito. Microtubule dynamics regulate cyclic stretch-induced cell alignment in human airway smooth muscle cells. *PLoS ONE*, 6(10):26384, 2011.

D. E. Moulton and A. Goriely. Possible role of differential growth in airway wall remodeling in asthma. *Journal of Applied Physiology*, 110:1003–1012, 2011.

J. S. Munger, J. G. Harpel, F. G. Giancotti, and D. B. Rifkin. Interactions between growth factors and integrins: Latent forms of transforming growth factor-β are ligands for the integrin αvβ1. *Molecular Biology of the Cell*, 9:2627–2638, 1998.

J. Naghshin, L. Wang, P. D. Paré, and C. Y. Seow. Adaptation to chronic length change in explanted airway smooth muscle. *Journal of Applied Physiology*, 95 (1):448–453, 2003.

P. B. Noble, C. D. Pascoe, B. Lan, S. Ito, L. E. M. Kistemaker, A. L. Tatler, T. Pera, B. S. Brook, R. Gosens, and A. R. West. Airway smooth muscle in asthma: linking contraction and mechanotransduction to disease pathogenesis and remodelling. *Pulmonary Pharmacology & Therapeutics*, 29(2):96–107, 2014.

T. A. Oenema, H. Maarsingh, M. Smit, G. M. M. Groothuis, H. Meurs, and R. Gosens. Bronchoconstriction induces TGF-β release and airway remodelling in guinea pig lung slices. *PloS one*, 8(6):65580, 2013.

R. W. Ogden. Large deformation isotropic elasticity - on the correlation of theory and experiment for incompressible rubberlike solids. *Proceedings of the Royal Society A: Mathematical, Physical and Engineering Sciences*, 326(1567):565–584, 1972.

R. W. Ogden. *Non-linear Elastic Deformations*. Dover Publications, 1997. ISBN 9780486696485.

R. W. Ogden. Nonlinear Elasticity, Anisotropy, Material Stability and Residual Stresses in Soft Tissue. In *Biomechanics of Soft Tissue in Cardiovascular Systems*, pages 65–108. Springer Vienna, 2003.

C. A. Ojiaku, G. Cao, W. Zhu, E. J. Yoo, M. Shumyatcher, B. E. Himes, S. S. An, and R. A. Panettieri. TGF-β1 evokes human airway smooth muscle cell shortening and hyperresponsiveness via smad3. *American Journal of Respiratory Cell and Molecular Biology*, 58(5):575–584, 2018.

R. A. Panettieri. Cellular and Molecular Mechanisms Regulating Airway Smooth Muscle Proliferation and Cell Adhesion Molecule Expression. *American Journal of Respiratory and Critical Care Medicine*, 158:133–140, 1998.

M. W. Parker, D. Rossi, M. Peterson, K. Smith, K. Sikström, E. S. White, J. E. Connett, C. A. Henke, O. Larsson, and P. B. Bitterman. Fibrotic extracellular matrix activates a profibrotic positive feedback loop. *Journal of Clinical Investigation*, 124(4):1622–1635, 2014.

N. Pearce, N. Aït-Khaled, R. Beasley, J. Mallol, U. Keil, E. A. Mitchell, C. Robertson, H. R. Anderson, M. I. Asher, B. Björkstén, B. Brunekreef, W. Cookson, J. Crane, P. Ellwood, S. Foliaki, C. K. W. Lai, C. F. Robertson, S. Montefort, J. Odhiambo, J. Shah, A. W. Stewart, D. Strachan, E. Von Mutius, S. K. Weiland, and H. Williams. Worldwide trends in the prevalence of asthma symptoms: Phase III of the International Study of Asthma and Allergies in Childhood (ISAAC). *Thorax*, 62(9):757–765, 2007.

G. Pelaia, T. Renda, L. Gallelli, A. Vatrella, M. T. Busceti, S. Agati, M. Caputi, M. Cazzola, R. Maselli, and S. A. Marsico. Molecular mechanisms underlying airway smooth muscle contraction and proliferation: implications for asthma. *Respiratory Medicine*, 102(8):1173–1181, 2008.

D.-W. Perng, Y.-C. Wu, K.-T. Chang, M.-T. Wu, Y.-C. Chiou, K.-C. Su, R.-P. Perng, and Y.-C. Lee. Leukotriene C4 induces TGF-β1 production in airway epithelium via p38 kinase pathway. *American Journal of Respiratory Cell and Molecular Biology*, 34:101–107, 2006.

C. G. Plopper and D. M. Hyde. The non-human primate as a model for studying COPD and asthma. *Pulmonary Pharmacology and Therapeutics*, 21(5):755–766, 2008.

S. V. Plotnikov and C. M. Waterman. Guiding cell migration by tugging. *Current Opinion in Cell Biology*, 25:619–626, 2013.

D. Pohlers, J. Brenmoehl, I. Löffler, C. K. Müller, C. Leipner, S. Schultze Mosgau, A. Stallmach, R. W. Kinne, and G. Wolf. TGF-β and fibrosis in different organs - molecular pathway imprints. *Biochimica et Biophysica Acta*, 1792:746–756, 2009.

S. R. Polio, S. E. Stasiak, R. R. Jamieson, J. L. Balestrini, R. Krishnan, and H. Parameswaran. Extracellular matrix stiffness regulates human airway smooth muscle contraction by altering the cell-cell coupling. *Scientific Reports*, 9(9564), 2019.

A. Z. Politi, G. M. Donovan, M. H. Tawhai, M. J. Sanderson, A. M. Lauzon, J. H. T. Bates, and J. Sneyd. A multiscale, spatially distributed model of asthmatic airway hyper-responsiveness. *Journal of Theoretical Biology*, 266:614–624, 2010.

D. S. Postma and H. A. M. Kerstjens. Characteristics of airway hyperresponsiveness in asthma and chronic obstructive pulmonary disease. *American Journal of Respiratory and Critical Care Medicine*, 158(5):187–192, 1998.

Y. S. Prakash, A. J. Halayko, R. Gosens, R. A. Panettieri, and B. Camoretti Mercado. An Official American Thoracic Society Research Statement : Current challenges facing research and therapeutic advances in airway remodeling. *American Journal of Respiratory and Critical Care Medicine*, 195(2), 2017.

P. Pundir, X. Wang, and M. Kulk. Asthma in the 21st Century - Unexpected Applications of Ancient Treatments. In *Using Old Solutions to New Problems - Natural Drug Discovery in the 21st Century*, chapter 10. InTech, 2013.

A. Rachev and T. Shazly. A structure-based constitutive model of arterial tissue considering individual natural configurations of elastin and collagen. *Journal of the Mechanical Behavior of Biomedical Materials*, 90:61–72, 2019.

J. Ramis and A. L. Tatler. Unpublished personal communication, 2019.

M. K. Rausch and E. Kuhl. On the mechanics of growing thin biological membranes. *Journal of the Mechanics and Physics of Solids*, 63:128–140, 2014.

S. R. Reeves, T. Kolstad, T. Y. Lien, S. Herrington Shaner, and J. S. Debley. Fibroblast-myofibroblast transition is differentially regulated by bronchial epithelial cells from asthmatic children. *Respiratory Research*, 16(1), 2015.

R. S. Rivlin. Large elastic deformations of isotropic materials. IV. Further eevelopments of the general theory. *Philosophical Transactions of the Royal Society of London. Series A, Mathematical and Physical Sciences*, 241:379–397, 1948.

F. F. Rocha, P. J. Blanco, P. J. Sánchez, and R. A. Feijóo. Multi-scale modelling of arterial tissue: Linking networks of fibres to continua. *Computer Methods in Applied Mechanics and Engineering*, 341:740–787, 2018.

D. F. Rogers. Airway mucus hypersecretion in asthma: An undervalued pathology? *Current Opinion in Pharmacology*, 4:241–250, 2004.

C. M. Royer, K. Rudolph, and E. G. Barrett. The neonatal susceptibility window for inhalant allergen sensitization in the atopically predisposed canine asthma model. *Immunology*, 138(4):361–369, 2013.

S. Saglani and C. M. Lloyd. Novel concepts in airway inflammation and remodelling in asthma. *The European Respiratory Journal*, 46(6):1796–804, 2015.

M. J. Sanderson. Exploring lung physiology in health and disease with lung slices. *Pulmonary Pharmacology and Therapeutics*, 24:452–465, 2011.

D. Schaafsma, K. D. Mcneill, G. L. Stelmack, R. Gosens, H. A. Baarsma, B. G. J. Dekkers, E. Frohwerk, J. M. Penninks, P. Sharma, K. M. Ens, S. A. Nelemans, J. Zaagsma, A. J. Halayko, and H. Meurs. Insulin increases the expression of contractile phenotypic markers in airway smooth muscle. *American Journal of Physiology - Cell Physiology*, 293:429–439, 2007.

C. Y. Seow. Hill's equation of muscle performance and its hidden insight on molecular mechanisms. *The Journal of General Physiology*, 142(6):561–573, 2013.

M. Shi, J. Zhu, R. Wang, X. Chen, L. Mi, T. Walz, and T. A. Springer. Latent TGF-β structure and activation. *Nature*, 474(7351):343–351, 2011.

A. Shifren and R. P. Mecham. The stumbling block in lung repair of emphysema: Elastic fiber assembly. In *Proceedings of the American Thoracic Society*, volume 3, pages 428–433, 2006.

J. Stålhand and G. A. Holzapfel. Length adaptation of smooth muscle contractile filaments in response to sustained activation. *Journal of Theoretical Biology*, 397:13–21, 2016.

B. C. Starcher. Elastin and the lung. *Thorax*, 41(8):577–85, 1986.

M. A. Stolarska, Y. Kim, and H. G. Othmer. Multi-scale models of cell and tissue dynamics. *Phil. Trans. R. Soc. A*, 367:3525–3553, 2009.

X. Tan and M. J. Sanderson. Bitter tasting compounds dilate airways by inhibiting airway smooth muscle calcium oscillations and calcium sensitivity. *British Journal of Pharmacology*, 171:646–662, 2014.

A. L. Tatler. Unpublished personal communication, 2016.

A. L. Tatler. Unpublished personal communication, 2019.

A. L. Tatler and G. Jenkins. TGF-β activation and lung fibrosis. *Annals of The American Thoracic Society*, 9(3), 2012.

A. L. Tatler and G. Jenkins. Reducing affinity of αvβ8 interactions with latent TGF-β: dialling down fibrosis. *Annals of Translational Medicine*, 3(1):8–10, 2015.

A. L. Tatler, A. E. John, L. Jolly, A. Habgood, J. Porte, C. E. Brightling, A. J. Knox, L. Pang, D. Sheppard, X. Huang, and G. Jenkins. Integrin αvβ5-mediated TGF-β activation by airway smooth muscle cells in asthma. *Journal of immunology (Baltimore, Md. : 1950)*, 187(11):6094–6107, 2011.

A. L. Tatler, A. T. Goodwin, O. Gbolahan, G. Saini, J. Porte, A. E. John, R. L. Clifford, S. M. Violette, P. H. Weinreb, H. Parfrey, P. J. Wolters, J. Gauldie,

M. Kolb, and G. Jenkins. Amplification of TGF-β induced ITGB6 gene transcription may promote pulmonary fibrosis. *PloS one*, 11(8):0158047, 2016.

H. A. W. M. Tiddens, W. Hofhuis, J. M. Bogaard, W. C. J. Hop, H. De Bruin, L. N. A. Willems, and J. C. De Jongste. Compliance, hysteresis, and collapsibility of human small airways. *American Journal of Respiratory and Critical Care Medicine*, 160(4):1110–1118, 1999.

T. Trian, G. Benard, H. Begueret, R. Rossignol, P. O. Girodet, D. Ghosh, O. Ousova, J. M. Vernejoux, R. Marthan, J. M. Tunon de Lara, and P. Berger. Bronchial smooth muscle remodeling involves calcium-dependent enhanced mitochondrial biogenesis in asthma. *The Journal of experimental medicine*, 204 (13):3173–81, 2007.

C. Truesdell and W. Noll. *The Non-Linear Field Theories of Mechanics*. Springer, Berlin, Heidelberg, 2nd edition, 1992. ISBN 978-3-662-13185-5.

C. Truesdell and R. Toupin. *The Classical Field Theories*. Springer Berlin Heidelberg, 1960.

P. Vehviläinen, M. Hyytiäinen, and J. Keski-Oja. Matrix association of latent TGF-beta binding protein-2 (LTBP-2) is dependent on fibrillin-1. *Journal of Cellular Physiology*, 221:586–593, 2009.

L. M. Wakefield, T. S. Winokur, R. S. Hollands, K. Christopherson, A. D. Levinson, and M. B. Sporn. Recombinant latent transforming growth factor β-1 has a longer plasma half-life in rats than active transforming growth factor β-1, and a different tissue distribution. *The Journal of Clinical Investigation*, 86(6): 1976–1984, 1990.

W. A. Wall, L. Wiechert, A. Comerford, and S. Rausch. Towards a comprehensive computational model for the respiratory system. *International Journal for Numerical Methods in Biomedical Engineering*, 26(7):807–827, 2010.

I. Wang, A. Z. Politi, N. Tania, Y. Bai, M. J. Sanderson, and J. Sneyd. A Mathematical Model of Airway and Pulmonary Arteriole Smooth Muscle. *Biophysical Journal*, 94(6):2053–2064, 2008.

L. Wang, P. D. Paré, and C. Y. Seow. Selected contribution: Effect of chronic passive length change on airway smooth muscle length-tension relationship. *Journal of Applied Physiology*, 90(2):734–740, 2001.

Y. Wang, S. Son, S. M. Swartz, and N. C. Goulbourne. A mixed von Mises distribution for modeling soft biological tissues with two distributed fiber properties. *International Journal of Solids and Structures*, 49(21):2914–2923, 2012.

J. E. Ward, T. Harris, T. Bamford, A. Mast, M. C. F. Pain, C. Robertson, D. Smallwood, T. Tran, J. Wilson, and A. G. Stewart. Proliferation is not increased in airway myofibroblasts isolated from asthmatics. *European Respiratory Journal*, 32(2):362–371, 2008.

R. G. Wells. Tissue mechanics and fibrosis. *Biochimica et Biophysica Acta - Molecular Basis of Disease*, 1832:884–890, 2013.

S. E. Wenzel. Asthma: defining of the persistent adult phenotypes. *Lancet*, 368: 804–813, 2006.

A. R. West, H. T. Syyong, S. Siddiqui, C. D. Pascoe, T. M. Murphy, H. Maarsingh, L. Deng, G. N. Maksym, and Y. Bossé. Airway contractility and remodeling: links to asthma symptoms. *Pulmonary Pharmacology and Therapeutics*, 26:3–12, 2013.

J. B. West. *Pulmonary Pathophysiology : The Essentials*. London : Lippincott Williams & Wilkins, Philadelphia, 7th edition, 2008. ISBN 9781451107135.

J. B. West. *Respiratory Physiology : The Essentials*. London : Lippincott Williams & Wilkins, Philadelphia, 9th edition, 2011. ISBN 1609136403.

B. R. Wiggs, C. A. Hrousis, J. M. Drazen, and R. D. Kamm. On the mechanism of mucosal folding in normal and asthmatic airways. *Journal of Applied Physiology*, 83(6):1814–1821, 1997.

P. J. Wipff, D. B. Rifkin, J. J. Meister, and B. Hinz. Myofibroblast contraction activates latent TGF-β1 from the extracellular matrix. *The Journal of cell biology*, 179(6):1311–23, 2007.

F. S. Wong and R. T. Shield. Large plane deformations of thin elastic sheets of neo-Hookean material. *Zeitschrift für angewandte Mathematik und Physik ZAMP*, 20(2):176–199, 1969.

P. G. Woodruff, G. M. Dolganov, R. E. Ferrando, S. Donnelly, S. R. Hays, O. D. Solberg, R. Carter, H. H. Wong, P. S. Cadbury, and J. V. Fahy. Hyperplasia of smooth muscle in mild to moderate asthma without changes in cell size or gene expression. *American Journal of Respiratory and Critical Care Medicine*, 169 (9):1001–1006, 2004.

Y. C. Xia, N. Singh Redhu, L. M. Moir, C. Koziol White, A. J. Ammit, L. Al Alwan, B. Camoretti Mercado, and R. L. Clifford. Pro-inflammatory and immunomodulatory functions of airway smooth muscle: emerging concepts. *Pulmonary Pharmacology & Therapeutics*, 26:64–74, 2013.

Y. D. Xu, J. Hua, A. Mui, R. O'Connor, G. Grotendorst, and N. Khalil. Release of biologically active TGF-β1 by alveolar epithelial cells results in pulmonary fibrosis. *American Journal of Physiology-Lung Cellular and Molecular Physiology*, 285:527–539, 2003.

W. H. Yang. Stress concentration in a rubber sheet under axially symmetric stretching. *Journal of Applied Mechanics, Transactions ASME*, 34(4):942–946, 1967.

Y. Yano, M. Yoshida, S. Hoshino, K. Inoue, H. Kida, M. Yanagita, T. Takimoto, H. Hirata, T. Kijima, T. Kumagai, T. Osaki, I. Tachibana, and I. Kawase. Antifibrotic effects of theophylline on lung fibroblasts. *Biochemical and Biophysical Research Communications*, 341:684–690, 2006.

L. Yu, M. C. Hébert, and Y. E. Zhang. TGF-β receptor-activated p38 MAP kinase mediates smad-independent TGF-β responses. *The European Molecular Biology Organization Journal*, 21(14):3749–3759, 2002.